UNIVERSIDAD COMPLUTENSE DE MADRID

FACULTAD DE CIENCIAS FÍSICAS

Departamento de Física de Materiales

TESIS DOCTORAL

Alta eficiencia termoeléctrica en películas delgadas nanoestructuradas de SiGe, Cu_2Se y Ag_2Se depositadas por pulverización catódica

MEMORIA PARA OPTAR AL GRADO DE DOCTOR

PRESENTADA POR

Jaime Andrés Pérez Taborda

Directores

María Soledad Martín González
Fernando Briones Fernández-Pola

Madrid, 2018

UNIVERSIDAD COMPLUTENSE MADRID

FACULTAD DE CIENCIAS FÍSICAS

DEPARTAMENTO DE FÍSICA DE MATERIALES

ALTA EFICIENCIA TERMOELÉCTRICA EN PELÍCULAS DELGADAS NANOESTRUCTURADAS DE SiGe, Cu_2Se Y Ag_2Se DEPOSITADAS POR PULVERIZACIÓN CATÓDICA

Memoria presentada por

JAIME ANDRÉS PÉREZ TABORDA

Para optar al grado de Doctor en Ciencias Físicas

por la Universidad Complutense de Madrid

Directores

Dra. MARÍA SOLEDAD MARTÍN GONZÁLEZ

Prof. FERNANDO BRIONES FERNÁNDEZ-POLA

INSTITUTO DE MICRO Y NANOTECNOLOGÍA

CONSEJO SUPERIOR DE INVESTIGACIONES CIENTÍFICAS

2017

Este trabajo doctoral ha sido realizado en el Instituto de Micro y Nanotecnología (IMN), perteneciente a la Agencia Estatal Consejo Superior de Investigaciones Científicas (CSIC). Ha sido dirigido por la *Dra. MARÍA SOLEDAD MARTÍN GONZÁLEZ* y el *Prof. FERNANDO BRIONES FERNÁNDEZ-POLA*. La realización de esta tesis doctoral ha sido posible gracias a la financiación del proyecto europeo NANOHITEC 263306, el proyecto nacional PHOMENTA MAT2011-27911, proyecto Intramural INFANTE y a la concesión de una ayuda FPI del Ministerio de Economía, Industria y Competitividad - Gobierno de España.

Agradecimientos

Deseo expresar mi mas sincera gratitud y reconocimineto a mis directores de tesis, la Dra. *Marisol Martín González* y el Profesor Dr. *Fernando Briones*, por su permanente apoyo y acompañamiento en el desarrollo de esta tesis. Sin su dirección y dedicación no hubiese sido posible este logro personal y profesional. A mi codirectora la Dra. *Marisol Martín González*, mi gratitud por dirigirme y apoyarme durante estos cuatro años. Su constante disposición, entusiasmo y oportuna orientación, han hecho posible la exitosa finalización de esta tesis doctoral. Gracias por compartir su experiencia y criterio científico a lo largo de estos años y por la confianza depositada en mí al acogerme en su grupo de investigación.

A mi codirector el Profesor Dr. *Fernando Briones*, gracias por el tiempo dedicado en el laboratorio y compartirme allí una parte de su experiencia científica. Gracias por inculcarme la pasión y el respeto por lo que se hace y por mostrarme nuevas facetas del mundo de la investigación durante estos años. Ha sido un verdadero honor tenerles como directores y espero poder seguir contando con ustedes en mi futuro cercano.

Gracias a todos mis compañeros de grupo, esa familia con la que he tenido el placer de estar día tras día a lo largo de estos años: *Alejandra, Begoña, Blanca, Cristina, David, Jaime, Jon, Juanjo, Liliana, Marina, Marta, Miguel, Olga, Pedro, Rafael, Rut.* Al trio de locos *Marta, Miguel* gracias por abrirme su corazón al momento de llegar al grupo. A la Dra. *Olga Caballero* por su apoyo, preocupación y los buenos momentos que hemos compartido como compañeros de despacho en esta etapa final.

Gracias a todos y todas los que han convertido el Instituto de Microelectrónica de Madrid en mas que el IMM, en un hogar lejos de casa. A *Manuel* por su amistad, bondad y carisma. A los integrantes de Nano4Energy, Dr. *Iván Fernández* y *Ambiörn Wennberg*, gracias compañero.

Especial agradecimiento a los integrantes del Grupo de Pesquisa e Laboratório de Superfícies e Nanoestruturas - *LabSurf*, del Centro Brasileiro de Pesquisas Físicas en Rio de Janeiro en Brasil. A su director Dr. *Alexandre Mello* gracias por abrirme las puertas de su grupo durante las dos estancias que curse allí y a sus integrantes *Bene, Denise, Elvis, Henrique, Luisa, Rogelio* por su hospitalidad y camaradería. Al Dr. *Elvis López* por su amistad y compañía en las largas noches de medidas en el sincrotrón en campinas.

Gracias a los integrantes del grupo Quantum Engineered Systems and Technology en Birck Nanotechnology Center en Purdue University. En especial a su director el Prof. *Ali Shakouri* por permitirme compartir con él y su grupo *Kerry, Amr, Yu Gong, Shengyu Jin* y en especial *Yee Rui Koh* un intenso verano de trabajo. Ha sido todo un privilegio.

Gracias a *Lili*, por ser siempre mí compañera, mí pedacito de utopía. A mi madre de quien solo he recibido amor, y a toda mi familia por su incondicionalidad y alegría. A mis amigos y mi pueblo, a los que espero recuperar después de esta larga ausencia.

Estos agradecimientos no pretenden ser un compendio detallado, ni mucho menos una despedida. Con estas lineas, solo pretendo materializar mi profundo y sincero agradecimiento a todos y todas las personas con las que desde la cotidianidad, hemos entretejido vínculos de amistad y compañerismo; con la excusa de esta tesis, hemos podido compartir los últimos cuatro años, que han sido los mas intensos de mi vida. Espero en otro tiempo-espacio poder seguir contando con cada uno de ustedes, tienen en mí un fiel amigo y tal como aseguraba el gran escritor colombiano Álvaro Mutis: *Cuando la gratitud es tan absoluta las palabras sobran.*

Dedicatoria

A Juan David, cuanto me disminuye tu ausencia,

es como tener siempre la primavera, pero con una esquina rota...

« Me atrevo a pensar, que es esta realidad descomunal, y no sólo su expresión literaria, la que este año ha merecido la atención de la Academia Sueca de las Letras. Una realidad que no es la del papel, sino que vive con nosotros y determina cada instante de nuestras incontables muertes cotidianas, y que sustenta un manantial de creación insaciable, pleno de desdicha y de belleza, del cual este colombiano errante y nostálgico no es más que una cifra más señalada por la suerte. Poetas y mendigos, músicos y profetas, guerreros y malandrines, todas las criaturas de aquella realidad desaforada hemos tenido que pedirle muy poco a la imaginación, porque el desafío mayor para nosotros ha sido la insuficiencia de los recursos convencionales para hacer creíble nuestra vida. Este es, amigos, el nudo de nuestra soledad. Un día como el de hoy, mi maestro William Faulkner dijo en este lugar: "Me niego a admitir el fin del hombre". No me sentiría digno de ocupar este sitio que fue suyo si no tuviera la conciencia plena de que por primera vez desde los orígenes de la humanidad, el desastre colosal que él se negaba a admitir hace 32 años es ahora nada más que una simple posibilidad científica. Ante esta realidad sobrecogedora que a través de todo el tiempo humano debió de parecer una utopía, los inventores de fábulas que todo lo creemos nos sentimos con el derecho de creer que todavía no es demasiado tarde para emprender la creación de la utopía contraria. Una nueva y arrasadora utopía de la vida, donde nadie pueda decidir por otros hasta la forma de morir, donde de veras sea cierto el amor y sea posible la felicidad, y donde las estirpes condenadas a cien años de soledad tengan por fin y para siempre una segunda oportunidad sobre la tierra.»

Gabriel García Márquez
"Nobel Lecture: La soledad de America Latina"
Stockholm, 1983

Índice general

Resumen iv

Abstract v

1. Introducción 1

1.1. Termoelectricidad: Efectos Seebeck y Peltier . . . 1

1.1.1. La eficiencia termoeléctrica y la figura de mérito zT . . . 4

1.1.2. Escenario actual de los materiales termoeléctricos . . . 7

1.1.3. Materiales abordados durante esta tesis . . . 9

1.2. Silicio Germanio . . . 15

1.3. Seleniuros . . . 19

1.3.1. Conductores superiónicos . . . 20

1.3.1.1. Termoeléctricos superiónicos . . . 21

1.3.1.2. Seleniuro de Cobre . . . 21

1.3.1.3. Seleniuro de Plata . . . 24

1.4. Pulverización catódica . . . 28

1.4.1. Pulverización catódica reactiva . . . 30

2. Métodos de caracterización 32

2.1. Técnicas de caracterización estructural . . . 32

2.1.1. Difracción de rayos X en ángulo rasante con fuente de radiación de sincrotrón . . . 32

2.1.2. Espectroscopía de fotoelectrones emitidos por Rayos X - (XPS) . . . 33

2.1.3. Microscopía Raman . . . 35

2.1.4. Microscopía de sonda Kelvin . . . 36

2.2. Caracterización Termoeléctrica . . . 37

2.2.1. Medidas de coeficiente Seebeck y resistividad eléctrica . . . 37

2.2.2. Medidas de las propiedades de transporte . . . 39

2.2.3. Microscopía de barrido térmico - SThM . . . 41

2.2.4. Otros equipos de caracterización utilizados . . . 43

2.2.4.1. Difracción de rayos X . . . 43

2.2.4.2. Microscopía electrónica de barrido con emisión de campo . . . 43

2.2.4.3. Energía dispersiva de rayos X . . . 43

2.2.4.4. Perfilometría . . . 43

Bibliografía 44

Publicaciones **59**

Publicaciones contenidas en esta tesis doctoral 63

Articulo I **64**

Articulo II **65**

Articulo III **66**

Articulo IV **67**

Articulo V **68**

Índice de figuras

1.1. Esquema del *efecto Seebeck* y *efecto Peltier* 3
1.2. Relaciones entre los componentes de la figura de mérito zT 5
1.3. Mecanismos de dispersion fonónica 6
1.4. Mecanismos de acumulación en la dispersión fonónica 7
1.5. Figura de mérito termoeléctrica en función de la temperatura para algunos de los mejores materiales *tipo p* y *tipo n* 8
1.6. Evolución de la figura de mérito en las últimas décadas 12
1.7. Consolidado de los principales materiales termoeléctricos 13
1.8. Representación esquemática de los valores de escasez, producción y reservas de para gran parte de la tabla tabla periódica de los elementos 14
1.9. Esquema de la estructura cúbica del Silicio Germanio 15
1.10. Estructura Cu_2Se y diagrama de Fase 22
1.11. Estado del arte de la figura de mérito para los calcogenuros binarios basados en Cobre 24
1.12. Estructura de baja y alta temperatura Ag_2Se 27
1.13. Diagrama de Fase Ag_2Se 27
1.14. Esquema del proceso de pulverización catódica 30
1.15. Montaje experimental de sistema de pulverización catódica reactiva pulsado de selenio y la*Sonda plana de Langmuir* y *copa de Faraday* 31

2.1. Esquema de la línea de sincrotrón en donde se ha llevado a cabo las medidas de difracción de rayos X en ángulo rasante en diferentes temperaturas 33
2.2. Descripción esquemática del proceso de medida de espectroscopía de fotoelectrones emitidos por Rayos X con calentamiento $In - Situ$ 35
2.3. Microscopía Raman 37
2.4. Microscopía por sonda Kelvin - KPM 38
2.5. Esquema del sistema comercial LSR-3 Linseis y la disposición para realizar medidas de películas delgadas 39
2.6. Montaje experimental de la Microscopía de barrido térmico - SThM 42

Resumen

Los materiales termoeléctricos convierten energía térmica en energía eléctrica y viceversa. Las ventajas de los materiales termoeléctricos son que no poseen partes móviles, son dispositivos de larga duración, son silenciosos, pueden utilizarse en aplicaciones para enfriar y calentar, y también pueden emplearse para la recuperación de energía proveniente del calor residual. En los últimos años se han propuesto diferentes alternativas prometedoras destinadas a conseguir sistemas con coeficientes zT superiores a 1. Un coeficiente zT de 1 supone una eficiencia de generación de energía eléctrica a partir de energía térmica de un 10 % del límite teórico, dado por el ciclo de Carnot, mientras que un valor de 4 supondría un 30 %.

Para este propósito, esto es, estudiar cómo aumentar la eficiencia termoeléctrica en distintos materiales, en primer lugar se han obtenido películas delgadas de $Si_{0,8}Ge_{0,2}$ a través de un sistema de pulverización catódica de ultra alto vacío construido para este fin. El primer objetivo ha sido lograr obtener películas delgadas de $Si_{0,8}Ge_{0,2}$ policristalinas con bajos valores de conductividad térmica (cercanos a los reportados en la literatura para los nanohilo) y a bajas temperaturas de fabricación. Adicionalmente, un segundo objetivo ha consistido en la fabricación de nanomallas de $Si_{0,8}Ge_{0,2}$ con un control del tamaño de poro y del espesor de la nanoestructura. Este nuevo enfoque en la fabricación se realiza en un único paso, sin necesidad de procesos litográficos o tratamientos térmicos adicionales.

El segundo núcleo de estudio en esta tesis doctoral ha estado alrededor de la fabricación de películas delgadas de seleniuros de cobre $Cu_{2-x}Se$ y plata $Ag_{2-x}Se$. Estos materiales han exhibido recientemente prometedores valores de zT, así como algunas propiedades particularmente curiosas, como una conducción eléctrica similar a un líquido iónico a altas temperaturas. Dentro de esta tesis doctoral, un tercer objetivo ha sido el diseño y construcción de un sistema para la deposición de estos materiales en forma de películas delgadas por procesos de sputtering reactivo. De esta forma somos capaces de obtener películas con una composición bien definida mediante un adecuado control de los parámetros de crecimiento. Esto nos permite de forma sencilla realizar estudios de la variación de las propiedades con la composición del material. Además, nuestro sistema nos permite modificar con gran celeridad los parámetros de crecimiento, de tal manera que se pueden obtener multicapas que den lugar a procesos de dispersión de fonones, reduciendo así la conductividad térmica del material (y mejorando por lo tanto el factor zT).

Abstract

Thermoelectric materials are those that convert thermal energy into electrical energy and vice-versa. The advantages of thermoelectric devices are many, such as being solid state devices, that is, with no mobile parts and no noise, and they are durable, among others. They can be used in applications for heating and cooling, but more importantly, they can be used to recover wasted heat converting it into electrical energy. In the last years there have been different promising ways of obtaining thermoelectric systems with figures of merit zT higher than 1. A zT of 1 means to have an electric energy generation efficiency from thermal gradients of 10 % of the theoretical limit, which is given by the Carnot cycle, while a value of zT of 4 would mean a 30 % efficiency.

In order to study one route of increasing the thermoelectric efficiency of different materials, thin films of $Si_{0,8}Ge_{0,2}$ have been fabricated with a sputtering system at ultrahigh vacuum, which was constructed specifically to this purpose. The first objective was to obtain polycrystalline thin films of $Si_{0,8}Ge_{0,2}$ fabricated at low temperatures and with reduced thermal conductivity (with values near the ones reported in literature for nanowires of the same material). Additionally, a second objective consisted in the fabrication of nano-meshes of $Si_{0,8}Ge_{0,2}$ with controlled pore size and thickness of the nano-structure. This new approach in the fabrication was performed in a single step, without any lithographical process or additional thermal treatments.

The second nucleus of this PhD Thesis has been on the fabrication of thin films of copper selenides ($Cu_{2-x}Se$) and silver selenides ($Ag_{2-x}Se$). This materials have recently exhibited quite promising values of zT, as well as some quite particular properties, such as an electrical conductivity similar to that of an ionic liquid at high temperatures. In the frame of this PhD Thesis, the design and construction of a system for the deposit of such materials in the form of thin films via reactive sputtering has been also performed. With the aid of this reactive sputtering system we are able to obtain films with a well-defined and controlled composition due to an adequate regulation of the growth parameters. This allows us to perform studies on the different properties of the films as a function of the stoichiometry, for instance. Moreover, with our system one can modify the growth parameters rapidly, which provides a way to obtain multi-layers which provide a higher phonon dispersion and thus, a reduction of the thermal conductivity of the material (which produces a further increase the thermoelectric figure of merit,zT).

Capítulo 1

Introducción

1.1. Termoelectricidad: Efectos Seebeck y Peltier

La termoelectricidad (TE) es un fenómeno físico en el cual un gradiente de temperatura se transforma en energía eléctrica y viceversa. Los orígenes de la termoelectricidad se remontan a principios del siglo XIX, cuando en 1822, *Thomas Johann Seebeck*, físico-médico estonio de origen alemán descubrió uno de los fenómenos termoeléctricos más importantes y que lleva en su honor su apellido. Seebeck observó la desviación en la aguja de una brújula al mantener dos uniones de diferentes metales a diferentes temperaturas [1–3]. Esto se debía a que los niveles de energía de los electrones para cada metal cambiaban de forma diferente y provocando una diferencia de voltaje entre las uniones lo que se traducía en una corriente eléctrica y en últimas en el campo magnético alrededor de los cables, lo que afectaba la brújula. En ese momento, Seebeck no reconoció que había una corriente eléctrica involucrada, por lo que llamó al fenómeno *efecto termomagnético*[1–3]. El responsable de utilizar por primera vez el término termoelectricidad fue el físico danés *Hans Christian Ørsted* en 1827 [3, 4].
Este efecto fue conocido posteriormente como **coeficiente Seebeck (S)** y es en cierta manera, una medida de la entropía transportada por partícula cargada en el material. Cuantos más estados disponibles haya para los portadores de carga, mayor será el *coeficiente Seebeck (S)*. Es decir, S aumenta a medida que disminuye la concentración de portadores de carga. Para los metales, S es del orden de unos pocos microvoltios por Kelvin, para los semiconductores es del orden de decenas a cientos de microvoltios por Kelvin y para los aislantes es del orden de cientos a miles de microvoltios por Kelvin [5]. En lo que respecta a su signo, el coeficiente Seebeck es positivo para materiales semiconductores *tipo p* (aquellos con huecos como portadores mayoritarios) y negativo para semiconductores de *tipo n* (aquellos con electrones como portadores mayoritarios). Poco después, en 1834 el físico francés *Jean Charles Athanase Peltier* descubrió el efecto inverso, el cual se define a partir de un gradiente de temperatura originado a partir de una diferencia de voltaje que atraviesa la unión de dos metales. El efecto Peltier consiste básicamente en que los portadores de carga también pueden transportar calor o energía térmica cuando éstos fluyen[6]. Si el material está en equilibrio, y se impone un flujo de electrones como consecuencia de la aplicación de

un voltaje externo, no sólo habrá un flujo de corriente eléctrica, sino también un flujo de calor. Este flujo de corriente se traduce en la separación de una fuente de calor y frío en la unión de ambos materiales dependiendo de su dirección. Un par de décadas más tarde, en 1851 *William Thomson* [7] (conocido más tarde como *Lord Kelvin*) logró, mediante el uso de argumentos termodinámicos, unificar el *efecto Seebeck* y *Peltier* en una única expresión completa y compacta [7–9]. Este tercer efecto lleva su nombre y describe la absorción o generación de calor a lo largo de un conductor que transporta corriente bajo un gradiente térmico. En definitiva, si consideramos tanto para el *efecto Seebeck* como para el *efecto Peltier* un circuito formado a partir de dos conductores de materiales distintos que están conectados eléctricamente en serie, pero térmicamente en paralelo como se muestra en la **Figura 1.1** podemos definir el voltaje inducido como el producto del *coeficiente Seebeck (S)* por la diferencia de temperatura como se muestra en la Ecuación 1.1:

$$\mathbf{V} = \boldsymbol{S}(T_1 - T_2) \implies \boldsymbol{S} = \frac{\mathbf{V}}{\boldsymbol{\Delta} T} \tag{1.1}$$

A principios del siglo XX, los avances en el campo de la termoelectricidad estuvieron más centrados en el desarrollo de una teoría que explicara los fenómenos observados en el siglo anterior[11, 12]. Desarrollos teóricos como los llevados a cabo por *Edmund Altenkirch* [11, 13]continuaron los trabajos previos realizados por *Lord Rayleigh* [14] sobre la eficiencia de una termopila [11, 13]. Para ese momento las ideas de *Sadi Carnot* recogidas en su libro *"Reflexiones sobre la potencia motriz del fuego y sobre las máquinas propias a desarrollar esta potencia"* [15] (*Réflexions sur la puissance motrice du feu et sur les machines propres à développer cette puissance*)[16], publicado en 1824, ya eran ampliamente conocidas y se consideraba a la termopila como un *"motor termodinámico bastante imperfecto"*. Es en este momento cuando *Altenkirch* propuso la primera descripción sobre la característica fundamental que debería cumplir un buen material termoeléctrico (TE). Su conclusión fue que éstos materiales deben exhibir un alto *coeficiente de Seebeck (S)*, acompañado de una alta conductividad eléctrica σ, es decir, una baja resistencia eléctrica con el fin de minimizar el calentamiento por efecto Joule [17, 18]. Adicionalmente, deben de tener una baja conductividad térmica κ, con el fin de poder retener el calor en las uniones y mantener así un gradiente de temperatura definido que promueva un coeficiente Seebeck continuo [19, 20].

Desde el punto de vista experimental, algunos trabajos pioneros en metales y aleaciones metálicas fueron descartados debido a sus bajos valores de coeficiente de Seebeck. No fue hasta finales de la década de 1950, con el desarrollo de materiales semiconductores y la aplicación de los nuevos enfoques de la física del estado sólido, que los materiales termoeléctricos lograron su resurgimiento [21–27]. Estas nuevas ideas inspiraron al físico ruso *Abram Ioffe* [25] (antiguo estudiante de *Wilhelm Röntgen*[28]) a introducir la *figura de mérito (zT)* como una relación que contiene los diferentes coeficientes de transporte, realizando la primera clasificación eficiente de los diferentes materiales TE. Una lectura más profunda de su trabajo puede ser consultada en detalle en estas referencias[21–27]. Estas contribuciones

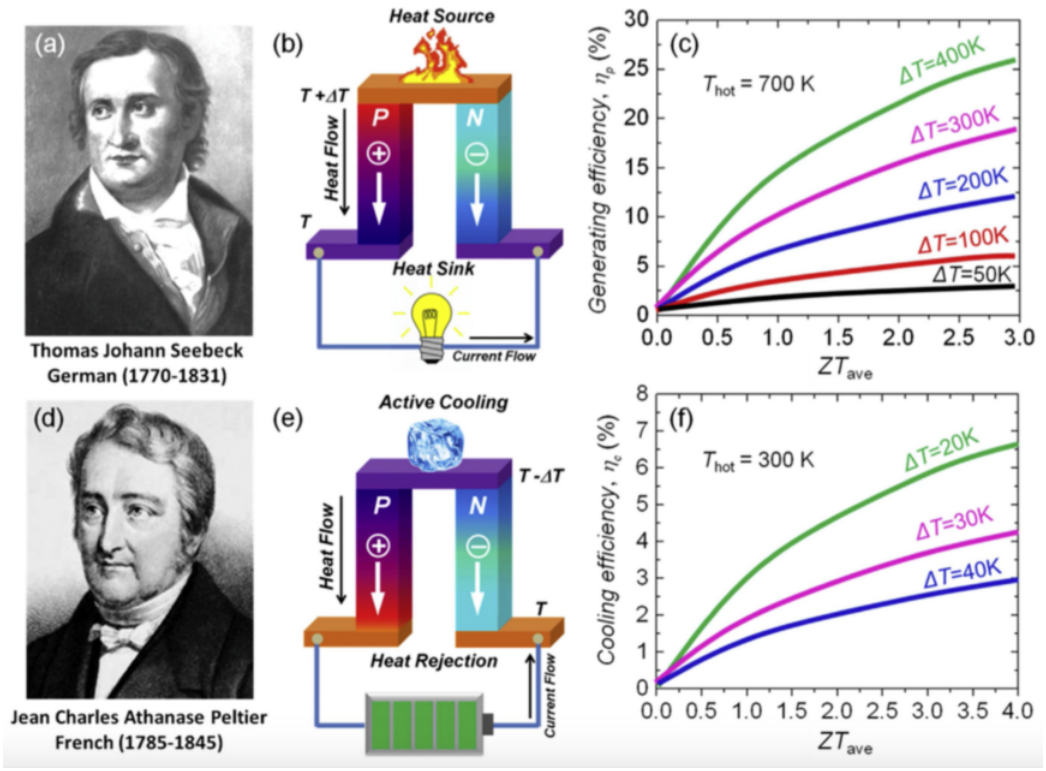

Figura 1.1: En la figura **(a)** se muestra una imagen del físico alemán *Thomas Johann Seebeck*, en **(b)** un esquema del *efecto Seebeck* para la generación de energía a partir de una diferencia de temperatura aplicada, con la representación del flujo de los portadores de carga (electrones o huecos) que fluyen desde el lado caliente al lado frío y su el correspondiente flujo de corriente a través del circuito. En **(c)** se muestra la eficiencia de generación de energía en función del promedio del módulo $zT_{promedio}$; Asimismo, la imagen **(d)** corresponde a una imagen del físico francés *Jean Charles Athanase Peltier*, en **(e)** el *Efecto Peltier* en honor a su nombre. En el proceso de refrigeración el calor es tomado en la unión superior del módulo y es absorbido en la unión inferior cuando se hace fluir una corriente a través del circuito. Finalmente, **(f)** se detalla la eficiencia de enfriamiento en función del promedio del módulo $zT_{promedio}$. Imagen tomada de la referencia [10]

propiciaron un período muy activo de investigaciones teóricas y experimentales alrededor de los materiales TE, pero a mediados de los años sesenta, el interés la termoelectricidad se derrumbó bajo el peso de esperanzas exageradas y pocos avances significativos en aumentar la eficiencia de los materiales. Durante al menos 30 años, la termoelectricidad experimentó un marcado desaceleramiento en la investigación básica con algunos avances entre los que se resaltan los trabajos publicados en las referencias [29–34]. Entrados en la última década del siglo XX, nuevas ideas - entre las que sobresalen los aportes de *Hicks y Dresselhaus* en 1993 -[35], así como avances en nuevos materiales, renovaron el interés en la TE. La búsqueda de tecnologías más amigables con el medio ambiente y el naciente interés en la conversión del calor residual (como el generado por los motores de los automóviles), en energía eléctrica, principalmente impulsados por la necesidad de reducir el consumo de petróleo a nivel global, llevó a retomar la investigación en termoelectricidad.

1.1.1. La eficiencia termoeléctrica y la figura de mérito zT

Retomando el concepto de eficiencia de un material termoeléctrico propuesta por *Ioffe*[25], esta se define como:

$$\boldsymbol{zT = \frac{S^2\sigma}{\kappa}T} \tag{1.2}$$

donde $\boldsymbol{S}$ es el *coeficiente de Seebeck*, $\boldsymbol{T}$ es la *temperatura absoluta*, $\boldsymbol{\sigma}$ es la *conductividad eléctrica* y $\boldsymbol{\kappa}$ es la *conductividad térmica*. Esta figura de mérito es adimensional y se define para un solo material, y es distinta de la figura de mérito de un dispositivo donde zT_{Mdulo} es el promedio de las temperaturas entre el lado caliente y del lado frío del dispositivo [10, 36, 37]. La eficiencia de un módulo termoeléctrico de generación de potencia $\boldsymbol{n_{max}}$ viene dada por la Ecuación 1.3:

$$\boldsymbol{n_{max} = \frac{T_C - T_F}{T_C}\frac{\sqrt{1+zT}-1}{\sqrt{1+zT}+\frac{T_F}{T_C}}} \tag{1.3}$$

En el lado derecho de la fracción en 1.3 se define la eficiencia de Carnot, que es la misma para cualquier motor térmico que funcione entre un foco frío T_F y uno caliente T_C. La fracción restante es aproximadamente proporcional a $\sqrt{zT}$, y representa las pérdidas irreversibles de energía útil para la conducción eléctrica y térmica. Actualmente, los mejores materiales termoeléctricos en uso tienen una figura de mérito zT superior a 1 [36–40]. Para que las soluciones termoeléctricas se utilicen más allá del laboratorio o de nichos muy específicos y se integren en el esquema energético global, se necesitan valores de zT>1 [36–40]. Para entender cómo incrementar la figura de mérito de un material, podemos reescribir la ecuación 1.2 en términos de la conductividad eléctrica σ, como la suma de la contribución de la conductividad térmica en la red κ_{Red} y la conductividad térmica electrónica igual a $\boldsymbol{\kappa} = \boldsymbol{L\sigma T}$, donde L es la constante de proporcionalidad o «número de Lorenz:

$$\boldsymbol{L = \frac{\kappa}{\sigma T} = \frac{\pi^2}{3}\left(\frac{k_B}{e}\right)^2 = 2{,}44 \times 10^{-8}\,\mathrm{W\,\Omega\,K^{-2}}.} \tag{1.4}$$

$$\boldsymbol{zT = \frac{S^2\sigma T}{\kappa_{Red} + L\sigma T}} \tag{1.5}$$

En la **Figura 1.2** se detalla este comportamiento en función de los portadores de cargas *(n)*. De este esquema, podemos deducir que existe una concentración óptima de portadores n para cuando el valor de zT es máximo. Esto es sólo cierto en una primera aproximación, debido a que el desacoplamiento de estas propiedades no es algo trivial y depende de muchos otros factores como las características intrínsecas del material, dimensionalidad, dopaje, geometría, entre otros aspectos que determinan la eficiencia TE.

De la **Figura 1.2** podemos observar la dependencia entre el numerador conocido como factor de potencia ($S^2\sigma$) y el denominador, que es conductividad térmica κ (en donde $\kappa = \kappa_{Electrnica}+\kappa_{Red}$)[41–44].

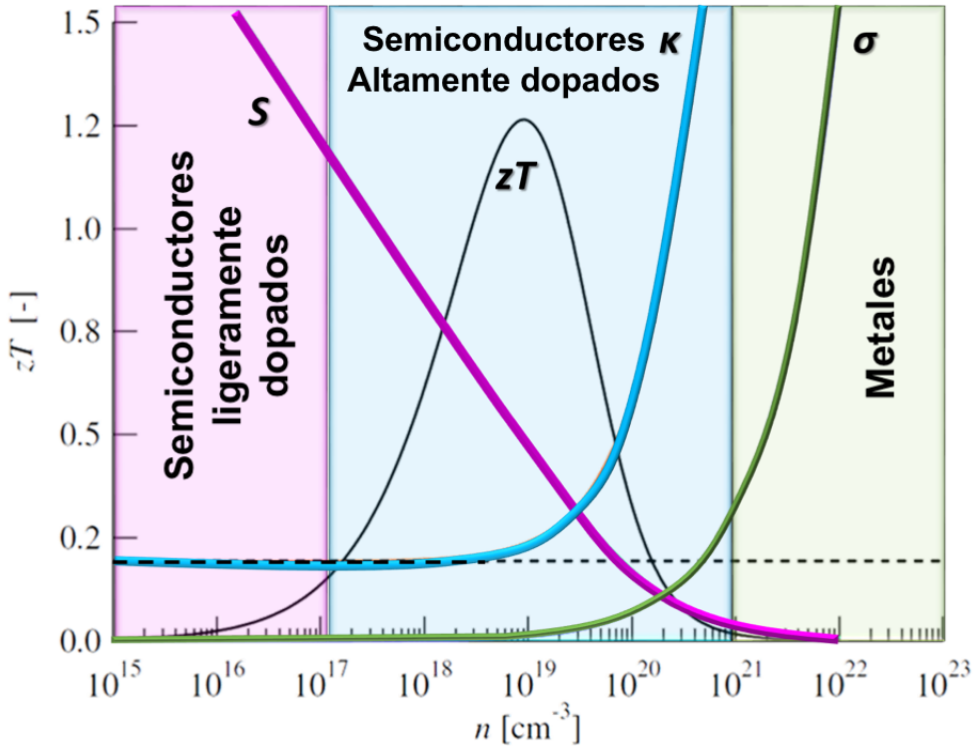

Figura 1.2: Resumen del valor de zT para algunos de los mejores materiales termoeléctricos en volumen en función de la temperatura. Imagen adaptada de la referencia [36]

Dentro de las estrategias para aumentar la figura de mérito se encuentra la incrementar el factor de potencia, lo cual es todo un desafío, ya que S y σ son inversamente proporcionales. Adicionalmente, el aumento en la σ ocasiona un aumento en la conductividad térmica electrónica κ_{Ele}. Algunas aproximaciones para aumentar el factor de potencia incluyen la creación de estados resonantes en el nivel de Fermi[45, 46], la convergencia de las bandas electrónicas [39, 47], y la optimización de la concentración de los portadores de carga [38–40]. La segunda aproximación para aumentar el valor de la figura de mérito en termoelectricidad es reducir la conductividad térmica. Con este objetivo se pueden incluir el uso de fases secundarias dentro del material con el fin de dispersar fonones [39, 42, 43, 48]. Asimismo, mediante la nanoestructuración [35, 40, 49] y la formación de aleaciones [43, 48, 50] se incrementa este tipo de dispersiones fonónicas. Las aleaciones propician una deformación debido al contraste de masa, lo que reduce la velocidad de grupo de los fonones. Un esquema de los diferentes procesos de dispersión fonónica se muestra en la **Figura 1.3**
En la **Figura 1.3** se representan algunos de los mecanismos más importantes de dispersión fonónica cómo son las nanoinclusiones, defectos o vacantes en el cristal los cuales reducen la trayectoria libre media de los diferentes fonones, reduciendo así la conductividad térmica de la red. En materiales puros (no-aleaciones o sin dopar), los mecanismos de dispersión de fonones dominantes van desde la dispersión por bordes de grano hasta la dispersión por colisiones fonón-fonón.

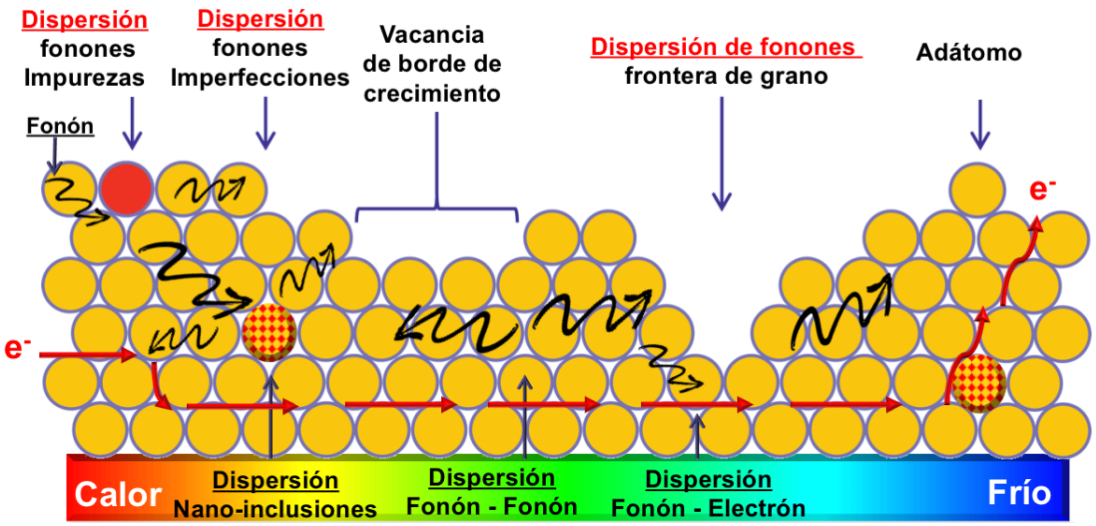

Figura 1.3: Mecanismos de dispersión de fonones: difusión de fonón-fonón Umklapp, dispersión de electrón-fonón, dispersión en un borde de grano, en nanoinclusiones, en defectos puntuales dislocaciones. Como puede verse, en los bordes de grano, las dislocaciones y los defectos puntuales, respectivamente, se dirigen a fonones con frecuencias bajas, medias y altas.

Una estrategia para reducir la conductividad térmica, es introducir inhomogeneidades puntuales, tales como átomos de otros materiales (formación de aleaciones), variaciones estructurales del material (cambios en la anisotropía) o defectos puntuales, por ejemplo. A través de éstos mecanismos, no sólo los fonones, sino también los electrones son dispersados, provocando una reducción de κ [42, 43, 51, 52]. En el caso de la fabricación de nanoestructuras, la idea es formar estructuras con tamaños más pequeños que las trayectorias libres medias de los fonones, pero mayores que las trayectorias libres medias de electrones o huecos, dado que los fonones son más fuertemente dispersados por las intercaras que los electrones o huecos [53]. Podemos ver fácilmente como el recorrido libre de los fonones influye en la conductividad térmica $\boldsymbol{k}$ a través de la relación:

$$\boldsymbol{k} = \frac{1}{3}\boldsymbol{\rho\lambda V_s C_v} \tag{1.6}$$

en donde $\boldsymbol{\rho}$ es la densidad, $\boldsymbol{V_s}$ es la velocidad del sonido en el sólido y $\boldsymbol{C_V}$ es su capacidad calorífica específica. En la **Figura 1.4**. Se muestra un ejemplo de cómo influye el camino libre medio en los diferentes procesos de dispersión y su contribución en la conductividad térmica. Es importante resaltar que para la reducción de la conductividad térmica no existe una única estrategia válida, sino que es necesario la suma de múltiples mecanismos de dispersión fonónica que incluyen desde las características intrínsecas del material TE, la dimensionalidad y el diseño en sí del módulo TE, hasta las temperaturas de operación, entre otros muchos factores. Éstos factores han sido tenidos en cuenta durante el desarrollo de esta tesis doctoral, en donde se han incluido diferentes aproximaciones para aumentar el factor de potencia y reducir la conductividad térmica.

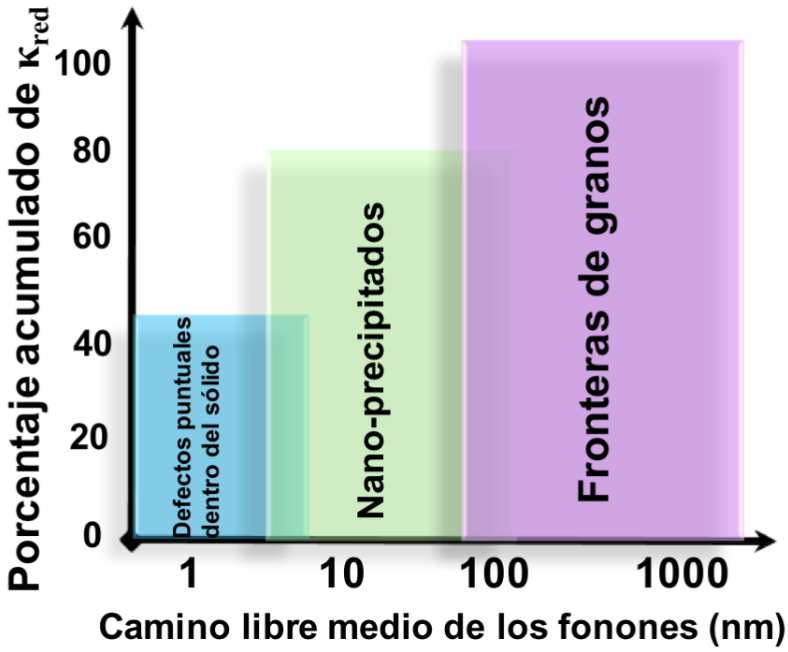

Figura 1.4: La imagen representa los diferentes mecanismos que contribuyen a la reducción en la conductividad térmica debido a la acumulación en la dispersión de fonones respecto a la trayectoria libre media del fonón en Si o PbTe en volumen. Imagen adaptada de [54]

1.1.2. Escenario actual de los materiales termoeléctricos

La eficiencia en los generadores termoeléctricos de última generación ha experimentado un aumentado de más de un 15 % debido a los nuevos desarrollos en materiales nanoestructurados en las últimas décadas [46, 55, 56]. Históricamente, la evolución en los materiales termoeléctricos (TE) ha dependido en gran medida de la extrapolación de algunos materiales conocidos a partir de los cuales se han sugerido nuevos compuestos y así se ha iniciado una nueva investigación. En la actualidad, sólo un reducido grupo de materiales han sido estudiados para su uso en termoelectricidad de las casi 40.000 posibles combinaciones estequiometrícas de sólidos orgánicos e inorgánicos que hay propuestos [55]. En la **Figura 1.6** se muestra un breve resumen de la evolución histórica a partir de la década de 1960 de algunos de los materiales TE más importantes. A mediados del siglo pasado, una primera generación de materiales en volumen fueron ampliamente estudiados con la intención de cubrir todo el rango de temperaturas para sus futuras aplicaciones como dispositivos, éstos son: Bi_2Te_3, PbTe y SiGe para *baja, media* y *alta* temperatura respectivamente. En la **Figura 1.5** se muestra el actual panorama de la eficiencia para los materiales TE. Durante las siguientes décadas la principal estrategia para mejorar los valores de zT consistió en controlar el dopaje en éstos materiales en volumen, reportando importantes avances en Bi_2Te_3-Sb_2Te_3, PbTe-SnTe, y $Si_{1-x}Ge_x$. Aunque éstos dopajes ciertamente ofrecían una reducción en la conductividad térmica, también provocaban una simultánea reducción en la movilidad de los portadores de carga, lo que limitaba el aumento total del zT (como se explicó en la sección anterior) [31].

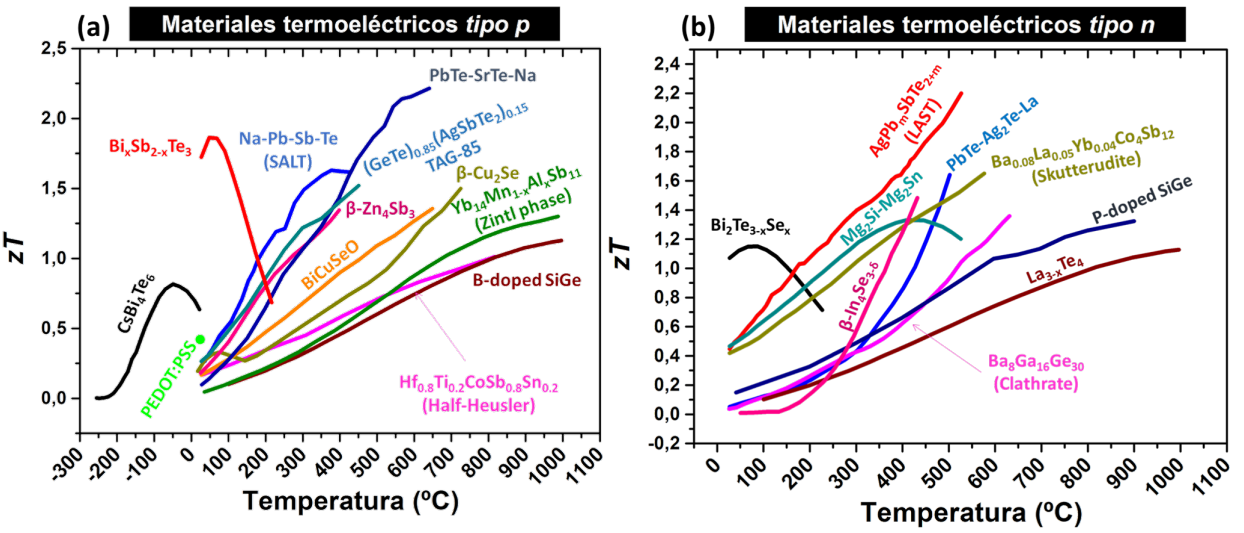

Figura 1.5: Figura de mérito termoeléctrica en función de la temperatura para materiales termoeléctricos tipo *tipo p* y *tipo n*. Gráfica tomada de la referencia [57]

Durante las siguientes tres décadas las investigaciones se centraron básicamente en éstos tres materiales; sobresaliendo los avances obtenidos en el SiGe debido a su amplio uso durante la carrera espacial por parte de NASA. En la próxima **el apartado 1.2** abordaremos este tema con más detalle. Como ya se mencionó, los trabajos de *Hicks y Dresselhaus* [35, 58] despertaron gran interés, debido a que proponían un aumento teórico en la zT a partir de la reducción de la dimensionalidad, lo que condujo a un renacimiento en el interés en el desarrollo de materiales TE de alto zT. En las dos últimas décadas se han consolidado dos enfoques diferentes para buscar la próxima generación de materiales termoeléctricos: el primero centrado en materiales termoeléctricos en volumen, específicamente en las nuevas familias de materiales con estructuras cristalinas mucho más complejas tales como: *escuteruditas* [44, 57], *clatratos*[59, 60], *calcogenuros*[39, 40, 48, 61] (Bi_2Te_3, $PbTe$, $AgSbTe_2$, etc.), aleaciones *Half-Heusler* [41] y fases de *Zintl*[41, 59, 60].

Algunos autores han logrado desacoplar total o parcialmente el factor de potencia de la conductividad térmica en éstos materiales complejos. Esto ha sido posible gracias a la utilización de nuevas aproximaciones que van desde complejos efectos de resonancia dentro de la celda unitaria, que han permitido la reducción adicional de κ_{Red}, hasta la nanoprecipitación en PbTe [45], nanogranos en Bi_2Te_3 y comportamiento similar a un líquido iónico en el caso de Zn_4Sb_3 [62], Cu_2Se [56] [63], interfaces activas de oxido en $CoSb_3$ [44] y SnSe[64]. El segundo enfoque se centra en reducir la dimensionalidad de los materiales con el fin reducir drásticamente la conductividad térmica, enfocándose en películas delgadas (incluyendo multicapas), nanohilos, nanotubos, nanomallas, puntos cuánticos, por mencionar sólo algunos ejemplos. Una importante revisión de éstos fenómenos puede ser encontrada en éstos artículos de revisión[39, 40, 47, 48, 50, 61].

Adicionalmente, el confinamiento cuántico en el plano ha aumentado sustancialmente el factor de potencia, mejorando las propiedades de transporte, lo que ha llevado a un incremento en las investigaciones sobre materiales TE en película delgada[58]. Los resultados han demostrado lo altamente dependientes que son las nanoestructuras TE de factores como tensión en la intercara muestra/sustrato, la orientación y fases cristalográficas presentes, incluyendo los cambios de fase en temperaturas y su reversibilidad; confinamiento fonónico en el caso de las multicapas, entre otros [42, 43, 61, 65]. En lo que respecta a los nanohilos, ha sido reportada una mejora en el zT, principalmente debido al confinamiento cuántico que sufre el material, proporcionando dispersiones fonónicas adicionales [42, 66]. Progreso similar se ha reportado con los nanotubos, en donde la dispersión de fonones en las superficies internas y externa, ha reducido drásticamente la κ [57, 59].
Estas nuevas aproximaciones de la nanoingeniería en los materiales TE han logrado resolver antiguos problemas, pero a su vez han generado nuevos desafíos como: garantizar un buen contacto eléctrico en todo un arreglo de alta densidad de nanohilos o nanotubos, la manipulación en la nanoescala y el desarrollo de técnicas de medida[61]. Una detallada recopilación de los principales materiales termoeléctricos que actualmente están en escena además de sus máximos valores de zT y mínimos valores de κ_L obtenidos por diferentes métodos se muestra en la **Figura 1.7**.

1.1.3. Materiales abordados durante esta tesis

Uno de los parámetros más críticos dentro del diseño de un dispositivo termoeléctricos es la selección de los materiales que se utilizarán. Dependiendo de su abundancia en la corteza terrestre, la técnica de fabricación a emplear, la necesidad de tratamientos posteriores a la fabricación (tratamientos térmicos, dopados, implantaciones, etc) y en últimas, el precio de los materiales, son factores que harán viable una producción a gran escala y una transferencia tecnológica exitosa. La **Figura 1.8** resume un detallado y cuidadoso estudio en el que se consideran los factores de producción, reserva y abundancia de todos los elementos de la tabla periódica. Esto nos da una perspectiva muy interesante del panorama al que se enfrentan no sólo los TE, sino todas las investigaciones en materiales que tengan como objetivo final el escalamiento de la investigación que se hace en el laboratorio de cara a su implementación en la sociedad. Además de éstos indicadores (de producción y escasez) hay factores sociales, políticos, medioambientales, económicos y de salubridad que hay que tener presentes, en especial con los llamados materiales estratégicos. Específicamente en lo que respecta a la comunidad europea, desde el 1 de julio de 2006 esta en vigor la directiva Europea *2002/95/CE* que restringe el uso de plomo (Pb), mercurio (Hg), cadmio (Cd), Cromo hexavalente (Cr^6) por su impacto ambiental y de salud pública. Esto deja sin posibilidad de uso y/o investigación a los teluros de plomo (PbTe) que como se muestra en la **Figura 1.6** y **Figura 1.7** tiene altos valores de zT.

Dentro del condicionamiento políticos y económico el ejemplo mas claro es el de las tierras raras. A excepción de la India, que aporta a la producción global sólo el 2 %, y Brasil con un discreto 0.4 %, la producción mundial de tierras raras depende casi y exclusivamente de China. Esta dependencia mundial al mercado chino es más crítica ahora, ya que la demanda se ha incrementado en un 10 % en los últimos años y con tendencia al alza.
Ante esta realidad, en el caso especifico de Europa se esta incentivando con fondos del programa *H2020* a través del proyecto *Novamag* la investigación en materiales magnéticos alternativos a las tierras raras [73, 74]. Esto es debido a que éstos materiales son fundamentales en los procesos de fabricación de discos duros de ordenador, teléfonos móviles, pantallas de TV, pantallas táctiles, vehículos híbridos, turbinas eólicas, paneles solares y módulos TE, por ejemplo [75, 76].
En lo que respecta a la escasez, el caso más típico es el del Teluro [77–79]. Actualmente su producción global es de 2,8 x 10^{14} toneladas métricas [78], lo que le convierte en un material escaso (ver **Figura 1.8**).El precio de un elemento suele estar estrechamente ligado a la abundancia de este elemento en la corteza terrestre. Esta escasez dificultaría una implantación tecnología a gran escala en el caso que los módulos TE incluyan altas cantidades de Teluro. En este escenario, una posibilidad de hacer viable este material estaría en el proceso de fabricación, es decir, reduciendo la cantidad de material empleado, pasando de dispositivos en volumen a dispositivos que necesiten menos Teluro, como películas delgadas, nanohilos o nanotubos. Durante la realización de esta tesis doctoral, hemos utilizado nuevas aproximaciones a través de la pulverización catódica, para la obtención de películas delgadas y nanomallas de $Si_{0,8}Ge_{0,2}$, Ag_2Se, Cu_2Se, en un solo proceso de fabricación sin necesidad de procesos litográficos, tratamientos térmicos o de dopado adicionales.
En la **Figura 1.8** hemos resaltado el Silicio, Germanio, Cobre, Plata y Selenio que son los materiales que hemos utilizado durante esta tesis. Una rápida comparación entre los distintos elementos nos deja como conclusión que el Germanio es el material que tiene menores reservas y más baja producción de los cinco elementos seleccionados. Tomando como referencia el Silicio-Germanio, con una producción anual de 2,6 x 10^{17} toneladas métricas [78].
En este contexto, si tomamos la **Figura 1.8** como referencia de los materiales TE más utilizados el Ge no llega a la escasez del Bi, Te, Sb, sino que se encuentra en valores similares a otros materiales TE ampliamente utilizados como Pb, Sn, In, Co, Zn. Adicionalmente, hay un 35 % de germanio procedente del reciclado de la industria de semiconductores en donde ha sido ampliamente utilizado los últimos 50 años.
En nuestro caso, hemos recurrido a la fabricación de películas mediante la técnica de *pulverización catódica no reactiva* en el caso del Silicio-Germanio [80–82] **apartado 1.2** y *reactiva* (en el caso de los seleniuros de Cobre [83] y Plata **apartado 1.3**). Esta técnica (que es brevemente detallada en la **sección 2**) es versátil y ampliamente utilizada en la industria de recubrimientos, lo que ayuda al proceso de escalamiento al poder recubrir grandes áreas con pocas cantidades de material en comparación con el volumen y en condiciones de baja temperatura.

Además, se evitan otros inconvenientes tales como, en el caso del del $Si_{0,8}Ge_{0,2}$ la necesidad de largos tiempos de recocido (incluso días) y a altas temperaturas (superiores a 900 °C) necesarias para inducir la cristalización en el material, son un problema debido a que estas altas temperaturas ocasionan la pérdida de los dopantes reduciendo su conductividad eléctrica. Asimismo, los altos valores de conductividad térmica que siguen presentando el material en volumen siguen siendo su principal desventaja. Por último, en lo que respecta a los seleniuros del tipo $Ag_{2-x}Se$ y $Cu_{2-x}Se$, el control estequiométrico, estructural y composicional es todo un desafío tecnológico que hemos afrontado desde la fabricación de un *sistema pulverización catódica híbrido reactivo y pulsado de selenio* que nos proporciona un método de fabricación con alto control de estas propiedades. [83].

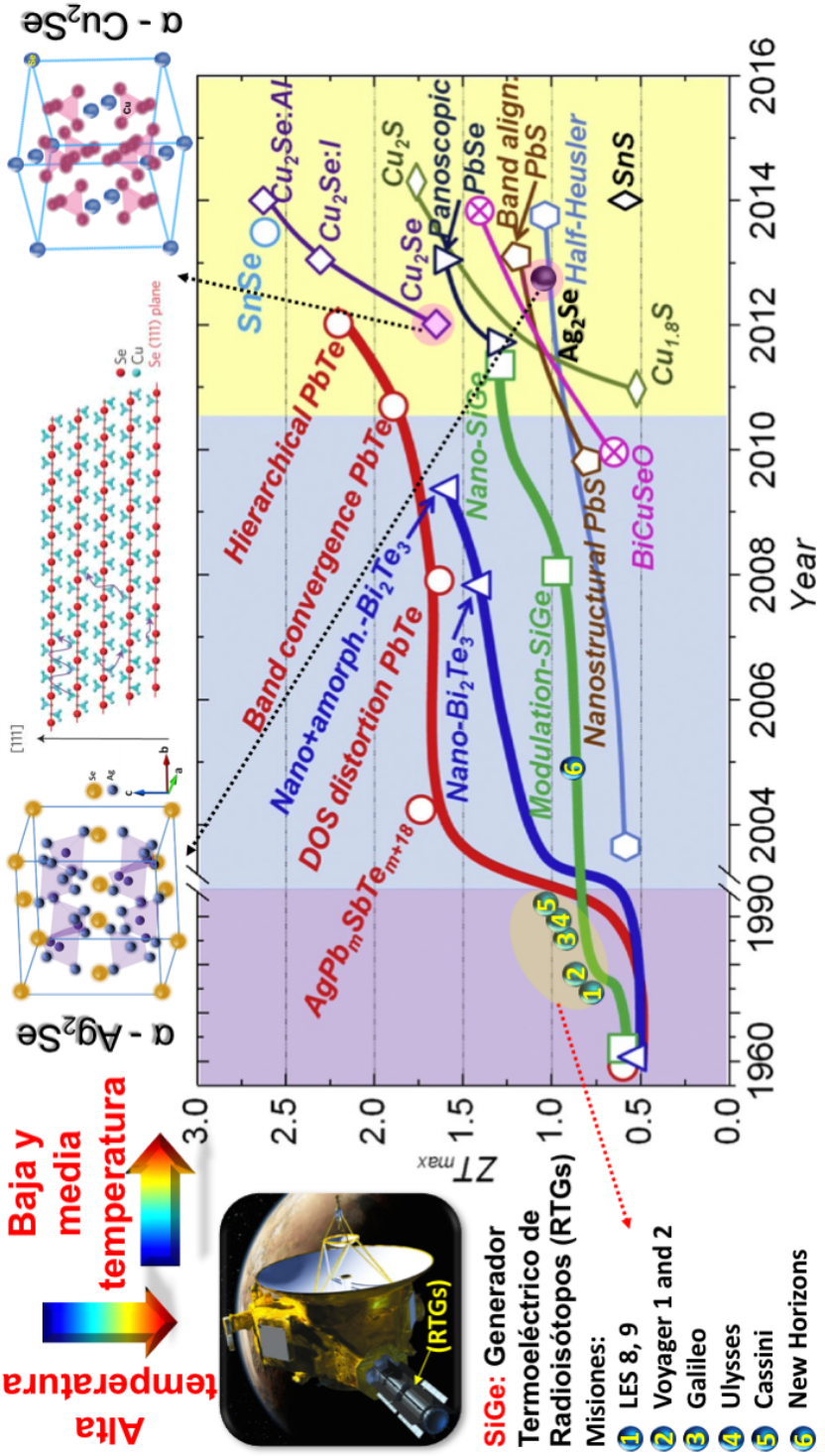

Figura 1.6: En la imagen se muestra una evolución de la figura de mérito zT frente a los años para algunos de los principales materiales TE. Hemos resaltado a los *seleniuros* Ag_2Se y Cu_2Se como posibles candidatos a cubrir las aplicaciones cercanas a la temperatura ambiente. Asimismo, hemos detallado la evolución que ha presentado el *Silicio-Germanio* como material TE para altas temperaturas. Por último se muestran las diferentes misiones espaciales: *LES 8 - 9, Voyager 1 - 2, Galileo, Ulysses, Cassini y New Horizons*, en las cuales los generadores termoeléctricos de radioisótopos (RTGs por sus siglas en ingles *Radioisotope thermoelectric generators*), han sido utilizados exitosamente. Esta imagen es adaptada de la referencia [67–71]

.

Material systems	Carrier type	ZT	κ_L [W m^{-1} K^{-1}]	T	Synthetic method*
Skutterudites $CoSb_3$					
$Yb_{0.19}Co_4Sb_{12}$	n	1	–	600 K	HP
$In_{0.25}Co_4Sb_{12}$	n	1.2	2	575 K	SSR
$CoSb_{2.75}Sn_{0.05}Te_{0.20}$	n	1.1	2.04	823 K	MA+SPS
$Ba_{0.14}In_{0.23}Co_4Sb_{11.84}$	n	1.34	0.74	850 K	MAG+SPS
$Yb_{0.2}Co_4Sb_{12.3}$	n	1.26	–	800 K	MAG+SPS
$Yb_{0.3}Co_4Sb_{12.3}$	n	1.3	–	800 K	MS+SPS
$Na_{0.48}Co_4Sb_{12}$	–	1.25	–	850 K	MAG+HP
$Ba_{0.08}La_{0.05}Yb_{0.04}Co_4Sb_{12}$	n	1.7	–	850 K	MAG+SPS
2D Materials: quantum well or superlattices					
$PbTe/Pb_{1-x}Eu_xTe$	–	2.0	–	RT	MBE
PbSeTe/PbTe	n	2.0	0.58	RT	MBE
Bi_2Te_3/Sb_2Te_3	p	2.4	0.22	300 K	–
$Bi_2Te_3/Bi_2Te_{2.83}Se_{0.17}$	N	1.4	0.58	300 K	–
Nanowire-based materials					
Si nanowires	–	0.6	1.2	RT	EE
Si nanowires	p	1	–	200 K	SNAP
Bi_2Te_3-based nanocomposites					
BiSbTe	p	1.2	–	RT	HEBM+HP
BiSbTe	p	1.4	–	373 K	HEBM+HP
BiSbTe	p	1.3	–	373 K	HEBM+HP
BiSbTe	p	1.4	–	373 K	HEBM+HP
$Bi_2Te_{2.7}Se_{0.3}$	n	1.04	–	498 K	HEBM+HP
$(Bi,Sb)_2Te_3$	p	1.5	–	390 K	MS+SPS
$(BiSb)_2Te_3$	p	1.47	–	440 K	HS+HP
$Bi_{0.52}Sb_{1.48}Te_3$	p	1.56	0.26	300 K	MS+SPS
Bi_2Te_3	n	1	0.3	450 K	HS+HP
$Bi_{0.4}Sb_{1.6}Te_3$	p	1.5	0.16	RT	MS+HP
$Bi_{0.4}Sb_{1.6}Te_3$	p	1.8	–	316 K	MS+HP
PbTe-based nanocomposites					
$AgPb_{18}SbTe_{20}$	n	2.2	–	800 K	NP
$Ag_{0.5}Pb_6Sn_2Sb_{0.2}Te_{10}$	p	1.45	0.43	630 K	NP
$Ag_{0.53}Pb_{18}Sb_{1.2}Te_{20}$	n	1.7	–	700 K	NP
$K_{0.95}Pb_{20}Sb_{1.2}Te_{22}$	n	1.6	0.4	750 K	NP
$Na_{0.95}Pb_{20}SbTe_{22}$	p	1.7	0.74	700 K	NP
PbTe–PbS8%	n	1.4	–	750 K	NP
PbTe–Pb–Sb	n	1.4	0.6	700 K	NP
PbTe–Si	n	0.9	–	675 K	NP
$Pb_{9.6}Sb_{0.2}Te_3Se_7$	n	1.2	0.4	650 K	NP
$(Pb_{0.95}Sn_{0.05}Te)_{0.92}(PbS)_{0.08}$	n	1.50	0.4	642 K	NP
2%SrTe-containing PbTe	P	1.7	0.45	800 K	NP
$NaPb_{18}BiTe_{20}$	p	1.3	–	670 K	NP
$Ag_{0.8}Pb_{22.5}SbTe_{20}$	n	1.5	0.89	700 K	MA+SPS
SiGe-based nanocomposites					
$Si_{80}Ge_{20}$	p	0.95	–	1073 K	HEBM+HP
$Si_{80}Ge_{20}P_2$	n	1.3		1173 K	HEBM+HP
New thermoelectric materials					
$In_4Se_{3-\delta}$	n	1.48	–	705 K	Bridgeman method
$In_4Se_{3-x}Cl_{0.03}$	n	1.53	–	698 K	Bridgeman method
β-$Cu_{2-x}Se$	p	1.5	0.4	1000 K	MAG+SPS
β-Zn_4Sb_3	p	1.35	–	673 K	Bridgeman method

Figura 1.7: Se muestran las propiedades termoeléctricas de los principales materiales sintetizados por diversos métodos sintéticos en las últimas dos décadas. Las abreviaturas utilizadas en la columna del método sintético representan los siguientes significados: SSR = solid state reaction; MA = mechanical alloying; HEBM=high energy ball milling; MAG=melting, annealing and grounding; MS=melt spinning; NP = nanoprecipitation; SS=solvothermal synthesis; HS=hydrothermal synthesis; EE = electroless etching; SNAP = self-assembled nanophase particle; MBE=molecular-beam epitaxy; HP=hot pressing; SPS = spark plasma sintering. Tabla tomada de la referencia [72]

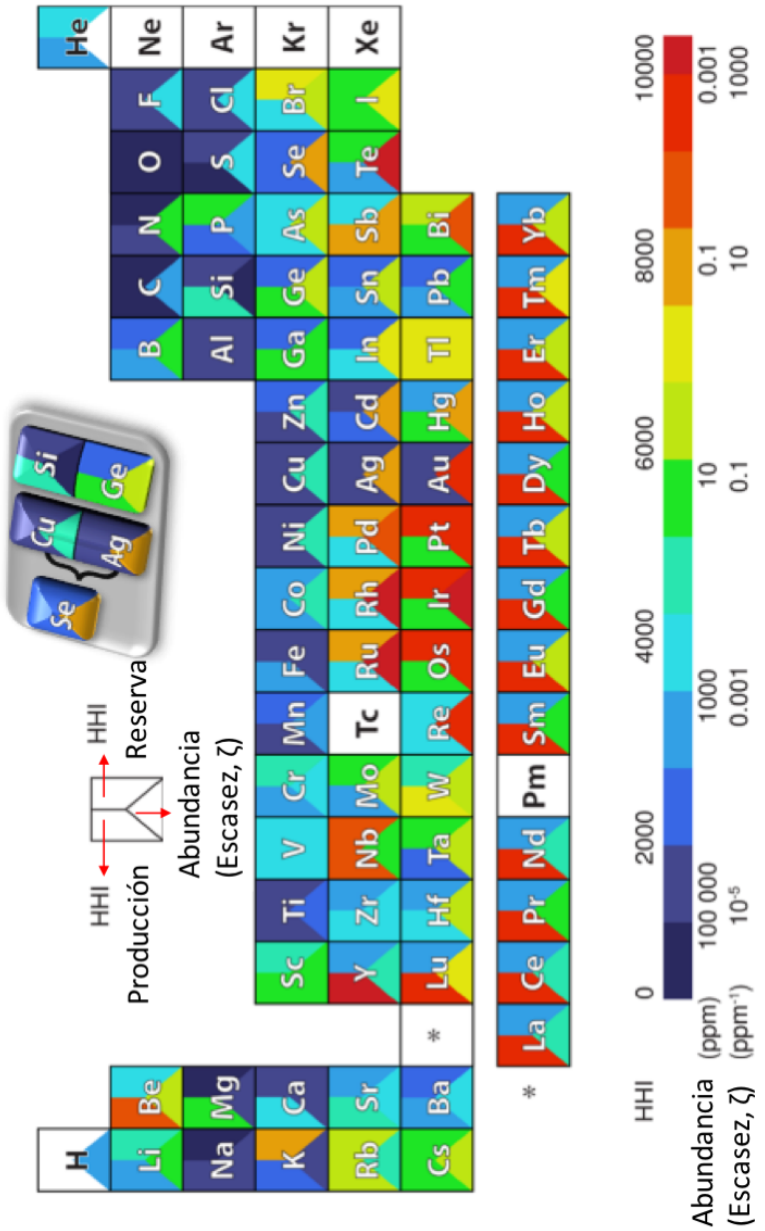

Figura 1.8: Se muestra una representación de la tabla periódica de los elementos, en donde se indican los valores de escasez (ζ), producción y reservas para gran parte de los elementos. HHI representa el índice *Herfindahl-Hirschman* que en este caso identifica el valor de producción y reservas en una escala de colores que aumenta de azul a rojo. Por otro lado, la variación de abundancia varia de un elemento muy escaso que se representa en color rojo hasta uno muy abundante en color azul. La imagen es tomada y adaptada de la referencia [79]

1.2. Silicio Germanio

El silicio es el semiconductor más común y ampliamente utilizado en los procesos industriales de la actualidad [84, 85]. Esto es debido a su bajo coste, alta abundancia en la corteza terrestre, y bajo impacto medioambiental, con lo que ha logrando consolidarse como una *piedra angular* (en alegoría a su raíz latina *sílex*) de nuestra sociedad. Las proyecciones en 2017 prevén ventas de semiconductores de silicio por 346.000 millones de dólares estadounidenses en todo el mundo.[86, 87]. Nuestra sociedad esta inmersa en la era del silicio y esto es una realidad incontestable. La integración tecnológica, es decir, asegurar una compatibilidad de las nuevas tecnologías con el silicio, es un reclamo que las soluciones termoeléctricas deben satisfacer.

Recientes progresos en dispositivos termoeléctricos, fotovoltaicos [88, 89] y microelectrónicos [85] basados en silicio y germanio, han sido publicados recientemente por *Pérez-Taborda et al.* [81] en un capítulo de libro. En él realizamos una detallada cronología del SiGe y su evolución con especial énfasis en las aplicaciones en termoelectricidad. En lo que se refiere a su estructura, el silicio cristalino, el germanio monocristalino y el silicio-germanio utilizados en la industria de la microelectrónica son estructuralmente cúbicos, tipo diamante con una celda unitaria subdividida en dos celdas tipo (FCC) interpenetradas entre sí y separadas por una distancia $a/4$ a lo largo de cada eje de la celda unidad. La **Figura 1.9** muestra la estructura del SiGe.

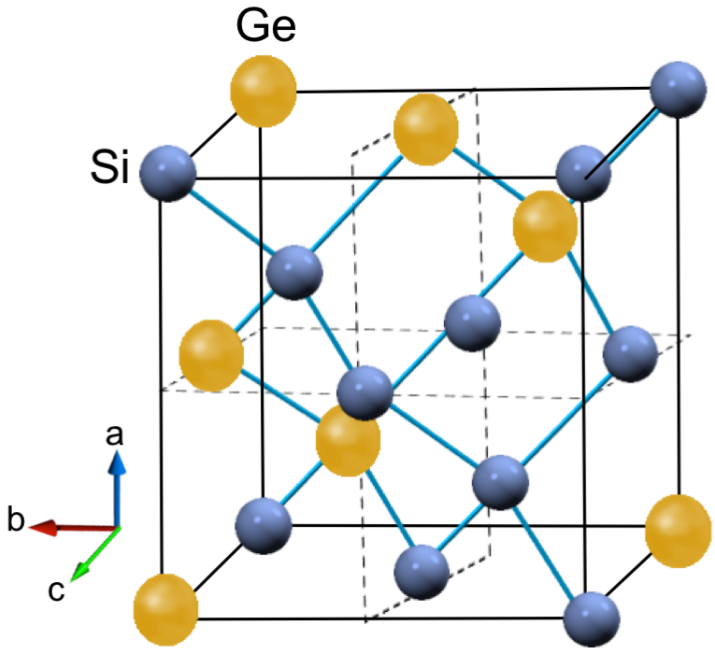

Figura 1.9: Esquema simplificado de la estructura del SiGe. Se muestra en azul los átomos para el silicio y en amarillo para el germanio. Su estructura es cúbica tipo diamante centrada en las caras. Uno de los lados del cubo para el silicio es 0.543 nm mientras que para el germanio es de 0.566 nm para el material en volumen [90]

En lo que respecta a las aplicaciones TE, la utilización del silicio es todo un reto tecnológico. Su alta conductividad térmica ($\kappa_L = 140\, Wm^{-1}\mathrm{K}^{-1}$) se traduce en bajos valores de $zT = 0.01$ a temperatura ambiente para el material en volumen [53, 91, 92]. Este desafío se ha afrontado históricamente a través de la reducción de la dimensionalidad del material y la formación de aleaciones, [93, 94] principalmente con germanio, lo cual provoca un cambio en el camino libre medio de los electrones y fonones, traduciéndose en una reducción en la conductividad térmica de hasta un 90 % [66, 95–98]. Más importante aún, es que esta reducción no afecta el uso de esta aleación en las aplicaciones de altas temperaturas (≈1000 °C) donde tiene su máximos valores de eficiencia (ver **Figura 1.5**). La aplicación más exitosa de las aleaciones de SiGe como termoeléctrico ha llegado de la mano de la NASA, a través de su programa espacial [69] [68, 70, 71]. Como se muestra en la **Figura 1.6**, en los últimos 50 años los generadores termoeléctricos de radioisótopos (RTGs) basados en aleaciones de SiGe han sido utilizados en las misiones en donde los paneles solares no son la mejor alternativa, debido a la poca disponibilidad de luz en los largos ciclos de día/noche de algunas misiones o bajo flujo solar, además de los escenarios en los que hay zonas que tienen demasiadas partículas en suspensión que pueden inutilizar los módulos fotovoltaicos[67–70]. Los RTGs utilizan como fuente de calor la desintegración del PuO_2 238, el cual tiene un período de desintegración de 87.7 años, lo cual ofrece una prolongada autonomía en misiones de largo tiempo [99, 100]. En lo que respecta a la robustez y fiabilidad de éstos módulos, en la actualidad los dispositivos de SiGe han acumulado más de 250 millones de horas (cerca de 40 años de las misiones *Voyager*) sin que se reportara de momento algún fallo[67–70]. Además, poseen una alta resistencia mecánica y alto punto de fusión. Una ventaja adicional es que son dispositivos de estado sólido, es decir, sin partes móviles con lo cual pueden superar las vibraciones de despegue sin problemas mecánicos y sólo necesitan un gradiente de temperatura permanente (entre el espacio exterior y el radioisótopo) para su funcionamiento ininterrumpido.

A la par de estas investigaciones espaciales llevadas a cabo por NASA-JPL, muchos autores han realizado contribuciones para incrementar la figura de mérito de esta aleación y escalar éstos resultados a procesos industriales. Si bien se ha demostrado que la incorporación del germanio reduce la conductividad térmica, su precio y menor abundancia es un verdadero impedimento a la hora de escalarlo a procesos industriales. Con el fin de reducir los costes de producción, se han realizado varios intentos para disminuir la concentración de germanio pero conservando bajos valores de conductividad térmica. Uno de los primero trabajos alrededor de la aleación $Si_{1-x}Ge_x$ fue el desarrollado por *Dismukes et al.* [101] en 1964 quienes, utilizando boro y fósforo como dopantes en una relación de 15 % de Ge y 85 % de Si, obtuvieron un zT máximo de 0.8 para la aleación $Ge_{15}Si_{85}$ de *tipo p* y un zT de alrededor de 1 para la aleación $Ge_{15}Si_{85}$ de *tipo n* a 950°C. Recientemente, se ha logrado una mejora significativa en los valores de zT tanto en las aleaciones de $Si_{1-x}Ge_x$ de *tipo p* como en las de *tipo n*. Debido se ha llevado a cabo mediante la aplicación de nuevos enfoques como la nanoestructuración [102], la reducción de la conductividad térmica a través de la dispersión de fonones por: aumento de los límites de grano, nanoinclusiones [103], multicapas de Si-Ge [104], entre

otros. Además, del aumento en el dopaje favorece el incremento en la conductividad eléctrica y por consiguiente el factor de potencia.

En el año 2008, *Joshi et al.* [98] reportaron valores de zT de 0.95 a 800 °C para muestras nanoestructuras en volumen de $Si_{0,8}Ge_{0,2}$ *tipo n.* Esto es un incremento de alrededor del 50 % en comparación con los valores de eficiencia del momento y alrededor de un $\approx 90\,\%$ en comparación con los RTGs de SiGe utilizado en aplicaciones espaciales de NASA. En este trabajo, los autores asocian esta mejora a la drástica reducción de la conductividad térmica ($\kappa \approx 2.5\ Wm^{-1}K^{-1}$) debido al aumento de la dispersión de fonones en las intercaras de los nanogranos, combinado con una alta densidad del nanocompuesto, lo que se traduce en una mejora del factor de potencia. Para el mismo período, *Wang et al.* [105] sintetizaron a través de molienda de bolas y prensado en caliente a 1200 °C, lingotes de $Si_{80}Ge_{20}$ con una incorporación exitosa de hasta un 2 % de fósforo. Como consecuencia de esto, obtuvieron $Si_{80}Ge_{20}P_2$ nanoestructurado y altamente dopado con valores de zT de hasta 1.3 a 900 °C, lo cual equivale a un incremento del 40 % con previos reportes. Adicional a la reducción de la conductividad térmica, la otra vía para obtener altos valores de zT, es mediante el una mejora del factor de potencia; para esto uno de los enfoque más exitosos es el dopaje por modulación[92]. Al respecto, en el año 2012, *Yu et al. y Chen et al.* [97] reportaron un aumento en el factor de potencia de nanocompuestos de $(Si_{80}Ge_{20})_{70}(Si_{100}B_5)_{30}$, a través del incremento en la movilidad de los portadores. Lamentablemente, esto no se tradujo en un una mejora de la figura de mérito, debido al aumento de la conductividad térmica en las nanopartículas de silicio puro presentes en éstos nanocompuestos. Ese mismo año, un diseño alternativo de dopaje fue introducido por el mismo grupo de investigación, utilizando una aleación $Si_{70}Ge_{30}$ la cual es más rica en germanio, en lugar de nanopartículas de silicio puro como en el caso anterior. En su lugar, los autores utilizaron una matriz fija de $Si_{95}Ge_5$, con el fin de aumentar significativamente el factor de potencia mientras que la conductividad térmica permanecía baja. Como resultado, reportaron un incremento en los valores de zT, llegando a 1.3 a 900°C. Los autores concluyeron que esto es debido a una mejora en la conductividad eléctrica y, por ende, en el factor de potencia, que a su vez está ocasionado por el aumento en la movilidad de los portadores. Todo esto, es que esto se produce sin provocar un incremento en la conductividad térmica al contar con una alta incorporación de germanio en una relación de $Si_{70}Ge_{30}$.

Estos resultados evidencian que es en el material en volumen, donde el SiGe ha logrado su mayor progreso. Sin embargo, los elevados costes por el alto contenido de germanio empleado, la necesidad de largos tiempos de fabricación, y altas temperaturas de tratamiento térmico, necesarios para obtener un material cristalino, son una desventaja a la hora de escalar e integrar estas soluciones TE a la industria actual.

En 2012, *Lee et al.* [106] calcularon teóricamente para nanoestructuras de SiGe nanoporoso valores de zT tan altos como 2.2 a 530 °C. Según los autores, esta mejora en la figura de mérito se debe a la drástica disminución de la conductividad térmica a $\kappa \approx 1.2 Wm^{-1}K^{-1}$.

Tres años después, *Yi et al. y Yu et al.* [97] propusieron modelos mejorados para nanohilos de $Si_{0,73}Ge_{0,27}$ con 10 nm de diámetro y altamente dopados, llegando a valores similares a los obtenidos por *Lee et al.* [106].
Un nuevo enfoque experimental ha sido reportado por *Tang et al.* [107], quienes han empleado procesos de litografía electrónica para generar nanomallas y alterar la conductividad térmica por el atrapamiento de fonones en los nanoporos. Consecuencia de esto, se ha reportado una reducción de hasta un 98 % de la conductividad térmica respecto al silicio en volumen, correspondiente a $\kappa = 1.73 W m^{-1} K^{-1}$, para nanomallas de silicio con diámetros de poro de 55 nm.
Éstos prometedores resultados, al reducir la dimensionalidad a través de nanohilos, nanotubos y nanomallas con el fin de reducir la conductividad térmica del material, contrastan con la posibilidad de escalar estas aproximaciones a la industria. Actualmente es un verdadero desafío el obtener estas nanoestructuras por métodos industriales o fácilmente integrables con la actual tecnología de semiconductores.
En esta tesis doctoral, hemos realizado una serie de nuevas aproximaciones en la fabricación de películas delgadas de SiGe, obtenido valores que se encuentran dentro del estado del arte, los cuales hemos reportado en un capítulo de libro [81] y dos artículos en revistas especializadas [80].
Mediante la pulverización catódica por descarga continua - tecnología ampliamente conocida e integrada en la industria de semiconductores y recubrimientos- hemos depositado películas delgadas de $Si_{0,8}Ge_{0,2}$ a 500 °C de temperatura, logrando una drástica reducción en la conductividad térmica.
Adicionalmente, inspirados por el trabajo de *Tang et al.* [107] hemos propuesto un nuevo enfoque, el cual consiste en la obtención de nanomallas de $Si_{0,8}Ge_{0,2}$ a través de pulverización catódica. Valiéndonos de la experticia y alto control que tiene nuestro grupo de investigación en la fabricación de membranas de alúmina anódica altamente ordenadas [108–113] hemos utilizado 3 diferentes tamaños de diámetros de poro comprendidos entre 294 ± 5nm y 31 ± 4 nm los cuales hemos utilizado como sustrato durante el crecimiento de $Si_{0,8}Ge_{0,2}$ [80]. Esta réplica de la alúmina nos permite obtener nanomallas de SiGe, con un alto control del espesor y del tamaño de poro en grandes áreas (limitados únicamente por el tamaño del objetivo que utilicemos y del sustrato). Adicionalmente, estas nanomallas de $_{80}Ge_{20}$ [80] son depositadas en un solo paso y sin necesidad de altas temperaturas, siendo fácilmente escalable a la industria. La fabricación de estas nanomallas de $Si_{0,8}Ge_{0,2}$ se ha realizado en un sistema de ultra alto vacío de pulverización catódica que hemos diseñado especialmente y construido en el Instituto de Micro y Nanotecnología-CNM, CSIC.

1.3. Seleniuros

La investigación alrededor de los calcogenuros del tipo $\mathbf{X_{2-\delta}Y}$ (con $\mathbf{X} = Ag, Cu$ y $\mathbf{Y} = S, Se, Te$) es una historia de altibajos, permeada por la serendipia que acompaña a la ciencia y que se remonta desde el inicio mismo de la termoelectricidad. Solo 5 años después del descubrimiento del *efecto termomagnético* por parte de *Seebeck*, en 1827 *Antoine César Becquerel* realizó un importante descubrimiento. Utilizando velas calentó un primitivo termopar formado por alambres de platino y cobre generando electricidad [114]. Esto no hubiese pasado de ser una comprobación más del efecto *Seebeck*, si no fuese porque la combustión estuvo acompañada de algunos polvos de azufre, que accidentalmente se encontraban encima del alambre de cobre, ocasionando un aumento significativo en la generación eléctrica. Este es el primer reporte de que los calcogenuros basados en Cu, pueden exhibir buenas propiedades termoeléctricas. Más tarde, en 1866, *A. C. Becquerel* e hijo fabricaron la primera batería TE con sulfuro de cobre (Cu_2S) [115]. Ya en la mitad del siglo pasado, en 1947, *Hirahara* realizó un detallado estudio sobre el rendimiento eléctrico del Cu_2S siendo el primero en reportar las tres fases polimórficas de Cu_2S con propiedades eléctricas diferentes [116]. Este resultado fue confirmado a mediados de los años sesenta por *Ogorelec* et al. [117] y *Sorokin et al.* [118] Estos estudios propiciaron que en 1959 la Compañía Monsanto solicitara la primera patente del seleniuro de cobre (Cu_2Se) como un prometedor material TE con alto rendimiento en la generación eléctrica [119, 120]. Impulsados igualmente por la carrera espacial, como en el caso del SiGe, el Laboratorio de Propulsión de la NASA desarrolló generadores térmicos de radioisótopos basados en Cu_2Se (RTGs) [119, 120]. Igualmente, grandes compañías como 3M Corporation, General Atomics y Teledyne Energy Systems, realizaron importantes esfuerzos en investigación de este tipo de dispositivos [121]. Inicialmente se obtuvieron altos valores de figura de mérito, llegando a un valor de $zT = 1.2$ a 726 °C para una aleación de $Cu_{1,97}Ag_{0,03}Se_{1+y}$ (y < 0.01), los cuales fueron obtenidos por 3M Corporation. Experimentos de estabilidad del material reportaron más allá de 4000 horas sin degradación aparente [122]. Estos prometedores resultados perfilaron al Cu_2Se como un potencial competidor a los ya consolidados dispositivos de SiGe y PbTe del programa espacial de la NASA. Sin embargo, los esfuerzos de integración y desarrollo del Cu_2Se dentro del programa espacial fueron paralizados en 1979 debido a problemas de estabilidad, como consecuencia de la evaporación del selenio y las migraciones de iones de cobre [115]. Tres décadas más tarde, nuevas investigaciones en los calcogenuros basados en cobre $\mathbf{Cu_{2-\delta}X}$ ($\mathbf{X} = S, Se, Te$) han propiciado el resurgimiento y renovado el interés en esta familia de materiales [63, 122, 123]. El comportamiento líquido de los iones de cobre (que ha dado lugar a un nuevo concepto llamado *PLEC* (por sus siglas en ingles *"Phonon-Liquid Electron-Crystal"*), acompañado de conductividades térmicas ultra bajas, así como otras propiedades físicas interesantes y anómalas, que han provocado un creciente interés en esta campo de investigación. Más importante aún, ha sido el entusiasta estudio y comprensión de nuevos mecanismos físicos, como el comportamiento líquido y la dispersión crítica en estos conductores superiónicos [63, 123]. Estos nuevos en-

foques han arrojado una nueva luz en la investigación de otros materiales TE, que se creían engañosamente más simples, como es el caso del seleniuro de estaño (SnSe). En 2014, *Zhao et al.* [64] reportaron el valor más alto hasta la fecha de zT de 2.6 ± 0.3 a 650°C para muestras en volumen de SnSe. Estos sorprendentes resultados son explicados debido a la fuerte unión no armónica y anisotrópica, que reducen la conductividad térmica del material hasta valores tan bajos como 0.25 $Wm^{-1}\mathrm{K}^{-1}$. Adicionalmente, el material exhibe un factor de potencia excepcionalmente alto, alrededor de 0.4 m$W\mathrm{K}^{-1}$, como consecuencia de la alta conductividad eléctrica y un coeficiente de Seebeck fuertemente mejorado.
Impulsados por estas interesantes propiedades, los seleniuros, en especial el Cu_2Se, han llamado la atención de los investigadores, con un crecimiento exponencial de artículos de $Cu_{2-x}Se$ y $Cu_{2-x}S$ [120] convirtiéndose en un tema candente dentro de la comunidad científica que trabaja en materiales termoeléctricos.

1.3.1. Conductores superiónicos

En la mayoría de los (SICs) *superionic conductors por sus siglas en inglés*, la estructura cristalina consta de dos subredes distintas. La primera es generalmente una red rígida y ordenada, dentro de la cual la segunda se encuentra embebida, y en la que los iones metálicos pueden moverse de forma fluida entre varios sitios intersticiales. La principal característica en estos materiales superiónicos reside en las transiciones de fase que presentan los SICs cuando superan su temperatura crítica. Estas transiciones ocasionan que sus propiedades de transporte eléctrico cambien drásticamente. En este caso, una corriente en forma de iones se mueve a través del material mucho más rápido que a temperaturas más bajas. Estas transiciones a fases superiónicas ha fascinado a los investigadores desde 1830, cuando fueron descrita por el famoso científico británico *Michael Faraday*[124].
Los recientes avances en nanociencia han permitido a los científicos aprender que estas propiedades son totalmente dependientes de la dimensionalidad, es decir, que es completamente diferente el comportamiento del material en volumen que en películas delgadas o nanoestructuras, en donde las temperaturas críticas pueden ser más bajas. Esta es una línea de investigación que esta muy vigente y reporta grandes avances. Un ejemplo, es el reciente trabajo de *Lindenberg et al.* [125] y su equipo de la universidad de Stanford, quienes han realizado investigaciones en sulfuro de cobre, el cual típicamente cambia a SICs cuando se supera su temperatura crítica (103°C) provocando un movimiento colectivo del cobre dentro del nanocristal, con tiempos de conmutación entre fases que ocurren en escalas de 20 ps. Los investigadores encontraron que para nanodiscos de CuS con 10 nanómetros de diámetro, se produce una reducción en su temperatura de transición alrededor de 70 °C, además de presentar un comportamiento de conmutación en la transición de fase cristalográfica que puede ser controlado si es irradiado por luz externa. Estos sorprendentes resultados, demuestran la pertinencia de éstas investigaciones y que los SICs seguirán dando de que hablar en los próximos años.

1.3.1.1. Termoeléctricos superiónicos

En lo que respecta a los SICs dentro de las investigaciones termoeléctricas, éstas se han incrementado durante el último lustro debido al aumento en los reportes con altos valores de zT (incluso valores récord de zT>2) [56, 63, 119, 122, 123, 126], que es casi el doble de la eficiencia de los materiales TE tradicionales.
El comportamiento que más nos interesa para las aplicaciones TE es cuando se supera la temperatura crítica de transición. Es en este momento cuando ciertos iones (Cu^+ en el caso del Cu_2Se y Cu_2S o Ag^+ en el caso de Ag_2Se y Ag_2Te), adquieren un flujo direccional al ser sometidos a un campo eléctrico externo, en lugar de ocupar sitios rígidos dentro de la red. Las *conductividades iónicas* (definiéndose como $\sigma_I = j_I E^{-1}$ en donde j_I es la *densidad de corriente iónica* y E el *campo eléctrico*) de los *SICs* en su estado sólido, son similares a la σ_I de los conductores iónicos (por ejemplo, NaCl, CaF_2, etc.) en su estado líquido, con valores del orden de 1 Ω-cm^{-1} [125, 127, 128]. Este comportamiento es claramente el opuesto al de los sólidos convencionales que tienen σ_I del orden de10^8 Ω-cm^{-1} debido a que sus iones están fijos a la red cristalográfica. Estudios termodinámicos de esta transición de fase, muestran que en los *SICs* el cambio de entropía en cada átomo durante la transición superiónica es aproximadamente el mismo cambio de entropía que experimenta un átomo al fundirse. Esto indicaría que la mitad del cristal (o una subred del mismo) se comporta como un material fundido, o como se ha definido recientemente *"como un líquido"* [56, 63, 123]. Este comportamiento es muy interesante para aplicaciones TE, porque esta naturaleza de cuasi-fundido impide el transporte de calor por modos fonónicos transversales, o través de vibraciones de la red, mientras que la subred se encuentra fija proporcionando una vía cristalina para la conducción eléctrica[50, 59, 93]. Éstas características reducen κ (con una contribución insignificante de $\kappa_{Electrnica}$) sin afectar la σ, lo que conduce a una mejora significativa en zT. Sin embargo, muchos autores han reportado [119, 129, 130] que este movimiento similar a un fluido en los *SICs* da como resultado una fuerte electromigración y, en consecuencia, una degradación del material en volumen. Esto ocurre cuando el material supera su temperatura crítica y se producen degradaciones en él al no tener una reversibilidad total de su fase cuando se enfría. Para hacer que los conductores superiónicos sean viables y entender sus inusuales propiedades, los esfuerzos para estabilizar el movimiento iónico manteniendo excelentes propiedades TE y entender la física y la química del proceso son esenciales.

1.3.1.2. Seleniuro de Cobre

El seleniuro de cobre (Cu_2Se) es un semiconductor de *tipo p* con una banda prohibida de 1.23 eV [130] y dos fases cristalinas dependientes de la temperatura. Actualmente la nomenclatura que se da a éstas fase de alta y baja temperatura es bastante confusa [120, 131, 132]. A lo largo de esta tesis definiremos la fase de *baja temperatura* como (β) y (α) a la fase de *alta temperatura*. En el caso del Cu_2Se su temperatura crítica es de 137 °C [63, 121]. En la **Figura 1.10a** se muestra cómo, por encima de esta temperatura, el Cu_2Se exhibe una red *cúbica*

centrada en las caras para átomos Se (en color amarillo), mientras que los átomos Cu (más pequeños en color rojo) se distribuyen en los sitios centrados en el cuerpo (*8c*) o centrados en la cara (*32f*) del selenio [120, 131, 132]. En esta fase α-Cu_2Se, los iones de Cu^+ tienen acceso a un mayor número de sitios cristalográficos (formando una subred desordenada y comportándose como un líquido) dentro de una red cristalina (FCC) rígida formada por los aniones de Se^{2-}, los cuales son significativamente más grandes que los iones Cu^+ [14]. Este gran número de sitios vacantes disponibles, propicia un salto en los iones de Cu^+, traduciéndose en la primera manifestación del transporte superiónico en este sólido. Esta red móvil de Cu^+, soporta difusividades del orden de 10^{-5} a 10^{-4} cm^2 s^{-1} valores comparables al agua líquida [63, 127]. En cuanto a las conductividades iónicas resultantes, éstas están entre 1 y 2 Ωcm^{-1} (a 400 °C), lo cual es tres órdenes de magnitud mayor que el valor a temperatura ambiente [63, 127]. Este comportamiento superiónico es la clave a la hora de mejorar los valores de zT en aplicaciones termoeléctricas [127]. En lo que respecta a la fase *ortorrómbica* (β) es accesible hasta 123°C a través de una pequeña región estequiometríca (marcada en azul en la imagen **Figura 1.10b**). Actualmente, para esta fase de baja temperatura, no ha sido posible desarrollar una estructura a pesar de los múltiples esfuerzos en décadas de trabajo. En 1974, *Murray et al.* [133], *Heyding et al.* [134] y *Vucic et al.* [135], propusieron a través de los análisis de difracción de rayos X en polvo una estructura monoclínica para la fase β-Cu_2Se. Posteriormente, *Kashida et al.* [136] identificaron una fase pseudomonoclínica para el β-Cu_2Se al ajustar la estructura como una serie periódica de átomos de cobre tetraédricos en las vacantes intersticiales, formando una estructura en forma de escalera. Una corroboración parcial fue realizada por *Nguyen et al.* [137] quienes realizaron cálculos teóricos llegando a una estructura similar pero no especificada en capas.

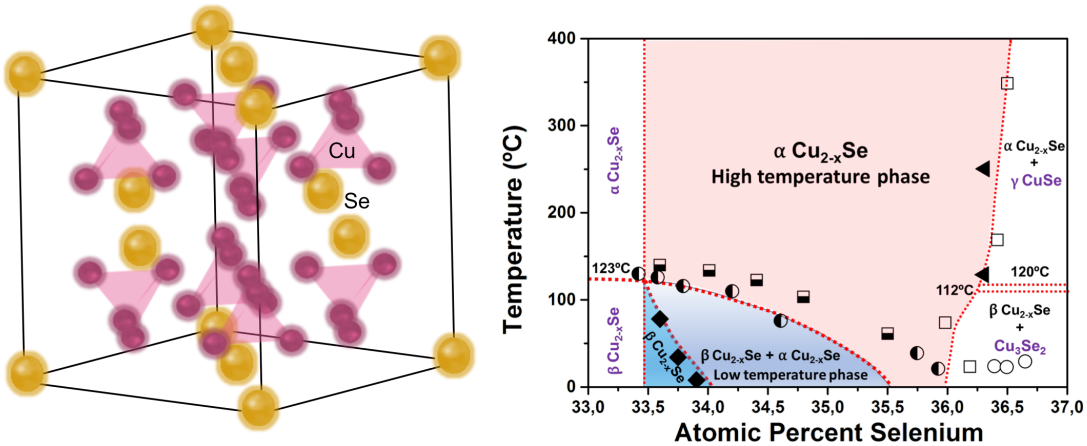

a) Estructura Cu_2Se alta temperatura **b) Diagrama de fases $Cu_{2-x}Se$**

Figura 1.10: En la Figura 1.10b. se muestra una detallada recopilación bibliográfica [134, 138–140] de la región nonestequiometrica que es el factor clave en estos seleniuros de cobre. y mezcla de fases ha sido estudiada con interés

Una gran numero de autores, [56, 63, 72, 123, 141, 142] han asociado los altos valores de

zT al acomodamiento estructural del $Cu_{2-x}Se$, en una estructura cristalina cúbica (FCC) centrada en la cara y simetría estructural correspondiente al grupo espacial *($Fm\bar{3}m$)*, similar a la mostrada en la **Figura 1.10a**. En este ordenamiento, la red de átomos de selenio proporcionan una vía de andamiaje para un libre movimiento de los iones de cobre los cuales se mueven desordenadamente a través del selenio con un comportamiento como si fuese un líquido. Esta estructura extraordinaria y especial de $Cu_{2-x}Se$ brinda un cierto desacople de las propiedades termoeléctricas al exhibir una conductividad térmica (κ_{Red}) intrínsecamente baja y una alta conductividad eléctrica asociada a la conducción superiónica. En 2012 *Liu et al.* [63] denominaron *"copper ion liquid-like"* este nuevo comportamiento a la hora de reportar los más altos valores de figura de mérito (zT 1,5 a 726ºC) obtenidos para la fase α-$Cu_{2-x}Se$ sin dopar en la fase de alta temperatura [63, 123]. Sus investigaciones teóricas y experimentales concluyeron que pueden existir diferentes estructuras a temperatura ambiente para Cu_2Se y que la incertidumbre puede surgir de su posible multiformidad, lo cual es difícil de aclarar por difracción de rayos X. Posteriormente, en otro artículo *Yu et al.* [142] informaron de una zT de 1,6 a 700 °C también para la fase α de Cu_2Se. En 2015, *Lu et al.* [143] realizaron una interesante investigación de la estructura de la Cu_2Se fase β a través de microscopía electrónica de transmisión (TEM) con calentamiento $In-situ$ [123]. Los autores atribuyen los altos valores de zT a la drástica fluctuación estructural que implica un heterogéneo ordenamiento del cobre durante la transición de fase. Inicialmente, el ordenamiento del Cu_2Se consiste en dominios de diferentes estructuras laminares ordenadas de átomos de Cu que se organizan a lo largo de una $pseudo-red$ FCC de selenio. Este ordenamiento de baja temperatura facilita la dispersión de fonones sin afectar la movilidad en los portadores de carga. Al aumentar la temperatura hasta la transición de fase, las estructuras experimentan intensos cambios que incluyen la aparición de nuevas estructuras ordenadas para el cobre, causando difusión y desorden en los átomos de cobre que se difunden a través de las capas intermedias del $Cu_{2-x}Se$, hasta situarse aleatoriamente en la subred cúbica fija del Selenio [143].

Más recientemente, *Zhao et al.* [138] reportaron para $Cu_{2-x}Se$ en volumen altos valores de zT de hasta 1.8 a 700ºC. Los resultados descubren una nueva estrategia y dirección para materiales termoeléctricos de alta eficiencia, mediante la exploración de estructuras en las que un subred cristalina enmarca el movimiento electrónico rodeado por iones líquidos [63, 127, 144]. Sin embargo, el seleniuro de cobre ha demostrado que tiene un potencial como material termoeléctrico a alta temperatura, pero su conductividad iónica ha causado problemas de estabilidad a largo plazo para su uso en generadores termoeléctricos [119, 130]. Esto ha estimulado nuestro interés en las propiedades del selenuro de cobre por debajo de la transición de fase, donde la conductividad iónica no sería motivo de preocupación. Recientemente, hemos reportado valores de zT que se encuentran el estado del arte ver **Figura 1.10**.

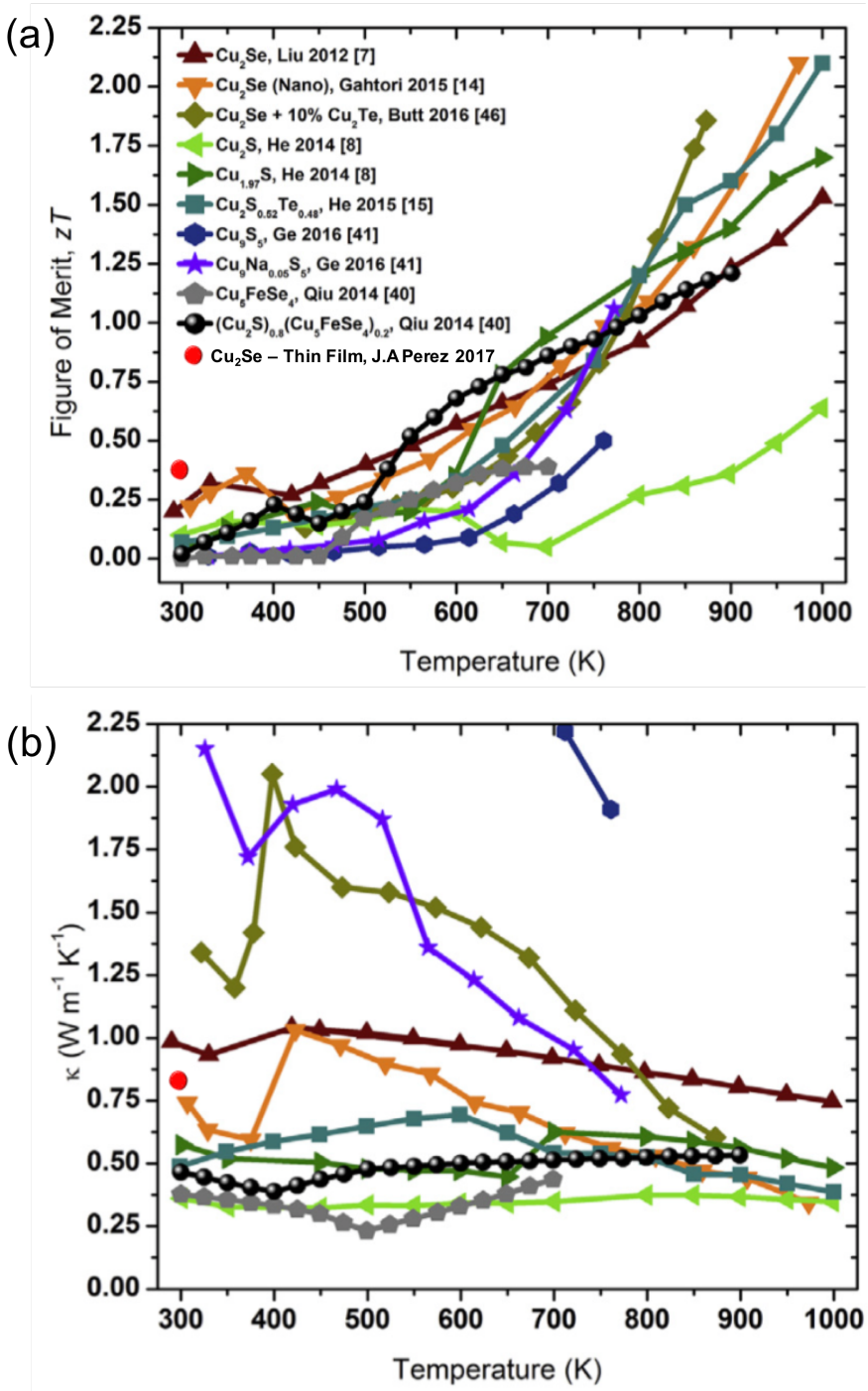

Figura 1.11: Estado del arte para la figura de mérito zT, (**Figura (a)**) y conductividad térmica, κ, (**Figura (b)**) para los calcogenuros binarios basados en Cu [130].

1.3.1.3. Seleniuro de Plata

Como se detalló en la apartado anterior, estos *materiales superiónicos* han despertado mucho interés debido a sus transiciones de fase y su conducción superiónica. Estas transiciones de fase de podrían implicar cambios en la configuración atómica y cambios en los estados del espín electrónico, dando lugar a posibles ensanchamientos/estrechamientos de la banda de conducción (generando estados metálicos o aislantes) como algunos autores lo han propuesto

[145, 146]. Ciertamente Esto despliega un abanico de posibilidades de cara a poder controlar la concentración de portadores modulando las propiedades electrónicas. Uno de los principales candidatos para esto es el *seleniuro de plata*. De hecho, $Ag_{2+x}Se$ es un semiconductor de *tipo n* de banda estrecha, que al igual que el $Cu_{2+x}Se$, presenta una estructura polimórficas con una transición fase de (β de *baja temperatura*) y (α de *alta temperatura*).
Trabajos independientes llevados a cabo por *Wiegers et al.* [147] y *Billetter et al.* [148] han demostrado que para la fase *ortorrómbica* a temperatura ambiente, el $Ag_{2+x}Se$ tienen dos átomos de plata cristalográficamente distintos. El primero $Ag_{(1)}$ está coordinado tetraédricamente, mientras que para $Ag_{(2)}$ su coordinación es casi triangular como se muestra en la **Figura 1.12a**. Esta estructura aún no ha sido completamente desarrollada.
Además de esta fase β a baja temperatura, el $Ag_{2+x}Se$ puede ordenarse metaestablemente en una fase *tetragonal* (τ-$Ag_{2+x}Se$). Esta fase tampoco está desprovista de polémica debido a controvertidos e incluso contradictorios reportes en la literatura. Por ejemplo, *Boettcher et al.* [149] reportó hasta cuatro fases tetragonales con diferentes parámetros de red para películas delgadas de $Ag_{(2+x)}Se$. Asimismo, el τ-$Ag_{2+x}Se$ tetragonal fue erróneamente indexado al ser confundido con el β-$Ag_{2+x}Se$ *ortorrómbico* como se detalla en[150, 151].
En un trabajo más reciente realizado por *Wang et al.* [152] ha detallado como esta fase metaestablemente *tetragonal* (τ) no es reversible durante el ciclo térmico y solo es estable a bajas temperaturas. Es decir, partiendo de una fase τ, es posible una transición de fase *tetragonal* τ a una *ortorrómbica* β y a una fase *cúbica* α. La transición $\tau \rightarrow \beta$ es exotérmica e irreversible mientras que la transición $\beta \rightarrow \alpha$ es reversible.
A medida que aumenta la temperatura por encima de la temperatura crítica ($\approx 133^oC), el Ag_2Se$ se reordena en una fase cúbica. La fase α-cúbica de *alta temperatura*, se muestra en la **Figura 1.12a**. Esta fase superiónica se compone de aniones de selenio, (en amarillo) que forman una disposición cúbica centrada en el cuerpo a través de la cual los cationes Ag^+ se difunden rápidamente en los sitios intersticiales tetraédricos distorsionados (mostrados en rojo). En el caso del α-Ag_2Se estequiométrico, trabajos como los llevados a cabo por *Boolchand et al.* [153] han asociado los 4 átomos de plata y los 2 átomos de selenio en cada celda unitaria, requiriendo así 8 sitios intersticiales tetraédricos (átomos rojos), los cuales pueden ser ocupados por la plata en las caras del cubo, ya que éstas son compartidas por dos cubos adyacentes. Esto conduce a una coordinación de 4 y 8 para la plata y el selenio. Estos notables cambios que experimenta el material alrededor de su temperatura crítica ($\approx$ 133°C) provocan un cambio en las propiedades de transporte, pasando de tener 0.098 eV de banda prohibida para la fase *ortorrómbica*-Ag_2Se a 0 eV para la fase Ag_2Se cúbica, como han sido reportado experimentalmente por *Xiao et al.* [128]. Este comportamiento metálico en su conductividad electrónica es de particular interés si se logra una modulación de las propiedades eléctricas en las temperatura de transición -o incluso por debajo de éstas-, lo que podría traducirse en un significativo incremento en el factor de potencia termoeléctrico. Además de la contribución que tiene esta transición de fase en las propiedades de transporte eléctrico, la conductividad térmica (κ) también es dependiente del comportamiento super-

iónico que presenta el $Ag_{2-x}Se$. Investigaciones llevadas a cabo en Ag_2Se en volumen por *Day et al.* [154] han asociado que alrededor del 70 % al 80 % de la conductividad térmica total κ es contribución de la conductividad térmica electrónica $\kappa_{Electrnica}$, alrededor de la región de transición de fase. Esta porción electrónica domina la conductividad térmica total κ, pasando de $1,5 \mathrm{Wm^{-1}K^{-1}}$ a temperatura ambiente hasta valores de entre 2 y 3 $Wm^{-1}\mathrm{K}^{-1}$ por encima de la transición de fase.

En la **Figura 1.13**, se muestra una detallada revisión bibliográfica [90, 155–158] en donde se muestra como en una limitada región de la estequiometría $Ag_{2+x}Se$, las fases *ortorrómbica* y *cúbica* coexisten en una zona de mezcla α-Ag_2Se + β-Ag_2Se.

Al igual que en el caso del Cu_2Se, la complejidad de los procesos involucrados durante estas transiciones de fase, ha originado un intenso debate dentro de la comunidad y ciertas discrepancias en los valores de zT de la temperatura ambiente. Actualmente, podemos encontrar valores de zT para muestras en volumen que varían desde 0.32 a 0.96 a temperatura ambiente [36, 37, 154].

Como se trato previamente en la **apartado 1.1.1**, una estrategia exitosa para reducir la conductividad térmica es mediante la reducción de tamaño de grano, como en el caso de las películas delgadas, en donde se introducen una gran densidad de intercaras, generando una dispersión de fonones. Adicionalmente, debido al desorden ocasionado por los cationes de Ag^+ en la red, los fonones puede ser dispersados, lo que ayudaría a reducir la conductividad térmica.

Los prometedores valores de zT cercanos a 1 a temperatura ambiente, así como los obtenidos por [154] para Ag_2Se en volumen, demuestran la potencialidad de este material como un posible candidato a sustituir el Bi_2Te_3 en el rango de las bajas temperaturas. Paro para que esta potencialidad sea una realidad, es necesario esclarecer los procesos involucrados alrededor de la transición de fase y de cómo esta influye en las propiedades de transporte. Asimismo, al igual que en el caso del Cu_2Se, la estabilidad del material en lo que se refiere a las posibles segregaciones de los cationes metálicos debe ser esclarecida; es decir, si se debe al proceso de manufactura o es intrínseco del material y qué estrategias se pueden utilizar para contener esta migración.

Durante esta tesis doctoral, nuestra aproximación ha sido la de desarrollar un nuevo sistema de deposición en el cuál es posible crecer películas delgadas de $Ag_{2+x}Se$ como de $Ag_{2+x}Se$ con un preciso control estequiométrico x de la relación Ag/Se y Cu/Se. Información del sistema de pulverización catódico modificado puede ser consultada en [83] y en la **apartado 2**.

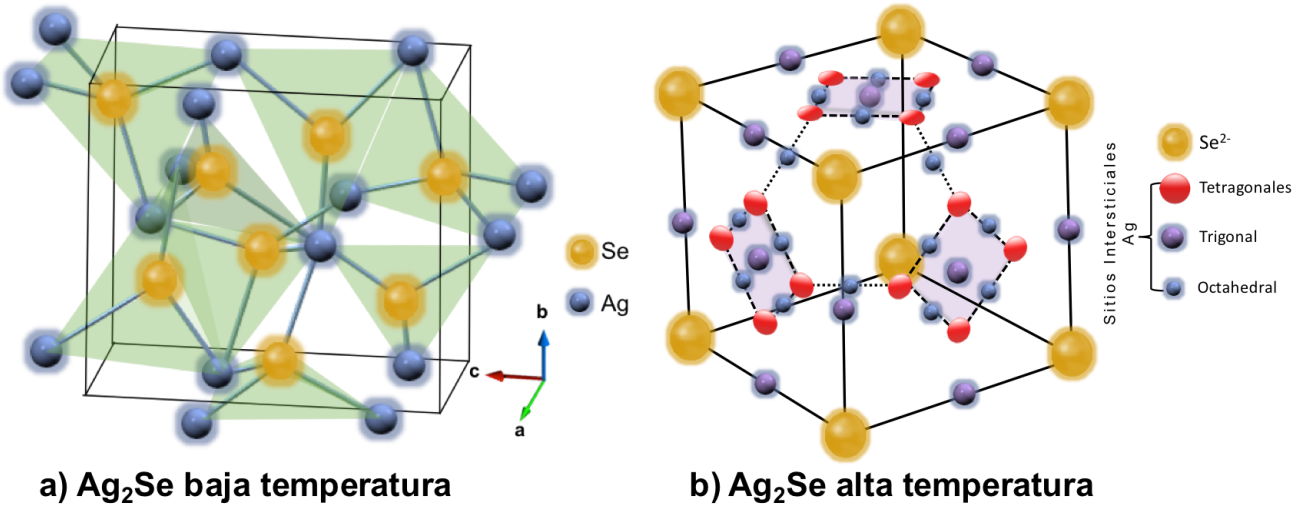

Figura 1.12: Este ordenamiento de la fase cúbica que presenta el α-Ag_2Se en alta temperatura es debido a que la subred del selenio se ordena en una red BCC mientras que los átomos de plata se distribuyen estadísticamente sobre varios sitios intersticiales y se deslocalizan a lo largo de los sitios octaédricos y tetraédricos, en los cuales los cationes Ag^+ exhiben una conductividad superiónica. Imagen adaptada de la referencia [153]

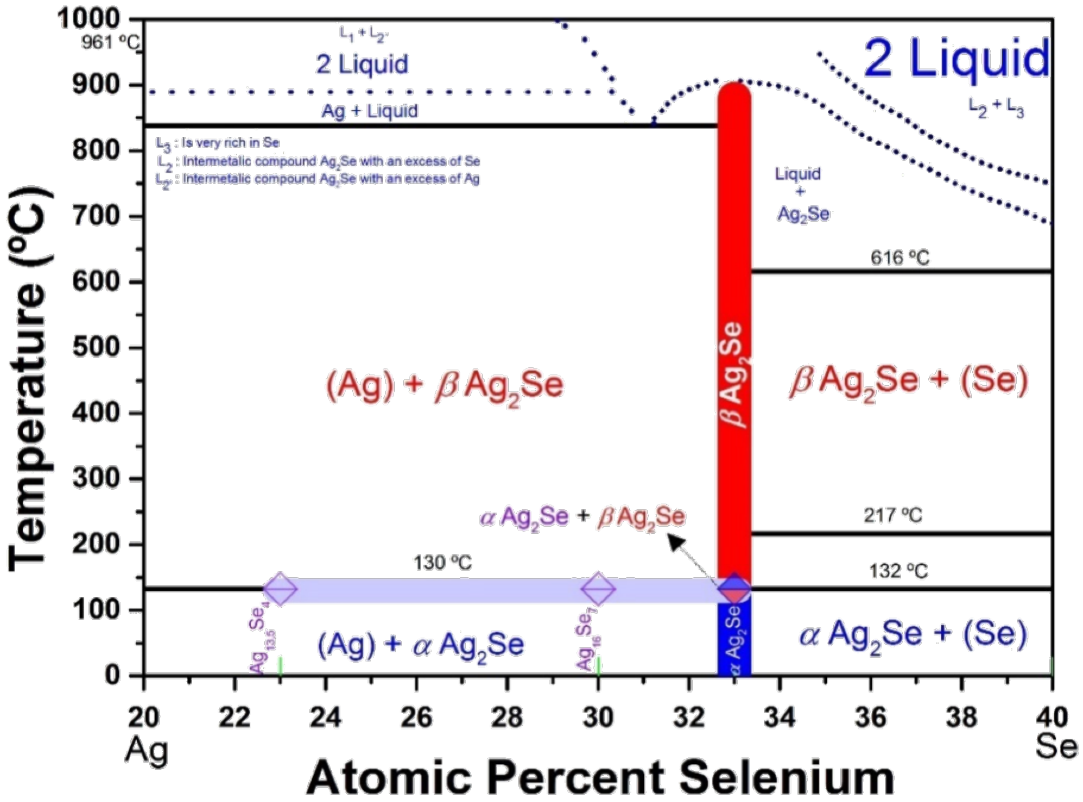

Figura 1.13: El diagrama de fase para el Ag_2Se recoge una detallada revisión de la literatura que hemos realizado. En la imagen se muestran las posibles estequiometrías en las que pueden coexistir las fases de alta y baja temperatura del $Ag_{2+x}Se$. [90, 155–158]

1.4. Pulverización catódica

El recubrimiento por pulverización catódica es una de las técnicas de deposición de vapor físicas más populares y de más rápido crecimiento. La tecnología tiene aplicaciones importantes en el sector de electrónica, fotovoltaica y semiconductores. Se prevé que el mercado global de recubrimiento por pulverización catódica de materiales crezca de 4166.3 millones de dólares en 2014 a 5,600 millones de dólares en 2020, con un crecimiento anual del 4.96 % por año. Lo que hace que la pulverización sea atractiva para la investigación y la industria es que el procedimiento de síntesis generalmente se hace lejos del equilibrio termodinámico, y permiten sintetizar materiales metaestables.

El concepto básico de la deposición por *pulverización catódica* se basa en la *transferencia de momento*. Análogamente es similar a un juego de billar, en donde una partícula incidente de alta energía golpea la superficie del material blanco, expulsando los átomos del *material a evaporar* **Figura 1.14**. Las partículas eyectadas serán transportadas a través de la cámara de deposición y eventualmente se condensarán sobre el substrato. La deposición por pulverización catódica se realiza en vacío.

El *vacío* es necesario para favorecer el camino libre medio de los átomos, además de eliminar cualquier gas residual, especialmente el vapor de agua, que puede deteriorar el proceso de formación del plasma (ocasionando cortocircuitos en el magnetrón e interrumpiendo el proceso de deposición). Asimismo, evitar la contaminación con otros elementos en los recubrimientos. El máximo vacío alcanzable por el sistema antes de realizar el depósito se conoce como *presión base*.

Una presión de gas de trabajo demasiado alta dará como resultado que el material blanco sea pulverizado con facilidad, pero ocasionará una reducción en *el camino libre medio* de las partículas dificultando la nucleación en la superficie a recubrir. Para el caso en el que la *presión de trabajo* es mas baja, el recorrido libre medio de las partículas en el plasma es mayor, y por tanto mayor la energía con la que los átomos alcancen el blanco y el sustrato a recubrir. Sin embargo, si la presión es demasiado baja no existen suficientes átomos ionizados y por tanto la descarga se extingue rápidamente.

Como la transferencia de momento es más eficiente cuando la masa de los átomos del material blanco y el gas de trabajo son similares, generalmente se utilizan gases nobles. En especial gas argón, ya que es mas barato, abundante y adecuado para la mayoría de los materiales que otros gases nobles. Con el fin de ionizar el gas argón y guiar los iones hacia el blanco, se utiliza un campo eléctrico en el blanco que actúa como terminal negativo (cátodo) mientras que el ánodo del magnetrón actúan como terminal positivo (ver **Figura 1.14**). Si pensamos en un electrón libre disperso dentro de la cámara de vacío, este es acelerado por el campo eléctrico desde el cátodo hacia el ánodo. Cuando el electrón alcanza la primera energía de ionización del argón (15,7eV), una colisión directa con un átomo de argón ionizará el átomo

y expulsará otro electrón, siguiendo un proceso del tipo:

$$\mathbf{e}^- + Ar \Rightarrow \mathbf{Ar}^+ + \mathbf{2e}^- \tag{1.7}$$

Este proceso de bombardeo iónico es el responsable de la deposición sobre el sustrato. Los iones (los cuales están ionizados por el fuerte campo eléctrico que ocasionan las colisiones entre las especies) están contenidos en el *plasma* y son acelerados hacia el blanco mediante un campo eléctrico. La alta diferencia de potencial entre el *cátodo* y el *ánodo* provoca que los iones del gas de trabajo golpeen el material blanco con una energía suficiente para desprender átomos de la superficie del cátodo mediante un proceso de transferencia de momento (como fue descrito anteriormente).

Producto de la colisión entre el ion del material desprendido y la superficie del material, se produce una transferencia de parte de su energía a los átomos que lo forman, lo cual ocasiona multiples colisiones con un *efecto de avalancha*. éstas colisiones en cascada hacen posible que algunos átomos del material adquieran la suficiente energía para abandonar la superficie del material pulverizado hasta alcanzar el sustrato y adherirse a él. La mayor parte de la energía proporcionada por los iones incidentes se transforma en calor, el cual debe ser disipado mediante un circuito de refrigeración que evita el sobrecalentamiento del cátodo por el riesgo de perdida de imantación en el magnetrón. El *magnetrón* consiste en dos o más imanes permanentes situados detrás del blanco con sus polos magnéticos opuestos entre sí para cerrar sus líneas de campo y refrigerados por agua para asegurar que su temperatura permanecerá por debajo de la temperatura de Curie. Un esquema se muestra en **Figura 1.14**.

Eventualmente, el resultado será una *avalancha de electrones* que constantemente ionizan el gas argón producto del campo eléctrico provocando una atracción hacia el cátodo. El resultado de un impacto directo con la superficie del blanco se traduce en la generación de átomos pulverizados y electrones secundarios. Los átomos pulverizados viajarán al substrato y, si la distancia entre el blanco - sustrato y la trayectoria libre media de los átomos se optimizan, una película delgada se depositará sobre el sustrato. Por otra parte, los electrones secundarios volverán a entrar en un proceso de “avalancha"para formar continuamente iones positivos de argón. El campo magnético generado atrapará a los electrones secundarios forzándolos a moverse en un movimiento helicoidal a lo largo de las líneas de campo, aumentando el camino libre medio cerca del material blanco antes de ser absorbido. Este fenómeno puede ser descrito en parte por la fuerza de Lorentz (F):

$$\mathbf{F} = \boldsymbol{e/m}(\nu \times \mathbf{B}) \tag{1.8}$$

En donde ν es la velocidad del electrón, m es la masa del electrón, e la carga elemental y B intensidad del campo magnético.

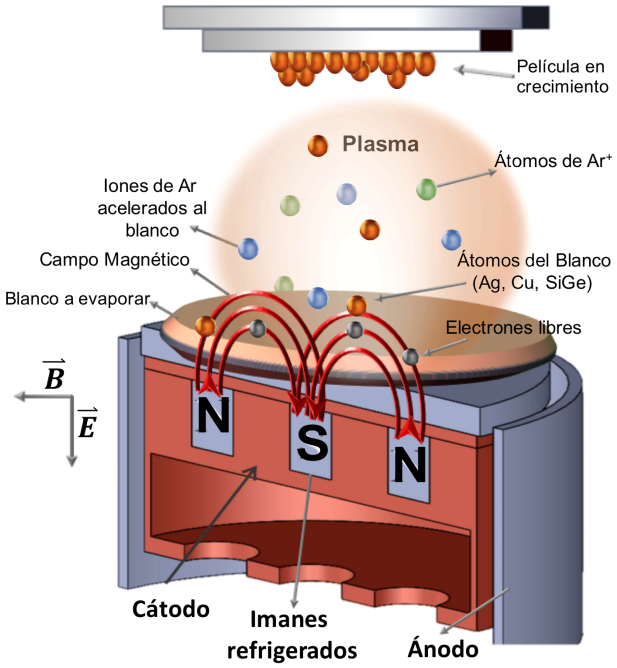

Figura 1.14: Un esquema del proceso de pulverización catódica es mostrado. En esta representación, se muestra los diferentes procesos de colisión entre las especies presentes en el plasma *iones del argón, electrones libres, átomos del material evaporado*. Asimismo, se muestra como el campo eléctrico y magnético causarán un movimiento helicoidal de éstas especies generando nuevas colisiones y produciendo así el crecimiento de la película delgada.

1.4.1. Pulverización catódica reactiva

La pulverización reactiva, se produce cuando se incluye un *gas reactivo* en el flujo de gas de trabajo para formar nitruros, óxidos, carburos, oxinitruros, sulfuros, y seleniuros, entre otros. Las moléculas/iones del gas reactivo se combinan con los átomos provenientes de la pulverización catódica formando un material compuesto. Uno de los mayores retos en la pulverización reactiva es que el gas reactivo también puede reaccionar con el material blanco y *"envenenar"* al material blanco creando una película de óxido, nitruro, seleniuros o del gas reactivo usado, según el caso. Esto provoca que el proceso de deposición continúe con un blanco envenenado, lo que puede influir en el rendimiento (*tasa de depósito*) y sobre la estequiometría obtenida en el recubrimiento. Con el fin de resolver este problema, el flujo del gas reactivo debe regularse para obtener las tasas de deposición y la estequiometría deseadas. Disminuir el flujo del gas reactivo no se traduce instantáneamente en la salida del sistema del estado envenenado; es necesario un cierto tiempo de evacuación para que el bombeo genere una desorción del material depositado en las paredes de la cámara. Esto puede ocasionar problemas de control estequiométrico y cortocircuitos en el magnetrón, interrumpiendo el proceso de depósito. Una de las soluciones mas comúnmente utilizadas es la de usar ciclos automatizados de alimentación del gas reactivo, (controlando su apertura) intentado mantener el flujo de gas reactivo en la región de transición entre el modo envenenado y la pulverización del blanco.

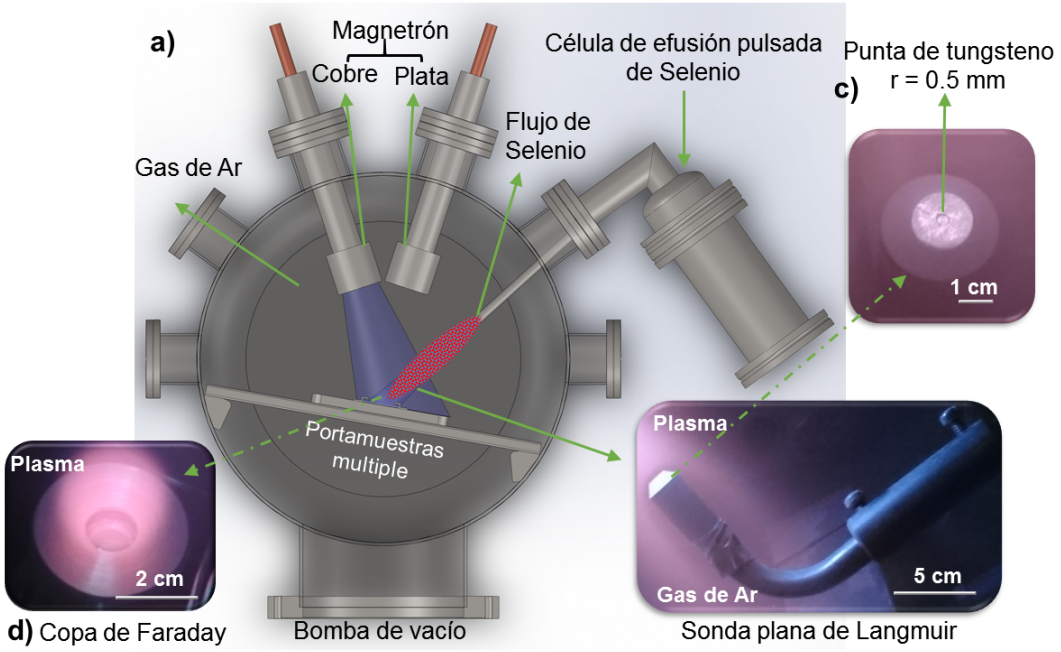

Figura 1.15: En **(a)** se muestra un esquema del montaje experimental en donde se detallan las partes que componen a nuestra técnica de pulverización catódica reactiva pulsada de selenio. En **(b-c)** fotografías de la *Sonda plana de Langmuir* y en **(d)** la *copa de Faraday* con las cuales hemos medido algunos de los principales parámetros del plasma como *(*densidad iónica del plasma, temperatura electrónica/iónica, distribución de energía).

Durante la realización de esta tesis doctoral hemos llevado a cabo la puesta en marcha de dos sistemas independientes de pulverización catódica. El primero un sistema de ultra alto vacío, no reactivo y con un uso exclusivo para la fabricación de nanoestructuras de $Si_{0,8}Ge_{0,2}$ *tipo p* y *tipo n*. Ver [80, 82].
En lo que respecta a la fabricación de las nanoestructuras de $Ag_{2-x}Se$ y $Cu_{2-x}Se$, un sistema convencional de pulverización catódica ha sido modificado (ver **Figura 1.15a**) con una célula pulsada especialmente diseñada y construida para realizar una incorporación controlada (en pulsos cuadrados en (ms) y frecuencias en (Hz)) de Selenio atómico. Como consecuencia de esto, obtenemos un muy particular proceso de plasma reactivo el cual ha sido estudiado en algunos de sus principales parámetros como: *densidad iónica del plasma, temperatura electrónica/iónica y distribución de energía* a través de *sonda de Langmuir* (**Figura 1.15 b,c**) y *copa de Faraday* (**Figura 1.15d**). Estas herramientas de diagnóstico del plasma han sido diseñadas y construidas durante esta tesis doctoral.
Las características propias del método *Pulsed Hybrid Reactive Magnetron Sputtering (PHRMS)* [83], que se ha diseñado y construido durante el desarrollo de esta tesis, permite una reacción de superficie y una cinética de incorporación controlada, con lo cual, obtenemos directamente en un solo paso películas delgadas de $Ag_{2-x}Se$ y $Cu_{2-x}Se$ con valores de figura de mérito que se encuentran en el estado del arte [83]. Estas películas ha sido crecidas a una temperatura menor que la utilizada en los procesos actuales de este tipo y a altas tasas de depósito, compatible con sustratos flexibles poliméricos.

Capítulo 2

Métodos de caracterización

2.1. Técnicas de caracterización estructural

2.1.1. Difracción de rayos X en ángulo rasante con fuente de radiación de sincrotrón

Todas las medidas en las que se ha utilizado *difracción de rayos X con fuente de radiación de sincrotrón* (synchrotron radiation-grazing incidence X-ray diffraction (**SR-GIXRD**)) han sido realizadas en la línea de sincrotrón **XRD2** del *Laboratorio de Luz de Sincrotrón de Brasil (LNLS, Campinas - Brasil)*. Se ha utilizado una energía de 9 keV, que corresponde a una longitud de onda $\lambda = 0.13775$ nm. La disposición general de los principales elementos ópticos de la línea de luz se muestra en la **Figura 2.1**. Específicamente esta línea está dotada de un espejo cilíndrico de ultra baja expansión térmica revestido con rodio, situado a 7 m del dispositivo de inserción, lo que permite la variación de la divergencia vertical del haz y suprimir los armónicos de mayor energía superiores a 17 keV. Adicionalmente, la línea de luz está provista de un monocromador compuesto por dos espejos sagitales de Si (111). Los patrones de difracción de la muestra patrón de silicio utilizada han presentado una resolución instrumental angular máxima de 0.01º en su anchura a media altura (FWHM) en 2θ para cada difractograma de difracción. Información adicional se puede encontrar en las referencias [159, 160].

En lo que respecta a la detección que hemos utilizado, la línea esta provista de un detector de silicio unidimensional que funciona en modo de recuento de fotones individuales de la empresa Dectris. El *Mythen1K* es un detector de 1280 tiras con 50 μm de ancho para cada tira. Las medidas han sido llevadas a cabo en incidencia rasante con un ángulo fijo de penetración de $\theta = 5$º. En lo que respecta a la detección, durante la medida un rango de detección en 2θ fue fijado entre 10º hasta 65º con 0.025º por paso, lo que corresponde a $1x10^5$ recuentos de luz por paso con una rejilla de detección de 0.5 mm. La línea de luz está provista de una cámara de calentamiento (**Figura 2.1b**) con la cual realizar experimentos dinámicos en temperatura; logrando un calentamiento - enfriamiento controlado. En nuestro caso, se realizaron mediciones de *SR-GIXRD* en películas delgadas de $Si_{0,8}Ge_{0,2}$, $Ag_{2-x}Se$ y $Cu_{2-x}Se$.

Específicamente para los seleniuros ($Ag_{2-x}Se$ y $Cu_{2-x}Se$) se ha variando las temperaturas en un ambiente de argón controlado debido al interés de estudiar su transición de fase y su reversibilidad. El horno se programó para seguir una rampa de 5 °C/min hasta llegar a cada punto de medida variando desde 25 °C hasta 300 °C y su posterior enfriamiento controlado hasta temperatura ambiente. En total se han realizado 46 medidas (una para cada temperatura) para cada muestra de $Ag_{2-x}Se$ y $Cu_{2-x}Se$ estudiada. El tiempo total en cada medida para cada temperatura especifica fue de 12 min (7 min para la estabilización de la temperatura y 5 minutos para cada medida). Debido al alto consumo de tiempo que requieren éstos experimentos, las mediciones se han realizado durante dos estancias y gracias a dos ventanas de tiempo de tiempo de sincrotrón que nos han concedido.

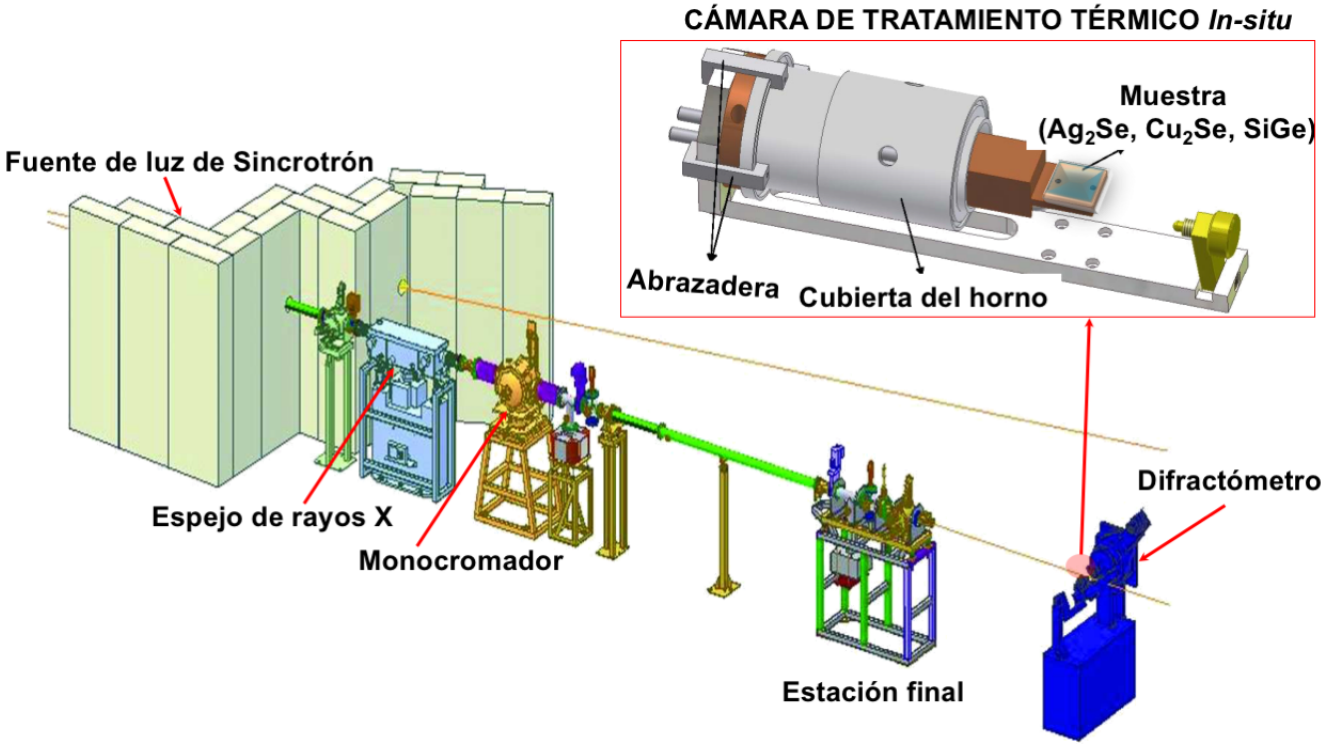

Figura 2.1: En la figura se muestra un esquema básico de los componentes principales de la línea de luz XRD2 en LNLS. De izquierda a derecha se puede ver: Dispositivo de extracción del anillo de sincrotrón, espejo de rayos X, monocromador de doble cristal, estación óptica final, difractómetro de seis círculos. Esta imagen es adaptada de la referencia [159, 160]. Una ampliación en la Figura **(b)** muestra el horno utilizado para el tratamiento térmico $In-situ$ durante los experimentos dinámicos.

2.1.2. Espectroscopía de fotoelectrones emitidos por Rayos X - (XPS)

La *espectroscopía de fotoelectrones emitidos por Rayos X - (XPS)*, es una técnica de estudio superficial, semicuantitativa, altamente sensible y de baja resolución espacial. XPS brinda información de la composición y estequiometría de todos los elementos que están presentes en

un material, en concentraciones mayores al 0.1 % atómico (a excepción de Hidrogeno y Helio los cuales no son posibles de detectar por su baja sección eficaz). Una de las grandes ventajas que tiene el XPS, es que permite diferenciar distintos estados de oxidación y/o entornos de coordinación de los elemento en las películas analizadas. Además, es posible realizar un estudio en profundidad mediante perfiles composicionales, mediante un decapado iónico a través del uso de un cañon de iones en ambiente de argón Ar^+ y posterior medida. Además este decapado se realiza en todas las muestras para eliminar la contaminación superficial resultante de la manipulación y transferencia de la muestra desde su fabricación hasta la medida. El área que se puede analizar mediante XPS varía entre 50 nm y 600 μm de diámetro (dependiendo si se mide con el monocromador y del ángulo de medida). Para una superficie de película delgada, la energía de unión E_b se mide convencionalmente con respecto al nivel de Fermi E_f en lugar del nivel de vacío (**Figura 2.1.2b**), escribiéndose de la forma:

$$\mathbf{E_{Kin}} = \hbar_{\boldsymbol{\omega}}\boldsymbol{\omega} - \mathbf{E_b} - \mathbf{\Phi}_{\omega} \tag{2.1}$$

En donde Φ_ω es la función de trabajo del material, $\hbar_\omega$ es la constante de Plank, ω es la frecuencia del fotón. La medida de la energía cinética del fotoelectrón permite determinar su energía de ligación, E_b, la cual es característica para cada elemento. Además, el número de electrones colectados es proporcional a la concentración de los elementos en la muestra. Valiéndonos de ésto, el análisis de un espectro de XPS permite determinar la naturaleza de los elementos presentes y su concentración. Como el camino libre medio de los electrones en los sólidos es muy pequeño, los electrones detectados provienen principalmente de las últimas capas atómicas de la superficie (una profundidad del orden de decenas de ngstroms). Un esquema de ésto se puede ver en la **Figura 2.1.2**

En nuestro caso, hemos realizado un estudio mediante XPS de la composición elemental de las superficies y estado químico de las películas delgadas ($Si_{0,8}Ge_{0,2}$, $Ag_{2-x}Se$ y $Cu_{2-x}Se$) en que se ha centrado esta tesis doctoral. Las medidas de XPS se han realizado en una cámara de UHV con una presión base de $3 \cdot 10^{-10}$ mbar, utilizando un analizador *SPECS PHOIBOS 100/150* equipado con una fuente de rayos X Al Kα de 1486.6 eV y un espejo monocromador con una resolución = 0.5 eV en anchura a media altura. Las mediciones de alta resolución se llevaron a cabo usando un paso de 0.02 eV. Para el análisis de los datos, los espectros fueron sujetos al ajuste de sustracción de fondo del tipo Shirley. La escala de las energías de enlace se calibró con respecto al pico del nivel interno Au $4f_{7/2}$ a 84 eV, Ag $3d_{5/2}$ y del C $1s = 284.6$ eV. Este análisis y ajuste de los espectros se realizó con el software CASA-XPS de SPECS. Una de las principales ventajas del equipo utilizado, es que está provisto de un soporte especialmente diseñado para calentamientos $In-situ$ con el cual estudiar las transiciones de fase, como en el caso de selenuros de plata y cobre. En la **Figura 2.1.2c** se muestra una imagen de la cámara de muestras utilizada durante nuestras mediciones. La temperatura de la muestra se mide con un termopar de tipo K (cromel-alumel) adaptado al porta-muestras transferible del XPS. El termopar está en contacto directo con la muestra, mientras la muestra es

calentada/enfriada y durante toda la obtención de los espectros de XPS, con una precisión de ±0,7°C. éstas medidas las he realizado en el transcurso de dos estancias de investigación bajo la supervision del Prof. Alexandre Mello de Paula y del Dr. Elvis López en el grupo de superficies y nanoestructuras del Centro Brasileño de Investigaciones Físicas de Rio de Janeiro, Brasil.

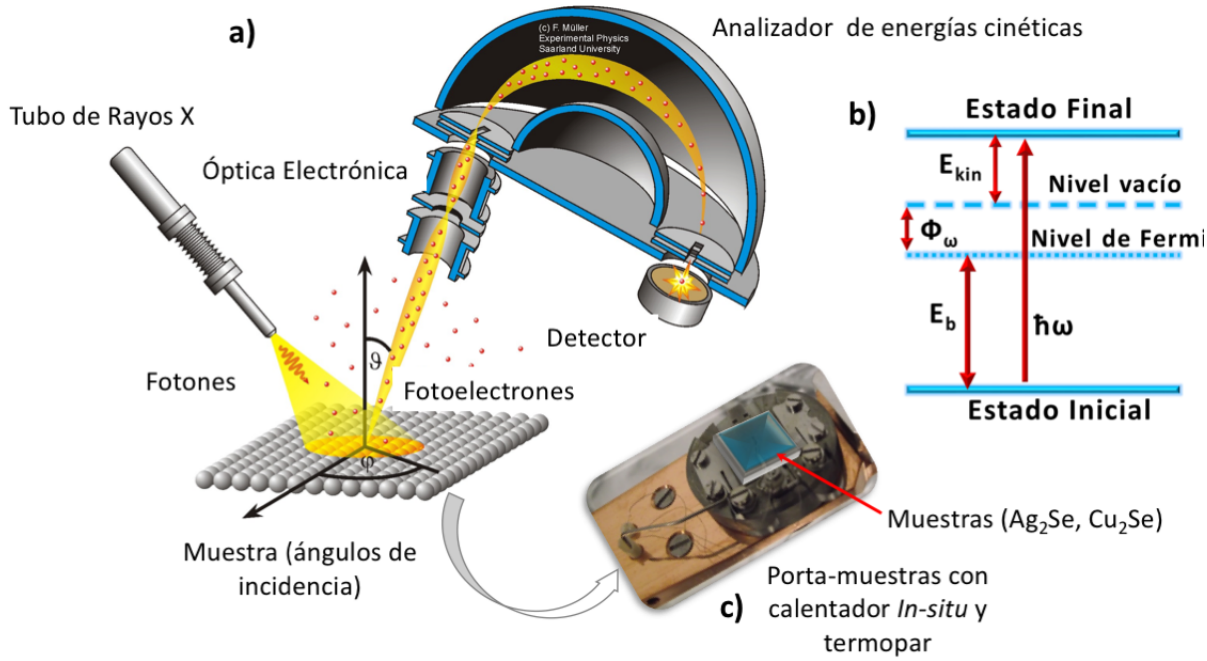

Figura 2.2: Vista esquemática del proceso de fotoemisión es mostrado en: **(a)** un fotón de energía procedente del tubo de rayos X incide sobre una superficie de película delgada provocando la absorción del fotón en el material y causando el desprendimiento de fotoelectrones en una dirección ϑ con respecto al sistema de referencia (la superficie de la muestra en este caso) en donde en **(b)** Φ_ω denota la función de trabajo del material y $\hbar_\omega$ es la constante de Plank, ω es la frecuencia del fotón. El origen de las energías de enlace está relacionado con el nivel de Fermi E_f, mientras que las energías cinéticas tienen como referencia el nivel de vacío. La diferencia entre ambos niveles se corresponde con la función de trabajo, Φ_ω. Esta imagen ha sido adaptada del grupo de investigación del *Prof. Dr. Karin Jacobs*, [161]. En la Figura **(c)** se muestra una imagen del portamuestras utilizado para mediciones con calentamiento controlado *In-situ* dentro del XPS.

2.1.3. Microscopía Raman

Con el fin de obtener información sobre las propiedades vibracionales de los materiales obtenidos en esta tesis doctoral ($Ag_{2-x}Se$, $Cu_{2-x}Se$ y $Si_{0,8}Ge_{0,8}$) se han realizado medidas de espectroscopía Raman. La *espectroscopía Raman* consiste en detectar la dispersión inelástica en el material originada por los fotones que llegan a la misma, normalmente desde una fuente monocromática. Éstos fotones chocan con la muestra originando un desplazamiento de éstos en energía al absorber o excitar un modo de vibración del material. Por lo tanto, este desplazamiento en energía proporciona información sobre los modos de vibración del material.

La *espectroscopía Raman* es una técnica no destructiva que es utilizada tanto en materiales orgánicos como inorgánicos. Dependiendo de si los fotones dispersados tienen mayor o menor longitud de onda que los incidentes, se originan dos tipos de dispersiones Raman inelásticas: *Stokes (menos longitud de onda)* y *anti-Stokes (mayor longitud de onda)*. En nuestro caso, las medidas de espectroscopía Raman se realizaron con un espectrómetro Raman de alta resolución (Horiba Jobin Yvon) acoplado a un microscopio óptico con un láser Nd:YAG en aire a temperatura ambiente. Nuestro sistema esta provisto con dos láseres λ_{Verde}= 532 nm y λ_{Rojo}= 633 nm.

$$\xi = \frac{\mathbf{1,22}\lambda}{\mathbf{NA}} \tag{2.2}$$

$$\zeta = \frac{\mathbf{4}\lambda}{(\mathbf{NA})^{\mathbf{2}}} \tag{2.3}$$

Donde ζ es la penetración, ξ es la resolución espacial, λ es la longitud de onda del láser utilizado y NA es la apertura numérica del objetivo del microscopio, en nuestro caso: NA = 0.25, 0.75 y 0.90 para los objetivos $10x$, $50x$ y $100x$ respectivamente. En la **Figura 2.3(a)** se muestra la relación de penetración del Silicio, Germanio y el $Si_{0,8}Ge_{0,8}$ en función de la longitud de onda del láser utilizado. Este es un factor importante a tener en cuenta para garantizar que las mediciones describen un promedio de la muestra en todo su conjunto. En el caso del λ_{Verde} la penetración en las muestras de $Si_{0,8}Ge_{0,8}$ esta en torno a 700 nm, mientras que para el λ_{Rojo} es de 1.1 μm. En el caso de las películas de $Si_{0,8}Ge_{0,8}$, éstas se midieron en un rango de 200 a 600 cm^{-1}. En esta región es posible obtener los modos vibracionales $Ge - Ge$ alrededor de 300 cm^{-1}, $Si - Ge$ alrededor de 400 cm^{-1} y $Si - Si$ alrededor de 500 cm^{-1} como se muestra en la **Figura 2.3(b)** . En lo que respecta a la resolución espacial en nuestras medidas, están alrededor de 720 nm (con un láser de λ_{Verde}= 532 nm y un objetivo de $100x$ con NA 0.90). éstas medidas las he llevado acabo en nuestro grupo de investigación el Instituto de Micro y Nanotecnología-CNM, CSIC.

2.1.4. Microscopía de sonda Kelvin

La técnica de microscopía por sonda Kelvin (KPM de sus siglas en inglés *"Kelvin Probe Microscopy"*), es un modo no contacto del AFM, en el que se utiliza una punta conductora para estudiar en el material, el potencial de superficie (en simiconductores) o la función de trabajo (en conductores). El modo de trabajo que se usó es modulación en frecuencia (FM) ó gradiente de fuerza KPFM de *"Kelvin Probe Force Microscopy"*. Este modo detecta un corrimiento de la frecuencia de resonancia de la oscilación del cantiléver a una frecuencia eléctrica. Los experimentos fueron realizados en un sistema AFM de Nanotec electrónica equipado con dos tarjetas dinámicas; la primera permite aplicar un potencial eléctrico AC para generar una fuerza electrostática entre la punta y la muestra, y retroalimentar con esta señal en una segunda tarjeta dinámica para hacer cero la fuerza del primer armónico, esto

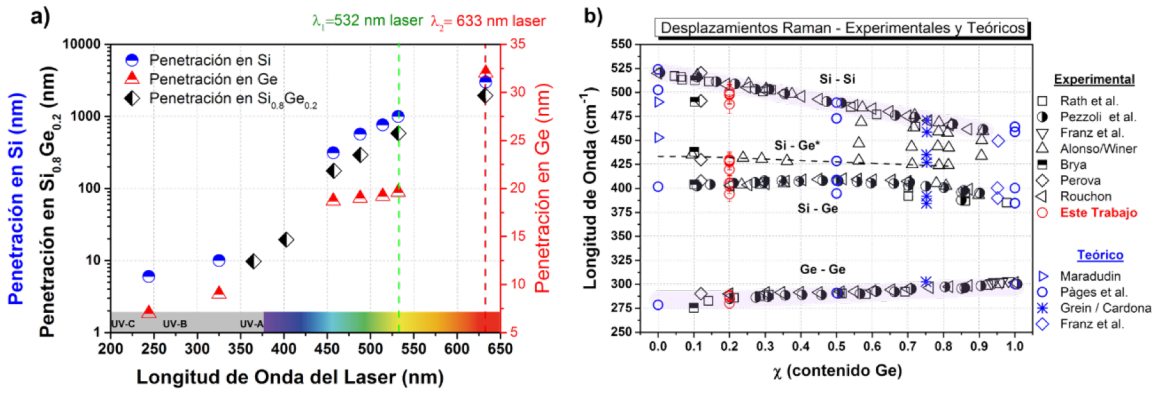

Figura 2.3: En **(a)** se detalla los diferentes valores de penetración del Silicio, Germanio y el $Si_{0,8}Ge_{0,8}$ en función de la longitud de onda del láser utilizado. En nuestras mediciones hemos utilizado como fuente de excitación láseres con λ_{Verde}= 532 nm y λ_{Rojo}= 633 nm. En **(b)** una cuidadosa revisión del estado del arte [162–168] es presentada para los diferentes concentraciones de $Si_{1-x}Ge_x$ en donde se incluyen nuestro valores.

mediante la aplicación de un voltaje de polarización externo DC_{Bias}. Con ésto obtenemos un mapa que nos da información de la diferencia de potencial de contacto, y al mismo tiempo de la topografía. El experimento es realizado en aire a temperatura ambiente y se utiliza una punta con un recubrimiento conductor de Cr/Pt, con frecuencia de resonancia de 75 KHz y una constante de fuerza de 3N/m. Con esta técnica estudiamos el potencial superficial de las muestras y verificamos si hay homogeneidad o cambios en la composición (que pueden afectar el potencial superficial o los estados electrónicos de la estructura local en la superficie de la muestra). Esta técnica ha sido implementada en nuestro grupo de investigación en el Instituto de Micro y Nanotecnología-CNM, y las mediciones han sido llevadas a cabo por integrantes de nuestro grupo, en el caso de $Si_{0,8}Ge_{0,2}$ [80] por el Dr. Miguel Muñoz, y en las muestras de Cu_2Se por la doctoranda Liliana Vera.

2.2. Caracterización Termoeléctrica

2.2.1. Medidas de coeficiente Seebeck y resistividad eléctrica

La *resistividad eléctrica* ρ y el *coeficiente Seebeck* S han sido medidos simultáneamente en un sistema comercial *LSR-3* de la compañía Linseis en una atmósfera de helio. En este sistema las medidas se realizan en el plano en donde la muestra es situada entre dos electrodos de platino (Pt) que generan la diferencia de temperatura ΔT como se detalla en la **Figura 2.5**. A lo largo de la muestra se contactan dos termopares tipo S (Pt-PtRh10 %) los cuales están embebidos dentro de una alumina para evitar el cortocircuito entre el hilo de Pt y otro hilo de PtRh. Una corriente es aplicada entre ambos electrodos, generando una diferencia de voltaje ΔV en la muestra. De esta manera, es obtenida la resistencia R de la intensidad y diferencia de potencial, mediante la ley de Ohm. A partir de la resistencia R y las dimensiones del

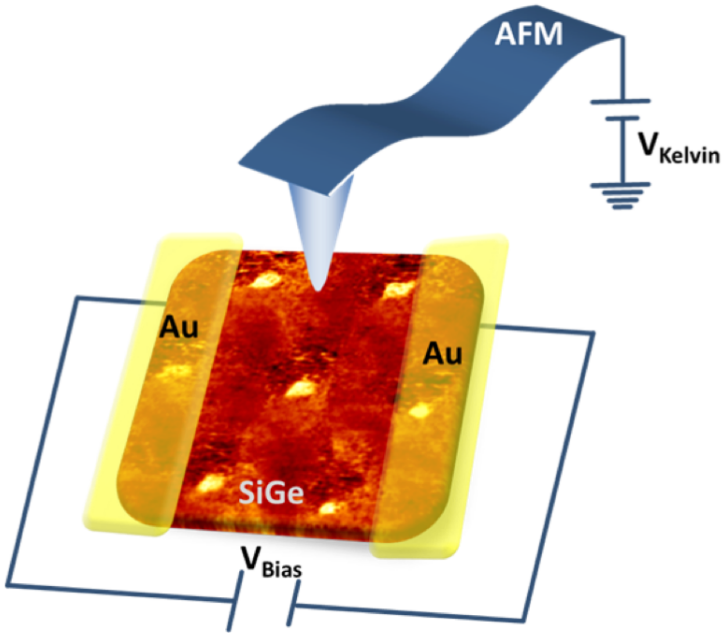

Figura 2.4: En la imagen se muestra un esquema de las nanomallas de $Si_{0,8}Ge_{0,2}$ con los dos contacto de Au definidos mediante litografía por haz de electrones en la parte superior de la película con los cuales se aplica el voltaje de polarización externo.

material es posible obtener la resistividad eléctrica mediante:

$$\mathbf{R} = \rho \frac{l}{s} \tag{2.4}$$

Donde l es la distancia entre los termopares y s es la sección (la anchura de la muestra por el espesor de ésta).

En lo que respecta al *coeficiente Seebeck*, el gradiente de temperatura generado en el electrodo inferior de Pt (marcado en rojo) y el superior frío (marcado en azul) provocan un voltaje termoeléctrico inducido en respuesta a esta diferencia de temperatura a través de la muestra. Este coeficiente se expresa en unidades de V/K (o, más comúnmente, $\mu V/K$).

Este valor obtenido es el *coeficiente Seebeck relativo - (S_{AB})*, por lo que es necesario realizar una corrección para restar la contribución del voltaje termoeléctrico de los termopares de Pt (S_B). Finalmente a partir de ambos valores se obtiene el *coeficiente Seebeck* de la muestra en estudio (S_{AB}) según la ecuación:

$$\mathbf{S_{AB} = S_B - S_A = \frac{\Delta V_B}{\Delta T} - \frac{\Delta V_A}{\Delta T}} \tag{2.5}$$

En lo que respecta al signo, S_{AB} es positivo si los portadores de carga de la muestra responden a un gradiente de temperatura moviéndose del electrodo caliente (marcado en rojo) al electrodo frío (marcado en azul). Las cargas positivas se moverán en la misma dirección del campo eléctrico, mientras que las cargas negativas se mueven en la dirección opuesta del campo aplicado. De este modo para materiales *tipo p* con cargas móviles positivas (huecos), el campo eléctrico y el gradiente de temperatura deberían apuntar en la misma dirección, es

decir un *coeficiente Seebeck* positivo. Asimismo, para materiales *tipo n* con cargas negativas (electrones), el campo eléctrico y el gradiente de temperatura deberían apuntar en direcciones opuéstas en equilibrio, es decir *coeficiente Seebeck* negativo. En términos de la corriente eléctrica generada por el gradiente de temperatura, esta se define como:

$$\mathbf{J} = -\sigma \mathbf{\Delta} V - \sigma S \mathbf{\Delta} T \tag{2.6}$$

Donde $\mathbf{J}$ es la densidad de corriente, σ es la conductividad eléctrica, $\mathbf{\Delta} V$ es el gradiente de voltaje y $\mathbf{\Delta} T$ es el gradiente de temperatura.

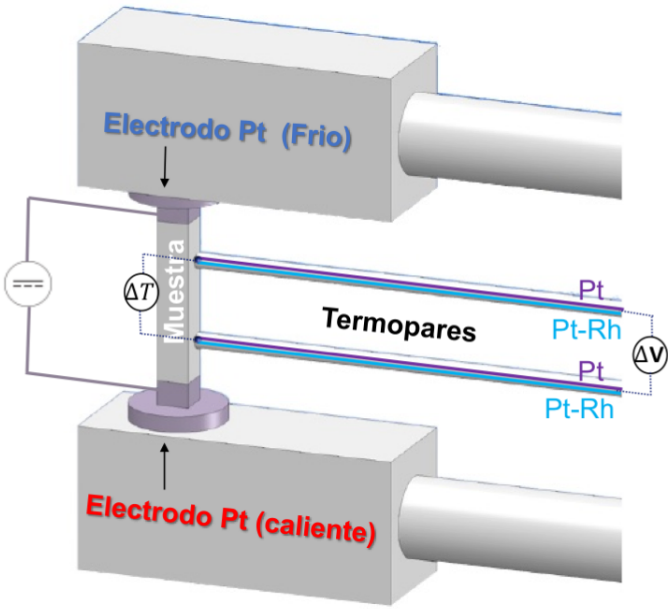

Figura 2.5: En la imagen se muestra un esquema del sistema comercial LSR-3 Linseis con el cual hemos realizado las medidas de resistividad eléctrica y el coeficiente Seebeck en las películas delgadas. Esta imagen es modificada del catálogo de la empresa LINSEIS Messgeräte GmbH. [169]

2.2.2. Medidas de las propiedades de transporte

Un detallado estudio de la concentración de portadores, coeficiente Hall, variación de la movilidad de portadores, y conductividad eléctrica (como comprobación adicional al LSR-3) se han llevado en un equipo comercial HMS-5000 de cuatro puntas (recubiertas de oro para reducir la resistencia de contacto) de la casa comercial ECOPIA. Este equipo está provisto de dos módulos de calentamiento con los cuales se estabiliza la temperatura durante cada una de las medidas. El primer módulo está especialmente diseñado para bajas temperaturas y cuenta con un contenedor de nitrógeno líquido el cual permite realizar medidas desde -193°C hasta 50°C. El segundo módulo esta acondicionado con una resistencia calefactora con la cual realizar medidas desde temperatura ambiente hasta 500°C en un ambiente de

nitrógeno. Éstas medidas las he llevado acabo en el Instituto de Micro y Nanotecnología-CNM - CSIC.

El equipo HMS-5000 realiza las *medidas de resistividad y efecto Hall* a través de la configuración de cuatro puntas con el método de *van der Pauw*. El método de cuatro puntas de *van der Pauw* es una técnica comúnmente usada para medir la resistividad y el coeficiente Hall de una muestra. En una primera aproximación es posible medir con precisión las propiedades de una muestra de cualquier forma arbitraria, siempre y cuando la muestra sea aproximadamente bidimensional (es decir, es mucho más delgada que ancha), continua (sin agujeros) y con una configuración en la que las cuatro puntas sean colocadas en el perímetro de la muestra. Para hacer una medición, se hace circular una corriente conocida a lo largo de un borde de la muestra (por ejemplo, I_{12}) y se mide la tensión provocada a través del borde opuesto (en este caso, V_{34}). A partir de éstos dos valores, es posible obtener una resistencia mediante la ley de Ohm:

$$R_{12,34} = \frac{V_{34}}{I_{12}}$$

Mediante la aproximación utilizada por *van der Pauw* se tiene que la resistencia total de la muestra se puede determinar a partir de dos resistencias (*una medida a lo largo de un borde vertical*), como $R_{12,34}$ y otra que correspondiente *a lo largo de un borde vertical*) $\mathrm{R}_{23,41}.R_{\mathrm{vertical}} = \frac{R_{12,34}+R_{34,12}}{2}(2.7)$

$$R_{\mathrm{horizontal}} = \frac{R_{23,41} + R_{41,23}}{2} \tag{2.8}$$

La resistencia real de la muestra está relacionada con éstas resistencias por la fórmula de *van der Pauw*:

$$e^{-\pi R_{12,34}/R_s} + e^{-\pi R_{23,41}/R_s} = 1 \tag{2.9}$$

$$e^{-\pi R_{\mathrm{vertical}}/R_S} + e^{-\pi R_{\mathrm{horizontal}}/R_S} = 1 \tag{2.10}$$

Una de las principales fortalezas de realizar las mediciones en este equipo HMS-5000 es la obtención simultánea de las propiedades de transporte para una temperatura determinada. Cuando aplicamos una densidad de corriente j_x en una de nuestras películas delgadas en presencia del campo magnético permanente B del equipo, los portadores de carga experimentan una fuerza en una dirección perpendicular tanto al campo magnético como al campo eléctrico inducido E_y. Como resultando, un voltaje V_H aparece en los bordes del semiconductor; el cual definimos como coeficiente Hall:

$$R_H = \frac{E_y}{j_x B} = \frac{V_H t}{IB} = -\frac{1}{ne}. \tag{2.11}$$

O equivalentemente:

$$R_H = \frac{p\mu_h^2 - n\mu_e^2}{e(p\mu_h + n\mu_e)^2} \tag{2.12}$$

Este lo podemos reescribir reemplazando con $b = \frac{\mu_e}{\mu_h}$ como:

$$R_H = \frac{(p - nb^2)}{e(p + nb)^2} \tag{2.13}$$

Donde n es la concentración de electrones, p la concentración de huecos, μ_e la movilidad de los electrones, μ_h la movilidad de los huecos y e es la carga elemental.
La magnitud del voltaje Hall es simplemente la fuerza del campo eléctrico ϵ multiplicada por el ancho de la película delgada w; es decir:

$$\begin{aligned} V_H &= w\epsilon \\ &= \frac{dIB}{qnA} \\ &= \frac{IB}{qnd} \end{aligned} \tag{2.14}$$

Donde d es el espesor de la película delgada, n_s es la densidad de electrones multiplicada por el espesor, A es el área de la sección transversal y q es la carga elemental. Finalmente, podemos definir la tensión Hall como:

$$V_H = \frac{IB}{qn_s} \tag{2.15}$$

Éstas medidas las he llevado acabo en el Instituto de Instituto de Micro y Nanotecnología-CNM, CSIC.

2.2.3. Microscopía de barrido térmico - SThM

La microscopía de barrido térmico (*SThM* por sus iniciales en ingles *"scanning termal microscopy"*), utiliza una sonda térmica acoplada a un microscopio de fuerza atómica (*AFM* de sus siglas en inglés *atomic force microscope*) [65], para estudiar cualitativa y cuantitativamente el transporte de calor en la micro y nanoescala. Midiendo en modo activo, es decir calentando la punta y transfiriendo ésta a su vez el calor a la muestra, se pueden determinar propiedades tales como la conductividad térmica del material a estudio. Para realizar éstas medidas de conductividad térmica, la punta (que tiene un elemento termo-resistivo en su ápice), es conectada a un generador de frecuencias para inducir una corriente alterna, la cual debido al efecto Joule, va a calentar la punta de la sonda. De este modo, cuando se mide en modo contacto, se produce una transferencia de calor desde la punta hacia la muestra. En este proceso la punta pierde calor, pero su cambio de temperatura depende de la facilidad que tenga la muestra para disipar o retener el calor que se esta transfiriendo; es decir, depende de la conductividad térmica propia del material. Como además la resistencia eléctrica de la punta depende su temperatura, al entrar en contacto, el cambio de temperatura en la punta originará un cambio en su resistencia y la temperatura que se relaciona con el segundo armónico (2ω) de la frecuencia de trabajo, sufrirá una fluctuación que es proporcional a un cambio de voltaje en el tercer armónico (3ω) como se muestra en **Figura 2.6a**. Si se trabaja

con el *SThM* y con la señal del 3ω, es posible determinar -a través de unas calibraciones previas y un modelo de transferencia de calor, la conductividad térmica del material, y esto es lo que se conoce como 3ω-SThM [170].

En el desarrollo de esta tesis doctoral las medidas de conductividad térmica llevadas a cabo mediante esta técnica, han sido realizadas en nuestro grupo de investigación, en el Instituto de Micro y Nanotecnología-CNM - CSIC, en un AFM de Nanotec electrónica con dos tipos de sondas térmicas diferentes de la compañía Bruker. La primera es una sonda Wollaston (ver **Figura 2.6b**) y fue utilizada para determinar la conductividad térmica en $Si_{0,8}Ge_{0,2}$[80–82, 170], por el Dr. Miguel Muñoz Rojo. La segunda sonda es micro-fabricada de SiN/Pd **Figura 2.6c**, y ha sido utilizada para obtener simultáneamente imágenes térmicas y topográficas de la muestra, permitiendo realizar medidas locales con alta resolución espacial ($\approx$ 50 nm) y térmica ($\approx$ 80 nm), y determinar la conductividad térmica en la muestras de Cu_2Se [83] y Ag_2Se; éstas medidas han sido realizadas por la estudiante de doctorado Liliana Vera, integrante de nuestro grupo de investigación.

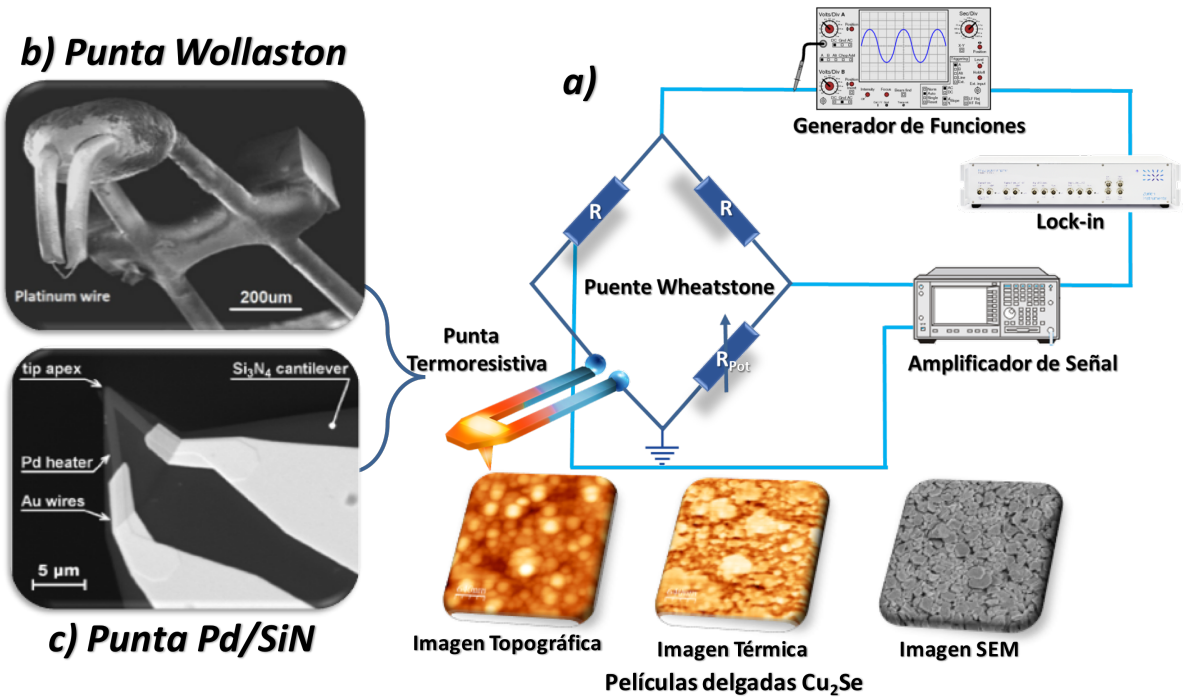

Figura 2.6: En la Figura **(a)** se muestra el montaje experimental para realizar las mediciones de conductividad térmica, en donde la sonda Wollaston mostrada en **(b)** o micro-fabricada de SiN/Pd en **(c)** tienen un elemento termo-resistivo con el cual inducen a una corriente alterna para calentar la punta de la sonda y a través del cambio del voltaje en el tercer armónico (3ω) determinar la conductividad térmica de la película delgada.

2.2.4. Otros equipos de caracterización utilizados

2.2.4.1. Difracción de rayos X

Las propiedades estructurales de los materiales depositados en esta tesis doctoral han sido realizado mediante difracción de rayos X (*XRD, del inglés "X-Ray Diffraction"*). Este análisis se ha realizado en todas las muestras en un difractómetro convencional de rayos X de alta resolución Philips (XPert Pro) en la configuración de Bragg-Brentano (θ-2θ) con una longitud de onda de $\lambda = 0.15418$ nm. Este sistema está disponible en el Instituto de Micro y Nanotecnología-CNM - CSIC.

2.2.4.2. Microscopía electrónica de barrido con emisión de campo

La caracterización morfológica de las películas delgadas, nanomallas y de las membranas porosas de alúmina anódica han sido obtenida mediante microscopía electrónica de barrido con emisión de campo (SEM-FE, del inglés *"Scanning Electron Microscopy Field Emission"*), en un equipo SEM de la casa comercial FEI referencia Verios 460 a una energía de 3 kV. Este sistema está disponible en el Instituto de Micro y Nanotecnología-CNM - CSIC gracias a la financiación del MINECO bajo el proyecto CSIC 13-4E-1794 con el apoyo de la UE (FEDER, FSE).

2.2.4.3. Energía dispersiva de rayos X

La composición química de las películas delgadas y nanomallas han sido analizadas mediante energía dispersiva de rayos X (*EDX, del inglés "Energy Dispersive X-Ray"*), a través de un microscopio SEM con análisis de rayos X de dispersión de electrones de la marca JEOL JSM6335F en el Servicio Interdepartamental de Investigación de la Universidad Autónoma de Madrid (SIdI-UAM).

2.2.4.4. Perfilometría

El espesor de las muestras fue determinado mediante un perfilómetro de la casa comercial Veeco Dektak Stylus. Este sistema está disponible a través del servicio de micro y nanofabricación (MiNa) del Instituto de Micro y Nanotecnología-CNM, (CSIC).

Bibliografía

[1] Thomas Johann Seebeck. *Ueber den Magnetismus der galvanischen Kette*. 1822.

[2] Thomas Johann Seebeck. Ueber die magnetische polarisation der metalle und erze durch temperaturdifferenz. *Annalen der Physik*, 82(3):253–286, 1826.

[3] Enn Velmre. Thomas johann seebeck (1770-1831). In *Proceedings of the Estonian Academy of Sciences: Engineering*, volume 13, pages 276–283. Estonian Academy Publishers, 2007.

[4] J Rud Nielsen. Hans christian oerstedóscientist, humanist and teacher. *American Journal of Physics*, 7(1):10–22, 1939.

[5] J Blatt. *Thermoelectric power of metals*. Springer Science & Business Media, 2012.

[6] JC Peltier. Nouvelles expériences sur la caloricité des courants électrique. In *Annales de Chimie et de Physique*, volume 56, pages 371–386, 1834.

[7] William Thomson. 4. on a mechanical theory of thermo-electric currents. *Proceedings of the Royal society of Edinburgh*, 3:91–98, 1857.

[8] W Thomson. Account of researches in thermo-electricity. *Proceedings of the Royal Society of London*, 7:49–58, 1854.

[9] W Thomson. 5. dynamical theory of heat, part vi. continued. a mechanical theory of thermo-electric currents in crystalline solids. *Proceedings of the Royal Society of Edinburgh*, 3:255–256, 1857.

[10] Xiao Zhang and Li-Dong Zhao. Thermoelectric materials: energy conversion between heat and electricity. *Journal of Materiomics*, 1(2):92–105, 2015.

[11] Edmund Altenkirch. Über den nutzeffekt der thermosäule. *Physikalische Zeitschrift*, 10:560, 1909.

[12] H Diesselhorst. Über das problem eines elektrisch erwärmten leiters. *Annalen der Physik*, 306(2):312–325, 1900.

[13] Ea Altenkirch. Elektrothermische kälteerzeugung und reversible elektrische heizung. *Physikalische Zeitschrift*, 12:920–924, 1911.

[14] Lord Rayleigh. Xliii. on the thermodynamic efficiency of the thermopile. *The London, Edinburgh, and Dublin Philosophical Magazine and Journal of Science*, 20(125):361–363, 1885.

[15] Sadi Carnot. *Réflexions sur la puissance motrice du feu.* Number 26. Vrin, 1978.

[16] Sadi Carnot, Hippolyte Carnot, and William Thomson Baron Kelvin. *Reflections on the Motive Power of Heat: From the Original French of N.-L.-S. Carnot.* John Wiley, 1897.

[17] James Prescott Joule. Xvii. on the effects of magnetism upon the dimensions of iron and steel bars. *The London, Edinburgh, and Dublin Philosophical Magazine and Journal of Science*, 30(199):76–87, 1847.

[18] James Prescott Joule. On some thermo-dynamic properties of solids. *Philosophical Transactions of the Royal Society of London*, 149:91–131, 1859.

[19] Maria Telkes. The efficiency of thermoelectric generators. i. *Journal of Applied Physics*, 18(12):1116–1127, 1947.

[20] Lars Onsager. Reciprocal relations in irreversible processes. i. *Physical review*, 37(4):405, 1931.

[21] AF Joffe. Heat transfer in semiconductors. *Canadian Journal of Physics*, 34(12A):1342–1355, 1956.

[22] Abram F Joffe. The revival of thermoelectricity. *Scientific American*, 199:31–37, 1958.

[23] AF Joffe and LS Stil'bans. Physical problems of thermoelectricity. *Reports on Progress in Physics*, 22(1):167, 1959.

[24] HJ Goldsmid and RW Douglas. The use of semiconductors in thermoelectric refrigeration. *British Journal of Applied Physics*, 5(11):386, 1954.

[25] Abram Fedorovich Ioffe. *Physics of semiconductors.* Infosearch, 1960.

[26] Sybren Ruurds De Groot and Sybren Ruurds De Groot. *Thermodynamics of irreversible processes*, volume 336. North-Holland Amsterdam, 1951.

[27] R Fieschi, SR De Groot, P Mazur, and J Vlieger. Thermodynamical theory of galvanomagnetic and thermomagnetic phenomena ii: Reciprocal relations for moving anisotropic mixtures. *Physica*, 20(1-6):245–258, 1954.

[28] Wilhelm Conrad Röntgen. On a new kind of rays. *Science*, pages 227–231, 1896.

[29] FL Curzon and B Ahlborn. Efficiency of a carnot engine at maximum power output. *American Journal of Physics*, 43(1):22–24, 1975.

[30] Bjarne Andresen, Peter Salamon, and R Stephen Berry. Thermodynamics in finite time: extremals for imperfect heat engines. *The Journal of Chemical Physics*, 66(4):1571–1577, 1977.

[31] Peter Salamon and Abrahan Nitzan. Finite time optimizations of a newtonís law carnot cycle. *The Journal of Chemical Physics*, 74(6):3546–3560, 1981.

[32] Mary Jo Ondrechen, Morton H Rubin, and Yehuda B Band. The generalized carnot cycle: A working fluid operating in finite time between finite heat sources and sinks. *The Journal of Chemical Physics*, 78(7):4721–4727, 1983.

[33] Alan L Rockwood. Relationship of thermoelectricity to electronic entropy. *Physical Review A*, 30(5):2843, 1984.

[34] Alexis De Vos. Thermodynamics of radiation energy conversion in one and in three physical dimensions. *Journal of Physics and Chemistry of Solids*, 49(6):725–730, 1988.

[35] LD Hicks and MS Dresselhaus. Effect of quantum-well structures on the thermoelectric figure of merit. *Physical Review B*, 47(19):12727, 1993.

[36] David Michael Rowe. *CRC handbook of thermoelectrics*. CRC press, 1995.

[37] David Michael Rowe. *Thermoelectrics handbook: macro to nano*. CRC press, 2005.

[38] R Ovik, BD Long, MC Barma, M Riaz, MFM Sabri, SM Said, R Saidur, et al. A review on nanostructures of high-temperature thermoelectric materials for waste heat recovery. *Renewable and Sustainable Energy Reviews*, 64:635–659, 2016.

[39] Hilaal Alam and Seeram Ramakrishna. A review on the enhancement of figure of merit from bulk to nano-thermoelectric materials. *Nano Energy*, 2(2):190–212, 2013.

[40] Marisol Martín-González, Olga Caballero-Calero, and Pablo Díaz-Chao. Nanoengineering thermoelectrics for 21st century: Energy harvesting and other trends in the field. *Renewable and Sustainable Energy Reviews*, 24:288–305, 2013.

[41] Wolfgang G Zeier, Jennifer Schmitt, Geoffroy Hautier, Umut Aydemir, Zachary M Gibbs, Claudia Felser, and G Jeffrey Snyder. Engineering half-heusler thermoelectric materials using zintl chemistry. *Nature Reviews Materials*, 1:16032, 2016.

[42] Eric S Toberer, Lauryn L Baranowski, and Chris Dames. Advances in thermal conductivity. *Annual Review of Materials Research*, 42:179–209, 2012.

[43] Ali Shakouri. Recent developments in semiconductor thermoelectric physics and materials. *Annual Review of Materials Research*, 41:399–431, 2011.

[44] A Moure, M Rull-Bravo, B Abad, A Del Campo, Miguel Muñoz Rojo, MH Aguirre, A Jacquot, JF Fernandez, and M Martin-Gonzalez. Thermoelectric skutterudite/oxide nanocomposites: Effective decoupling of electrical and thermal conductivity by functional interfaces. *Nano Energy*, 31:393–402, 2017.

[45] Joseph P Heremans, Vladimir Jovovic, Eric S Toberer, Ali Saramat, Ken Kurosaki, Anek Charoenphakdee, Shinsuke Yamanaka, and G Jeffrey Snyder. Enhancement of thermoelectric efficiency in pbte by distortion of the electronic density of states. *Science*, 321(5888):554–557, 2008.

[46] Joseph P Heremans, Mildred S Dresselhaus, Lon E Bell, and Donald T Morelli. When thermoelectrics reached the nanoscale. *Nature nanotechnology*, 8(7):471–473, 2013.

[47] Mohamed Hamid Elsheikh, Dhafer Abdulameer Shnawah, Mohd Faizul Mohd Sabri, Suhana Binti Mohd Said, Masjuki Haji Hassan, Mohamed Bashir Ali Bashir, and Mahazani Mohamad. A review on thermoelectric renewable energy: Principle parameters that affect their performance. *Renewable and Sustainable Energy Reviews*, 30:337–355, 2014.

[48] Terry M Tritt. Thermoelectric phenomena, materials, and applications. *Annual review of materials research*, 41:433–448, 2011.

[49] Shiyun Xiong and Sebastian Volz. Nanostructuration for thermoelectricity: The path to an unlimited reduction of phonon transport. *Comptes Rendus Physique*, 17(10):1146–1153, 2016.

[50] Joseph R Sootsman, Duck Young Chung, and Mercouri G Kanatzidis. New and old concepts in thermoelectric materials. *Angewandte Chemie International Edition*, 48(46):8616–8639, 2009.

[51] Mona Zebarjadi, Keivan Esfarjani, MS Dresselhaus, ZF Ren, and Gang Chen. Perspectives on thermoelectrics: from fundamentals to device applications. *Energy & Environmental Science*, 5(1):5147–5162, 2012.

[52] Chunlei Wan, Yifeng Wang, Ning Wang, Wataru Norimatsu, Michiko Kusunoki, and Kunihito Koumoto. Development of novel thermoelectric materials by reduction of lattice thermal conductivity. *Science and Technology of Advanced Materials*, 11(4):044306, 2010.

[53] AJl Minnich, MS Dresselhaus, ZF Ren, and G Chen. Bulk nanostructured thermoelectric materials: current research and future prospects. *Energy & Environmental Science*, 2(5):466–479, 2009.

[54] Li-Dong Zhao, Vinayak P Dravid, and Mercouri G Kanatzidis. The panoscopic approach to high performance thermoelectrics. *Energy & Environmental Science*, 7(1):251–268, 2014.

[55] Eric S Toberer, Prashun Gorai, and Vladan Stevanovi'c. Chapter 1 discovery and design of new thermoelectric materials. In *Materials Aspect of Thermoelectricity*, pages 1–38. CRC Press, 2016.

[56] Hang Chi, Wei Liu, and Ctirad Uher. Chapter 3 growth and transport properties of tetradymite thin films. In *Materials Aspect of Thermoelectricity*, pages 95–124. CRC Press, 2016.

[57] Marta Rull-Bravo, A Moure, JF Fernandez, and M Martin-Gonzalez. Skutterudites as thermoelectric materials: revisited. *Rsc Advances*, 5(52):41653–41667, 2015.

[58] Mildred S Dresselhaus, Gang Chen, Ming Y Tang, RG Yang, Hohyun Lee, DZ Wang, ZF Ren, J-P Fleurial, and Pawan Gogna. New directions for low-dimensional thermoelectric materials. *Advanced Materials*, 19(8):1043–1053, 2007.

[59] George S Nolas, Jeffrey Sharp, and Julian Goldsmid. *Thermoelectrics: basic principles and new materials developments*, volume 45. Springer Science & Business Media, 2013.

[60] George S Nolas, Jeffrey Sharp, et al. Historical development. In *Thermoelectrics*, pages 1–14. Springer, 2001.

[61] Saffa B Riffat and Xiaoli Ma. Thermoelectrics: a review of present and potential applications. *Applied thermal engineering*, 23(8):913–935, 2003.

[62] G Jeffrey Snyder, Mogens Christensen, Eiji Nishibori, Thierry Caillat, and Bo Brummerstedt Iversen. Disordered zinc in zn4sb3 with phonon-glass and electron-crystal thermoelectric properties. *Nature materials*, 3(7):458–463, 2004.

[63] Huili Liu, Xun Shi, Fangfang Xu, Linlin Zhang, Wenqing Zhang, Lidong Chen, Qiang Li, Ctirad Uher, Tristan Day, and G Jeffrey Snyder. Copper ion liquid-like thermoelectrics. *Nature Materials*, 11(5):422–425, 2012.

[64] Li-Dong Zhao, Shih-Han Lo, Yongsheng Zhang, Hui Sun, Gangjian Tan, Ctirad Uher, Christopher Wolverton, Vinayak P Dravid, and Mercouri G Kanatzidis. Ultralow thermal conductivity and high thermoelectric figure of merit in snse crystals. *Nature*, 508(7496):373–377, 2014.

[65] Annu Majumdar. Scanning thermal microscopy. *Annual review of materials science*, 29(1):505–585, 1999.

[66] Woochul Kim, Joshua Zide, Arthur Gossard, Dmitri Klenov, Susanne Stemmer, Ali Shakouri, and Arun Majumdar. Thermal conductivity reduction and thermoelectric figure of merit increase by embedding nanoparticles in crystalline semiconductors. *Physical Review Letters*, 96(4):045901, 2006.

[67] Gary L Bennett, Marcus A Watkins, David C Byers, and John W Barnett. Enhancing space transportation: the nasa program to develop electric propulsion. 1990.

[68] Gary Bennett. Space nuclear power: opening the final frontier. In *4th International Energy Conversion Engineering Conference and Exhibit (IECEC)*, page 4191, 2006.

[69] Richard R Furlong and Earl J Wahlquist. Us space missions using radioisotope power systems. *Nuclear news*, 42:26–35, 1999.

[70] David Anderson, Wayne Wong, and Karen Tuttle. An overview and status of nasa's radioisotope power conversion technology nra. In *3rd International Energy Conversion Engineering Conference*, page 5713, 2005.

[71] Mukund R Patel. *Spacecraft power systems*. CRC press, 2004.

[72] Zhi-Gang Chen, Guang Han, Lei Yang, Lina Cheng, and Jin Zou. Nanostructured thermoelectric materials: Current research and future challenge. *Progress in Natural Science: Materials International*, 22(6):535–549, 2012.

[73] Marc Humphries. Rare earth elements: The global supply chain. *Congressional Research Service*, 16, 2013.

[74] Alexander Kovacs, Harald Ozelt, Johann Fischbacher, Thomas Schrefl, Andreas Kaidatzis, Ruslan Salikhof, Michael Farle, George Giannopoulos, and Dimitris Niarchos. Micromagnetic simulations for coercivity improvement through nano-structuring of rare-earth free l1 0-feni magnets. *IEEE Transactions on Magnetics*, 2017.

[75] Stefania Massari and Marcello Ruberti. Rare earth elements as critical raw materials: Focus on international markets and future strategies. *Resources Policy*, 38(1):36–43, 2013.

[76] Shuo Chen and Zhifeng Ren. Recent progress of half-heusler for moderate temperature thermoelectric applications. *Materials today*, 16(10):387–395, 2013.

[77] Martin A Green. Estimates of te and in prices from direct mining of known ores. *Progress in Photovoltaics: Research and Applications*, 17(5):347–359, 2009.

[78] Reja Amatya and Rajeev J Ram. Trend for thermoelectric materials and their earth abundance. *Journal of electronic materials*, 41(6):1011–1019, 2012.

[79] Michael W Gaultois, Taylor D Sparks, Christopher KH Borg, Ram Seshadri, William D Bonificio, and David R Clarke. Data-driven review of thermoelectric materials: performance and resource considerations. *Chemistry of Materials*, 25(15):2911–2920, 2013.

[80] Jaime Andres Perez-Taborda, Miguel Muñoz Rojo, Jon Maiz, Neophytos Neophytou, and Marisol Martin-Gonzalez. Ultra-low thermal conductivities in large-area si-ge nanomeshes for thermoelectric applications. *Scientific Reports*, 6, 2016.

[81] Jaime Andrés Pérez-Taborda, Olga Caballero-Calero, and Marisol Martín-González. Silicon-germanium (sige) nanostructures for thermoelectric devices: Recent advances and new approaches to high thermoelectric efficiency. In *New Research on Silicon-Structure, Properties, Technology*. InTech, 2017.

[82] JA Perez Taborda, JJ Romero, B Abad, M Muñoz-Rojo, A Mello, F Briones, and MS Martin Gonzalez. Low thermal conductivity and improved thermoelectric performance of nanocrystalline silicon germanium films by sputtering. *Nanotechnology*, 27(17):175401, 2016.

[83] Jaime A Perez-Taborda, Liliana Vera, Olga Caballero-Calero, Elvis O Lopez, Juan J Romero, Daniel G Stroppa, Fernando Briones, and Marisol Martin-Gonzalez. Pulsed hybrid reactive magnetron sputtering for high zt cu2se thermoelectric films. *Advanced Materials Technologies*, 2017.

[84] David C Brock and Gordon E Moore. *Understanding Moore's law: four decades of innovation*. Chemical Heritage Foundation, 2006.

[85] Thomas Ihn. *Semiconductor Nanostructures: Quantum states and electronic transport*. Oxford University Press, 2010.

[86] S Venkataraman, S Venkataraman, Nicholas Dew, and Nicholas Dew. Intel corporate venturing. *Darden Business Publishing Cases*, pages 1–8, 2017.

[87] Douglas Jamison and Stephen Waite. *Venture Investing in Science*. Columbia University Press, 2017.

[88] Ralf B Wehrspohn, Uwe Rau, and Andreas Gombert. *Photon management in solar cells*. John Wiley & Sons, 2015.

[89] Martin A Green, Keith Emery, Yoshihiro Hishikawa, Wilhelm Warta, and Ewan D Dunlop. Solar cell efficiency tables (version 45). *Progress in photovoltaics: research and applications*, 23(1):1–9, 2015.

[90] HJ Herzog. Crystal structure, lattice parameters and liquidus-solidus curve of the sige system. e. kasper. *Properties of strained and relaxed silicon-germanium*, 1995.

[91] Yucheng Lan, Austin Jerome Minnich, Gang Chen, and Zhifeng Ren. Enhancement of thermoelectric figure-of-merit by a bulk nanostructuring approach. *Advanced Functional Materials*, 20(3):357–376, 2010.

[92] Mona Zebarjadi, Giri Joshi, Gaohua Zhu, Bo Yu, Austin Minnich, Yucheng Lan, Xiaowei Wang, Mildred Dresselhaus, Zhifeng Ren, and Gang Chen. Power factor enhancement by modulation doping in bulk nanocomposites. *Nano letters*, 11(6):2225–2230, 2011.

[93] HJ Goldsmid and AW Penn. Boundary scattering of phonons in solid solutions. *Physics Letters A*, 27(8):523–524, 1968.

[94] JE Parrott. The thermal conductivity of sintered semiconductor alloys. *Journal of Physics C: Solid State Physics*, 2(1):147, 1969.

[95] Ramez Cheaito, John C Duda, Thomas E Beechem, Khalid Hattar, Jon F Ihlefeld, Douglas L Medlin, Mark A Rodriguez, Michael J Campion, Edward S Piekos, and Patrick E Hopkins. Experimental investigation of size effects on the thermal conductivity of silicon-germanium alloy thin films. *Physical review letters*, 109(19):195901, 2012.

[96] DM Rowe, VS Shukla, and N Savvides. Phonon scattering at grain boundaries in heavily doped fine-grained silicon–germanium alloys. *Nature*, 290(5809):765–766, 1981.

[97] Bo Yu, Mona Zebarjadi, Hui Wang, Kevin Lukas, Hengzhi Wang, Dezhi Wang, Cyril Opeil, Mildred Dresselhaus, Gang Chen, and Zhifeng Ren. Enhancement of thermoelectric properties by modulation-doping in silicon germanium alloy nanocomposites. *Nano letters*, 12(4):2077–2082, 2012.

[98] Giri Joshi, Hohyun Lee, Yucheng Lan, Xiaowei Wang, Gaohua Zhu, Dezhi Wang, Ryan W Gould, Diana C Cuff, Ming Y Tang, Mildred S Dresselhaus, et al. Enhanced thermoelectric figure-of-merit in nanostructured p-type silicon germanium bulk alloys. *Nano letters*, 8(12):4670–4674, 2008.

[99] Alexey Pustovalov. Mini-rtgs on plutonium-238: development and application. In *Thermoelectrics, 1999. Eighteenth International Conference on*, pages 509–520. IEEE, 1999.

[100] Antonio Sanchez-Torres. Radioisotope power systems for space applications. In *Radioisotopes-Applications in Physical Sciences*. InTech, 2011.

[101] JP Dismukes, L Ekstrom, and RJ Paff. Lattice parameter and density in germanium-silicon alloys1. *The Journal of Physical Chemistry*, 68(10):3021–3027, 1964.

[102] CM Bhandari and DM Rowe. Boundary scattering of phonons. *Journal of Physics C: Solid State Physics*, 11(9):1787, 1978.

[103] ZS Tan, WA Jesser, and FD Rosi. Microstructure of thermoelectric sige alloys containing fullerite. *Materials Science and Engineering: B*, 33(2-3):195–203, 1995.

[104] BA Cook, JL Harringa, and S Loughin. Fullerite additions as a phonon scattering mechanism in p-type si-20 at. % ge. *Materials Science and Engineering: B*, 41(2):280–288, 1996.

[105] XW Wang, H Lee, YC Lan, GH Zhu, G Joshi, DZ Wang, J Yang, AJ Muto, MY Tang, J Klatsky, et al. Enhanced thermoelectric figure of merit in nanostructured n-type silicon germanium bulk alloy. *Applied Physics Letters*, 93(19):193121, 2008.

[106] Eun Kyung Lee, Liang Yin, Yongjin Lee, Jong Woon Lee, Sang Jin Lee, Junho Lee, Seung Nam Cha, Dongmok Whang, Gyeong S Hwang, Kedar Hippalgaonkar, et al. Large thermoelectric figure-of-merits from sige nanowires by simultaneously measuring electrical and thermal transport properties. *Nano letters*, 12(6):2918–2923, 2012.

[107] Jinyao Tang, Hung-Ta Wang, Dong Hyun Lee, Melissa Fardy, Ziyang Huo, Thomas P Russell, and Peidong Yang. Holey silicon as an efficient thermoelectric material. *Nano letters*, 10(10):4279–4283, 2010.

[108] Begoña Abad, Jon Maiz, and Marisol Martin-Gonzalez. Rules to determine thermal conductivity and density of anodic aluminum oxide (aao) membranes. *The Journal of Physical Chemistry C*, 120(10):5361–5370, 2016.

[109] Cristina V Manzano, J Martín, and Marisol S Martín-González. Ultra-narrow 12nm pore diameter self-ordered anodic alumina templates. *Microporous and Mesoporous Materials*, 184:177–183, 2014.

[110] Jaime Martín, Cristina V Manzano, and Marisol Martín-González. In-depth study of self-ordered porous alumina in the 140–400nm pore diameter range. *Microporous and Mesoporous Materials*, 151:311–316, 2012.

[111] Jaime Martín, Cristina V Manzano, Olga Caballero-Calero, and Marisol Martín-GonzaÂlez. High-aspect-ratio and highly ordered 15-nm porous alumina templates. *ACS applied materials & interfaces*, 5(1):72–79, 2012.

[112] Jaime Martín, Marisol Martín-González, Jose Francisco Fernández, and Olga Caballero-Calero. Ordered three-dimensional interconnected nanoarchitectures in anodic porous alumina. *Nature communications*, 5, 2014.

[113] Pedro M Resende, Ruy Sanz, Alejandra Ruiz-de Clavijo, Olga Caballero-Calero, and Marisol Martin-Gonzalez. Cylindrical three-dimensional porous anodic alumina networks. *Coatings*, 6(4):59, 2016.

[114] Antoine-Cesar Becquerel. Memoire sur líeiectro-chimie et líemploi de líelectricite pour operer des combinaisons. *Ann. Chim. Phys*, 41:23–26, 1829.

[115] Pengfei Qiu, Xun Shi, and Lidong Chen. Cu-based thermoelectric materials. *Energy Storage Materials*, 3:85–97, 2016.

[116] Eiji Hirahara. Experimental studies on the electric conduction and heat capacity of cuprous sulfide semiconductors. *Journal of the Physical Society of Japan*, 2(6):211–213, 1947.

[117] Z Ogorelec and B Celustka. Thermoelectric power and phase transitions of the non-stoichiometric cuprous selenide. *Journal of Physics and Chemistry of Solids*, 27(3):615–617, 1966.

[118] GP Sorokin and AP Paradenko. Electrical properties of cu2s. *Soviet Physics Journal*, 9(5):59–61, 1966.

[119] Gilles Dennler, Radoslaw Chmielowski, Stéphane Jacob, Frédéric Capet, Pascal Roussel, Sebastian Zastrow, Kornelius Nielsch, Ingo Opahle, and Georg KH Madsen. Are binary copper sulfides/selenides really new and promising thermoelectric materials? *Advanced Energy Materials*, 4(9), 2014.

[120] Pengfei Qiu, Xun Shi, and Lidong Chen. Thermoelectric properties of cu2- δx (x= s, se, and te). *Materials Aspect of Thermoelectricity*, page 289, 2016.

[121] David R Brown, Tristan Day, Thierry Caillat, and G JeffREY Snyder. Chemical stability of (ag, cu) 2se: a historical overview. *Journal of electronic materials*, 42(7):2014–2019, 2013.

[122] Pengfei Qiu, Xun Shi, and Lidong Chen. Chapter 8 thermoelectric properties of cu2-δx (x= s, se, and te). In *Materials Aspect of Thermoelectricity*, pages 289–316. CRC Press, 2016.

[123] Huili Liu, Xun Yuan, Ping Lu, Xun Shi, Fangfang Xu, Ying He, Yunshan Tang, Shengqiang Bai, Wenqing Zhang, Lidong Chen, et al. Ultrahigh thermoelectric performance by electron and phonon critical scattering in cu2se1-xix. *Advanced Materials*, 25(45):6607–6612, 2013.

[124] Michael Faraday. Experimental researches in electricity. fifteenth series. *Philosophical Transactions of the Royal Society of London*, 129:1–12, 1839.

[125] TA Miller, JS Wittenberg, H Wen, S Connor, Y Cui, and AM Lindenberg. The mechanism of ultrafast structural switching in superionic copper (i) sulphide nanocrystals. *Nature communications*, 4:1369, 2013.

[126] Li-Dong Zhao, Gangjian Tan, Shiqiang Hao, Jiaqing He, Yanling Pei, Hang Chi, Heng Wang, Shengkai Gong, Huibin Xu, Vinayak P Dravid, et al. Ultrahigh power factor and thermoelectric performance in hole-doped single-crystal snse. *Science*, page aad3749, 2015.

[127] Sarah L White, Progna Banerjee, and Prashant K Jain. Liquid-like cationic sub-lattice in copper selenide clusters. *Nature Communications*, 8, 2017.

[128] Chong Xiao, Jie Xu, Kun Li, Jun Feng, Jinlong Yang, and Yi Xie. Superionic phase transition in silver chalcogenide nanocrystals realizing optimized thermoelectric performance. *Journal of the American Chemical Society*, 134(9):4287–4293, 2012.

[129] David R Brown. *Enhanced Thermoelectric Performance at the Superionic Phase Transitions of Mixed Ion-Electron Conducting Materials*. California Institute of Technology, 2015.

[130] Trevor P Bailey and Ctirad Uher. Potential for superionic conductors in thermoelectric applications. *Current Opinion in Green and Sustainable Chemistry*, 2017.

[131] Hang Chi, Hyoungchul Kim, John C Thomas, Guangsha Shi, Kai Sun, Milinda Abeykoon, Emil S Bozin, Xiaoya Shi, Qiang Li, Xun Shi, et al. Low-temperature structural and transport anomalies in cu 2 se. *Physical Review B*, 89(19):195209, 2014.

[132] X Shi, L Chen, and C Uher. Recent advances in high-performance bulk thermoelectric materials. *International Materials Reviews*, 61(6):379–415, 2016.

[133] Robert Donald Heyding and Ritchie MacLaren Murray. The crystal structures of cu1* 8se, cu3se2, α-and γcuse, cuse2, and cuse2ii. *Canadian Journal of Chemistry*, 54(6):841–848, 1976.

[134] RD Heyding. The copper/selenium system. *Canadian Journal of Chemistry*, 44(10):1233–1236, 1966.

[135] Z Vučić, O Milat, V Horvatić, and Z Ogorelec. Composition-induced phase-transition splitting in cuprous selenide. *Physical Review B*, 24(9):5398, 1981.

[136] S Kashida and J Akai. X-ray diffraction and electron microscopy studies of the room-temperature structure of cu2se. *Journal of Physics C: Solid State Physics*, 21(31):5329, 1988.

[137] Manh Cuong Nguyen, Jin-Ho Choi, Xin Zhao, Cai-Zhuang Wang, Zhenyu Zhang, and Kai-Ming Ho. New layered structures of cuprous chalcogenides as thin film solar cell materials: Cu 2 te and cu 2 se. *Physical review letters*, 111(16):165502, 2013.

[138] Lan-ling Zhao, Xiao-lin Wang, Ji-yang Wang, Zhen-xiang Cheng, Shi-xue Dou, Jun Wang, and Li-qiang Liu. Superior intrinsic thermoelectric performance with zt of 1.8 in single-crystal and melt-quenched highly dense cu2-xse bulks. *Scientific reports*, 5:7671, 2015.

[139] DJ Chakrabarti and DE Laughlin. The cu- se (copper-selenium) system. *Journal of Phase Equilibria*, 2(3):305–315, 1981.

[140] VM Glazov, AS Pashinkin, and VA Fedorov. Phase equilibria in the cu-se system. *Inorganic materials*, 36(7):641–652, 2000.

[141] Ying He, Ping Lu, Xun Shi, Fangfang Xu, Tiansong Zhang, Gerald Jeffrey Snyder, Ctirad Uher, and Lidong Chen. Ultrahigh thermoelectric performance in mosaic crystals. *Advanced Materials*, 27(24):3639–3644, 2015.

[142] Bo Yu, Weishu Liu, Shuo Chen, Hui Wang, Hengzhi Wang, Gang Chen, and Zhifeng Ren. Thermoelectric properties of copper selenide with ordered selenium layer and disordered copper layer. *Nano Energy*, 1(3):472–478, 2012.

[143] Ping Lu, Huili Liu, Xun Yuan, Fangfang Xu, Xun Shi, Kunpeng Zhao, Wujie Qiu, Wenqing Zhang, and Lidong Chen. Multiformity and fluctuation of cu ordering in cu 2 se thermoelectric materials. *Journal of Materials Chemistry A*, 3(13):6901–6908, 2015.

[144] Ryoichi Sadanaga, Masaaki Ohmasa, and NOBUO MORIMOTO. On the statistical distribution of copper ions in the structure of β-chalcocite. *Mineralogical Journal*, 4(4):275–290, 1965.

[145] Masatoshi Imada, Atsushi Fujimori, and Yoshinori Tokura. Metal-insulator transitions. *Rev. Mod. Phys.*, 70:1039–1263, Oct 1998.

[146] Changzheng Wu, Feng Feng, Jun Feng, Jun Dai, Lele Peng, Jiyin Zhao, Jinlong Yang, Cheng Si, Ziyu Wu, and Yi Xie. Hydrogen-incorporation stabilization of metallic vo2 (r) phase to room temperature, displaying promising low-temperature thermoelectric effect. *Journal of the American Chemical Society*, 133(35):13798–13801, 2011.

[147] GA Wiegers. Crystal-structure of low-temperature form of silver selenide. *American Mineralogist*, 56(11-1):1882, 1971.

[148] Heinrich Billetter and Uwe Ruschewitz. Structural phase transitions in ag2se (naumannite). *Zeitschrift für anorganische und allgemeine Chemie*, 634(2):241–246, 2008.

[149] G. Treupel H. Z. Boettcher, Von A. Haase. Aip conference proceedings. *Angew. Phys.*, 7(478–487), 1954.

[150] Hidejiro Miki. Superlattice formation and phase transition in silver selenide. *Japanese journal of applied physics*, 30(8R):1765, 1991.

[151] James William Earley. Description and synthesis of the selenide minerals. *American Mineralogist (US)*, 35, 1950.

[152] Junli Wang, Weiling Fan, Juan Yang, Zulin Da, Xiaofei Yang, Kangmin Chen, Huan Yu, and Xiaonong Cheng. Tetragonal–orthorhombic–cubic phase transitions in ag2se nanocrystals. *Chemistry of Materials*, 26(19):5647–5653, 2014.

[153] P Boolchand and WJ Bresser. Mobile silver ions and glass formation in solid electrolytes. *Nature*, 410(6832):1070–1073, 2001.

[154] Tristan Day, Fivos Drymiotis, Tiansong Zhang, Daniel Rhodes, Xun Shi, Lidong Chen, and G Jeffrey Snyder. Evaluating the potential for high thermoelectric efficiency of silver selenide. *Journal of Materials Chemistry C*, 1(45):7568–7573, 2013.

[155] Gesa Beck and Jürgen Janek. Coulometric titration at low temperatures—nonstoichiometric silver selenide. *Solid State Ionics*, 170(1):129–133, 2004.

[156] Robert W Cahn. Ternary alloys: A comprehensive compendium of evaluated constitutional data and phase diagrams. volumes 3 and 4: Al-ar-o to al-ca-zn and al-cd-ce to al-cu-ru. g. petzow and g. effenberg, editors. vch, weinheim april 1991. xix, 646 pp.; xix, 652 pp., hardback. dm 980 per volume. *Advanced Materials*, 3(12):628–629, 1991.

[157] G Beck, C Korte, J Janek, Fr Gruhl, and M v Kreutzbruck. The magnetoresistance of homogeneous and heterogeneous silver-rich silver selenide. *Journal of applied physics*, 96(10):5619–5624, 2004.

[158] J Janek, B Mogwitz, G Beck, M v Kreutzbruck, L Kienle, and C Korte. The magnetoresistance of metal-rich ag 2+ x se–a prototype nanoscale metal/semiconductor dispersion? *Progress in solid state chemistry*, 32(3):179–205, 2004.

[159] C Giles, F Yokaichiya, SW Kycia, LC Sampaio, DC Ardiles-Saravia, MKK Franco, and RT Neuenschwander. High-resolution x-ray diffraction beamline at the lnls for the study of charge, orbital and magnetic structures. *Journal of synchrotron radiation*, 10(6):430–434, 2003.

[160] Marcelo G Hönnicke, Fabio Masiello, Steven N Ehrlich, Edson M Kakuno, Yong Q Cai, and Jürgen Härtwig. Sagittal focusing inducing energy structure in medium to high energy resolution x-ray monochromators. In *SPIE Optical Engineering+ Applications*, pages 884809–884809. International Society for Optics and Photonics, 2013.

[161] June 2017.

[162] O Pagès, J Souhabi, VJB Torres, AV Postnikov, and KC Rustagi. Re-examination of the sige raman spectra: Percolation/one-dimensional-cluster scheme and ab initio calculations. *Physical Review B*, 86(4):045201, 2012.

[163] O Pagès, R Hajj Hussein, and VJB Torres. Gesi raman spectra vs. local clustering/anticlustering: Percolation scheme and ab initio calculations. *Journal of Applied Physics*, 114(3):033513, 2013.

[164] TS Perova, J Wasyluk, K Lyutovich, E Kasper, M Oehme, K Rode, and A Waldron. Composition and strain in thin si 1- x ge x virtual substrates measured by micro-raman spectroscopy and x-ray diffraction. *Journal of Applied Physics*, 109(3):033502, 2011.

[165] F Pezzoli, E Bonera, E Grilli, M Guzzi, S Sanguinetti, D Chrastina, G Isella, H Von Känel, E Wintersberger, J Stangl, et al. Raman spectroscopy determination of composition and strain in si1-xgex/si heterostructures. *Materials science in semiconductor processing*, 11(5):279–284, 2008.

[166] M. I. Alonso and K. Winer. Raman spectra of c-$si_{1-x}ge_x$ alloys. *Phys. Rev. B*, 39:10056–10062, May 1989.

[167] D Rouchon, M Mermoux, F Bertin, and JM Hartmann. Germanium content and strain in si 1- x ge x alloys characterized by raman spectroscopy. *Journal of Crystal Growth*, 392:66–73, 2014.

[168] AS Vasin, OV Vikhrova, and MI Vasilevskiy. Effects of alloy disorder and confinement on phonon modes and raman scattering in sixge1- x nanocrystals: A microscopic modeling. *Journal of Applied Physics*, 115(14):143505, 2014.

[169] June 2017.

[170] Adam A Wilson, Miguel Muñoz Rojo, Begoña Abad, Jaime Andrés Perez, Jon Maiz, Jason Schomacker, Marisol Martín-Gonzalez, Diana-Andra Borca-Tasciuc, and Theodorian Borca-Tasciuc. Thermal conductivity measurements of high and low thermal conductivity films using a scanning hot probe method in the 3 ω mode and novel calibration strategies. *Nanoscale*, 7(37):15404–15412, 2015.

Publicaciones

Durante los cuatro años de realización de esta tesis doctoral él doctorando ha participado en un total de 13 publicaciones, consistentes en 2 capítulos de libro y 11 publicaciones. Ademas, 2 publicaciones enviadas y 8 artículos en preparación.

Publicaciones contenidas en esta tesis doctoral

1. **Book Chapter - Invited** - Pérez Taborda, Jaime Andrés and Olga Caballero Calero and Marisol Martin Gonzalez, *Silicon Germanium (SiGe) nanostructures for thermoelectric devices: Recent advances and new approaches to high thermoelectric efficiency*, In Silicon - Properties and Applications, ISBN 978-953-51-5360-3, Book edited by: V. I. Talanin, **InTechOpen**, 183-206 *2017*, 10.5772/67730 **See Paper I**
   En este capítulo de libro, el doctorando llevo a cabo la revisión bibliográfica además de la diagramación de figuras y la participación activa en la escritura del documento.

2. *Low thermal conductivity and improved thermoelectric performance of nanocrystalline silicon germanium films by sputtering*, Pérez Taborda, Jaime Andrés and and Romero, JJ and Abad, B and Muñoz-Rojo, M and Mello, A and Briones, F and Gonzalez, MS Martin, **Nanotechnology Journal** ISSN: 1742-6596: ed: IOP Publishing v.27 - 17 p.175401, *2016*, 10.1088/0957-4484/27/17/175401 **See Paper II**
   En este artículo el doctorando hace parte de la planeación y ejecución del trabajo, responsable de la fabricación de las muestras y de gran parte de la caracterización, análisis y escritura de la mayor parte del artículo.

3. *Ultra-low thermal conductivities in large-area Si-Ge nanomeshes for thermoelectric applications*, Pérez Taborda, Jaime Andrés and Rojo, Miguel Muñoz and Maiz, Jon and Neophytou, Neophytos and Martin-Gonzalez, Marisol, **Scientific Reports** ISSN: 2045-2322 ed: Nature Publishing Group, v.6 fasc. p.32778, *2016*, 10.1038/srep32778 **See Paper III**
   En este artículo el doctorando hace parte de la planeación y ejecución del trabajo, responsable de la fabricación de las muestras y de gran parte de la caracterización, análisis y escritura de la mayor parte del artículo.

4. *Pulsed Hybrid Reactive Magnetron Sputtering for High zT Cu2Se Thermoelectric Films*, Pérez Taborda, Jaime Andrés and Vera, Liliana and Caballero-Calero, Olga and Lopez, Elvis O and Romero, Juan J and Stroppa, Daniel G and Briones, Fernando and Martin-Gonzalez, Marisol, **Advanced Materials Technologies** ISSN: 2365-709X ed: John Wiley Sons, *2017*, 10.1038/srep32778 **See Paper IV**
   En este artículo el doctorando hace parte de la planeación y ejecución del trabajo, responsable de la fabricación de las muestras y de gran parte de la caracterización, análisis y escritura de la mayor parte del artículo.

5. *Ultra-high Thermoelectric Performance in n-type Silver Selenide films*, Pérez Taborda, Jaime Andrés, Olga Caballero-Calero, Liliana Vera-Londoño, Fernando Briones, Marisol Martin-Gonzalez. (Enviado a *Advanced Energy Materials*) **See Paper V**
   En este artículo el doctorando hace parte de la planeación y ejecución del trabajo, responsable de la fabricación de las muestras y de gran parte de la caracterización, análisis y escritura de la mayor parte del artículo.

Otras publicaciones en preparación relacionadas con la tesis:

1. *Plasma characterization of the new technique pulsed hybrid reactive magnetron sputtering: new tools in Ag_2Se thin films with high thermoelectric efficiency*, Pérez Taborda, Jaime Andrés Elvis O. López, Henrique Sendão, Fernando Briones-Pola, Marisol Martin-Gonzalez. (Proceso de Sumisión)

2. *High Thermoelectric Performance of p-Type Cu_2Se thin films via Pulsed Hybrid Reactive Magnetron Sputtering*, Pérez Taborda, Jaime Andrés, Olga Caballero-Calero, Y. R. Koh, A. Shakouri, Fernando Briones, Marisol Martin-Gonzalez

3. *Correlation between electrical transport properties and Raman microscopy for thin films of Silicon-Germanium*, Pérez Taborda, Jaime Andrés, Marisol Martin-Gonzalez

4. *Doping of $Si_{0,8}Ge_{0,2}$ films by mobility of oxygen from $SrTiO_3$ substrate at temperature*, Pérez Taborda, Jaime Andrés, Elvis O. López, Mello. A, Marisol Martin-Gonzalez

5. *Structural studies of thin films of silver selenide: a new approach as highly efficient thermoelectric material*, Pérez Taborda, Jaime Andrés, Elvis O. López, Paolo Souza, Fernando Briones, Marisol Martin-Gonzalez

6. *Structural study of Cu_2Se thin films: dependence of reversibility above the critical temperature of transition.* , Pérez Taborda, Jaime Andrés, Elvis O. López, Paolo Souza, Fernando Briones, Marisol Martin-Gonzalez

7. *$Cu_{2-x}Se$ thin films by RF: a comparison with the PHRMS technique*, Pérez Taborda, Jaime Andrés, Elvis O. López, Mello. A, Fernando Briones, Marisol Martin-Gonzalez

Publicaciones realizadas en esta tesis doctoral pero no contenidas

1. *Compensation of native donor doping in ScN: Carrier concentration control and p-type ScN*, Saha, Bivas and Garbrecht, Magnus and Pérez Taborda, Jaime Andres and Fawey, Mohammed H and Koh, Yee Rui and Shakouri, Ali and Martin-Gonzalez, Marisol and Hultman, Lars and Sands, Timothy D, **Applied Physics Letters** ISSN: 0003-6951 ed: American Institute of Physics,Volume 110, Issue 25, *2017*, 10.1063/1.4989530

2. **Chapter Book** - Pérez Taborda, Jaime Andrés and López, Elvis O, *Research Perspectives on Functional Micro and Nano Scale Coatings: New Advances in Nanocomposite*, In Research Perspectives on Functional Micro- and Nanoscale Coatings, ISBN13: 9781522500667, Book edited by: Ana Zuzuarregui and Maria Carmen Morant-Miñana, **IGI Global**, 136-169 *2016*, 10.4018/978-1-5225-0066-7.ch006

3. *Correlation Between Optical, Morphological, and Compositional Properties of Aluminum Nitride Thin Films by Pulsed Laser Deposition*, Pérez Taborda, Jaime Andrés and Lándazuri, Henry Riascos and Londoño, Liliana Patricia Vera, **IEEE Sensors Journal** ISSN: 1530-437X ed: IEEE, v.16 fasc 2. p.359-364, *2016*, 10.1109/JSEN.2015.2466467

4. *Spectroscopic analysis of coal plasma emission produced by laser ablation* Vera-Londoño, Liliana Patricia and Pérez Taborda, Jaime Andrés and Riascos-Landázuri, Henry **Revista Facultad de Ingeniería**, ISSN 0120-6230 ed: Universidad de Antioquia, v.78. p.69-72, *2016*, 10.17533/udea.redin.n78a09

5. *Thermal Conductivity Measurements of High and Low Thermal Conductivity Films Using a Scanning Hot Probe Method in the 3ω Mode and Novel Calibration Strategies*, Wilson, Adam A. and Munoz Rojo, Miguel and Abad, Begona and Pérez Taborda, Jaime Andrés and Maiz, Jon and Schomacker, Jason and Martin-Gonzalez, Marisol and Borca-Tasciuc, Diana-Andra and Borca-Tasciuc, Theodorian, **Nanoscale**, ISSN: 2040-337 ed: Royal Society of Chemistry ,v.32 p.15404 - 15412, *2015*, 10.1039/C5NR03274A

6. *Deposition pressure effect on chemical, morphological and optical properties of binary Al-nitrides*, Pérez Taborda, Jaime Andrés and Caicedo, Julio César and Grisales, M and Saldarriaga, W and Riascos, H, **Optics & Laser Technology** ISSN: 0030-3992 ed: Elsevier, v.69 fasc. p.92 - 103, *2015*, 10.1016/j.optlastec.2014.12.009

7. *Determination of physical response in (Mo/AlN) SAW devices*, Caicedo, JC and Pérez Taborda, Jaime Andrés and Caicedo, HH and Riascos, H, **Surface Review and Letters** ISSN: 1793-6667 ed: World Scientific Publishing Company v.20 fasc.2 p.1350017 , *2013*, 10.1142/S0218625X13500170

8. *Análisis espectroscópico de las películas delgadas de óxido de cobre y del plasma producido por deposición de láser pulsado*, Vera, Liliana and Pérez Taborda, Jaime Andrés and Riascos, H ed: **Revista de la Sociedad Colombiana de Física**, ISSN: 0120-2650; vol. 45, No. 3, p.146 -150 *2013*, Link

9. *AlN film deposition as a semiconductor device*, Caicedo, Julio Cesar and Pérez Taborda, Jaime Andrés and Aperador, W ed: **Revista Facultad de Ingeniería**, Universidad Nacional de Colombia, ISSN 0120-5609; vol. 33, No. 2, p.16 -23 *2013*, Link

Otras publicaciones en preparación

1. *Large thermoelectric power-factor in epitaxial n- and p-type scandium nitride (ScN)*, , B. Saha , Pérez Taborda, Jaime Andrés , Y. R. Koh , J. Bahk , M. M. Gonzalez , A. Shakouri , and T. D. Sands (Proceso de Sumisión).

2. *Pressure effect on optical and structural properties of ZnMnO thin films grown by pulsed laser deposition*, H. Riascos, K. L. Salcedo, Pérez Taborda, Jaime Andrés (En preparación).

Publicaciones contenidas en esta tesis doctoral

PAPER I

Chapter 8

Silicon-Germanium (SiGe) Nanostructures for Thermoelectric Devices: Recent Advances and New Approaches to High Thermoelectric Efficiency

Jaime Andrés Pérez-Taborda,
Olga Caballero-Calero and Marisol Martín-González

Additional information is available at the end of the chapter

http://dx.doi.org/10.5772/67730

Abstract

Silicon and germanium present distinct and interesting transport properties. However, composites made of silicon-germanium (SiGe) have resulted in a breakthrough in terms of their transport properties. Currently, these alloys are used in different applications, such as microelectronic devices and integrated circuits, photovoltaic cells, and thermoelectric applications. With respect to thermoelectricity, in the last decades, $Si_{0.8}Ge_{0.2}$ has attracted significant attention as an energy harvesting material, for powering space applications and other industrial applications. This chapter focuses on the recent advances and new approaches in silicon-germanium ($Si_{1-x}Ge_x$) nanostructures for thermoelectric devices with high thermoelectric efficiency obtained through magnetron sputtering.

Keywords: silicon-germanium nanostructures, magnetron sputtering deposition, thin films, nanomesh, thermoelectric, Raman spectroscopy

1. Introduction

Several chapters of this book describe different approaches, properties, and applications of silicon and its undeniable impact on our culture, technology, and commerce. Its usefulness has made us talk about the silicon era [1]. In this chapter, we are going to focus on the use of silicon-based materials in one of the main pillars of our life nowadays: the obtainment of energy to power up all the resources in which our society is based (transport, communications, and human infrastructures in general).

Although silicon is mainly associated with microchip devices and advances in computing, the alloy that silicon forms with germanium can be used as a thermoelectric material, which is, in the presence of a gradient of temperature, able to generate an electrical voltage and *vice versa*. This thermoelectric effect has been long known. Nevertheless, it has not been widely used because of its modest efficiency. In recent years, the interest on thermoelectricity has revamped due to the use of thermoelectric devices for micro-energy harvesting or as a large-scale conversion of residual heat into electricity. This increase in the research on thermoelectrics is mostly due to the impact nanostructuration has on improving the efficiency of these materials, which has been increased almost a factor of three over the last 20 years. The purpose of this chapter is to highlight the ways in which silicon-germanium has improved its efficiency by nanostructuration.

Considering the decreasing fossil fuels and increasing energy demand worldwide, a pressing need for improved direct thermal (wasted heat) into electrical energy conversion is imposed. The wasted heat comes from the energy transportation, vehicles, electricity generating sources, industry, etc., which tampers the actual efficiency of the initial resources. For instance, around 30% of the energy obtained from the fuel of a car is actually used in its movement. The other 70% is lost in the form of heat, friction, and cooling the car. Furthermore, it is completely reasonable to look for alternative energy technologies to reduce our dependence on fossil fuels and greenhouse gas effects. This necessity has fostered multiple lines of research, including the conversion of thermal energy through thermoelectricity [2]. As an example, the most recent International Energy Outlook 2016 (IEO2016) [3] prepared by the USA Energy Information Administration shows the energy production predictions for the year 2040, based on the data recorded previously (**Figure 1a**). It is shown that the total world consumption of energy will increase a 48% from 2012 to 2040. Renewable energies are the fastest-growing energy sources over the predicted period, with a foreseen increase in their consumption of around 2.6%/year between 2012 and 2040. In **Figure 1a**, CPP refers to a Clean Power Plan (CPP), which is a USA regulation that aims to reduce carbon dioxide emissions from electric power generation by 32% within 25 years, relative to the levels of 2005 in the USA.

Focusing on the future of the different sources of energies, that is **Figure 1b**, world net electricity generation is envisioned to increase by 69%, in 2040, going from 21.6 trillion kilowatt hours (10^{12} kWh) registered in 2012 to 25.8 trillion kWh predicted for 2020 and to 36.5 trillion kWh in 2040. It is worth noting that, even with initiatives as the CPP, or the development predicted for renewable energies, fossil fuels will still account for a 78% of the energy used in 2040 [3].

For these reasons, in late 2015, representatives from 185 countries and the European Union (EU) met in Paris to reach a commitment to addressing climate change, called Paris-COP21. This worldwide engagement is expected to drive innovation in renewable energies, battery storage, energy efficiency, and energy recovery. One of the main conclusions obtained in the conference is that climate change is often discussed as a single problem, but solving it will require a wide variety of solutions [4]. The EU budget for low carbon-related research under Horizon 2020 has been effectively doubled for the period 2014–2020, and the EU has promised to invest at least 35% of Horizon 2020 resources into climate-related activities [5]. In the United States, hundreds of major companies, including energy-related companies such as ExxonMobil, Shell, DuPont, Rio Tinto, Berkshire Hathaway Energy, Cal-pine, and Pacific Gas and Electric Company, have supported the Paris-COP21 [6]. In the coming decades, there will be a need for more energy-efficient technologies, easily compatible with the non-renewable

http://dx.doi.org/10.5772/67730

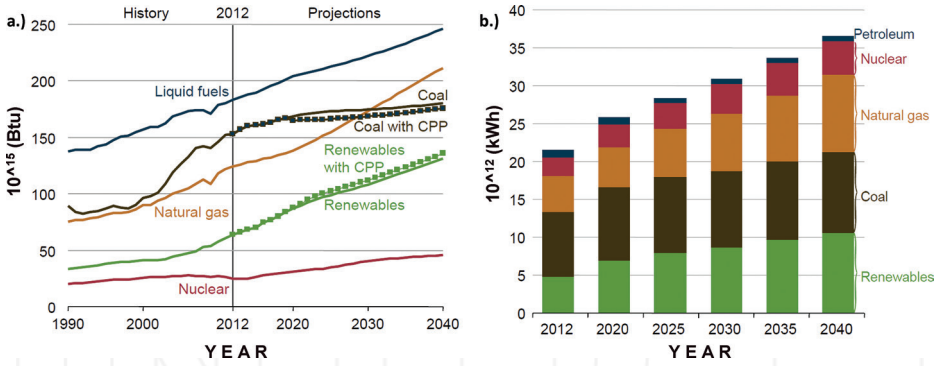

Figure 1. (a) Total world energy consumption sorted by energy source between the period 1990 and 2040. Dotted lines for coal (black) and renewables (green) show the predicted effects of the USA Clean Power Plan (CPP) regulation. (b) World net electricity generation predictions sorted by energy source, for the period of 2012–2040. Both figures are reprinted with permission from Ref. [3]. Copyright 2016.

energies (that will not disappear in the near future as it can be seen in **Figure 1b**). Certainly, thermoelectric materials and especially thin films are interesting players in this scenario. Its ability to convert waste heat into electricity regardless of the source of heat generation, stability over time, and the ability to generate electricity locally without the need for transportation are some of its many advantages.

Likewise, **Figure 2** and **Table 1** show some of the most outstanding historical facts and current state of the art of Si and SiGe in thermoelectric, microelectronic, and photovoltaic applications.

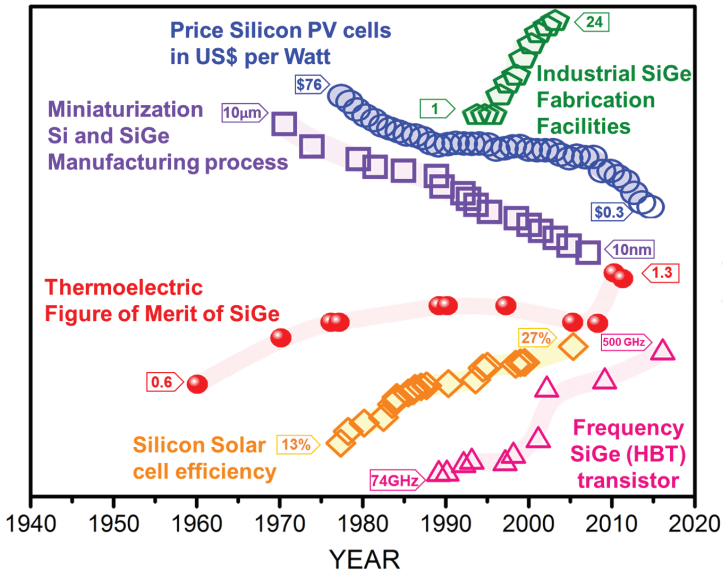

Figure 2. Timeline of some breakthrough or historical event in Si-Ge in thermoelectric, photovoltaic cells and microelectronics. References in **Table 1**.

	Some breakthrough or historical event in SiGe	Year	Refs
Microelectronics and Manufacturing	First epitaxial silicon transistors	1960	[7]
	First oxidation study of SiGe	1971	[8]
	First SiGe n-type MODFET	1986	[9]
	First SiGe p-type MODFET	1986	[10]
	First SiGe photodetector	1986	[11]
	First SiGe HBT (heterojunction bipolar transistor)	1987	[12]
	First SiGe hole RTD (resonant-tunneling diode)	1988	[13]
	First SiGe (BiCFET) (bipolar inversion channel FET)	1989	[14]
	First SiGe HBT grown by CVD (chemical vapor deposition)	1989	[15]
	First SiGe gate (CMOS) technology	1990	[16]
	First SiGe waveguide	1990	[17]
	First SiGe LED	1991	[18]
	First SiGe solar cell	1992	[19]
	First SiGe phototransistor	1993	[20, 21]
	First SiGe HBT with peak cutoff frequency above 100 GHz	1993	[22]
	First SiGe HBT with peak cutoff frequency above 200 GHz	2001	[23]
	First SiGe HBT with peak cutoff frequency above 300 GHz	2002	[7]
	Current Record SiGe HBT with peak cutoff frequency 500 GHz	2016	[24]
Thermoelectric figure of merit	SiGe radioisotope thermoelectric generators (RTGs) Mission LES 8, 9	1976	*[25–28]*
	SiGe (RTGs) in mission Voyager 1 and 2 spacecraft	1977	[25–27]
	SiGe (RTGs) in mission Galileo spacecraft	1989	[25–27, 29]
	SiGe (RTGs) in mission Ulysses spacecraft	1990	[25–27, 29]
	SiGe (RTGs) in mission Cassini spacecraft	1997	[25, 26]
	SiGe (RTGs) in mission New Horizons spacecraft	2005	[25–27]
	Bulk material (zT)~ 1.3 at 1073 K	2014	[30]
	Historical evolution zT SiGe	2016	[31, 32]

http://dx.doi.org/10.5772/67730

	Some breakthrough or historical event in SiGe	Year	Refs
✹	% Solar cell efficiency	1998	[33]
		2003	[34]
		2014	[35]
		2015	[36, 37]
		2016	[38]
$	Price history photovoltaic cells in US$ per watt	2012	[39–41]
		2015	[42, 43]
↓	Recent progress of the miniaturization of semiconductors Si and SiGe	1988	[44]
		2000	[45]
		2004	[46]
		2010	[47]
↑	Number of industrial SiGe and strained Si fabrication facilities	2000	[48]
		2007	[49]

Table 1. This table highlights historical events and the latest advances in silicon and silicon-germanium in thermoelectric, microelectronic, and photovoltaic applications.

2. Thermoelectric concepts: current overview and strategies for improving the thermoelectric efficiency

The efficiency of a thermoelectric material is controlled by its figure of merit, denoted as zT. This parameter is defined as follows:

$$zT = \alpha^2 \cdot \sigma \cdot T \cdot \kappa^{-1} \tag{1}$$

where the parameters are the following: the square of the Seebeck coefficient, α, times the electrical conductivity, σ, times the operating temperature, T (in Kelvin), divided by the thermal conductivity, κ. The thermal conductivity itself is a sum of its lattice and electronic contributions, κ_L and κ_e, respectively.

Most of these parameters are heavily interdependent [50–53], as it is shown in **Figure 3**. If one takes into account the material properties in classical physics, large α usually results in a low σ, and a large σ increases κ_e, given that these parameters depend on the carrier concentration. Therefore, the fabrication of materials with high power factor ($\alpha^2 \cdot \sigma$) and low thermal conductivity (κ) necessary for obtaining a high zT is quite challenging. The energy conversion efficiency (η_{max}) of thermoelectric devices is determined by Eq. (2), with T_H and T_C being the hot and cold temperatures, respectively.

$$n_{\max} = \frac{T_H - T_C}{T_H} \frac{\sqrt{1+ZT}-1}{\sqrt{1+ZT}+\frac{T_C}{T_H}} \tag{2}$$

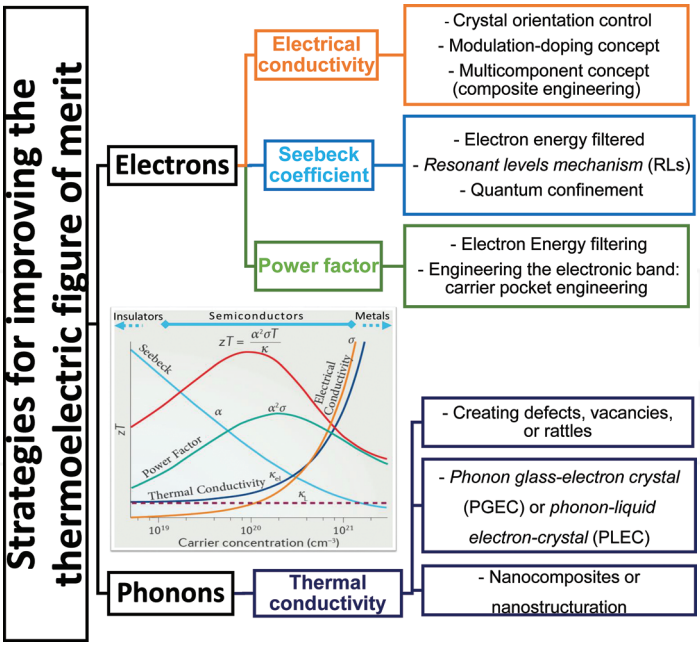

Figure 3. Schematic diagram that briefly summarizes some of the main strategies for the improvement of the figure of merit through the increase in the power factor and the decrease in the thermal conductivity. The graph shows the behavior of the Seebeck coefficient, electrical conductivity, and thermal conductivity versus carrier concentration. This figure is adapted from Ref. [50].

As it can be seen from the definition of the figure of merit, a large value of zT can be obtained by having a high power factor ($\alpha^2 \cdot \sigma$) and a low thermal conductivity (κ). In **Figure 3**, there is also a scheme with some of the strategies that are being used nowadays to improve the figure of merit.

As it can be seen in **Figure 3**, there are two main routes to improve the thermoelectric figure of merit, which are tailoring to improve the power factor and lowering the thermal conductivity. In the first case, there have been different ideas proposed recently. Some of them are aimed to increase the Seebeck coefficient, such as quantum confinement in low-dimensional structures, which was first proposed by Hicks and Dresselhaus in 1993 [54]. It is based on the dependence of the Seebeck coefficient on the gradient of the density of states (DOS) with energy. Then, given that very sharp DOS would be found in quantum confined structures, the Seebeck coefficient would be greatly enhanced. Other approaches to obtain higher Seebeck coefficients are electron energy filtering [55], which proposes the filtering of the electrons with the lowest mean energy, and resonant scattering [56] by introducing distortions into the DOS. In the case of the electrical conductivity, modulation doping has been used to improve carrier mobility [57]. Also, controlling the crystal orientation or composite engineering has shown results in this sense [58]. The main problem is that an increase in the Seebeck coefficient comes along with a decrease in electrical conductivity, as it is the case in energy filtering.

http://dx.doi.org/10.5772/67730

Therefore, other routes to obtain both an increase in the Seebeck coefficient and electrical conductivity have been proposed, such as band engineering [59], and electron energy filtering are nowadays under study. A recent review on all these strategies can be found in Ref. [58].

The other mentioned route to improving the thermoelectric performance is to engineering the structure of the material to reduce lattice thermal conductivity, what is called phononics engineering [60–62]. This last approach can be understood if one takes into account that classical thermoelectric materials are usually semiconductors. Indeed, for metals, κ is dominated by free electrons, whereas in semimetals and heavily doped semiconductors, both κ_L (lattice thermal conductivity) and κ_e (electron thermal conductivity) play an important role in the total thermal conductivity. In particular, in the case of semiconductors, heat is conducted primarily by the acoustic phonons [51, 52, 63]. Undoubtedly, in recent years, there has been an explosion in the research and understanding of the tailoring of thermal conductivity through nanostructure fabrication [51, 52, 64]. In these cases, low thermal conductivity can be achieved by inhibiting the transport of heat through the lattice vibrations, which are called phonons. Phonons can be divided into those having low, medium, or long wavelengths. **Figure 4** depicts how the nano-inclusions, defects, or vacancies significantly reduce the mean free path of the different phonons, thereby reducing the lattice thermal conductivity [64, 65]. In pure materials (non-alloys or doped), the dominant phonon scattering mechanisms go from boundary scattering to phonon-phonon Umklapp scattering with increasing temperature. Then, in order to reduce the thermal conductivity, point inhomogeneities are usually introduced, such as alloy atoms, dopants, isotope variations, rattlers, and point defects. Through these mechanisms, not only phonons, but also electrons are scattered, and thus, the κ is reduced [51, 52, 62, 66]. In the case of nanostructure fabrication, the idea is to form structures with smaller sizes than the phonon mean free paths, but greater than the electron or hole mean free paths, given that phonons are more strongly scattered by the interfaces than are electrons or holes [67], giving

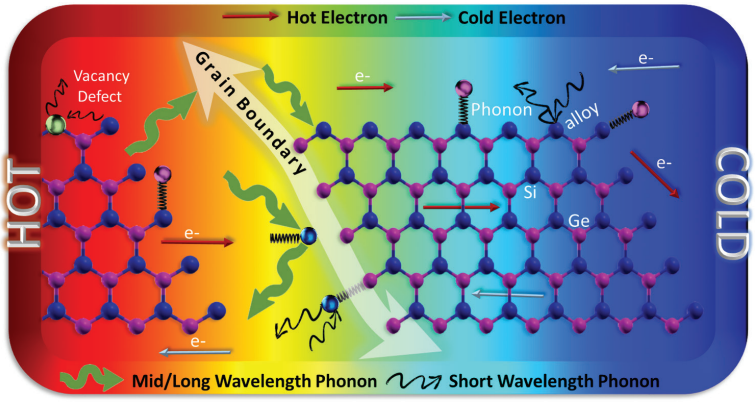

Figure 4. Scheme of the most used strategies for reducing thermal conductivity and their effect on phonon scattering. Grain boundaries scatter mid-long wavelength phonons at their interfaces, while alloy atoms, dopants, defects, lattice vibrations, and nano-inclusions scatter short-wavelength phonons. The electrons, which are depicted as arrows in the figure, are supposedly not scattered and thus electrical conductivity is not altered.

rise to phonon glass-electron crystals (PGEC). As it was said before, the lower the thermal conductivity is, the higher and longer the temperature gradient is maintained and thus more efficient the material results.

3. Thermoelectric properties of silicon-germanium alloys

Silicon-germanium alloys (SiGe) have played a primary role in thermoelectricity in the last decades, although its potential for thermoelectric application was first shown in the 1950s [68–70]. Less than 10 years later, in 1964, a study on how to improve silicon-rich SiGe alloys was published [71, 72], and, the next year, they were used for the first time in a spatial mission from NASA (the SNAP-10 [71]). From that moment onward, they have been successfully used in radioisotope thermoelectric generators (RTGs) for deep-space NASA missions. Bulk silicon-germanium nanostructures (that is, compacted nanograins) are used in the RTGs that power different spacecraft's such as Voyager 1, Voyager 2, Galileo, Ulysses, Cassini, and New Horizons missions [25, 26, 73]. For instance, missions Voyager and Cassini spacecrafts are equipped with RTGs that use a pellet of $^{238}PuO_2$ as the thermal energy source and SiGe as the thermoelectric conversion material. In addition to having very attractive thermoelectric and physical properties, SiGe devices can operate at temperatures up to about 1050°C without significant degradation [25, 73]. For high-temperature applications (above 600°C), SiGe alloys have a high thermoelectric efficiency and have been the type of conduction and the carrier concentration in SiGe can be controlled by doping with phosphorous (*n*-type) or boron (*p*-type). As a consequence, a total of 28 USA space missions have safely flown powered by RTGs [26, 73]. In this field, SiGe used as thermoelectric conversion material has accumulated over 250 million devices working hours in space applications (running for over 40 years in Voyager missions) without failure [25, 26, 74].

In all these years, different studies on how to increase the efficiency of these materials, such as the use of grain-refined alloys [75, 76], nano-inclusions [77], SiGe superlattices fabrication [78], and understanding how the grain size affects thermal conductivity [79], were performed. Also, novel methods for the fabrication of SiGe, such as the chill casting method [80], milling and sintering techniques [81], high-energy ball milling [82], spark plasma sintering [83, 84], and mechanical alloying, were developed. The improvements achieved in SiGe were all related to nanostructuring the material and reducing the lattice thermal conductivity. In 2008, a theoretical work proposed that the introduction of silicide nanoparticles into the SiGe matrix would reduce drastically the thermal conductivity [85]. That is, if the grain size is smaller than the mean free path of the phonons, the total effect is a reduction in the effective mean free path and thus a reduction in the thermal conductivity. Another route studied has been the enhancement of the power factor in SiGe through the concept modulation doping [86]. In this case, a 40% power factor enhancement in $Si_{80}Ge_{20}$ bulk nanocomposites has been reported, and it was a direct result of the enhanced mobility due to this modulated doping [86]. With all these advances, zT values for nanostructured bulk SiGe as high as 1.3 for *n*-type and 0.95 for *p*-type have been measured [87–89].

Apart from these successes in the increase of thermoelectric efficiency and the space applications of SiGe, there is another outstanding property that makes SiGe appealing for many

http://dx.doi.org/10.5772/67730

other applications, which is the possibility of integration (compatibility) in the technology of semiconductors based on silicon. This can be made through thin films fabrication of SiGe on silicon like it is done in the complementary metal-oxide semiconductors (CMOS) industry [90]. In general, thermoelectricity struggles with the lack of cheap, abundant, and environmentally friendly materials. Recent works have emphasized the importance of considering the relationship between material's price, manufacturing costs, and efficiency to consider different thermoelectric materials [91]. Silicon-germanium could overcome this deficiency by proposing high harvested power density, abundant on earth, low toxicity, and cost-efficiency. These characteristics increase the interest of SiGe among other thermoelectric materials [90, 91].

3.1. Some strategies for reducing the thermal conductivity of silicon-germanium

The challenge of obtaining ultra-low thermal conductivities in silicon-germanium, in particular, for thermoelectric applications, is not recent. **Figure 5** represents the different strategies that have been followed to fabricate nanostructures with reduced thermal conductivity in SiGe.

In the case of pure silicon and germanium, measurements in bulk, the room temperature thermal conductivities are ~140 W K^{-1} m^{-1} [67] and ~60 W K^{-1} m^{-1}, respectively [30]. However, SiGe alloys provide a significant reduction in thermal conductivity versus the above-mentioned values. Depending on the germanium content, values ranging from ~20 to ~9 W K^{-1} m^{-1} have been measured in bulk [30]. The lowest value of room temperature thermal conductivity has been achieved for a stoichiometry of $Si_{0.8}Ge_{0.2}$ (~9 W K^{-1} m^{-1}), which is still large for thermoelectric applications. Nevertheless, an even lower value (<1 W K^{-1} m^{-1}) has been measured for films grown by sputtering with a $Si_{0.8}Ge_{0.2}$ stoichiometry [92]. The difference with the previous case is that these films were grown through metal-induced crystallization (MIC),

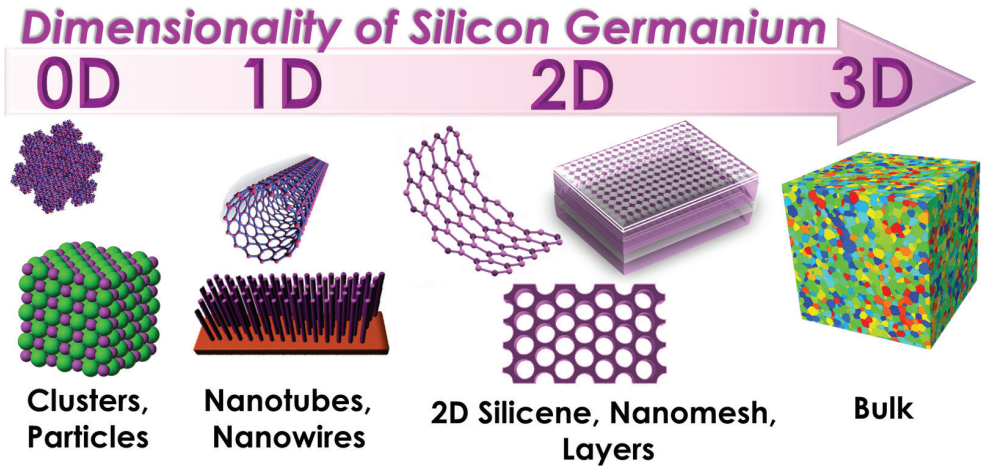

Figure 5. One of the strategies that has been proven to be useful in improving thermoelectric performance is to reduce dimensionality. Here, different configurations that the silicon-germanium has been fabricated at the nanometric scale to improve its thermoelectric properties are shown.

which allows the reduction of the crystallization temperature of the SiGe. With this technique, films with thermal conductivity values down to ~1.2 W K^{-1} m^{-1} at room temperature [92, 93] have been obtained. (See Section 4 for more details.)

At the same time, the growing interest in 2D materials has also triggered the study of 2D silicene [94], which has low thermal conductivity and high power factor. Although the thermal conductivity of silicene has not been measured experimentally due to the difficulty of synthesizing freestanding silicene (and also the complication to carry out thermal measurements in the in-plane direction), several numerical simulations have predicted a thermal conductivity of silicene at room temperature from 5 to 70 W K^{-1} m^{-1} [94–97]. Also graded $Si_{1-x}Ge_x$/Si superlattice structures have been theoretically proposed and fabricated. The idea behind these structures was to demonstrate a thermal rectification effect derived from a theoretical model (the kinetic collective model), which showed that the thermal boundary resistance of a $Si_{1-x}Ge_x$/Si depends on the direction of the heat flow if the structure is symmetric. The predicted effect would cause around 40% difference depending on the heat flow direction. Experimentally, these graded superlattices were fabricated via molecular beam epitaxy (MBE) on silicon substrates, and further studies on the impact of the composition, strain, or alloy inhomogeneities [98] showed that the transport properties could be engineered, obtaining values for the thermal conductivity as low as 2.2 W m^{-1} K^{-1} [99].

Another 2D structure that has recently been developed is the fabrication of nanomeshes (nanoporous or holey silicon or SiGe membranes). These structures can be fabricated by sputtering deposition in large areas [100], which offers the advantages of scalability and flexibility required for real applications [100–102]. Moreover, the variation of the geometry of the mesh influences its thermal conductivity [100, 102], allowing a further control on this parameter. In particular, the thermal conductivity of the nanomeshes was reduced as the diameter of the pores became smaller, achieving values that varied from $\kappa = 1.54 \pm 0.27$ W K^{-1} m^{-1}, down to the ultra-low $\kappa = 0.55 \pm 0.10$ W K^{-1} m^{-1} value [100]. The latter is well below the amorphous limit, while the Seebeck coefficient and electrical conductivity of the material were retained [100]. (More details of these nanomeshed structures will be given in Section 5.)

In addition to phonon transport engineering [59, 60], different technological strategies such as the fabrication multilayers [103] and channels with reduced dimensionality such as 1D nanotubes [104] and 1D nanowires [105] have achieved a significant reduction in the thermal conductivity. Furthermore, several authors have demonstrated that the obvious reduction in cross-plane thermal conductivity in SiGe 0D cluster—particle (quantum dots) [106] superlattices is primarily due to the increased physical roughness at the superlattice interfaces and not due to quantum confinement effects [107, 108].

Figure 6 summarizes the current state of the art for silicon-germanium in terms of thermoelectric properties. Here, the most promising materials in the form of bulk, thin films, nanomeshes, nanowires, and nanotubes are shown. It is worth noting in these figures that the results of our works, which will be explained later, namely the MIC films and the nanomeshes, are among the best-performing materials. In terms of Seebeck coefficient

http://dx.doi.org/10.5772/67730

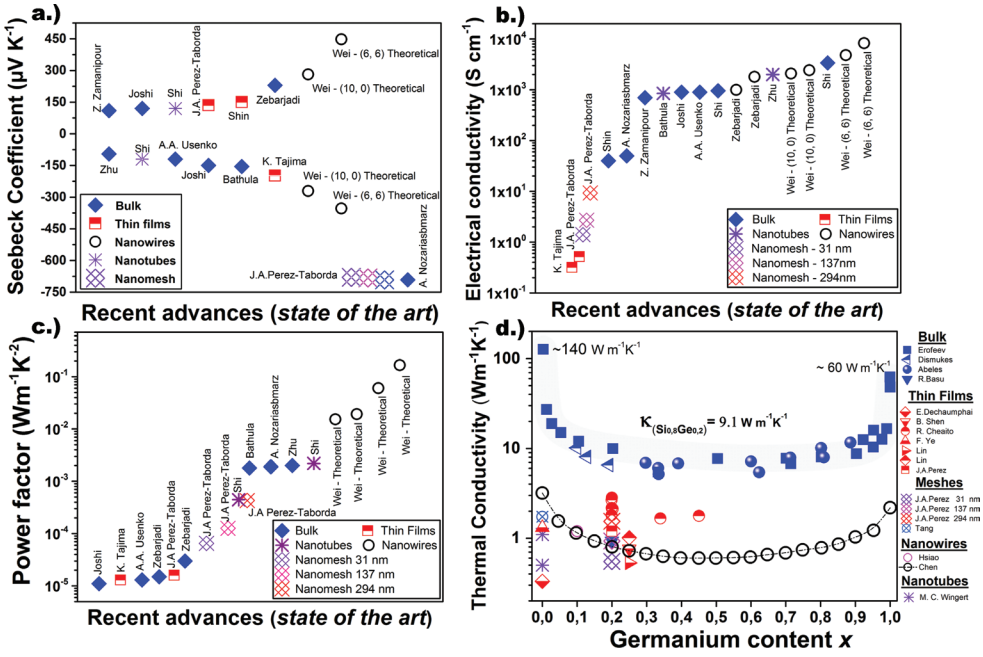

Figure 6. A summary of the latest reported measurements of different structures of Si_xGe_{1-x} is presented, shows (a) Seebeck coefficient, (b) electrical conductivity, and (c) power factor reported for bulk, thin films, nanomeshes, nanowires, and nanotubes. (d) The thermal conductivity for different Si_xGe_{1-x} nanostructures and bulk samples as a function of the alloy composition. This figure is adapted from Ref. [100].

(see **Figure 6a**), the values measured for MIC SiGe thin films are comparable to other values measured in different thin films fabricated with other techniques, while the nanomeshes present the highest Seebeck coefficients, only comparable to values measured in bulk. Nevertheless, the values of electrical conductivity (**Figure 6b**) are quite low, when compared to the values of bulk or nanotubes, but in the order or even better than the values given for thin films. The enhancement of the electrical conductivity within those structures is one of the improvements that are being studied nowadays.

On a whole, the power factor (presented in **Figure 6c**), which takes into account the square of the Seebeck coefficient times the electrical conductivity, shows that the MIC films have power factors compared to other thin films (even higher) and the values achieved in nanomeshes are only overridden by bulk materials and nanotubes [109] (note that the black circles are theoretical calculations, not actual measurements). The last data show the thermal conductivity of different alloy compositions for different kinds of structures (**Figure 6d**). Here, it is worth noting that the values measured for both MIC films and nanomeshes are well below the values measured for crystalline bulk SiGe and among the lowest ever recorded, comparable with the value of the amorphous material (which is 1 W m^{-1} K^{-1}).

4. Thin films: improvement of the thermoelectric performance through the reduction of thermal conductivity of nanocrystalline $Si_{0.8}Ge_{0.2}$ films by sputtering deposition

Silicon-germanium thin films can be easily *p*- or *n*-type doped at room temperature when the material is amorphous. Nevertheless, doping is particularly difficult when the material is crystalline, given that it is usually crystallized at high temperatures. Si_xGe_{1-x} films grown by different techniques, such as low-pressure chemical vapor deposition (LPCVD) or sputtering, turn out to be amorphous unless the deposition itself is performed at very high temperatures [110–112]. Certainly, amorphous SiGe layers are not an option to be used as thermoelectric materials, given their low Seebeck and low electrical conductivity. Therefore, the main challenge with these Si_xGe_{1-x} alloys, which are to be applied in large-scale practical applications, has not yet been overcome due to the difficulties in the growth of high-quality, highly crystalline, low-cost, and appropriately doped films. On that sense, some examples that can be found in the literature obtained in our lab are compiled in this section.

Recently, metal-induced crystallization (MIC) [92, 113, 114] has proved to be an interesting alternative to reduce the crystallization temperature required for SiGe. This process is based on the growth of the films on substrates with Au [115], Ag [116], Al [117], Ni [118], Cr [119], or Sn [120] layer. Then, an appropriate heat treatment is performed, allowing the gold from the film to migrate through the semiconductor film all the ways to the surface. This gives rise to a eutectic mixture. The Au-Si eutectic temperature occurs around 350°C, Au-Ge being at around 361°C [121]. Using this MIC technique, quite promising results have been reported recently for thin films of boron-doped $Si_{0.8}Ge_{0.2}$ (*n*-type) grown by sputtering, resulting in films with a good power factor and a very low thermal conductivity [92]. In that work, two different approaches were followed: (i) *in situ* MIC (depositing the films at different controlled temperatures during the sputtering process) and (ii) *ex situ* MIC (deposition of the films at room temperature in the sputtering chamber and subsequently post-annealing in an external furnace under a controlled atmosphere) [92].

The structural evolution from amorphous to crystalline as a function of the different treatment temperatures can be observed in **Figure 7** through the Raman spectra, both for *in situ* (left hand, red color) and *ex situ* (right hand, blue color) MIC films for different temperatures. It can be seen that the vibration modes appear as broad bands for room temperature treatments (see **Figure 7a** and **e**), which means that the material is amorphous. Then, the peaks become narrower as the treatment temperatures increase. Moreover, the Si-Si vibrational peak shows a clear red shift for the highest temperature (500°C) of the *ex situ* samples (**Figure 7d**). This shift may be related to the formation of silicon-rich clusters. Moreover, the relative intensities and frequencies corresponding to the main peaks present in the Raman spectra are strongly dependent on the alloy composition.

A closer look at the Si-Si peak reveals that it is, in fact, a convolution of two peaks; a very narrow peak corresponding to the Raman spectrum of crystalline silicon-rich SiGe and a broader, smaller peak corresponding to the Si-Si vibrations are typically found in $Si_{0.8}Ge_{0.2}$. This could be an indication that silicon is partially segregated in the *ex situ* samples. The peaks observed in the *in situ* samples are narrower than those of the *ex situ* annealed samples, which confirms the high

http://dx.doi.org/10.5772/67730

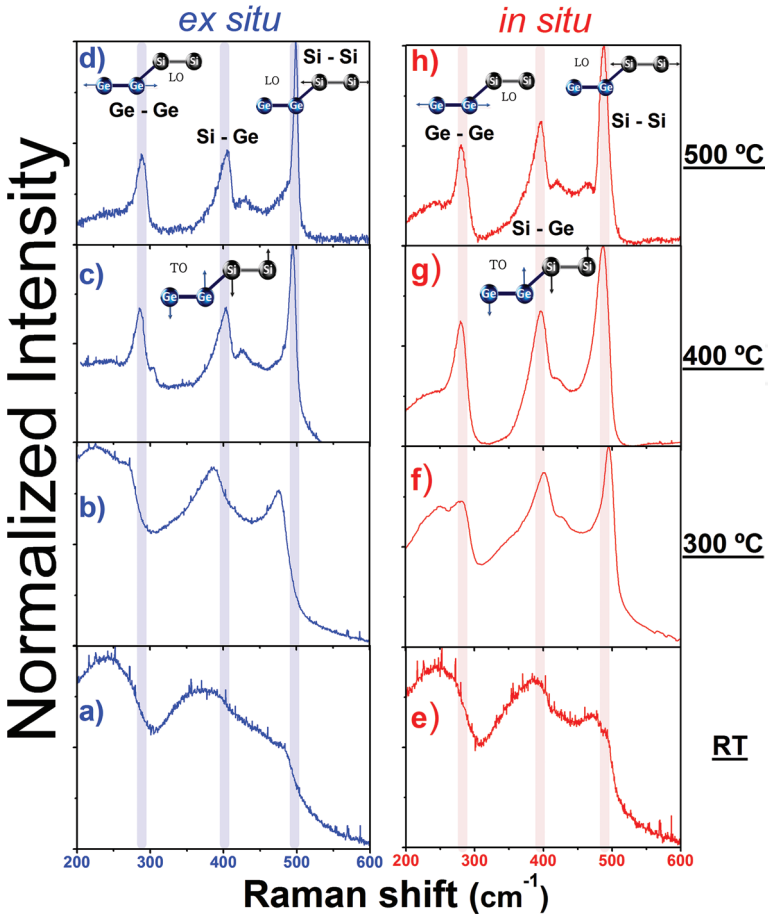

Figure 7. Raman spectra of thin films deposited on gold/glass substrates: *ex situ* thermal treatment (in blue: a, b, c, and d) and *in situ* thermal treatment (in red: e, f, g, and h) for samples treated at RT, 300, 400, and 500°C, respectively. The expected vibrational bands (schematically represented) corresponding to Ge-Ge, Si-Si, and Si-Ge bonds are marked on the figure. With permission from Ref. [92].

degree of crystalline order. Furthermore, these results clearly indicate that whereas, in the *in situ* treatment, the crystallization starts at 300°C, the crystallization onset is lower for *ex situ* treatments. It is interesting to note that in the 400–500 cm^{-1} region, secondary modes start to appear at high temperatures. These modes might be associated with the formation of a compositional gradient due to segregation of Si and Ge, which promotes predominantly Si cluster formation. These clusters would remain embedded in the SiGe matrix when the post-annealing is performed.

Then, the structural analysis by synchrotron radiation-grazing incidence X-ray diffraction (SR-GIXRD) for samples treated at 500°C is shown in **Figure 8**. In order to perform the XRD study, the gold layer was also selectively removed by potassium iodide etching. Nevertheless, gold diffraction maxima are dominant in the *ex situ* treated sample, which means that not all the gold was removed. This indicates that the gold, instead of migrating completely to the

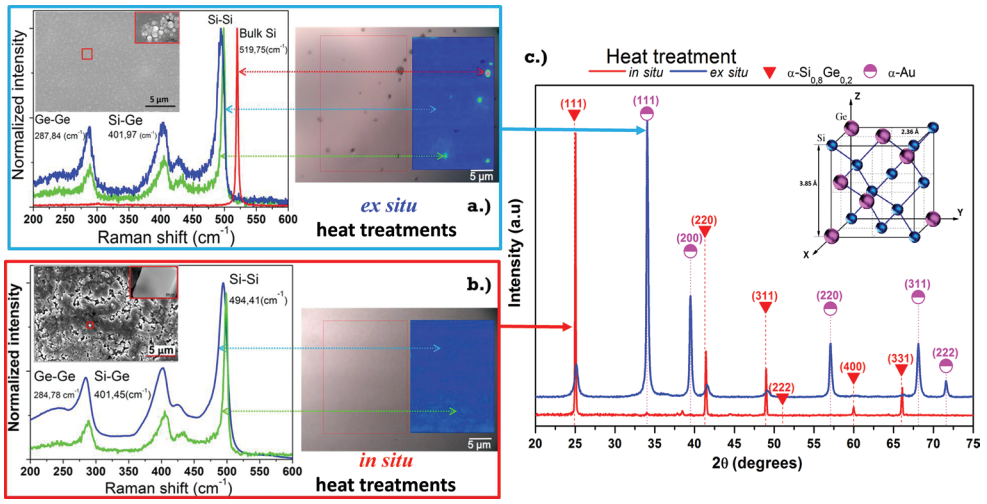

Figure 8. (a) and (b) present different measurements for the *ex situ* (a) and *in situ* (b) MIC fabricated films with 500°C treatment temperatures. On the right side, the optical image of the surface along with a Raman mapping of the surface is presented. In the left side, the different Raman spectra collected corresponding to $Si_{0.8}Ge_{0.2}$ (blue color), nano-$Si_{1-x}Ge_x$ (green color), and pure silicon (red color) are shown (note that for the *in situ* film, b), there is no evidence of silicon segregation). The inset at the left side presents SEM image of the film surface. (c) Synchrotron radiation SR-GIXRD diffractograms measured at 1.3775 Å wavelength for *ex situ* (blue color) and *in situ* (red color) MIC fabricated films, with heat treatments at 500°C. The heights of the intensities in dotted lines correspond to the Si-Ge phase intensity values given in the JCPDS 04-016-6750 data sheet. The inset shows the calculated lattice parameters for the Si-Ge films. This figure is adapted from Ref. [92].

surface during the *ex situ* MIC treatment, part of it stayed, trapped inside the film. In the case of samples deposited *in situ* at temperatures of 500°C, the diffraction peak intensities at (111), located at 2θ=25.33° for the synchrotron radiation source, are higher than the intensities of samples treated *ex situ*.

The low values of thermal conductivities (1.13 and 1.23 W m^{-1} K^{-1} for *in situ* and *ex situ* thermal treated at 500°C, respectively) obtained in Ref. [92] have been associated with the formation of Si-rich SiGe and Si clusters during the gold-induced crystallization, which creates plenty of phonon scattering sites at the grain boundaries. The best power factors were achieved for samples grown at 500°C, that is, *in situ* MIC. The results indicate a maximum of 16 µW m^{-1} K^{-2} at 315°C, which is the best-reported value, to date, for SiGe films grown by DC sputtering with Au-MIC—similar to the state-of-the-art values available in the literature for Si-Ge bulk samples. This is due to the fact that this sample is not contaminated with gold and also that the doping has not been lost by this thermal treatment.

In the same way, these results also suggest two different mechanisms of induced crystallization dependent on the type of heat treatment (*ex situ* and *in situ* MIC). For the *ex situ* samples, the gold layer travels through the Si-Ge film grown at RT when heated afterward at 500°C, while in the case of *in situ* treatment, a eutectic is formed and the nanocrystalline Si-Ge film seems to be formed underneath.

http://dx.doi.org/10.5772/67730

5. Nanomeshes: record low thermal conductivities in large-area nanoporous $Si_{0.8}Ge_{0.2}$ for enhanced thermoelectric applications

Another recent example of a reduction in thermal conductivity by using the low-dimensional concept has been recently reported [100]. These large-area nanomeshed films were fabricated by DC sputtering of $Si_{0.8}Ge_{0.2}$ on highly ordered porous alumina matrices (see **Figure 9a**), in such a way that the formed $Si_{0.8}Ge_{0.2}$ film replicated the porous alumina structure, resulting in the nanomeshed films shown in **Figure 9b**. A very good control of the nanomesh geometrical features (pore diameter, pitch, and neck) was achieved thanks to the alumina templates used, with pore diameters ranging from 294 ± 5 nm down to 31 ± 4 nm. The method developed is able to provide large areas of nanomeshes in a straightforward and reproducible way, being easily scalable for industrial applications.

Most importantly, as shown in **Figure 10a**, the thermal conductivity of the films was reduced as the diameter of the porous became smaller, achieving values that varied from $\kappa = 1.54 \pm 0.27$ W K^{-1} m^{-1}, down to the record low $\kappa = 0.55 \pm 0.10$ W K^{-1} m^{-1} value. The latter is well below the amorphous limit, while both the Seebeck coefficient and electrical conductivity of the material were maintained (see **Figure 10b**).

Likewise, as in the previous case for the nanocrystalline $Si_{0.8}Ge_{0.2}$ films grown by sputtering deposition, the nanomeshed SiGe films were oriented along the [111] direction, as revealed by XRD measurements (see **Figure 11a**). Raman spectra showed the three characteristic

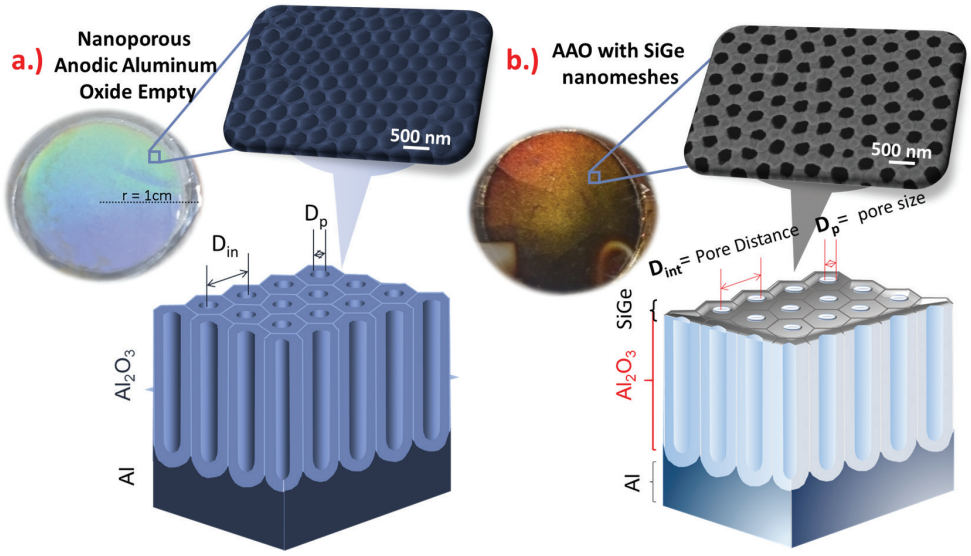

Figure 9. (a) Sketch and optical image of a porous alumina template and (b) the SiGe film nanomesh fabricated on top of it.

vibrational modes obtained for polycrystalline SiGe (see **Figure 11b**) and showed a homogenous phase in all the film.

Additionally, the chemical/surface potential of the $Si_{0.8}Ge_{0.2}$ nanomeshed films was studied by Kelvin probe microscopy (KPM). **Figure 12a** and **b** shows the SEM image and the AFM surface topography of a 294 ± 5 nm porous size nanomeshed film, which presents a homogeneous profile of the surface potential (see **Figure 12c**). This indicates that the work function of the films is homogeneous, confirming the homogeneity in the chemical composition obtained by Raman, and no potential drop is observed at the grain boundaries.

On the one hand, as far as the thermal conductivity is concerned, it is highly reduced when compared to bulk or thin films. This reduction is due to alloying, phonon boundary scattering on the upper/lower boundaries, and crystallite boundaries within the nanomeshes. Moreover, the measurements showed that the smaller the pore diameter is, the larger the thermal conductivity reduction in the $Si_{0.8}Ge_{0.2}$ nanomesh. This can be understood as a result of the enhanced scattering on the pore boundaries, along with the higher disorder or even coherent phonon effects that could be playing a role in the nanomeshed structures, when compared to plain films. Using this approach, it is possible to control thermal transport of these films

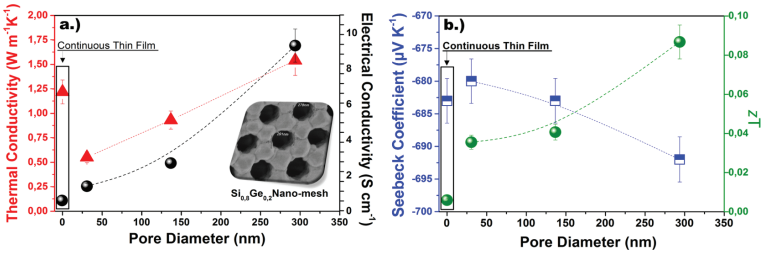

Figure 10. (a) Thermal conductivity (κ, red triangles) and electrical conductivity (σ, black spheres) and (b) Seebeck coefficient (*S*, blue squares) and figure of merit (*zT*, green spheres) plotted versus the pore diameter of the nanomesh. The transport properties obtained for a $Si_{0.8}Ge_{0.2}$ film grown under the same conditions are also plotted for comparison (inside the rectangle on the left of each graph, corresponding to continuous thin film). This figure is adapted from Ref. [100].

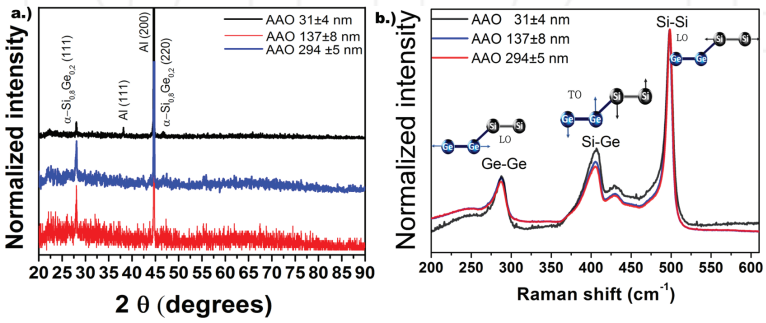

Figure 11. (a) X-ray diffraction and (b) Raman spectra of a $Si_{0.8}Ge_{0.2}$ grown on nanomeshes with a pore diameter of 31 nm (black line) 137 nm (blue line) and 294 nm (red line). This figure is adapted from Ref. [100].

http://dx.doi.org/10.5772/67730

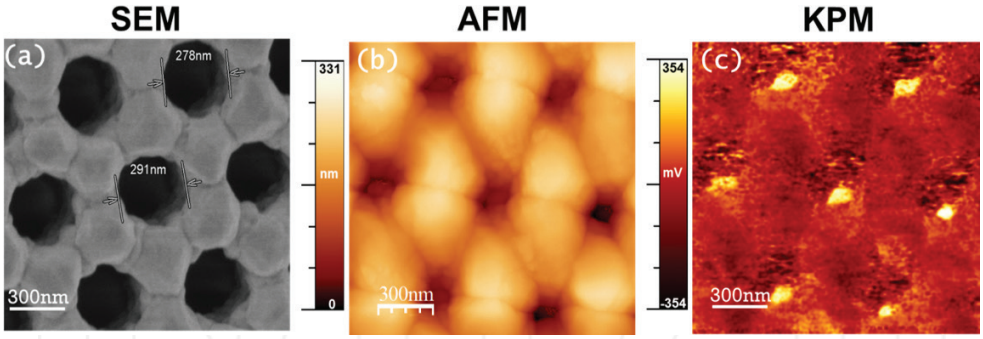

Figure 12. (a) SEM image of a $Si_{0.8}Ge_{0.2}$ nanomeshed film of 294 ± 5 nm pore size. (b) Topography image by AFM and (c) surface potential image by KPM. The uniformity in the contrast of the KPM image reveals homogeneity in the surface potential of the film. This figure is adapted from Ref. [100].

through nano-engineering. Moreover, the power factors of the nanomeshes are higher in the structures with larger pores (and larger distances between the pores), and consequently, they are found smaller in the more disordered structures, which comprise denser pore structure and smaller pore diameters.

The power factors are found to be between 65 and 455 $\mu W\,K^{-2}\,m^{-1}$, which seem to be as large as some of the last reported values for bulk $Si_{0.8}Ge_{0.2}$. This is attributed to the fact that the electrical conductivity in the nanomeshes with large interpore distance is much larger than the more dense nanomeshes, whereas the Seebeck coefficient remains almost the same [100]. while still retaining reasonable power factors, which opens the door for efficient thermoelectric applications for this alloy.

6. Concluding remarks and future directions

In summary, this chapter has shown how the nanostructuration of SiGe takes advantage of the reduction in the lattice thermal conductivity while maintaining the thermoelectric properties of the material, which makes the material quite competitive with others conventionally used. Moreover, the two examples of nanostructuration that have been described here in more detail, namely the sputtered MIC films and the nanomeshes present several advantages over other techniques, such as the possibility of coating large areas thanks to the sputtering process, which is also industrially scalable. Furthermore, the sputtering onto alumina templates, which gives rise to the nanomeshes, can also cover large areas, given that the aluminum oxide templates can be fabricated over large-area aluminum substrates. In the case of nanomeshes, the drastic reduction in the thermal conductivity achieved is due to alloying, phonon boundary scattering on the upper/lower boundaries, and crystallite boundaries. Therefore, this makes the method cost-effective to be scaled into the industry. Another key thing to remember is that both nanostructures (MIC films and nanomeshes) are compatible with silicon technology, opening the door to applications in electronic devices, which need to have thermal dissipation. This provides not only a novel approach to growing this kind of

structures in a simple and reliable way, but also an important route toward achieving high conversion efficiency and highly scalable thermoelectric materials.

This chapter presents the most recent advancements in SiGe alloys for its use as efficient thermoelectric material. To this end, it is important to understand the mechanisms that govern the thermal conductivity, in order to engineer the material to reduce it as much as possible without affecting other thermoelectric properties. The thriving expansion of new capabilities of 1D and two-dimensional SiGe has progressed rapidly during the last few years. Although most of the two-dimensional materials have a simple honeycomb lattice structure, understanding the phonon transport mechanism in such atomic thin SiGe seems not an easy task. It is obviously important to recognize that no single technology can meet the world's energy needs in the twenty-first century; one needs a combination of many technologies in which the thermoelectric materials can undoutebtedly play a role. Further, these large-area films or nanomeshes provide a novel approach to growing nanostructured thermoelectric materials in a simple and reliable way.

Author details

Jaime Andrés Pérez-Taborda, Olga Caballero-Calero and Marisol Martín-González*

*Address all correspondence to: marisol@imm.cnm.csic.es

IMM-Instituto de Microelectrónica de Madrid (CNM-CSIC), Madrid, Spain

References

[1] D.C. Brock (Ed.), Moore's law at forty. *Understanding Moore's law: four decades of innovation*, Chemical Heritage Foundation (2006) last access: https://issuu.com/chemheritage/docs/understanding-moores-law?e=1220

[2] M. Martín-González, O. Caballero-Calero, P. Díaz-Chao, Renewable and Sustainable Energy Reviews **24**, 288 (2013).

[3] J. Conti, International energy outlook 2016 Report No. DOE/EIA-0484 US Energy Information Administration (eia), Washington DC (2016).

[4] P. Fragkos, N. Tasios, L. Paroussos, P. Capros, S. Tsani, Energy Policy **100**, 216 (2017).

[5] Communication from the Commission to the European Parliament, The Council. The Road from Paris: assessing the implications of the Paris Agreement and accompanying the proposal for a Council decision on the signing, on behalf of the European Union, of the Paris agreement adopted under the United Nations Framework Convention on Climate Change. European Commission, Brussels, 2.3.2016 COM(2016) 110 final last access: https://ec.europa.eu/transparency/regdoc/rep/1/2016/EN/1-2016-110-EN-F1-1.PDF

[6] B. Obama, The irreversible momentum of Clean energy, Science 355 (January (6321)) (2017) 126–129

[7] H. Theuerer, J. Kleimack, H. Loar, H. Christensen, Proceedings of the Institute of Radio Engineers **48**, 1642 (1960).

[8] P. Balk, Journal of the Electrochemical Society **118**, 494 (1971).

[9] H. Daembkes, H.-J. Herzog, H. Jorke, H. Kibbel, E. Kasper, IEEE Transactions on Electron Devices **33**, 633 (1986).

[10] T. Pearsall, J. C. Bean, IEEE Electron Device Letters **7**, 308 (1986).

[11] H. Temkin, T. Pearsall, J. Bean, R. Logan, S. Luryi, Applied Physics Letters **48**, 963 (1986).

[12] G. L. Patton, S. S. Iyer, S. Delage, S. Tiwari, J. Stork, IEEE Electron Device Letters **9**, 165 (1988).

[13] H. Liu, D. Landheer, M. Buchanan, D. Houghton, Applied Physics Letters **52**, 1809 (1988).

[14] R. Taft, J. D. Plummer, S. Iyer, IEEE Electron Device Letters **10**, 14 (1989).

[15] T.-J. King, J. R. Pfiester, J. D. Shott, J. P. McVittie, K. C. Saraswat, in *Electron Devices Meeting, 1990. IEDM'90. Technical Digest., International* (IEEE, 1990), p. 253.

[16] R. Soref, F. Namavar, J. Lorenzo, Optics Letters **15**, 270 (1990).

[17] D. Houghton, J.-P. Noël, N. Rowell, Materials Science and Engineering: B **9**, 237 (1991).

[18] D. Shen, J. Conde, V. Chu, S. Aljishi, J. Z. Liu, S. Wagner, IEEE Electron Device Letters **13**, 5 (1992).

[19] S.-B. Hwang, Y. Fang, K.-H. Chen, C.-R. Liu, J.-D. Hwang, M.-H. Chou, IEEE Transactions on Electron Devices **40**, 721 (1993).

[20] E. Kasper, A. Gruhle, H. Kibbel, *in Electron Devices Meeting, 1993. IEDM'93. Technical Digest., International* (IEEE, 1993), p. 79.

[21] E. Crabbe, B. Meyerson, J. Stork, D. Harame, in *Electron Devices Meeting, 1993. IEDM'93. Technical Digest., International* (IEEE, 1993), p. 83.

[22] S. Jeng et al., IEEE Electron Device Letters **22**, 542 (2001).

[23] J.-S. Rieh et al., in Electron Devices Meeting, 2002. IEDM'02. International (IEEE, 2002), p. 771.

[24] J. D. Cressler, C. Coen, S. Zeinolabedinzadeh, P. Song, R. Schmid, M. Oakley, P. Chakraborty, in *2016 IEEE Compound Semiconductor Integrated Circuit Symposium (CSICS)*2016), p. 1.

[25] R. R. Furlong, E. J. Wahlquist, Nuclear News **42**, 26 (1999).

[26] George R. Schmidt, Robert L. Wiley, Rebecca L. Richardson, and Richard R. Furlong, AIP Conference Proceedings 746, 429 (2005); doi: http://dx.doi.org/10.1063/1.1867159

[27] PATEL, M. R. *Spacecraft Power Systems* CRC-Press, Boca Raton, Florida/USA, 2004. ISBN 0-8493-2768-5.

[28] C. Kelly, in Space Nuclear Power Systems (1987).

[29] G. L. Bennett, C. W. Whitmore, W. R. Amos, "On the Development of the Power Sources for the Ulysses and Galileo Missions", Proceedings of the European Space Power Conference, 1989-October-2-6.

[30] R. Basu et al., Journal of Materials Chemistry A **2**, 6922 (2014).

[31] M. Haras, V. Lacatena, T. M. Bah, S. Didenko, J. F. Robillard, S. Monfray, T. Skotnicki, E. Dubois, IEEE Electron Device Letters **37**, 1358 (2016).

[32] X. Zhang, L.-D. Zhao, Journal of Materiomics **1**, 92 (2015).

[33] Goetberger, Adolf; Knobloch, Joachim; Voss, Bernhard. Crystalline silicon solar cells. editorial John Wiley & Sons Ltd, 1998, vol. 1.

[34] A. Martí, A. Luque, Next Generation Photovoltaics: High Efficiency through Full Spectrum Utilization, edited by A. Martí and A. Luque, Eds.; Institute of Physics, Bristol, 2003.

[35] L.M. Fraas Low-Cost Solar Electric Power Springer International Publishing, Cham (2014) http://dx.doi.org/10.1007/978-3-319-07530-3

[36] U. Rau and T. Kirchartz, in Photon Management in Solar Cell, edited by R. B. Wehrspohn, U. Rau , and A. Gombert (Wiley-VCH, Weinheim, 2015)

[37] M. A. Green, K. Emery, Y. Hishikawa, W. Warta, E. D. Dunlop, Progress in Photovoltaics: Research and Applications **23**, 1 (2015).

[38] Green, M. A., Emery, K., Hishikawa, Y., Warta, W., & Dunlop, E. D. (2015). Solar cell efficiency tables (Version 45). Progress in photovoltaics: research and applications, 23(1), 1–9.

[39] P. J. Reddy, *Solar Power Generation: Technology, New Concepts & Policy* (CRC Press, 2012).

[40] G. Carr, The Economist **11**, 21 (2012).

[41] D. M. Powell, M. T. Winkler, H. Choi, C. B. Simmons, D. B. Needleman, T. Buonassisi, Energy & Environmental Science **5**, 5874 (2012).

[42] D. Feldman et al., Photovoltaic System Pricing Trends: Historical Recent Near-Term Projections 2013 Edition, Oak Ridge, TN, USA:U.S. Dept. Energy, 2013.

[43] M. P. Paranthaman, W. Wong-Ng, R. N. Bhattacharya, *Semiconductor materials for solar photovoltaic cells* (Springer, 2015), Vol. 218.

[44] R. Keyes, IBM Journal of Research and Development **32**, 84 (1988).

[45] P. S. Peercy, Nature **406**, 1023 (2000).

[46] M. Ieong, B. Doris, J. Kedzierski, K. Rim, M. Yang, Science **306**, 2057 (2004).

[47] T. Ihn, *Semiconductor Nanostructures: Quantum States and Electronic Transport* (Oxford University Press, 2010).

[48] Y. Nishi, R. Doering, *Handbook of Semiconductor Manufacturing Technology* (CRC Press, 2000).

[49] J. Cressler, *in SiGe and Si Strained-Layer Epitaxy for Silicon Heterostructure Devices* (CRC Press, 2007).

[50] W. G. Zeier, J. Schmitt, G. Hautier, U. Aydemir, Z. M. Gibbs, C. Felser, G. J. Snyder, Nature Reviews Materials **1**, 16032 (2016).

[51] E. S. Toberer, L. L. Baranowski, C. Dames, Annual Review of Materials Research **42**, 179 (2012).

[52] A. Shakouri, Materials Research **41**, 399 (2011).

[53] A. Moure, M. Rull-Bravo, B. Abad, A. Del Campo, M. M. Rojo, M. H. Aguirre, A. Jacquot, J. F. Fernandez, M. Martin-Gonzalez, Nano Energy **31**, 393 (2017).

[54] L. Hicks, M. Dresselhaus, Physical Review B **47**, 12727 (1993).

[55] D. Vashaee, A. Shakouri, Physical Review Letters **92**, 106103 (2004).

[56] J. P. Heremans, V. Jovovic, E. S. Toberer, A. Saramat, K. Kurosaki, A. Charoenphakdee, S. Yamanaka, G. J. Snyder, Science **321**, 554 (2008).

[57] Q. Hou, B. Gu, Y. Chen, Y. He, J. Sun, Applied Physics A **114**, 943 (2014).

[58] A. M. Dehkordi, M. Zebarjadi, J. He, T. M. Tritt, Materials Science and Engineering: R: Reports **97**, 1 (2015).

[59] Y. Pei, H. Wang, G. Snyder, Advanced Materials **24**, 6125 (2012).

[60] W. Kim, Journal of Materials Chemistry C **3**, 10336 (2015).

[61] G. Zhang, Y.-W. Zhang, in *Nanoscale Thermoelectrics*, edited by X. Wang, and Z. M. Wang (Springer International Publishing, Cham, 2014), p. 185.

[62] Wan, C., Wang, Y., Wang, N., Norimatsu, W., Kusunoki, M., & Koumoto, K. (2010). Development of novel thermoelectric materials by reduction of lattice thermal conductivity. Science and Technology of Advanced Materials, 11(4), 044306.

[63] A. Cantarero, F. X. Alvarez, in *Nanoscale Thermoelectrics* (Springer, 2014), p. 1.

[64] M. G. Kanatzidis, Chemistry of Materials **22**, 648 (2009).

[65] N. Satyala, P. Norouzzadeh, D. Vashaee, in *Nanoscale Thermoelectrics* (Springer, 2014), p. 141.

[66] M. Zebarjadi, K. Esfarjani, M. Dresselhaus, Z. Ren, G. Chen, Energy & Environmental Science **5**, 5147 (2012).

[67] A. Minnich, M. Dresselhaus, Z. Ren, G. Chen, Energy & Environmental Science **2**, 466 (2009).

[68] M. Steele, F. Rosi, Journal of Applied Physics **29**, 1517 (1958).

[69] V. A. Johnson, K. Lark-Horovitz, Physical Review **92**, 226 (1953).

[70] A. Middleton, W. Scanlon, Physical Review **92**, 219 (1953).

[71] D. M. Rowe, *CRC Handbook of Thermoelectrics* (CRC Press, 1995).

[72] J. Dismukes, L. Ekstrom, E. Steigmeier, I. Kudman, D. Beers, Journal of Applied Physics **35**, 2899 (1964).

[73] G. R. Schmidt, R. D. Abelson, R. L. Wiley, in SPACE TECHNOLOGY AND APPLICATIONS INT. FORUM-STAIF 2005: Conf. Thermophys in Micrograv; Conf Comm/Civil Next Gen. Space Transp; 22nd Symp Space Nucl. Powr Propuls.; Conf. Human/Robotic Techn. Nat'l Vision Space Expl.; 3rd Symp Space Colon.; 2nd Symp. New Frontiers (AIP Publishing, 2005), p. 295.

[74] C. Vining, *CRC Handbook of Thermoelectrics*, ed. Rowe, DM, CRC Press, Boca Raton, 328 (1995).

[75] H. Goldsmid, A. Penn, Physics Letters A **27**, 523 (1968).

[76] J. Parrott, Journal of Physics C: Solid State Physics **2**, 147 (1969).

[77] Z. Tan, W. Jesser, F. Rosi, Materials Science and Engineering: B **33**, 195 (1995).

[78] Cook, J. Harringa, S. Loughin, Materials Science and Engineering: B **41**, 280 (1996).

[79] Bhandari, D. Rowe, Journal of Physics C: Solid State Physics **11**, 1787 (1978).

[80] G. S. Nolas, J. Sharp, J. Goldsmid, *Thermoelectrics: basic principles and new materials developments* (Springer Science & Business Media, 2013), Vol. 45.

[81] R. Bunce, D. Rowe, Journal of Physics D: Applied Physics **10**, 941 (1977).

[82] C. B. Vining, W. Laskow, J. O. Hanson, R. R. Van der Beck, P. D. Gorsuch, Journal of Applied Physics **69**, 4333 (1991).

[83] T. Noguchi, *in Thermoelectrics*, 1997. Proceedings ICT'97. XVI International Conference on (IEEE, 1997), p. 207.

[84] D. Thompson, D. Hitchcock, A. Lahwal, T. Tritt, Emerging Mater Res **1**, 299 (2012).

[85] N. Mingo, D. Hauser, N. Kobayashi, M. Plissonnier, A. Shakouri, Nano Letters **9**, 711 (2009).

[86] M. Zebarjadi et al., Nano Letters **11**, 2225 (2011).

[87] G. Joshi et al., Nano Letters **8**, 4670 (2008).

[88] X. Wang et al., Applied Physics Letters **93**, 193121 (2008).

[89] A. Minnich, H. Lee, X. Wang, G. Joshi, M. Dresselhaus, Z. Ren, G. Chen, D. Vashaee, Physical Review B **80**, 155327 (2009).

[90] M. Haras, V. Lacatena, T. M. Bah, S. Didenko, J.-F. Robillard, S. Monfray, T. Skotnicki, E. Dubois, IEEE Electron Device Letters **37**, 1358 (2016).

[91] S. LeBlanc, S. K. Yee, M. L. Scullin, C. Dames, K. E. Goodson, Renewable and Sustainable Energy Reviews **32**, 313 (2014).

[92] J. P. Taborda, J. Romero, B. Abad, M. Muñoz-Rojo, A. Mello, F. Briones, M. M. Gonzalez, Nanotechnology **27**, 175401 (2016).

[93] A. A. Wilson, M. M. Rojo, B. Abad, J. A. Perez, J. Maiz, J. Schomacker, M. Martín-Gonzalez, D.-A. Borca-Tasciuc, T. Borca-Tasciuc, Nanoscale **7**, 15404 (2015).

[94] M. Hu, X. Zhang, D. Poulikakos, Physical Review B **87**, 195417 (2013).

[95] Y. D. Kuang, L. Lindsay, S. Q. Shi, G. Zheng, Nanoscale **8**, 3760 (2016).

[96] X. Gu, R. Yang, Journal of Applied Physics **117**, 025102 (2015).

[97] X. Zhang, H. Xie, M. Hu, H. Bao, S. Yue, G. Qin, G. Su, Physical Review B **89**, 054310 (2014).

[98] J. Reparaz, I. Marcus, A. Goñi, M. Garriga, M. Alonso, Journal of Applied Physics **112**, 023512 (2012).

[99] P. Ferrando-Villalba et al., Nano Research **8**, 2833 (2015).

[100] J. A. Perez-Taborda, M. Muñoz Rojo, J. Maiz, N. Neophytou, M. Martin-Gonzalez, Scientific Reports **6**, 32778 (2016).

[101] J.-K. Yu, S. Mitrovic, D. Tham, J. Varghese, J. R. Heath, Nature Nanotechnology **5**, 718 (2010).

[102] J. Tang, H.-T. Wang, D. H. Lee, M. Fardy, Z. Huo, T. P. Russell, P. Yang, Nano Letters **10**, 4279 (2010).

[103] E. Dechaumphai, D. Lu, J. J. Kan, J. Moon, E. E. Fullerton, Z. Liu, R. Chen, Nano Letters **14**, 2448 (2014).

[104] M. C. Wingert, S. Kwon, M. Hu, D. Poulikakos, J. Xiang, R. Chen, Nano Letters **15**, 2605 (2015).

[105] J. Chen, G. Zhang, B. Li, Applied Physics Letters **95**, 073117 (2009).

[106] J. J. Urban, Nature Nanotechnology **10**, 997 (2015).

[107] P. E. Hopkins, J. C. Duda, C. W. Petz, J. A. Floro, Physical Review B **84**, 035438 (2011).

[108] G. Chen, M. Dresselhaus, G. Dresselhaus, J.-P. Fleurial, T. Caillat, International Materials Reviews (2013).

[109] J. Wei, H. Liu, X. Tan, L. Cheng, J. Zhang, D. Fan, J. Shi, X. Tang, RSC Advances **4**, 53037 (2014).

[110] E. V. Jelenkovic, K. Tong, W. Cheung, S. Wong, B. Shi, G. Pang, Solid State Electron. **50**, 199 (2006).

[111] I. Nakamura, T. Ajiki, H. Abe, D. Hoshi, M. Isomura, Vacuum **80**, 712 (2006).

[112] W. Qin, D. G. Ast, T. I. Kamins, Journal of Applied Physics. **92**, 168 (2002).

[113] M. Lindorf, H. Rohrmann, G. Span, S. Raoux, J. Jordan-Sweet, M. Albrecht, Journal of Applied Physics **120**, 205304 (2016).

[114] M. Lindorf, H. Rohrmann, G. L. Katona, D. L. Beke, H. F. Pernau, M. Albrecht, Materials Today: Proceedings **2**, 557 (2015).

[115] M. Seibt, S. Buschbaum, U. Gnauert, W. Schröter, D. Oelgeschläger, Physical Review Letters **80**, 774 (1998).

[116] T. J. Konno, R. Sinclair, Philosophical Magazine B **71**, 163 (1995).

[117] Z. Wang, J. Wang, L. Jeurgens, E. Mittemeijer, Physical Review B **77**, 045424 (2008).

[118] K. U. M. Kumar, R. Brahma, M. G. Krishna, A. K. Bhatnagar, G. Dalba, Journal of Physics: Condensed Matter **19**, 496208 (2007).

[119] K. Kumar, M. G. Krishna, Journal of Nanomaterials **2008**, 57 (2008).

[120] S. Raoux, H.-Y. Cheng, J. L. Jordan-Sweet, B. Muñoz, M. Hitzbleck, Applied Physics Letters **94**, 183114 (2009).

[121] G. Gerlach, W. Dotzel, *Introduction to Microsystem Technology: A Guide for Students* (Wiley Microsystem and Nanotechnology) (Wiley Publishing, 2008).

PAPER II

IOP Publishing Nanotechnology
Nanotechnology 27 (2016) 175401 (8pp) doi:10.1088/0957-4484/27/17/175401

Low thermal conductivity and improved thermoelectric performance of nanocrystalline silicon germanium films by sputtering

J A Perez Taborda[1], J J Romero[1], B Abad[1], M Muñoz-Rojo[1], A Mello[2], F Briones[1] and M S Martin Gonzalez

[1] Instituto de Microelectrónica de Madrid, CSIC, 28760 Tres Cantos, Madrid, Spain
[2] Lab. of Surface and Nanostructures, Centro Brasileiro de Pesquisas Físicas, 22290-180, Rio de Janeiro-RJ, Brazil

E-mail: marisol@imm.cnm.csic.es

Received 20 July 2015, revised 25 January 2016
Accepted for publication 18 February 2016
Published 11 March 2016

Abstract

Si_xGe_{1-x} alloys are well-known thermoelectric materials with a high figure of merit at high temperatures. In this work, metal-induced crystallization (MIC) has been used to grow $Si_{0.8}Ge_{0.2}$ films that present improved thermoelectric performance ($zT = 5.6 \times 10^{-4}$ at room temperature) —according to previously reported values on films—with a relatively large power factor ($\sigma \cdot S^2 = 16\,\mu W \cdot m^{-1} \cdot K^{-2}$). More importantly, a reduction in the thermal conductivity at room temperature ($\kappa = 1.13 \pm 0.12\,W \cdot m^{-1} \cdot K^{-1}$) compared to other Si–Ge films ($\sim 3\,W \cdot m^{-1} \cdot K^{-1}$) has been found. Whereas the usual crystallization of amorphous SiGe (*a*-SiGe) is achieved at high temperatures and for long times, which triggers dopant loss, MIC reduces the crystallization temperature and the heating time. The associated dopant loss is thus avoided, resulting in a nanostructuration of the film. Using this method, we obtained $Si_{0.8}Ge_{0.2}$ films (grown by DC plasma sputtering) with appropriate compositional and structural properties. Different thermal treatments were tested *in situ* (by heating the sample inside the deposition chamber) and *ex situ* (annealed in an external furnace with controlled conditions). From the studies of the films by: x-ray diffraction (XRD), synchrotron radiation grazing incidence x-ray diffraction (SR-GIXRD), micro Raman, scanning electron microscopy (SEM), x-ray photoemission spectroscopy (XPS), Hall effect, Seebeck coefficient, electrical and thermal conductivity measurements, we observed that the *in situ* films at 500 °C presented the best zT values with no gold contamination.

S Online supplementary data available from stacks.iop.org/NANO/27/175401/mmedia

Keywords: thermal conductivity, thermoelectric materials, silicon germanium, sputtering

(Some figures may appear in colour only in the online journal)

1. Introduction

Thermoelectric materials are able to generate a voltage difference when subjected to a temperature difference and vice-versa [1]. They are considered as clean renewable sources because of their capability to harvest energy. Thermoelectric effect has been known since the 19th century, but its use as energy sources is still in niche applications, mainly due to two bottlenecks: low efficiency and high cost (mostly related to the use of scarce materials, which greatly increase the device cost). The thermoelectric community is trying to develop materials based on widely available elements [1].

Si_xGe_{1-x} has been broadly studied in the past and has been used, for example, in thermoelectric generators such as those used in *Voyager I*, *II* and *New Horizons* [2, 3] spacecrafts. Silicon and germanium are relatively inexpensive, universally abundant, and they are potentially compatible with the current technology of integrated circuits [4]. However, the use of these materials has been limited because of their low efficiency.

The efficiency of a thermoelectric material is related to its figure of merit through $zT = S^2 \cdot \sigma \cdot \kappa^{-1} \cdot T$, where S is the Seebeck coefficient, σ is the electrical conductivity, κ is the thermal conductivity, and T is the temperature. The production of Si_xGe_{1-x} thin films has been widely studied in the past years. Whereas Si_xGe_{1-x} can be easily p or n-type doped as an amorphous material grown at room temperature, the control of the doping is particularly difficult when it is crystallized at high temperatures. Si_xGe_{1-x} films can be grown by different techniques, such as low pressure chemical vapour deposition (LPCVD) or sputtering, which turns out to produce amorphous Si_xGe_{1-x} unless deposition is performed at very high temperatures [5–7]. The main challenge faced in the use of Si_xGe_{1-x} alloys is associated with the growth of high-quality, highly crystalline, low-cost and appropriately doped films, which must be overcome in order to use these materials in large scale practical applications.

Teh *et al* [8] applied annealing temperatures between 600 °C and 900 °C for 24 h to achieve the crystallization of $Si_{0.72}Ge_{0.28}$, and they found out that increasing the temperature and the heat treatment time improved the crystallization of the samples. However, the main drawback is the reduction in the thermoelectric performance of the films, since by increasing the annealing temperature the boron and phosphorous dopants are lost. It is therefore crucial to devise a method for producing Si_xGe_{1-x} thin films at lower temperatures.

Metal-induced crystallization (MIC) process was first reported in 1976 [9] as a method to convert amorphous silicon into crystalline at lower temperatures by the catalytic effect of pure metals such as Au [10], Ag [11], Al [12], Ni [13], Cr [14] or Sn [15]. Attempts have also been previously made to transform amorphous silicon germanium (a-Si_xGe_{1-x}) into a polycrystalline by MIC by thermal annealing at relatively low temperatures (above 250 °C) for long times (20 h) see for example [16]. In any case, to obtain a good quality Si_xGe_{1-x} film the metal selected for MIC has to be one that results in a reduction of the crystallization temperature, but without getting incorporated into the semiconductor (no extra doping should be produced by the metal). Gold has been shown to act as an efficient MIC material for Si_xGe_{1-x}, in which case the process is also known as 'gold-induced layer exchange process' [16, 17]. During isothermal heat treatment the gold is dissolved into the semiconductor film, giving rise to a eutectic mixture. The Au–Si eutectic temperature occurs around 350 °C, while for Au–Ge is observed at around 361 °C [18].

In this work, we have grown boron-doped $Si_{0.8}Ge_{0.2}$ films (*n-type*) on gold substrates by MIC. We used two different kinds of treatments to achieve crystallization: (a) *in situ* (depositing the films at different temperatures during the sputtering process) and (b) *ex situ* (deposition of the films at room temperature in the sputtering chamber and subsequently post annealing in an external furnace under controlled conditions).

We use a higher crystallization temperature in this work, compared to the one previously mentioned by Park *et al* [16]. However, it must be noted that the thermal treatment time was reduced from 20 h to 1 h. The gold crystallite size (or the FWHM of the diffraction maxima) was also found to be strongly decreased with the annealing temperature, as seen in (supplementary information table **S1**).

In [19] a Seebeck coefficient of $-100\,\mu V \cdot K^{-1}$, an electrical resistivity of $0.8\,m\Omega \cdot cm$, and a thermal conductivity of $\sim 5\,W \cdot m^{-1} \cdot K^{-2}$ were reported for the *n-type* bulk SiGe, with a $zT \sim 0.1$.

In this work, the transport properties of our MIC $Si_{0.8}Ge_{0.2}$ films under *in situ* and *ex situ* thermal treatment conditions have been studied, and found to show an improvement in their thermoelectric performance with respect to other films reported in the literature [20, 21]. Particularly interesting is the low value of thermal conductivity obtained ($\kappa = 1.2\,W \cdot m^{-1} \cdot K^{-1}$), which can be attributed to an increase in the phonon scattering at the boundaries between the nanocrystals and clusters generated during the growing process. To confirm this, a deep characterization of the structure and morphology of the film was performed.

2. Experimental details

Silicon–germanium thin films were grown in a lab-designed sputtering system with a base vacuum of 10^{-9} mbar. A boron-doped $Si_{0.8}Ge_{0.2}$ target (99.999% purity) was bonded onto a cylindrical magnetron cathode (4″) in a vertical configuration. The growth chamber was evacuated to a base pressure of 5×10^{-9} mbar by turbo pumping, using ultra-pure argon (99.9999%) as the sputtering gas. A DC plasma was activated by a voltage of 720 V and a 80 mA current at a pressure of 7×10^{-3} mbar. The silicate glass substrates, pre-cleaned in deionized water, were placed on a heated substrate holder positioned at a distance of 10 cm from the target. For the study of the MIC, 25 nm of Au previously evaporated at ultra-high vacuum by e-beam evaporation was used. $Si_{0.8}Ge_{0.2}$ thin films were deposited for 30 min in all cases.

For the *in situ* thermal treatment a lab-made substrate heater holder was designed, which can reach temperatures of up to 750 °C. The temperature was controlled by means of a *EUROTHERM* 3216 controller and measured by a K-type thermocouple attached to the center of the sample holder surface.

Post-deposition thermal treatments were carried out in an ULVAC Riko Mila 5000 RTA furnace for 1 h in a reducing atmosphere (H_2/N_2) with heating and cooling rates of 10 °C min^{-1}. After heat treatment, the gold was selectively removed by a chemical attack with potassium iodide (KI) solution (2.5% wt. I_2, 10% wt. KI in deionized water) for 20 min to selectively dissolve all possible superficial gold before performing x-ray diffraction (XRD) analysis. The crystalline

structure of the films was studied by XRD using a Philips X-PERT diffractometer with a Cu K_α radiation source of 1.5418 Å wavelength in Bragg-Brentano geometry, and by use of a synchrotron radiation grazing incidence x-ray diffraction (SR-GIXRD) system in the Brazilian Synchrotron XRD Light Laboratory (LNLS), Campinas. $Si_{0.8}Ge_{0.2}$ diffraction spectra were obtained using a synchrotron radiation of 1.3775 Å wavelength. The diffraction patterns were identified by standard reference patterns supplied by the International Centre for Diffraction Data (ICDD). A micro Raman spectrometer (Horiba Jobin Yvon) LabRam HR with a 532 nm Nd:YAG laser (8.5 mW) was used for compositional mapping and to study local crystallization. Scanning electron microscopy (SEM) was performed on a JEOL JSM-6460LV. X-ray photoemission spectroscopy (XPS) spectra were recorded on a custom Specs XPS system (hemispherical energy analyser PHOIBOS 100/150). A monochromatic Al K_α emission (E = 1486.6 eV) was used as the x-ray source in the XPS system. The analysis chamber was kept at 10^{-10} mbar pressure. The survey XPS and narrow scan (for recording high resolution peaks) XPS spectra were collected at pass energies of 0.5 eV and 0.02 eV, respectively. The analysed area was approximately 1.4 mm^2. The peak analysis was performed using Gaussian-Lorentzian convoluted bands, and a Shirley nonlinear sigmoid-type baseline. All the spectra were calibrated using the C1s peak located at 284.8 eV to set the binding energy scale. The data were analyzed using the CasaXPS® software (CasaSoftware Ltd). We performed carrier concentration measurements in an Ecopia Hall Effect Measurement System and took the resistivity and Seebeck coefficient measurements with a commercial Linseis LSR-3 system from room temperature to 315 °C. The Linseis LSR-3 system is periodically calibrated by a constantan standard sample to ensure its accuracy. The cross-plane thermal conductivity was measured at room temperature by a photoacoustic technique, where the sample is periodically heated by a pulse-modulated–diode-pumped ytterbium fiber laser of 1070 nm wavelength and an optical power of around 280 mW. As the sample heats and cools, the air in contact with the sample also does so that it expands and contracts periodically, generating acoustic waves that can be detected with a microphone. In this way, the thermal properties of the sample can be obtained by comparing the input signal from the laser with the signal recorded by the microphone and fitting the data to a multilayer model developed by Hu *et al* [22].

To ensure a good absorption of the laser beam, a titanium layer of 80 nm thickness was deposited by electro-beam evaporation. The C_p [23] used is $Si_{1-x}Ge_x$ ($J \cdot mol^{-1}\ K^{-1}$) = (19.6 + 2.9x), whereas the theoretical density of the alloy is $Si_{1-x}Ge_x$ ($g\ cm^{-3}$) = (2.329 + 3.493x − 0.499x^2) [24].

This lab-made system has been checked by measuring around ten different standard samples, from bulky samples to thick and thin films such as a 298 nm SiO_2 layer on a silicon substrate. Moreover, cross-checks of the obtained values have been carried out in other laboratories and with reference samples.

3. Results and discussion

$Si_{0.8}Ge_{0.2}$ films were deposited directly on 25 nm gold layers on silicate glass substrates. Two different types of thermal treatment were carried out, i.e., *in situ* and *ex situ*, at room temperature (RT), 300, 400 and 500 °C. The *ex situ* set of samples were deposited at RT and the treatment was performed in an external furnace under controlled conditions. The *in situ* set were grown with an internal heater inside the sputtering chamber. All the samples had a homogeneous thickness of about 500 nm, corresponding to a deposition rate of 16 nm min^{-1}.

X-Ray diffraction showed a crystalline orientation along the [1, 1, 1] direction for *in situ* and *ex situ* thermal-treated films at the different temperatures (supplementary information **S1**). Prior to thermoelectric characterization, the residual gold layers were selectively etched. To determine whether any residual gold from the MIC process may be present in the sample, the samples were studied by SR-GIXRD, (see supplementary information **S2**). From the SR-GIXRD analysis results, it can be concluded that samples grown *in situ* at 500 °C show a better migration of the gold to the surface, since no trace of gold can be detected after gold removal. An XPS depth profile indicates the absence of gold particles within these Si-Ge films. The general composition of $Si_{0.8}Ge_{0.2}$ is observed for all the films (supplementary information **S3**). From the results obtained, it was clear that the gold has migrated completely to the surface when the thermal treatment of the films was carried out at 500 °C, which is above its eutectic point. The samples prepared at 500 °C were therefore found to be the most suitable to measure their thermoelectric properties since no gold traces were detected.

3.1. Thermoelectric characterization

The thermoelectric efficiency is strongly associated with low thermal conductivity values. The thermal conductivity can be usually reduced by increasing phonon scattering [25]. The phenomenon of phonon scattering occurs when phonons interact with lattice defects. Such defects include vacancies, dislocations, pores, boundary scattering and atoms of different masses [26]. Due to the particular conditions of growth of our $Si_{0.8}Ge_{0.2}$ thin films, these have a polycrystalline nanostructure, with crystallite sizes of about 34 nm and roughness below 10 nm. The target is an alloy with a stoichiometry of 80% and 20% silicon germanium (observed by XPS—section 3.2) at a rate of 0.23% boron and n-type dopant. During the crystallization process induced gold migrates through SiGe, this produces a significant change in the thermal continuity of the thin film to induce the formation of clusters rich in crystalline silicon and nanocrystalline phases SiGe (observed by Raman spectroscopy—section 3.3). The surface morphology of the sample (observed by SEM—section 3.3) showing structures with large grains and a continuous porosity, which promotes the number of interfaces between grains. A drastic reduction in thermal conductivity is associated with nanopores structures generated by gold films have been discussed by other authors [27]. In our case, these

Table 1. Summary of the state of the art for $Si_{1-x}Ge$ alloys. Recent work has shown a trend towards a drastic reduction in thermal conductivity silicon and SiGe alloys. The measurements were performed mostly by SThM and TDTR [29–31]. Thermal conductivity values at RT for our *in situ* and *ex situ* film heat treated at 500 °C has also been added for comparison purposes.

κ ($W\,m^{-1}\cdot K^{-1}$)	Type of sample	Thickness (nm)	Reference
0.33	Au–Si Multilayers	10 periods with a total thickness of 87	[32]
0.5	Amorphous Si (a-Si)–nanotubes	~5	[33]
0.53	Amorphous $Si/Si_{0.75}Ge_{0.25}$ multilayer films with Au-interlayers	20 periods with a total thickness of 200	[34]
0.76	Amorphous $Si_{0.75}Ge_{0.25}$ multilayer films	200	[35]
0.9	$Si_{0.8}Ge_{0.2}$ bulk	1E7	[24]
1.01	Amorphous $Si/Si_{0.75}Ge_{0.25}$ multilayer films	20 periods with a total thickness of 200	[34]
1.1	Crystalline silicon (c-Si)–nanotubes	~5	[33]
1.13 ± 0.13	$Si_{0.8}Ge_{0.2}$ thin films—500 °C *in situ*	500	This Work
1.23 ± 0.12	$Si_{0.8}Ge_{0.2}$ thin films—500 °C *ex situ*	500	This Work
1.31	Si/Au – multilayers	209.9	[36]
1.6	$Si_{1-x}Ge_x$ thin Films	126 ± 10	[37]

structures migrate during heating (*in situ* or *ex situ*) to the surface causing nonporous structures, after performing surface etching and removal of all gold. The contribution phonon scattering is affected by the scattering at the surface and in the walls of the nanostructures. The increment of phonon scattering can therefore be reduced by introduction of pores as lattice imperfections Theoretical studies show a significant reduction in thermal conductivity for generating such micro-segregations local inhomogeneity that has an important role in reducing κ [28].

Table 1 shows the thermal conductivities of films treated at 500 °C, which were measured using the photoacoustic technique [29]. Thermal conductivities of $1.13\,W\cdot m^{-1}\cdot K^{-1}$ and $1.23\,W\cdot m^{-1}\cdot K^{-1}$ were found for *in situ* and *ex situ* thermal-treated films, respectively. Scanning thermal microscopy (SThM) measurements of these samples were also performed with reproducibility and they agree within the uncertainty associated with the experimental error [30].

Table 1 shows the thermal conductivity values in the out-of-plane direction for both the *in situ* and *ex situ* samples at 500 °C. In these films, we found a strong reduction in the thermal conductivity compared with other values reported in the available literature ($3\,W\cdot m^{-1}\cdot K^{-1}$) for similar thin films [19, 38]. Surprisingly, the out-of-plane thermal conductivity values are more similar to the values reported for SiGe nanowires [39] (~$1.2\,W\cdot m^{-1}\cdot K^{-1}$). An in-depth study of the origin of this behavior will be presented in the next section.

To determine the power factor of these SiGe films, their electrical resistivities and Seebeck coefficients were measured at room temperature with the commercial equipment Linseis LSR-3.

Figure 1 shows the results obtained for both *ex situ* and *in situ* samples treated at different temperatures after chemically removing the gold layer. The values of the samples treated at temperatures below 300 °C could not be measured because their resistivities ($>10^5\,\Omega\cdot cm$) were above the detection limit of our setup. This means that the films are highly resistive and the metal-induced crystallization process could not take place completely at such temperatures.

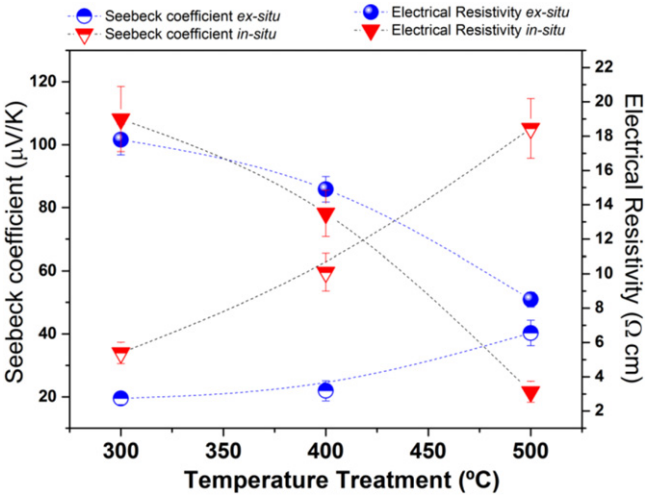

Figure 1. Seebeck coefficients (open symbols) and electrical resistivities (full symbols) for *in situ* (triangles) and *ex situ* (circles) samples as a function of the growth temperature. These measurements were performed at room temperature.

Increasing the temperature led to a reduction in the resistivity (to about $10^{-1}\,\Omega\cdot cm$) associated with gold migration towards the SiGe top surface during the MIC process and hence the initiation of the crystallization process. The resistivities of the *in situ* and *ex situ* samples measured at room temperature are shown in figure 1.

The Seebeck coefficient, related to the doping level, increases with the growth temperature for both types of treatment. However, for the *in situ* samples at 500 °C the Seebeck coefficient is higher, reaching values of ~$110\,\mu V\cdot K^{-1}$ at RT. As explained in the preceding paragraphs, these samples do not show gold contamination. The observed higher Seebeck-coefficient value can be explained by the fact that the boron content of the film is not lost. The measured carrier mobility is $n = 7.3\times10^{17}\,cm^{-3}$ at 300 K. When the Seebeck coefficient of the 500 °C *in situ* sample is measured against the temperature (figure 2), the Seebeck coefficient increases from $120\,\mu V\cdot K^{-1}$ at RT to

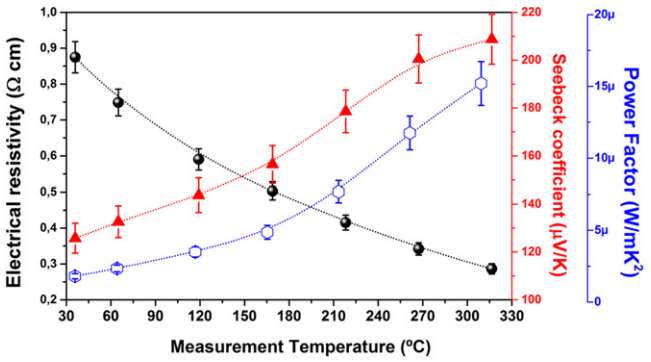

Figure 2. Seebeck coefficients (red triangles), electrical resistivities (black circles) and power factor, (blue empty hexagons) measured from RT until 315 °C for the sample grown *in situ* at 500 °C after selectively etched the gold layer on top.

210 $\mu V \cdot K^{-1}$ at 315 °C. For the samples treated *ex situ*, the low Seebeck-coefficient value at RT (40 $\mu V \cdot K^{-1}$) can be attributed to the gold contamination, as also revealed by the XPS depth analysis (supporting information—figure 3S).

The highest power factors were achieved for samples grown at 500 °C *in situ* (see figure 2). The results show a maximum of 16 $\mu W\, m^{-1}\, K^{-2}$ at 315 °C, which is the highest value reported for SiGe films grown by DC sputtering with Au-MIC (similar to the state of the art values in literature for Si–Ge bulk samples fabricated by hot isostatic pressing and annealing temperatures at 1250 °C [40, 41]).

From the previous thermal characterization, it can be concluded that thermal conductivity of $Si_{0.8}Ge_{0.2}$ prepared by an MIC process at 500 °C presents lower values than for *ex situ* films grown under similar conditions. However, the *in situ* prepared films present state of the art values of the power factor.

In order to better understand the low values of thermal conductivity obtained, a structural and compositional analysis was performed with different techniques for both films.

3.2. High resolution XPS analysis

High-resolution XPS spectra of the silicon and germanium peaks, figure 3, were carried out in samples treated at 500 °C (both *in situ* and *ex situ*). The films were etched to half the film depth using Ar ions (Ar^+ ions sputtering rate was about 8.57 nm min^{-1}). Figures 4(a) and (b), respectively, show the *ex situ* results corresponding to Ge 3d and Si 2p, whereas figures 4(c) and (d) show the *in situ* treatment results. The peak was fitted by a convolution of Gaussian and Lorentzian peaks.

The main Ge 3d peaks (shown in figures 3(a) and (c)) are around 29 eV, which correspond to Ge–Ge or Ge–Si bonds, since the positions of the peaks are independent of the alloy composition from the literature [42–44]. The core Ge 3d resolved level is composed of Ge $3d_{5/2}$ and Ge $3d_{3/2}$ sublevels, whose positions can be found in table 2. In our case, this peak is attributed to the $Si_{0.8}Ge_{0.2}$ phase (though a small difference of 0.2 eV is found between the Ge *in situ* and *ex situ* samples), probably associated with a small composition variation due to the segregation of pure silicon clusters which change the total amount to form the alloy. Similarly, the Si 2p core level was split into two sublevels—Si $2p_{3/2}$ and Si $2p_{1/2}$. The peak-deconvolution values are shown in table 2. As shown in figures 3(b) and (d), the predominant peak for silicon 2p is around 99.6 eV, which corresponds to silicon atoms bound to germanium atoms in the Si_xGe_{1-x} alloy. It is important to highlight that no difference in the Si 2p position is found in both types of treatments.

In both samples, a secondary phase of lower concentration is present. This implies that silicon and germanium are bound differently than in the Si–Ge alloy. Thus, a secondary phase is detected. For the *ex situ* sample, the minority phase is ~7% Ge and ~35% Si ($Si_{0.83}Ge_{0.17}$), whereas in the *in situ* case the minority phase obtained is 3% Ge and ~30% Si ($Si_{0.9}Ge_{0.1}$). Therefore, the *in situ* sample seems to present less secondary phase than the *ex situ,* although it seems to be more Si rich.

3.3. Raman spectra analysis

Raman spectroscopy was performed for films with different temperature treatments all the temperatures (see supplementary information figure 4S) as well as Raman mapping of the 500 °C treated samples (figure 4) in order to confirm the presence of these secondary phases as detected by XPS and if their presence could explain the observed thermal conductivity reduction. Figure 4(a) (*ex situ*) and figure 4(b) (*in situ*) provided a method to correlate the sample mappings with the crystallinity and phase segregation. In the case of *ex situ* samples, three different types of Raman spectra were detected: (*a*) associated with the $Si_{0.8}Ge_{0.2}$ (in blue), (*b*) associated with bulk silicon (in red), and (*c*) associated with the $Si_{1-x}Ge_x$ profile (in green), but displaced toward higher cm^{-1} values that could be associated with a $Si_{1-x}Ge_x$ phase richer in Si. In the *in situ* samples, only two different types of Raman spectra were observed: (*a*) one associated with the $Si_{0.8}Ge_{0.2}$ (in blue) and (*b*) the other one associated with the Si-rich $Si_{1-x}Ge_x$ phase (in green). No traces of Si-rich spectra were detected in the *in situ* case. On plotting the different spectra in a surface mapping, it could be clearly observed that the additional spectra are located in the sample forming clusters.

Therefore, both *ex situ* and *in situ* samples displayed phase segregation: silicon-rich/germanium clusters for *in situ* samples, whereas pure Si clusters and silicon-rich/germanium clusters are found in the case of the *ex situ* samples. It is interesting to note that silicon clusters are clearly identified by the Raman mapping (see red spectra of the Raman mapping on figure 4(a)). The formation of these clusters in both types of samples can be used to explain the reduction in the measured thermal conductivity. From this study, one can associate the low values of the thermal conductivities with the nanocrystallization and formation of clusters that create more phonon scattering sites at grain boundaries. This is consistent with the results from the SR-GIXRD, XPS, and Raman spectroscopy maps, in which nanocrystalline phases of $Si_{0.8}Ge_{0.2}$ with Si-rich clusters were detected. It is widely

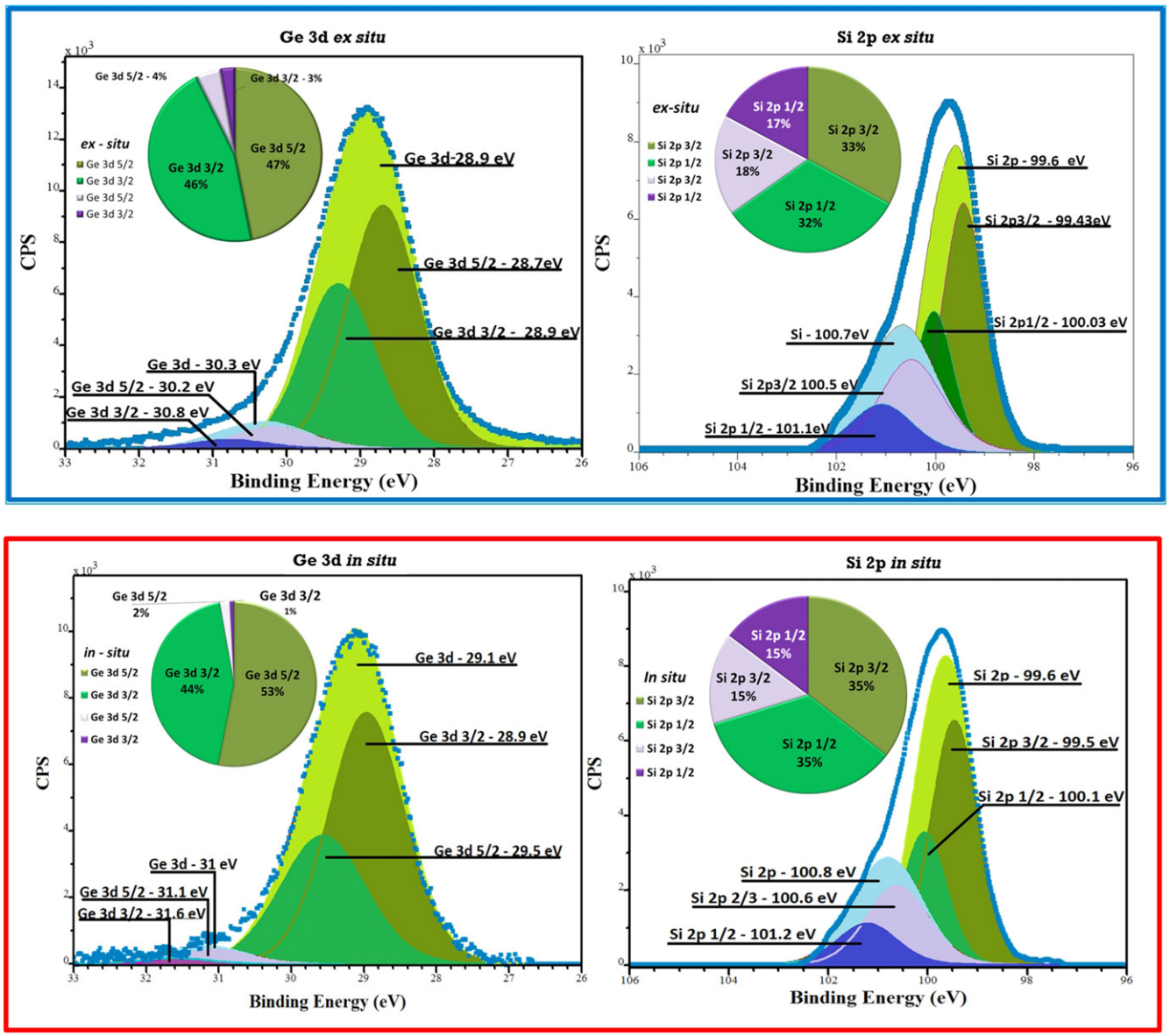

Figure 3. XPS spectra corresponding to the silicon 2p and Ge 3d peaks for the *ex situ* samples at 500°C (a) and (b) and the *in situ* cases at 500 °C (c) and (d).

accepted that the most effective way of decreasing the thermal conductivity is by nanostructurization. In our case this nanostructurization involves the formation of clusters that serve as centers for phonon dispersion, thus nanoparticles embedded in the thin film nanocrystals could be the explanation for the observed reduction in the thermal conductivity.

Finally, it is important to note that the mechanism involved in the MIC process for *ex situ* or *in situ* samples treated at 500 °C seems to be different. In the *ex situ* samples, the gold layer travels through the Si–Ge film when heated after growth at 500 °C, whereas in the case of *in situ* treatment a eutectic is formed and the nanocrystalline Si–Ge film seems to be formed underneath. No gold is found in the Si–Ge surface after potassium iodide etching in the 500 °C *in situ* films, and none is trapped. These different MIC mechanisms can explain the differences in the thermoelectric properties.

4. Conclusions

The lower values of thermal conductivities obtained in this study after metal induced crystallization with gold are associated with the formation of Si-rich SiGe and Si clusters that create an increment of phonon scattering at grain boundaries. The best power factor values were achieved for samples grown at 500 °C *in situ*. The results indicate a maximum of 16 μW m^{-1} K^{-2} at 315 °C, which is the highest reported value for SiGe films grown by DC sputtering with Au-MIC (they are similar to the state of the art values in the available literature for Si–Ge bulk samples). This is attributed to the gold-free sample (uncontaminated) and the negligible effect of the process on the doping level. In other words, the doping level seems not to be affected in these poly-crystallized films.

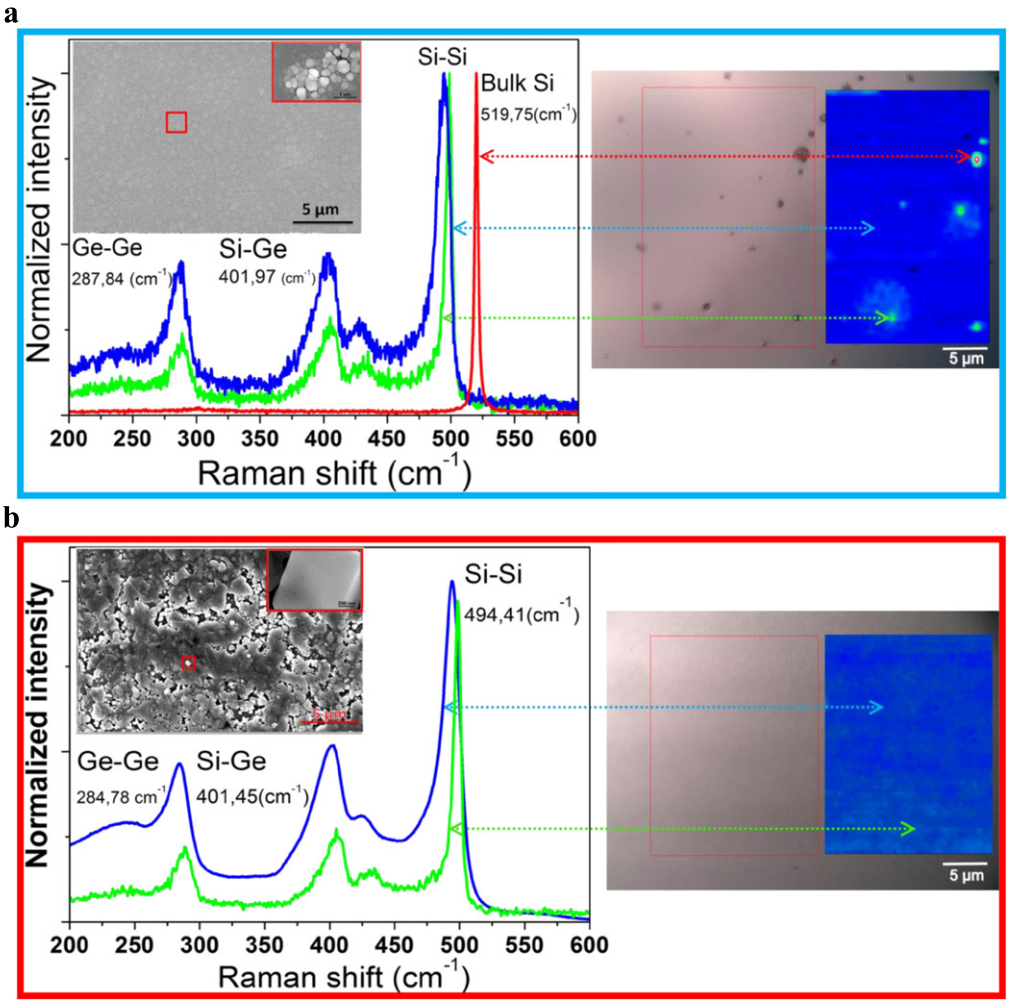

Figure 4. (a) Optical image and Raman mapping of a 500 °C *ex situ* sample. The inset shows an SEM image of the *ex situ* sample surfaces. The mapping has an area of 0.35 μm × 0.7 μm. The colours in the Raman mapping correspond to the different spectra collected, i.e., $Si_{0.8}Ge_{0.2}$ (blue), nano-$Si_{1-x}Ge_x$ (green), and pure Si (red). (b) Raman spectral images of samples grown at the 500 °C *in situ* process. The inset is an SEM image of the *in situ* sample surface. The mapping has an area of 0.35 μm × 0.7 μm, with a $Si_{0.8}Ge_{0.2}$ sample distribution (blue) and smaller quantities nano-$Si_{1-x}Ge_x$ (green).

Table 2. Binding energies for the resolved sublevels of Ge 3d and Si2p, for the *ex situ* and *in situ* treated samples.

Ge 3d (eV)	Ge $3d_{5/2}$ (eV)	Ge $3d_{3/2}$ (eV)	Si 2p (eV)	Si $2p_{3/2}$ (eV)	Si $2p_{1/2}$ (eV)	Assignation
			ex situ			
28.9	28.78	28.9	**99.6**	99.43	100.03	Majority phase $Si_{0.8}$–$Ge_{0.2}$
30.3	30.16	30.77	**100.7**	100.51	101.09	Minority phase Si_{1-x}–Ge_x
			in situ			
29.1	28.93	29.54	**99.6**	99.53	100.14	Majority phase $Si_{0.8}$–$Ge_{0.2}$
31	31.06	31.64	**100.8**	100.62	101.22	Minority phase Si_{1-x}–Ge_x

The results also suggest two different mechanisms for metal induced crystallization which are dependent on the type of heat treatment (*ex situ* and *in situ*). For the *ex situ* samples, the gold layer travels through the Si–Ge film grown at RT during the 500 °C thermal treatment, whereas in the case of *in situ* thermal treatment a eutectic is formed with a resulting nanocrystalline Si–Ge film formed underneath. These differences in the mechanism of crystallization explain the lack of gold traces within the experimental limits of the XPS technique in the Si–Ge surface after potassium iodide etching in the 500 °C *in situ* thermal films and the absence of trapped Au inside the *in situ* Si-Ge film.

Acknowledgments

This work has been supported by the 7th framework of the European project NANOHITEC 263306, the national project PHOMENTA MAT2011-27911, and Infante 201550E072. J A Pérez Taborda acknowledges the Spanish Ministerio de Economia y Competitividad for their FPI grant, and Banco Santander for their special grant for a short stay in Brazil (*Brazilian Center of Physical Researches*, *Rio de Janeiro*). Special thanks go to Marta Rull for her assistance in the treatment of the *ex situ* samples and I Fernández-Martínez of Nano4Energy for his assistance in the commissioning of the sputtering system. The authors wish to thank the Synchrotron Light Brazilian National Laboratory (LNLS)—XRD2 beam line—in Campinas, Brazil, for the XRD measurements (Dr Elvis Lopez and Dr R Ospina, Lab. of Surface and Nanostructures, Centro Brasileiro de Pesquisas Físicas-RJ, Brazil).

References

[1] Martín-González M, Caballero-Calero O and Díaz-Chao P 2013 *Renew. Sustain. Energy Rev.* **24** 288
[2] Bennett G L 2008 *Energy Convers. Manage.* **49** 382
[3] Cataldo R L and Bennett G L 2011 *US Space Radioisotope Power Systems and Applications: Past, Present and Future* (Rijeka: InTech)
[4] LeBlanc S, Yee S K, Scullin M L, Dames C and Goodson K E 2014 *Renew. Sustain. Energy Rev.* **32** 313
[5] Jelenkovic E V, Tong K, Cheung W, Wong S, Shi B and Pang G 2006 *Solid State Electron.* **50** 199
[6] Nakamura I, Ajiki T, Abe H, Hoshi D and Isomura M 2006 *Vacuu* **80** 712
[7] Qin W, Ast D G and Kamins T I 2002 *J. Appl. Phys.* **92** 168
[8] Teh L K, Choi W K, Bera L K and Chim W K 2001 *Solid State Electron.* **45** 1963
[9] Greene J E and Mei L 1976 *Thin Solid Films* **34** 27
[10] Seibt M, Buschbaum S, Gnauert U, Schröter W and Oelgeschläger D 1998 *Phys. Rev. Lett.* **80** 774
[11] Sinclair T J K A R 1995 Metal-mediated crystallization of amorphous-silicon in silicon silver layered systems *Phil. Mag.* B **71** 163–78
[12] Wang Z, Wang J, Jeurgens L and Mittemeijer E 2008 *Phys. Rev.* B **77** 045424
[13] Kumar K U M, Brahma R, Krishna M G, Bhatnagar A K and Dalba G 2007 *J. Phys.: Condens. Matter.* **19** 496208
[14] Kumar K U M and Krishna M G 2008 *Journal of Nanomaterials* **2008** 6
[15] Raoux S, Cheng H-Y, Jordan-Sweet J L, Munoz B and Hitzbleck M 2009 *Appl. Phys. Lett.* **94** 183114
[16] Park J-H, Kurosawa M, Kawabata N, Miyao M and Sadoh T 2011 *ECS Trans.* **35** 39
[17] Park J-H, Miyao M and Sadoh T 2014 *Jpn. J. Appl. Phys.* **53** 020302
[18] Gerlach G and Dotzel W 2008 *Introduction to Microsystem Technology: A Guide for Students (Wiley Microsystem and Nanotechnology)* (Chichester: Wiley)
[19] Rowe D M 2005 *Thermoelectrics Handbook: Macro to Nano* (New York: Taylor and Francis) ch 29
[20] Zamanipour Z, Shi X, Dehkordi A M, Krasinski J S and Vashaee D 2012 *Phys. Status Solidi* A **209** 2049
[21] White D P and Klemens P G 1992 *J. Appl. Phys.* **71** 4258
[22] Hu H, Wang X and Xu X 1999 *J. Appl. Phys.* **86** 3953
[23] Schaffler F, Levinshtein M E, Rumyantsev S L and Shur M S (ed) 2001 *Properties of Advanced Semiconductor Materials: GaN, AlN, InN, BN, SiC, SiGa* (New York: Wiley) p 149
[24] Basu R *et al* 2014 *J. Mater. Chem.* A **2** 6922
[25] Tritt T M 2004 *Thermal Conductivity: Theory, Properties, and Applications* (New York: Kluwer)
[26] Kim W 2015 *J. Mater. Chem.* C **3** 10336
[27] Hopkins P E, Norris P M, Phinney L M, Policastro S A and Kelly R G 2008 *J. Nanomater.* **2008** 22
[28] Lee Y and Hwang G S 2013 *J. Appl. Phys.* **114** 174910
[29] Abad B, Rull-Bravo M, Hodson S L, Xu X and Martin-Gonzalez M 2015 *Electrochim. Acta* **169** 37
[30] Wilson A A, Muñoz Rojo M, Abad B, Perez J A, Maiz J, Schomacker J, Martín-Gonzalez M, Borca-Tasciuc D-A and Borca-Tasciuc T 2015 *Nanoscale* **7** 15404
[31] Manzano B A C V, Rojo M M, Koh Y R, Hodson S L, Martinez A M L, Xu X, Shakouri A, Sands T D, Borca-Tasciuc T and Martín-González M 2016 *Sci. Rep.* **6** 19129
[32] Dechaumphai E, Lu D, Kan J J, Moon J, Fullerton E E, Liu Z and Chen R 2014 *Nano Lett.* **14** 2448
[33] Wingert M C, Kwon S, Hu M, Poulikakos D, Xiang J and Chen R 2015 *Nano Lett.* **15** 2605
[34] Lin C, Zeng Z, Ye F, Luo X, Shen B, Zhang X, Dai L and Hu Z 2014 *EPL (Europhysics Letters)* **105** 27003
[35] Shen B, Zeng Z, Lin C and Hu Z 2013 *Int. J. Therm. Sci.* **66** 19
[36] Ye F, Zeng Z, Lin C and Hu Z 2015 *J. Mater. Sci.* **50** 833
[37] Cheaito R *et al* 2012 *Phys. Rev. Lett.* **109** 195901
[38] Takashiri M, Borca-Tasciuc T, Jacquot A, Miyazaki K and Chen G 2006 *J. Appl. Phys.* **100**
[39] Aksamija Z and Knezevic I 2013 *Phys. Rev.* B **88** 155318
[40] Joshi G *et al* 2008 *Nano Lett.* **8** 4670
[41] Zhao R, Shen L and Guo F 2011 *J. Mater. Res.* **26** 1879
[42] Alonso M I and Winer K 1989 *Phys. Rev.* B **39** 10056
[43] Fischetti M V and Laux S E 1996 *J. Appl. Phys.* **80** 2234
[44] Perkowitz S 2012 *Optical Characterization of Semiconductors: Infrared, Raman, and Photoluminescence Spectroscopy* (New York: Elsevier)

Electronic Supplementary Information:

Low thermal conductivity of nanocrystalline Silicon Germanium films by sputtering

J. A. Pérez Taborda[1], J.J. Romero[1], B. Abad[1], M. Muñoz-Rojo[1], A. Mello[2], F. Briones[1], M.S. Martín González[1]*

[1]Instituto de Microelectrónica de Madrid, CSIC, 28760 Tres Cantos, Madrid, Spain
[2] Lab. of Surface and Nanostructures, Centro Brasileiro de Pesquisas Físicas, 22290-180, Rio de Janeiro-RJ, Brazil

Table of content

Accuracy of the thermal measurements.

S1. X-ray diffraction of $Si_{0.8}Ge_{0.2}$ thin films after *in situ* and *ex situ* thermal treatments

S2. Synchrotron Radiation Grazing Incidence X-Ray Diffraction (SR-GIXRD) diffractograms

S3. X-ray Photoelectron Spectroscopy analysis

S4. Raman Spectra Analysis

Electronic Supplementary Information:

The accuracy of the Photoacoustic (*PA*) system used to measure the thermal conductivity of the films in these work was checked by measuring around 10 different standard samples, from bulk samples to thick and thin films such as a 300nm SiO_2 layer on a silicon substrate. The results showed a deviation lower than 10% in all the cases. Moreover, some crosschecks have been carried out with other techniques and in other labs. Table I shows how the photoacoustic technique measurement was found to be in good agreement with those of the Scanning Thermal Microscopy (*SThM*) for a polymer film, a tellurium thick film deposited by electrodeposition and a 500 nm SiGe thin film [4]. Moreover, the photoacoustic technique measurement was also compared by the Time-Domain Thermoreflectance method (*TDTR*) by measuring a thick bismuth telluride film by both technique and showing a good agreement between them, 2.3 W $m^{-1} \cdot K^{-1}$ and 2.4 $Wm^{-1}K^{-1}$ by the *PA* technique and *TDTR* respectively [2]. Therefore, the accuracy and reliability of the photoacoustic experimental setup is confirmed.

Table I. Comparison of thermal conductivity values obtained by *PA* technique, SThM, and TDTR techniques.

	PA technique	***SThM***	***TDTR***	***Reference***
Polymer film	0.20 ± 0.02	0.25 ± 0.04	-	[4]
Tellurium film	0.78 ± 0.08	0.79 ± 0.04	-	[4]
SiGe film	1.23 ± 0.12	1.22 ± 0.21	-	[4]
Bi_2Te_3 film	2.3 ± 0.2	-	2.4 ± 0.2	[2]

Moreover, the precision of the photoacoustic technique has been deeply investigated for both reference samples and the samples under study. The systematic study about the accuracy for each measurement involves different types of error sources such as the equipment itself (systematic error), the influence of the operator (random error) and the uncertainties associated with the density, specific heat and thickness values needed to the data reduction process.

The systematic error is given by the result of the data fitting obtained when varying the phase shift ±1º which is the uncertainty associated to the lock-in amplifier, although the variation of the phase shift during a measurement is typically lower than 0.2º.

The random uncertainty error is calculated within the 95% confidence interval by performing several measurements per sample and using the following expression:

$$\kappa_{ran} = tn - 1\ \sigma\ \mathrm{n}$$

Where $tn - 1$ is the Student-t distribution, n is the number of measurements and σ is the standard deviation.

The specific heat and density values were taken from the literature [1] so that both were taken as constants. However, both values were varied in the data reduction by %5 which is the typical

Electronic Supplementary Information:

uncertainty of both magnitudes and no deviation of the thermal conductivity was found. Finally, the thickness uncertainty was also taken into account as 25 nm.
Taking all the uncertainties into account, the general expression used to quantify the overall uncertainty is given by:

$$(\Delta\kappa_{ran})^2 + (\Delta\kappa_{sist})^2 + \Delta ll^2$$

Where the uncertainty due to the thickness uncertainty is represented by the third term of the above expression since variations of 5% in the thickness value produces variations of 5% in the thermal conductivity value. This procedure typically yields to values of around 10 % of the experimental thermal conductivity measurement.

S1. X-ray diffraction of $Si_{0.8}Ge_{0.2}$ thin films after *in situ* and *ex situ* thermal treatments

For the *ex situ* samples, a dark gray color was observed after their extraction from the sputtering system, indicating that the films were grown on top of the gold layer. Only after a thermal treatment at 500 °C was a goldish film observed at the top surface. In all cases, the films treated *ex situ* were etched with potassium iodide solution to selectively dissolve any superficial gold present before performing the *XRD* analysis.

When the films were heated above 300 °C (Figure **1S.a**), the diffraction maxima began to appear, with a [111] preferential orientation. This indicates that at 300 °C the gold had started to migrate from its interface with glass to the top of the $Si_{0.8}Ge_{0.2}$ layer, inducing crystallization (see Figure.**1S**). Upon annealing the samples at higher temperatures, a higher degree of crystallization was observed (narrower and more intense $Si_{0.8}Ge_{0.2}$ diffraction maxima), whereas the gold peaks were reduced, becoming almost negligible for the samples annealed at 500 °C upon selective etching. The fact that small gold peaks were observed after gold etching in the $Si_{0.8}Ge_{0.2}$ sample shows that almost all the gold had migrated to the top of the film during the annealing process. For the gold at temperatures $<$ 500 °C, it is possible to identify gold-related peaks after the etching process; therefore, not all the gold had emerged to the surface after 1 h and probably it was on its way to the surface.

In the case of samples heated during the sputtering growth (*in situ*), the films showed gray colorations for RT and 300 °C, whereas they had a goldish color on the surface upon extraction from the sputtering chamber for 400 and 500 °C. In order to perform the XRD study, the gold layer was also selectively removed by KI etching. For the *in situ* treatment, the SiGe maxima showed narrower FWHM than in the *ex-situ* samples (see Figure **1S.b**. and Table **I S**). The crystallization process seems to be more effective in the *in-situ* case, since the crystallite size, as calculated by the Scherrer formula (assuming the same constant for all the calculations), is bigger. The *in-situ* films were also found to be preferentially oriented along the [111] direction. At 500 °C, no diffraction maxima related to the gold could be detected.

Electronic Supplementary Information:

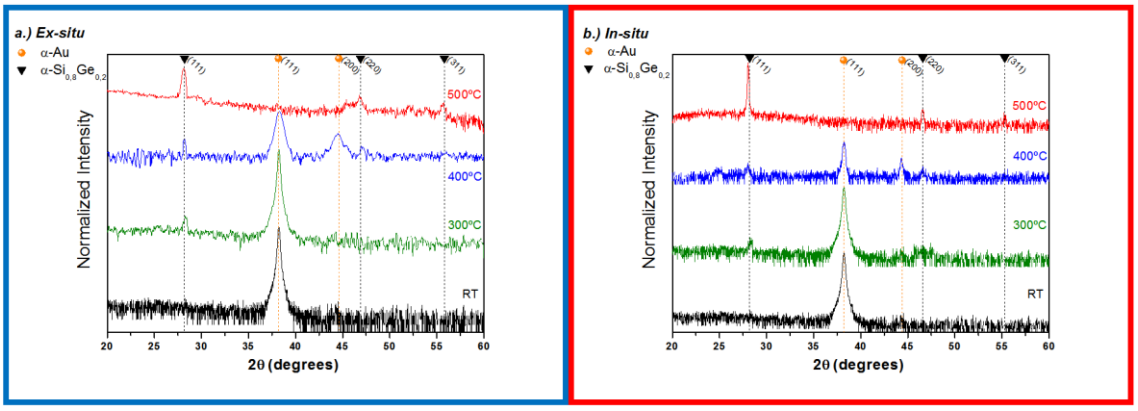

Figure 1S. XRD spectra of thin films deposited: (a) *Ex-situ* post annealed for one hour at the indicated temperatures; (b) *In-situ* grown films at the indicated temperatures. The diffraction peaks for (●) α-Au and (▼) α- $Si_{80}Ge_{20}$ phases are indicated in dashed lines.

Table I S. Approximate crystallite size calculated using the Scherrer formula [3] for (111) gold and (111) $Si_{0.8}Ge_{0.2}$ peaks of the films.

Temperature (°C)	Crystallite size SiGe (nm)		Crystallite size Au (nm)	
	Ex-situ	*In-situ*	*Ex-situ*	*In-situ*
RT	--	--	44	35
300	21	16	35	28
400	25	24	28	36
500	34	71	--	--

To confirm if all the gold had been removed from the Si–Ge surface after the etching, *SR-GIXRD* was performed in a synchrotron for both the 500 °C films (*Figure* ***2S***). These results were double checked and the evidence that no gold trap was present in the $Si_{0.8}Ge_{0.2}$ layer was determined through depth profiling by *XPS*. From these analyses, it can be concluded that for the *ex-situ* sample all the eutectic nanoparticles did not reach the top, but instead some remained embedded in the SiGe matrix, as can be observed in the depth profile. In principle, at depths of 171 nm and below, no gold can be detected by this technique within the resolution limit.

S2. Synchrotron Radiation Grazing Incidence X-Ray Diffraction (*SR-GIXRD*) diffractograms

Figure **2S** shows both diffractograms. As can be observed, the gold diffraction maxima are dominant in the *ex situ* treated sample – indicating that not all the gold was removed; whereas the *in situ* sample shows $Si_{0.8}$–$Ge_{0.2}$ peaks to be mainly oriented along the [111] direction. In the case of samples deposited at temperatures of 500 °C, the diffraction peak intensities at (111), located at $2\theta = 25.33°$ for the synchrotron radiation source, are higher than the intensities of samples treated *ex situ*. The orientations of the samples were studied by calculating the Harris texture coefficients. The texture coefficients ($TC_{(hkl)}$) were determined using the following equation:

Electronic Supplementary Information:

$$TC_{(hkl)} = \frac{\frac{I_{(hkl)}}{I^0_{(hkl)}}}{\frac{1}{N}\sum\frac{I_{(hkl)}}{I^0_{(hkl)}}} \quad (1)$$

where $I_{(hkl)}$ and $I^0_{(hkl)}$ are the intensity of the diffraction maxima observed in the experimental X-ray diffractogram and the intensity value obtained from the data sheet (JCPDS 04-016-6750 - wavelength 1.3775 Å), respectively, and N is the number of reflections used in the analysis.

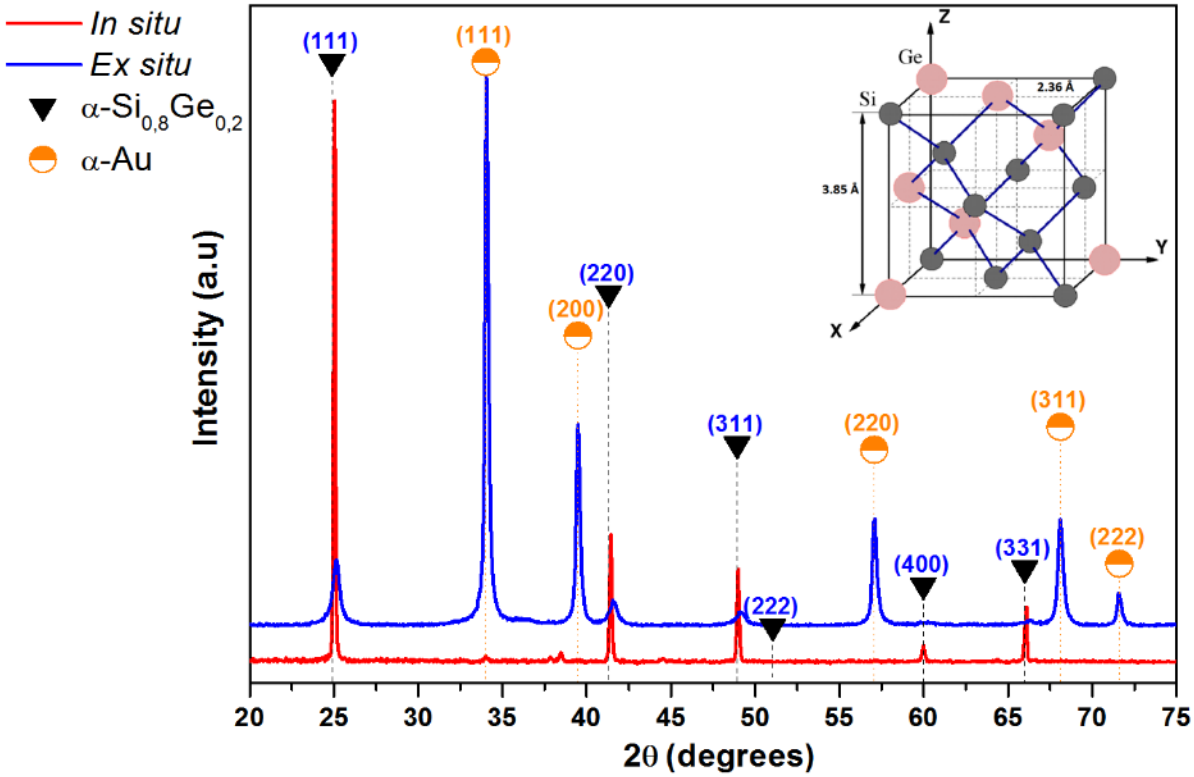

Figure. 2S Synchrotron radiation *SR-GIXRD* diffractograms measured at 1.3775 Å wavelength for *ex-situ* (blue) and *in-situ* (red) samples, with heat treatments at 500 °C. The heights of the intensities in dotted lines correspond to the Si–Ge phase intensity values given in the JCPDS 04-016-6750 data sheet. The inset shows the calculated lattice parameters for the Si-Ge films.

The standard deviations given in Table **II S** confirm that the samples deposited at 500 °C were highly oriented in the (111) direction, showing a higher preferential orientation in the *in situ* treated samples than in the *ex situ* treated. Hence, we can conclude that the golden appearance of the *ex situ XRD* corresponds to gold particles that did not reach the top surface yet.

Electronic Supplementary Information:

Table II S. Harris coefficients of the Si–Ge samples treated at 500 °C

	(hkl)	I*(hkl)*	I^0*(hkl)*	*TC (hkl)*	**Standard deviation**
Ex-situ	(111)	1201	999	1.20	0.20
	(220)	474	590	0.47	
	(311)	257	323	0.25	
In-situ	(111)	8800	999	1.58	0.42
	(220)	2010	590	0.61	
	(311)	1446	323	0.81	

***S3. X-ray Photoelectron Spectroscopy* analysis**

From the above information, it can be deduced that the gold layer migrates from the bottom of the $Si_{0.8}Ge_{0.2}$ film to the top during the MIC process. Thus, it is important to know at this stage if there is any gold trap inside the $Si_{0.8}Ge_{0.2}$ layer, preventing it from emerging to the surface. For this purpose, an in-depth profiling by *XPS* was performed on both the 500 °C samples with the gold layer on top.

Figure **3.1S** shows the *XPS* survey spectrum for $Si_{0.8}Ge_{0.2}$ thin films. The peaks at 29.1 eV, 84 eV, 99.4 eV, and 190.4 eV correspond to Ge 3d, Au 4f, Si 2p, and B 1s binding energies, respectively. Calculations of the peak areas without the B 1s and Au 4f contributions give an atomic ratio of Si : Ge = 0.804 : 0.196, which confirms the stoichiometry of $Si_{0.8}Ge_{0.2}$ in the film.

Figure **3.1S** shows the *XPS* survey spectrum for the surface of $Si_{0.8}Ge_{0.2}$. The peaks corresponding to the different transitions of Ge, Si, Au, and B are marked in the figure.

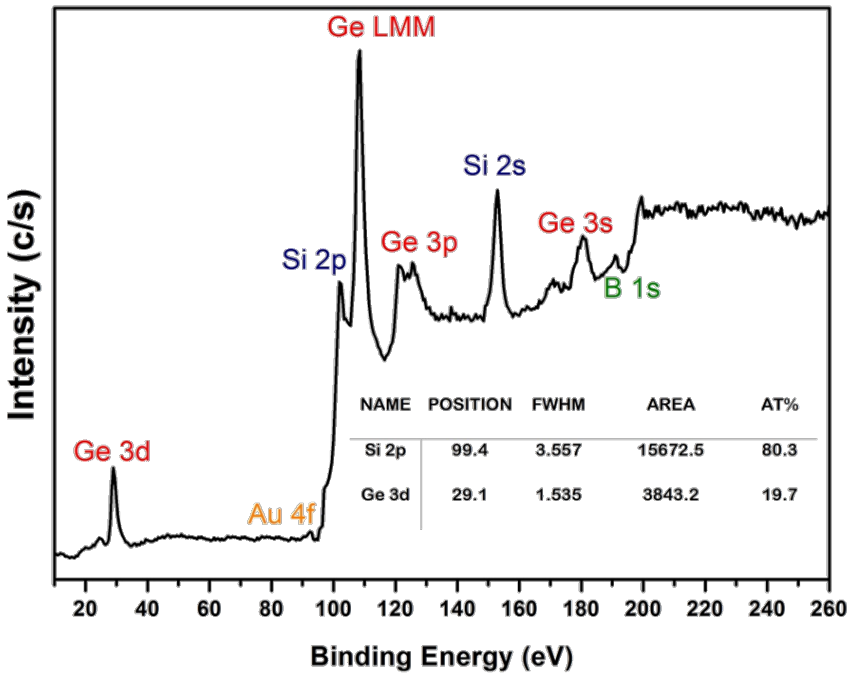

Electronic Supplementary Information:

Figure 3.1S. XPS survey spectrum for the surface of $Si_{0.8}$–$Ge_{0.2}$. The peaks corresponding to the different transitions of Ge, Si, Au, and B are marked in the figure.

Figure **3.2S.a** shows the peak shift, relative to gold, of the binding energy for the three different samples, i.e., *in situ*, *ex situ*, and 25 nm gold layer samples. The Au $4f_{5/2}$ and Au $4f_{7/2}$ peaks for pure metallic Au are observed at a binding energy of 84 eV, with a spin orbit splitting at 3.82 eV for 25 nm thin films of gold. There was a chemical interaction between the gold and the Si–Ge films during the *ex situ* heating process, possibly associated with the formation of Si–Au and/or Ge–Au eutectics. In the *in situ* case, there was almost no peak shift in binding energy – very similar to pure gold. At a surface temperature of 500 °C, the Au $4f_{5/2}$ and Au $4f_{7/2}$ presented a shoulder, unlike in the pure Au peaks. The presence of the shoulder is attributed to the existence of the Au–Si and Au–Ge eutectics.

Figure **3.2S.b** shows an in-depth profile of the gold *XPS* signal recorded for a sample treated *ex situ* at 500 °C before the gold etching. Gold was found on the sample surface, also confirming the results obtained by *SR-GIXRD*. The quantity of gold was estimated to be around 4% (*ex situ* samples), which explains why small diffraction maxima corresponding to gold are observed. However, clear maxima are observed when the samples are analyzed by *SR-GIXRD* in the synchrotron. The quantity of gold was observed to decrease while going more in depth in the XPS analysis upon Ar^+ etching of the samples. At a depth of about 40 nm from the surface, the quantity of the gold is below 1%. At depths > 100 nm, gold detection is under the resolution limits of the techniques. It can be concluded for the *ex-situ* sample, that the eutectic nanoparticles did not reach the top but remained embedded in the Si–Ge matrix, as can be observed in the depth profile. In principle, at depths of 171 nm and below, no gold could be detected within the resolution limit of this technique.

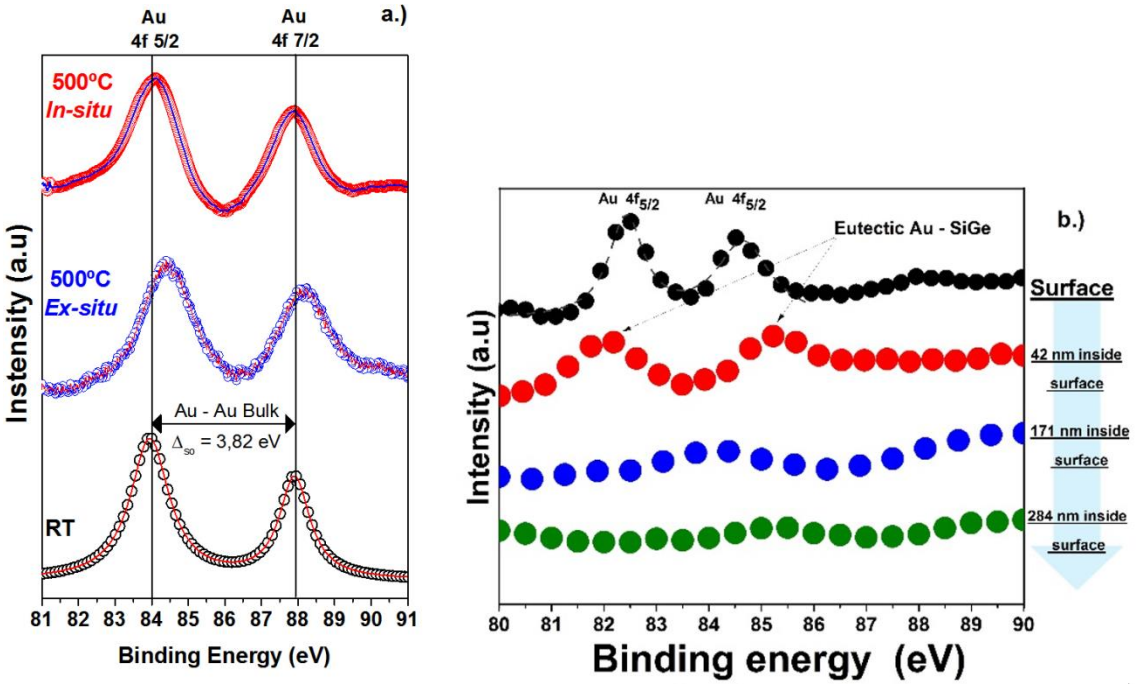

Figure 3.2S. a) *XPS* spectra of the core-level Au 4f measured at 500 °C for the *in-situ*, *ex-situ*, and a 25 nm gold layer grown on glass substrate for comparison purposes. b) *XPS* spectra

Electronic Supplementary Information:

corresponding to gold 4f peaks at different film depths from the surface for the *ex-situ* sample heated at 500 °C.

Electronic Supplementary Information:

S4. Raman Spectra Analysis

Figure **4S** shows the Raman spectra of the *in-situ* (red) and *ex-situ* (blue) films obtained at different temperatures. Three main vibrational modes corresponding to the first order Raman scattering, attributed to the phonon vibrations of Ge–Ge, Si–Ge, and Si–Si bonds, were detected. The samples deposited on gold/glass at room temperature (see Figure **4S.*a*** and ***e***) present broad bands centered at 250, 305, and 450 cm^{-1}, which are associated to amorphous Ge–Ge, Si–Ge, and Si–Si bond vibrations, respectively. The broadness of these vibrational bands confirms that the samples were amorphous. As shown in Figure **4S. *b*** and ***f*,** the samples treated at 300 °C have sharp peaks corresponding to the Ge–Ge, Si–Ge, and Si–Si bonding vibrations, and their presence confirms that the samples are crystallizing. The peaks become narrower as the temperatures are increased. Moreover, the Si–Si vibrational peak shows a clear red shift for the highest temperature (500 °C) of the *ex-situ* samples. This shift may be related to the formation of silicon-rich clusters. Moreover, the relative intensities and frequencies corresponding to the main peaks are strongly dependent on the alloy composition.

A closer look at the Si–Si peak reveals that it is, in fact, a convolution of two peaks; a very narrow peak corresponding to the Raman spectrum of crystalline silicon-rich SiGe, and a broader, smaller peak corresponding to the Si–Si vibrations typically found in $Si_{0.8}Ge_{0.2}$. This could be an indication that silicon is partially segregated from the *ex-situ* sample. The peaks observed in the *in-situ* samples are narrower than those of the *ex situ* annealed samples, which confirms the high degree of crystalline order.

Furthermore, these results clearly indicate that whereas in *ex situ* treatment the crystallization started at 300 °C, the crystallization onset is lower for *in situ* treatments. It is interesting to note that in the 400–500 cm^{-1} region secondary modes started to appear at high temperatures. These modes might be associated with the formation of a compositional gradient due to the segregation of Si and Ge, which promotes predominant Si cluster formation embedded in the SiGe matrix.

Electronic Supplementary Information:

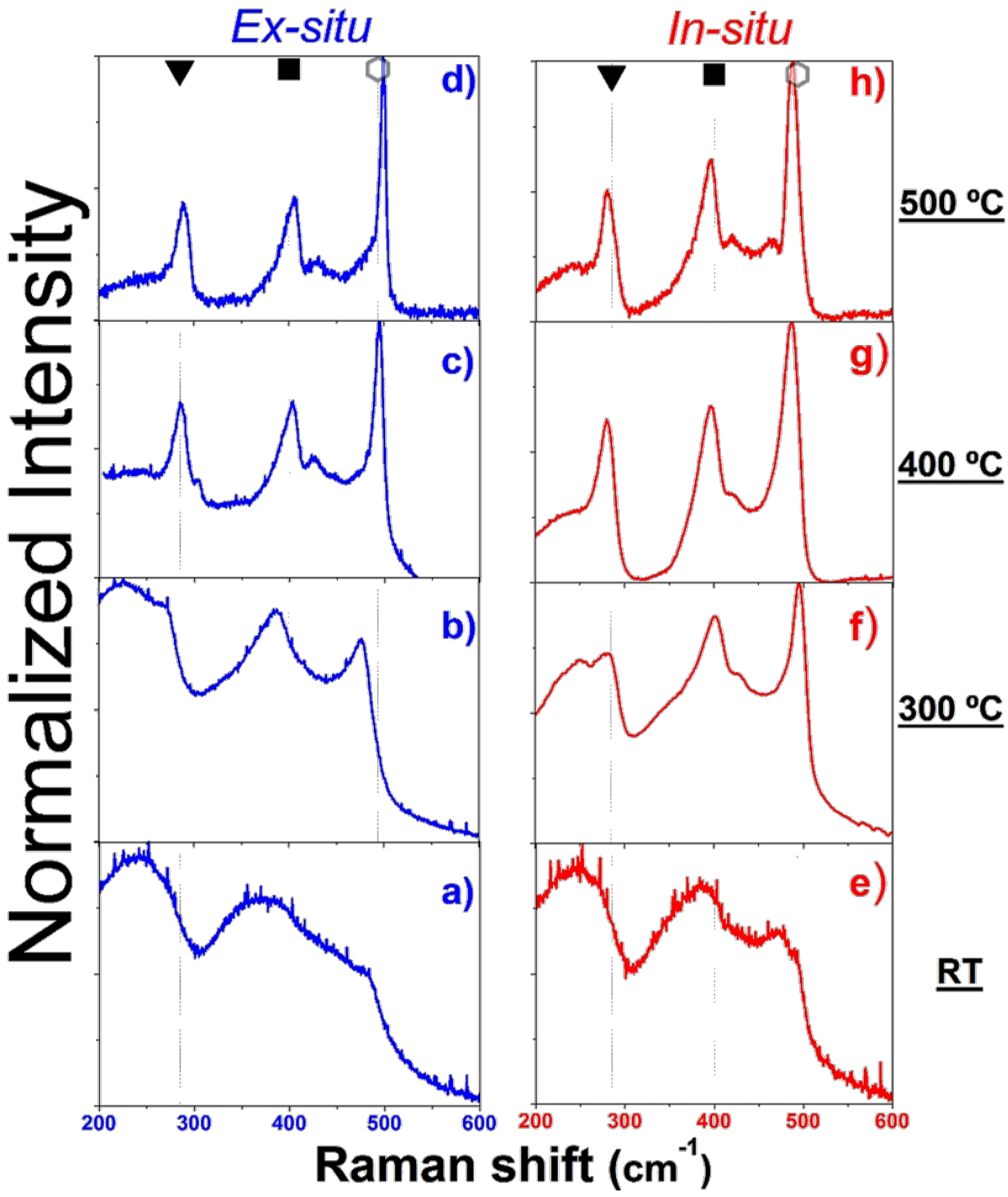

Figure 4S. Raman spectra of thin films deposited on gold/glass: *ex situ* thermal treatment (in blue: a, *b, c,* and *d*), and *in situ* thermal treatment (in red: *e, f, g,* and *h*). The expected vibrational bands corresponding to Ge–Ge, Si–Si, and Si–Ge bonds are marked on the figure.

Electronic Supplementary Information:

References

[1] Basu R, Bhattacharya S, Bhatt R, Roy M, Ahmad S, Singh A, Navaneethan M, Hayakawa Y, Aswal D and Gupta S Improved thermoelectric performance of hot pressed nanostructured n-type SiGe bulk alloys *Journal of Materials Chemistry A* **2** 6922-30 (2014)

[2] Cristina V. Manzano B A, Miguel Muñoz Rojo, Yee Rui Koh, Stephen L. Hodson, Antonio M. López Martinez, Xianfan Xu, Ali. Shakouri, Timothy D. Sands, Theodorian Borca-Tasciuc and Marisol Martín-González Anisotropy effect on the thermoelectric properties of highly oriented electrodeposited Bi_2Te_3 films *Scientific Reports **6**, 19129 (*2016)

[3] Patterson A The Scherrer formula for X-ray particle size determination *Phys. Rev.* **56** 978 (1939)

[4] Wilson A A, Muñoz Rojo M, Abad B, Perez J A, Maiz J, Schomacker J, Martín-Gonzalez M, Borca-Tasciuc D-A and Borca-Tasciuc T Thermal conductivity measurements of high and low thermal conductivity films using a scanning hot probe method in the 3 ω mode and novel calibration strategies *Nanoscale* **7** 15404-12 (2015)

PAPER III

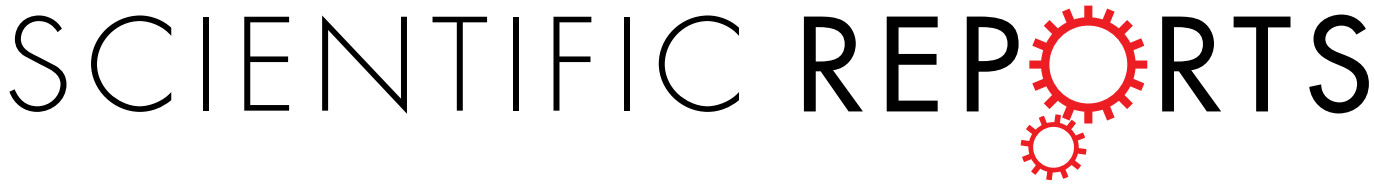

OPEN

Ultra-low thermal conductivities in large-area Si-Ge nanomeshes for thermoelectric applications

Received: 16 April 2016
Accepted: 15 August 2016
Published: 21 September 2016

Jaime Andres Perez-Taborda[1], Miguel Muñoz Rojo[1], Jon Maiz[1], Neophytos Neophytou[2] & Marisol Martin-Gonzalez[1]

In this work, we measure the thermal and thermoelectric properties of large-area $Si_{0.8}Ge_{0.2}$ nano-meshed films fabricated by DC sputtering of $Si_{0.8}Ge_{0.2}$ on highly ordered porous alumina matrices. The $Si_{0.8}Ge_{0.2}$ film replicated the porous alumina structure resulting in nano-meshed films. Very good control of the nanomesh geometrical features (pore diameter, pitch, neck) was achieved through the alumina template, with pore diameters ranging from 294 ± 5nm down to 31 ± 4 nm. The method we developed is able to provide large areas of nano-meshes in a simple and reproducible way, being easily scalable for industrial applications. Most importantly, the thermal conductivity of the films was reduced as the diameter of the porous became smaller to values that varied from $\kappa = 1.54 \pm 0.27\,W\,K^{-1}m^{-1}$, down to the ultra-low $\kappa = 0.55 \pm 0.10\,W\,K^{-1}m^{-1}$ value. The latter is well below the amorphous limit, while the Seebeck coefficient and electrical conductivity of the material were retained. These properties, together with our large area fabrication approach, can provide an important route towards achieving high conversion efficiency, large area, and high scalable thermoelectric materials.

Silicon based materials and alloys have been successfully used to satisfy the latest technological challenges of our society[1,2]. Silicon has several advantages, such as a low cost, abundance, non-toxic properties and easy industrial scalability. Silicon and Germanium present distinct and interesting transport properties. However, composites made of silicon-germanium (Si-Ge) have resulted in an improvement in terms of their transport properties. Currently, these alloys are used in different applications, such as microelectronic devices and integrated circuits, photovoltaic cells, and thermoelectric applications[3–5]. With respect to thermoelectricity, in the last decades Si-Ge has attracted significant attention as an energy harvesting material, for powering space applications[6–8]. Thermoelectric materials transform heat into electricity, and vice-versa, by means of the Seebeck and Peltier effects[9,10]. However, the use of these materials for energy harvesting is limited by their poor efficiency and high prices in comparison to other technologies. This efficiency is quantified by the dimensionless figure of merit, $zT = \frac{S^2\sigma}{\kappa}T$, which depends on the electrical conductivity (σ), Seebeck coefficient (S) and the thermal conductivity (κ) of the material at a temperature T[10,11]. Two different approaches are commonly used to increase the efficiency of those materials: *i*) the enhancement of the power factor ($S^2\sigma$) or/and *ii*) the reduction of the thermal conductivity (κ), while trying not to alter the other fundamental transport properties of the material. Generally, not only for Si-Ge films but also for different materials, the second approach is the one employed the most. Nanostructuring has been proven theoretically and experimentally to be a successful way to reduce significantly the thermal conductivity of materials[2,12–14]. A series of strategies (described in theoretical and experimental works) to reduce the thermal conductivity of nanoscale channels are currently employed, i.e. the use of superlattice or superlattice-like geometries[15–18], engineering the surface roughness[19–24], the use of core-shell channels or channel coating[25,26], twinning superlattice channels[27], channel surface decoration and amorphization techniques, periodic channel width-modulation[28–33].

Regarding the Si-Ge alloy, a stoichiometry of $Si_{0.8}Ge_{0.2}$ and crystalline orientation along (111) direction has been shown to provide the lower thermal conductivities and higher thermoelectric conversion efficiencies[2,11]. For bulk Silicon and Germanium, the room temperature thermal conductivities are ~140 $W\,K^{-1}m^{-1}$ and ~60 $W\,K^{-1}m^{-1}$ respectively[34,35]. However, Si-Ge alloys provide a significant reduction in thermal conductivity. Depending on the germanium content in silicon, values ranging from ~20 to ~9 $W\,K^{-1}m^{-1}$ can be achieved

[1]Instituto de Microelectrónica de Madrid (IMM-CSIC), Calle de Isaac Newton 8, Tres Cantos, 28760 Madrid, Spain. [2]School of Engineering, University of Warwick, Coventry, CV4 7AL, UK. Correspondence and requests for materials should be addressed to M.M.-G. (email: marisol@imm.cnm.csic.es)

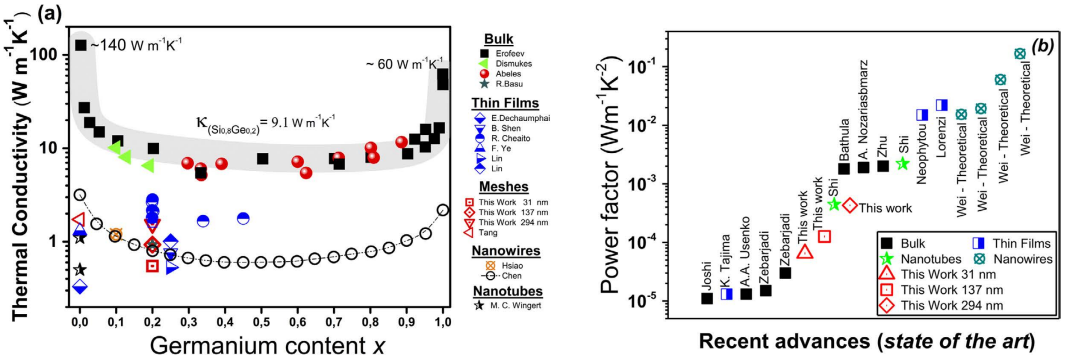

Figure 1. Literature reported (**a**) thermal conductivity values for Si-Ge structures versus germanium content[36,37,39–41,43,53,54,80–82] and (**b**) the state of the art of the power factor for $Si_{0.8}Ge_{0.2}$ structures.

for bulk samples. The lowest value at room temperature thermal conductivity is achieved for an alloy with 20% germanium concentration in silicon (~9 W $K^{-1}m^{-1}$), as expected, which however, is still large for thermoelectric applications. In order to reduce the thermal conductivity on these structures even more, advanced materials engineering is desired, which could limit the transport of phonons more effectively. Some examples consist of nanostructuring bulk samples with still high level of crystallinity, which largely increases phonon-boundary scattering[36], or the fabrication of multilayered films whose interfaces increase phonon scattering[37], among others. Recent works in nanostructured $Si_{0.8}Ge_{0.2}$ films grown through Metal Induced Crystallization (MIC)[38], have been able to achieve thermal conductivity values down to ~1.2 W $K^{-1}m^{-1}$ at room temperature. The reduction in thermal conductivity associated with the scattering alloying is ~9$Wm^{-1}K^{-1}$ for $Si_{0.8}Ge_{0.2}$[39–41]. Figure 1a shows a summary of the thermal conductivity of bulk (grey area) and nanostructures (square area) of silicon germanium as reported in the literature versus germanium content. This figure, based on previous theoretical and experimental studies on the Si-Ge alloys, shows that thermal conductivity of the alloy decreases drastically when the Ge concentration increases up to 20%, while it is approximately constant when the Ge concentration varies from 20% to 80%, exhibiting a U-shape dependence on Ge concentration[42,43]. This justifies the use of 20% Ge in most works that target thermal conductivity reduction. Figure 1b presents the state of the art values of the power factor achieved for $Si_{0.8}Ge_{0.2}$ structures[44–52]. For further phonon transport engineering, different technological strategies such as the fabrication multilayers and channel with reduced dimensionality such as nanotubes[53] and nanowires[54] have achieved significant reductions in the thermal conductivity.

A relatively new approach is to employ nano-meshes and vary the geometry of the mesh to alter the thermal conductivity. For that purpose, we fabricated pores in Si-Ge films as shown in Fig. 2. Silicon nano-meshed films with different pore diameters and highly ordered pore placement were grown previously using lithography process[55]. The lower thermal conductivity achieved was 1.73 W $K^{-1}m^{-1}$, corresponding to a silicon nano-mesh film with pore diameters of 55 nm. The effect of phonon confinement within the hollow structure and the coherent effects involved resulted in a thermal conductivity reduction of 99% in comparison to bulk silicon (~140 W $K^{-1}m^{-1}$). Theoretical works[56,57] that study the effects of the porosity and roughness of silicon nano-meshed films also predict that the thermal conductivity of these structures can be significantly reduced in the presence of pores with roughened surfaces. However, the drawback of these films is the high cost and time consuming of the fabrication process. Moreover, since they are obtained in small areas, their thermal transport properties must be measured in specific microchips and might also present limitations in some applications.

In this work, $Si_{0.8}Ge_{0.2}$ nano-mesh films were grown via sputtering process on different diameter porous alumina substrates in large sizes of the order of cm^2. During the sputtering growth, the $Si_{0.8}Ge_{0.2}$ films replicated the geometry of the porous alumina, giving rise to nano-meshed films in a quick, simple, and cheap way in comparison to other techniques[55]. Importantly, these matrices present high order and stability making them easy to handle. Thermal conductivities of 1.54 ± 0.27 W $K^{-1}m^{-1}$, 0.93 ± 0.15 W $K^{-1}m^{-1}$ and the ultra-low 0.55 ± 0.10 W $K^{-1}m^{-1}$ were found for our nano-meshed films with porous diameters of 294 ± 5 nm, 162 ± 11 nm and 31 ± 4 nm, respectively. Consequently, the geometry-dependent variation of the thermal conductivity observed for these nano-meshed films, opens the door for thermal engineering of these structures to achieve pre-specified thermal conductivities.

Sample fabrication and measurement techniques

In order to fabricate nano-meshed films, porous alumina matrices (AAO) highly oriented and with different pore diameters ranging from 436 ± 16 nm to 31 ± 4 nm were fabricated by different anodization procedures, as shown in refs 58 and 59 (see *Supporting Information*). Figure 2a–c show Scanning Electron Microscopy (SEM) images of the three different templates obtained, with 436 ± 16 nm, 162 ± 11 nm and 31 ± 4 nm diameters respectively. Then, these templates were used as substrates during the sputtering process, whose growing conditions are explained below in *Methods section*. The sputtered $Si_{0.8}Ge_{0.2}$ films replicated the porous structure of the alumina, resulting in the nano-meshed films with different pore sizes. This fabrication process allows growing large areas of $Si_{0.8}Ge_{0.2}$ nano-meshed films in a simple and reliable way, and can be easily industrially scalable. Figure 2d–f show the top view of the nano-meshed films that have replicated the pores of the alumina. In Fig. 2g–i the cross section

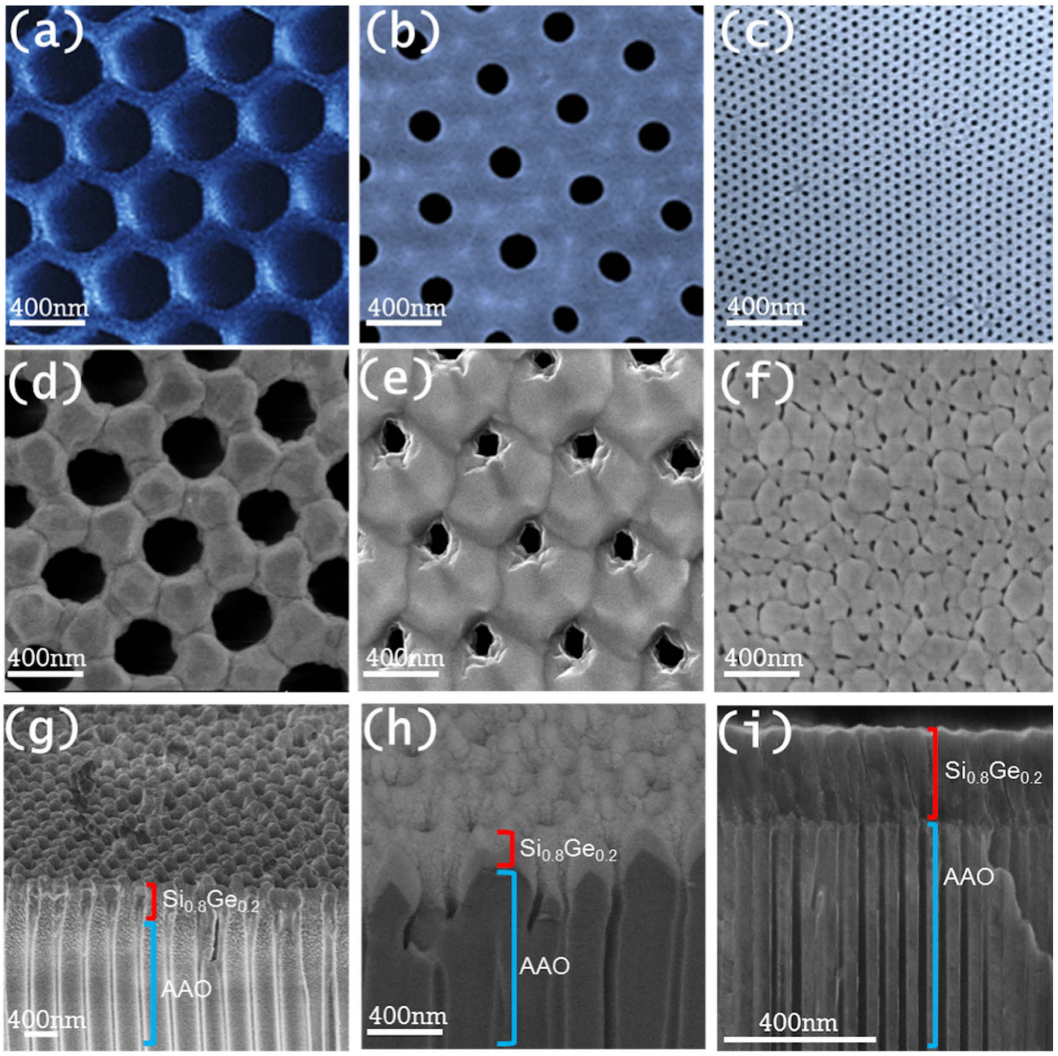

Figure 2. (**a–c**) are SEM images of porous alumina templates with 436 ± 16 nm, 162 ± 11 nm and 31 ± 4 nm diameters, respectively, that were used as substrates in the sputtering process. (**d–f**) show SEM images of the sputtered $Si_{0.8}Ge_{0.2}$ nano-meshed films grown on the previous templates, which have replicated the porous alumina. (**g–i**) are SEM images of the lateral of these samples, where the $Si_{0.8}Ge_{0.2}$ films and the alumina matrix can be observed.

view of these structures can be observed. The thickness of our $Si_{0.8}Ge_{0.2}$ films can be controlled depending on the time of the deposit (10 Å/s). Even for large thicknesses, ~3 μm, the replication of the pore structure is conserved. The porosity, diameter and distance between porous are summarized in Table 1 for both the alumina matrices and the nano-meshed films. (In Table 1, the smallest porous size of the Si-Ge film is not shown. Probably there is a huge dispersion (as seen from SEM image) but it might be interesting to show at least an average value (~31 nm).) It can be observed that the pore diameter and the porosity of the $Si_{0.8}Ge_{0.2}$ nano-meshed is slightly reduced from the pristine alumina template (AAO). The reason is that during the growing process, the $Si_{0.8}Ge_{0.2}$ prefers to replicate the structure widening the alumina template a bit and so reducing the pore size. In all the templates prepared during this study, the porous geometry is conserved, and the $Si_{0.8}Ge_{0.2}$ pores do not collapse.

All nano-meshed Si-Ge films were oriented along the [111] direction, as revealed from X-Ray measurements (see *Supporting Information*). Raman spectra showed the three characteristic vibrational modes obtained for polycrystalline Si-Ge. The composition of these films was studied by X-Ray Photoemission Spectroscopy (XPS), resulting in the optimum stoichiometry of $Si_{0.8}Ge_{0.2}$ for all the samples. Moreover, an in-depth profile of the nano-meshed films, showed a small migration of oxygen from the alumina to the film, resulting in less of 7% of oxygen content in the film. The structure of the $Si_{0.8}Ge_{0.2}$ is zinc-blende[60]. The micro-Raman spectroscopy shows a homogenous phase in all the film (see *Supporting Information*). Additionally, the surface potential of the $Si_{0.8}Ge_{0.2}$ nano-meshed films was studied by Kelvin Probe Microscopy (KPM) (see *Supporting information*). Figure 3 shows the image for 294 ± 5 nm porous size nano-meshed film, which presents a homogeneous profile of the surface potential. It indicates that the work function of the films is homogeneous (confirming the homogeneity in the chemical composition obtained by Raman) and no potential drop is observed at the grain boundaries.

Sample	Pore Diameter (nm)	Pore distance (nm)	Porosity %	Roughness (nm)
(a) AAO	436 ± 16	508 ± 22	51 ± 2	95 ± 8
(b) AAO	162 ± 11	480 ± 16	11 ± 1	75 ± 9
(c) AAO	31 ± 4	61 ± 1	13 ± 2	15 ± 4
Si-Ge Film	0	0	0	5.2 ± 2
(d) Si-Ge	294 ± 5	513 ± 8	30 ± 2	53.3 ± 7
(e) Si-Ge	137 ± 8	477 ± 16	5 ± 1	35 ± 3
(f) Si-Ge	19 ± 11	55 ± 13	3 ± 1	15 ± 4

Table 1. Summary of the geometrical properties observed for both the pristine alumina templates and the $Si_{0.8}Ge_{0.2}$ nano-meshed films grown on top. The Si-Ge film has been added for comparison purposes.

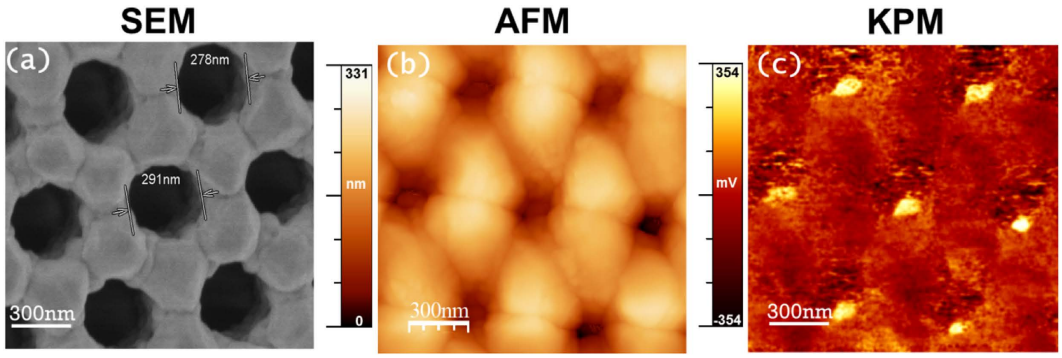

Figure 3. (**a**) SEM image of a $Si_{0.8}Ge_{0.2}$ nano-meshed film of ~294 nm porous size. (**b**) Topography by AFM And (**c**) surface potential image by KPM. The uniformity in the contrast of the KPM image reveals homogeneity in the surface potential of the film.

The fundamental thermal transport properties of the Si-Ge nano-meshed films were measured with three different setups. We measure the *out-of-plane* thermal conductivity at room temperature using a Scanning Thermal Microscope (*SThM*) working in *3ω*-mode, as shown in ref. 61. In this method, a thermo-resistive probe is brought into contact to the surface of the sample. When the probe contacts the sample, a heat flux flows through it. Depending on the thermal conductivity of the sample, the heat flux rate will be different, and so the temperature of the probe. As it is a thermo-resistive element, variations in the temperature of the probe involve changes in the electrical resistance of the probe. The third harmonic of the voltage response of the probe, $V_{3\omega}$, can be correlated with the thermal properties of the sample under study, as shown in ref. 61 This technique has been successfully used to measure the thermal conductivity of nano-structures, such as films[61,62] and nanowires[63–65]. For that purpose, a thermo-resistive probe called Wollaston was set on the head of a Nanotec® AFM system, which was used to position the probe on top of the samples[61]. Then, the third harmonic voltage response of the probe ($V_{3\omega}$) at low frequencies (10 Hz) was recorded with a lock in amplifier from Zurich Instruments®. Using this voltage signal, and after a proper calibration of the probe, the thermal conductivity of the sample can be calculated, as shown in ref. 61. The Supporting information summarizes the parameters and conditions used to measure these films.

Next, the *in-plane* electrical conductivity and Seebeck coefficient of both continuous and nano-meshed films prepared under the same conditions were measured with a home-built four probe system at room temperature, which has been previously successfully used to measure other samples (see *Supporting Information*). The home-made system consists of four electrical probes and two Peltier modules at the bottom. The electrical conductivity of the nano-meshed was carried out using the four probes of the system and the Van der Pauw method[66]. The Seebeck coefficient was measured by applying a temperature difference along the sample while measuring the voltage drop with two probes.

Results and Discussion

Figure 4a (left axis) shows the thermal conductivity results obtained at room temperature for the nano-meshed films with pore diameters ranging from 294 ± 5 nm to 31 ± 4 nm. The thermal conductivity reduction of the $Si_{0.8}Ge_{0.2}$ nano-meshed films varies from 1.54 ± 0.27 W $K^{-1}m^{-1}$ for the 294 ± 5 nm nanopore film, down to 0.55 ± 0.10 W $K^{-1}m^{-1}$ for the 31 ± 4 nm nanopore film. This figure reveals that the thermal conductivity of the nano-meshes can be engineered by the diameter of the pores (or alternatively the distance between the pores–and can be controlled in a linear fashion), while still keeping a higher order of crystallinity. At the left side of the figure, inside the dashed box, for comparison we show the thermal conductivity of a polycrystalline $Si_{0.8}Ge_{0.2}$ film without pores, grown under the same conditions as the nanomeshes, but on a $SrTiO_3$ substrate (rather than the alumina template). The thermal conductivity of this polycrystalline $Si_{0.8}Ge_{0.2}$ film is 1.22 ± 0.21 W $K^{-1}m^{-1}$ (slightly lower than the nano-meshed material with 294 ± 5 nm nanopore diameter). This is not completely surprising as

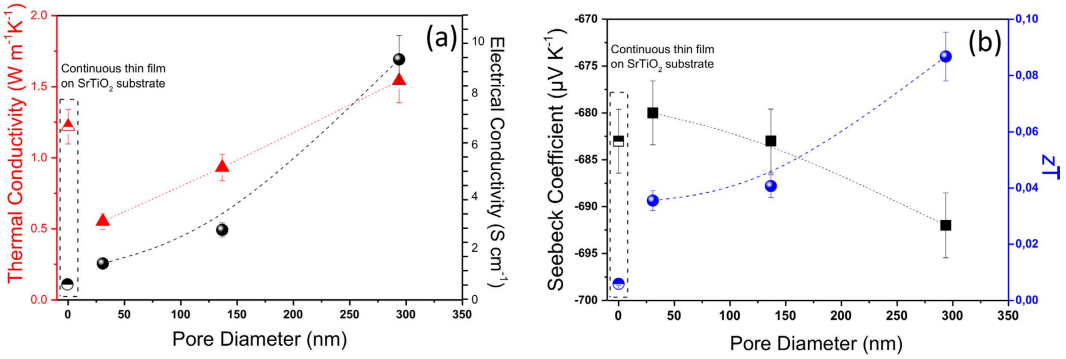

Figure 4. (**a**) Thermal conductivity (κ, red triangles) and electrical conductivity (σ, black spheres) and (**b**) Seebeck coefficient (S, black squares) and figure of merit (zT, blue spheres) plotted versus the pore diameter of the nano-mesh. The transport properties results obtained for a $Si_{0.8}Ge_{0.2}$ continuous thin film on $SrTiO_3$ substrate grown under the same conditions are also plotted (the bullets/shapes inside the dotted rectangle on the left of each graph).

the continuous film is grown on a different substrate so it will present slightly different nanocrystals sizes than the nano-meshed film due to the difference in the way its nucleates, for example, but it provides an indication that large diameter holes (distanced further away from each other) might not affect the thermal conductivity significantly, but as the diameter (and the pitch) is reduced, this property is reduced significantly.

In order to explain the dependence of the thermal conductivity of our $Si_{0.8}Ge_{0.2}$ nano-meshed films with the diameter of the pores, the different phonon scattering mechanisms that play a role in these structures need to be considered. In ref. 56 it was observed that the thermal conductivity of silicon nano-meshed films can suffer a strong reduction in comparison to bulk silicon. The phonon scattering mechanisms occurring in these films were studied considering Monte Carlo simulations, including Umklapp scattering, boundary scattering, and pore scattering. While the contribution of the roughness to this reduction is low, the influence of the porosity and the placement of the porous contribute largely to this reduction. In another work, Tang *et al.*[55] observed experimentally a reduction in thermal conductivity of silicon nano-meshed films when the diameter of the porous became smaller. The thermal conductivity was observed to depend on the small distances of the porous, which affect the mean free path of the phonons, the surface phonon scattering and a possible necking effect, which refers to phonons trapped in the holes/pores of the nano-meshed films that contribute to reduce the thermal conductivity. The authors showed that this last effect becomes more important as the diameter of the pore reduces.

Based on the previous theories and observations, the variation of the thermal conductivity of $Si_{0.8}Ge_{0.2}$ nano-meshed films versus the diameter of the pores, which is shown in Fig. 4, can be studied considering scattering effects similar to those occurring in the silicon nano-meshed films. For that purpose, in order to provide a first order understanding of phonon transport and the exceptionally-low thermal conductivity measured in the nano-meshes, we carried out thermal conductivity simulations based on the Callaway model theory. Using the Callaway model, the thermal conductivity is computed as follows:

$$\kappa = \frac{1}{2\pi^2 \nu_s} \frac{1}{k_B T^2} \int_0^{\omega_D} (\hbar\omega)^2 \omega^2 \frac{e^{\hbar\omega/k_B T}}{(e^{\hbar\omega/k_B T} - 1)^2} \tau(\omega) d\omega \tag{1}$$

where ν_s is the sound velocity of the material, and $\tau(\omega)$ is the phonon energy dependent relaxation time, for which in our case we include the effects of Umklapp three-phonon scattering τ_U, boundary scattering on the top-bottom interfaces of the nano-mesh τ_b, alloy scattering τ_a, scattering by the crystallite boundaries τ_d, and scattering by the pores τ_p. These are connected using Matthiensen's rule for a single relaxation time. We employ the usual formalism for all of the above mechanisms, i.e.:

$$\tau_{b/d/p}(\omega)^{-1} = \frac{(1-p)}{(1+p)} \frac{\nu(\omega)}{L_{width}}, \quad \text{where } p = 0, \text{ for fully diffusive boundaries} \tag{2}$$

$$\tau_U(\omega)^{-1} = BT\omega^2 e^{-C/T} \tag{3}$$

$$\tau_a(\omega)^{-1} = x(1-x)A\omega^4 \tag{4}$$

Above, L_{width} is the width of the material, or in general the distance between scattering interfaces, x is the Si fraction in the Si-Ge alloy, B, and C are numerical parameters used to fit the bulk material thermal conductivity[67–69], and A is analytically determined from the usual alloy/impurity atoms scattering model[70–72]. For the sound velocity, as well as the parameters in the scattering mechanisms, we average the parameters used in literature for Si and Ge according to the alloy composition.

First of all, we evaluated the thermal conductivity of bulk Si and bulk Germanium at room temperature as ~140 W $K^{-1}m^{-1}$ and ~60 W $K^{-1}m^{-1}$, respectively. We then calculated the thermal conductivity of the Si_xGe_{1-x} alloy, and validate the values we obtain with the literature values for Si_xGe_{1-x} alloys of different compositions,

especially for $x = 0.8$, which is the composition of the nano-meshes under consideration. For this calculation we included the effect of alloy scattering and phonon-phonon scattering (3-phonon Umklapp processes). Our results for $x = 0.8$ gives $\kappa \sim 9$ W/mK, which is approximately what the literature agrees on for $Si_{0.8}Ge_{0.2}$. To describe the thermal conductivity of the initial film, without the pores, we include in addition the effect of phonon scattering off the boundaries on the top and bottom of the film and the effect of phonon scattering on the boundaries of the nanocrystallites that form within the film (which form domains of ~70 nm in side lengths). In describing nanocrystalline domain boundary scattering we employ the same model as boundary scattering shown above. After this, our calculations indicate that the thermal conductivity drops to values $\kappa \sim 1.7\,W\,K^{-1}m^{-1}$. Note that in the case of boundary scattering, we assume fully diffusive boundary scattering with $p = 0$, an approximation commonly employed in the literature to describe the boundary scattering in nanostructures[73,74]. This calculated value is slightly higher than that of the largest pore diameter nano-meshed film (294 nm, $\kappa \sim 1.54 \pm 0.27\,W\,K^{-1}m^{-1}$). On the other hand, the thermal conductivity of the continuous film on $SrTiO_3$ substrate (Fig. 4a, left box), continuous film with no pores, is $\kappa \sim 1.22 \pm 0.21\,W\,K^{-1}m^{-1}$, which is somewhat lower compared to our calculations. Various reasons could be responsible for this, such as the presence of nucleation sites and clusters, and grain sizes. A more in detail information of the differences between the film grown on $SrTiO_3$ and the mesh grown on amorphous gamma-alumina can be seen in the *Supporting Information*. In addition, the film contains ~7% oxygen doping, which could provide this further reduction in the thermal conductivity, possibly by introducing an additional alloy scattering mechanism, or by introducing changes in the phonon dispersion which reduce the sound velocity. Indeed, just by lowering the sound velocity of the material by ~10% in the simulations, the thermal conductivity drops to values $\kappa \sim 1.4\,W\,K^{-1}m^{-1}$, which resides within the error bars of the measured continuous films. Whether this oxygen alloy actually reduces the sound velocity in the material, or introduces further scattering (or both) to account for the reduction in κ is still under investigation, but it seems that at first order the effects of boundary scattering and alloying significantly reduce the thermal conductivity down to $1.7\,W\,K^{-1}m^{-1}$, and possibly oxygen presence, nucleation sites/clusters, and/or smaller grains, could provide another smaller, but still significant, reduction.

We next consider the influence of the nanopores on the thermal conductivity. In the calculations, scattering off the pores is again considered in a simplified manner as in the case of boundary scattering, *i.e.* by introducing an additional phonon randomizing scattering mechanism with characteristic length the distance between the pores. In the case of nano-meshed films with pore diameters of 294 ± 5 nm and 137 ± 8 nm, the calculations show that the thermal conductivity is indeed not reduced significantly, *i.e.* it is reduced to values $\kappa \sim 1.3\,W\,K^{-1}m^{-1}$ and $\kappa \sim 1.24\,W\,K^{-1}m^{-1}$, respectively. For the largest pore diameter nano-meshed film (294 nm), the measured thermal conductivity value is $\kappa \sim 1.54 \pm 0.27\,W\,K^{-1}m^{-1}$ and the calculated value ($\kappa \sim 1.3\,W\,K^{-1}m^{-1}$) is within the measured error. Thus, both measurements and simulations indicate that the thermal conductivity is not much affected by the introduction of large diameter pores, despite the large porosity (~30%) with calculations suggesting that only a small reduction should be present. Note that the simulations used are based on models that take into account scattering in a simplified way, but still we are able to capture to a large extend the behavior of thermal conductivity in these films. More importantly, measurements and simulations are in agreement that more of the reduction of the thermal conductivity originates from alloying and boundary scattering, whereas the introduction of pores at least of large diameters does not alter this conclusion significantly.

As the pore diameter is reduced further the thermal conductivity drops (despite the fact that the actual porosity is less). For the nano-meshed films with pore diameter of 137 ± 8 nm, the measured value is $\kappa \sim 0.9\,W\,K^{-1}m^{-1}$. This is lower compared to the calculated one ($\kappa \sim 1.24\,W\,K^{-1}m^{-1}$), possibly due to more complicated effects that take place in the structure that are not captured by the simplified model we employ, or possibly due to coherent effects that reduce the sound velocity or introduce phononic bandgaps, that our semi classical model also does not capture.

Finally, as the pore diameter is reduced further, in the case of nano-meshed film with porous diameter of 31 ± 4 nm, measured thermal conductivity is $\kappa \sim 0.55 \pm 0.10\,W\,K^{-1}m^{-1}$, whereas the calculated thermal conductivity drops less to values $\kappa \sim 0.9\,W\,K^{-1}m^{-1}$, somewhat higher compared to the measured value. Considering the worst case scenario, *i.e.* the smaller feature sizes that were measured (rather than the average feature size) and that phonons scatter diffusively on boundaries defined by the smaller features (56 nm), the thermal conductivity drops to $\kappa \sim 0.8\,W\,K^{-1}m^{-1}$, still somewhat higher compared to the measured values. This indicates that densely placed pores could introduce further disorder in the lattice (see Fig. 2f), or even coherent effects that reduce the sound velocity further, or even slight transport gaps that were observed in different cases[55], which could account for this lower measured thermal conductivity and not captured by our simplified model.

In general, however, it is well described that most of the reduction in the thermal conductivity originates from the alloying and the grain-boundary scattering. The inclusion of oxygen has a smaller, but noticeable degrading effect. The introduction of pores with large feature sizes does not affect the thermal conductivity significantly, but as the feature sizes get smaller, a significant reduction can further be introduced. Still, however, in all cases the values of the thermal conductivity in both measurements and calculated data agree to be within $\kappa \sim 0.5$–$1.5\,W\,K^{-1}m^{-1}$, a significant reduction with respect to the uniform $Si_{0.8}Ge_{0.2}$ alloy, which could be largely beneficial for thermoelectric applications since the power factor still remains considerable (see Fig. 2b). Finally, other scattering effects, such as necking effect[55] or clusters formed in the several locations of the nano-meshes, might also be affecting the thermal conductivity, but were not considered here. We further note here that the structures we fabricated have some of the lowest thermal conductivities ever reported, at least for a Si-Ge based nanostructured system. Zhang *et al.* have reported slightly lower values ($0.44\,W\,K^{-1}m^{-1}$) for a multilayer Sb_2Te_3/Au system[75], whereas Chen *et al.* predicted by molecular dynamics simulations that a Si/Ge superlattice could also provide ultra-low thermal conductivities down to $\sim 0.55\,W\,K^{-1}m^{-1}$ [42]. In addition, Zhang *et al.* reported thermal conductivities of 0.5–1 $W\,K^{-1}m^{-1}$ in Bi/Bi_2Te_3 core-shell nanorods[76]. The nanomeshes presented in this work, however, provide the flexibility of cost effective fabrication of a large area material, which could be interesting for large scale applications.

Beyond the thermal conductivity, the rest of the thermoelectric coefficients, *i.e.* the electrical conductivities and the Seebeck coefficients of the nano-meshes versus the diameter of the pores, are shown in Fig. 4a,b. The electrical conductivity is larger for the larger diameter nano-meshes (even larger than that of the uniform film), and it reduces as the diameter of the pore becomes smaller by up to even an order of magnitude, approaching that of the uniform film (Fig. 4a-right axis). The reason for such behavior could be correlated to the fact that as the diameter of the pore becomes smaller the separation between pores also does (from 513 to 61 nm), as shown in Table 1, which could degrade the electronic transport. Nevertheless, the Seebeck coefficient shown in Fig. 4b (left axis) remains practically unaltered with values around $-685\,\mu V\,K^{-1}$. The power factors of the $Si_{0.8}Ge_{0.2}$ nano-meshed films varied from ~$445\,\mu W\,m^{-1}\,K^{-2}$ to ~$65\,\mu W\,m^{-1}\,K^{-2}$ at room temperature for the largest diameter pore nano-mesh (294 ± 5 nm) and the smallest one (31 ± 4 nm), respectively. Moreover, as the diameter of the pores reduces (Table 1), the power factor becomes more similar to the one obtained for the continuous film, ~$24\,\mu W\,m^{-1}\,K^{-2}$[38]. As the diameter of the pores is reduced, the porosity also reduces, and the structure starts to look more like a continuous film (with an additional scattering mechanism introduced by the pores). Moreover, it is worth mentioning that all these power factors are similar to those obtained for bulk $Si_{0.8}Ge_{0.2}$, reported in ref. 77. Finally, the values of the Figure of Merit obtained for these nano-meshes were plotted in Fig. 4b (right axis). These values are up to ~0.08 at room temperature for the nano-meshes with the larger pore diameters, which can be very useful for any industrial applications that work under this condition (room temperatures) and that require large sample areas based on an cost-effective materials and processes. Nevertheless, as explained above, the thermal conductivity is still much lower for the smaller pore diameter structures, as they are affected strongly by the scattering mechanics due to the presence of the small pores. We believe that these structures could be even more useful to thermoelectric and heat management applications once they are optimized to improve their electrical conductivity. Please also note that the zT value is just an estimation, since the power factor have been measured *in-plane* and the thermal conductivity in *out-of-plane* configuration, so we can only estimate the zT value. This assumption is only valid if this film has the same isotropic behaviors that the bulk Si-Ge alloy. In any case, we expect the in-plane thermal conductivity to be even lower, as phonons need to travel around the holes in the nanomesh.

We note that in a previous experimental study for Si nanomeshes[55], zT ~0.4 at room temperature has been achieved with thermal conductivity ~$1.73\,W\,K^{-1}m^{-1}$. In this work, however, the highest zT achieved is less than 0.1 at room temperature, resulting from the fact that the thermoelectric power factor in our system is lower. The lower power factor in our samples originates from a low electrical conductivity and a further reduction is observed as the pore diameter is reduced. While the Seebeck coefficient remains more or less unchanged and at relatively high values compared to literature. Higher power factors can be found for example in Neophytou[78]. However, it was not our intention to optimize the electrical conductivity, in this work we focused on reducing the thermal conductivity, which is significantly reduced further down to $0.55\,W\,K^{-1}m^{-1}$. Since high power factors have been previously achieved in such systems, one could think of combining the two methods (low thermal conductivity and high power factor) and achieve higher zT.

Conclusions

Large area $Si_{0.8}Ge_{0.2}$ nano-meshed films with different porous sizes were fabricated through sputtering processes using alumina matrices as templates. This provides a novel approach to grow this kind of structures in a simple and reliable way. A large reduction in the thermal conductivity was observed due to alloying, and phonon boundary scattering on the upper/lower boundaries and crystallite boundaries within the nano-meshes. This is well explained within the Callaway model assuming fully diffusive boundary scattering. The thermal conductivity additionally drops with the introduction of pores, and seems to depend on the pore diameter and the distance between the pores. The smaller the pore diameter is, the larger the thermal conductivity reduction of the $Si_{0.8}Ge_{0.2}$ nano-mesh, due to enhanced scattering on the pore boundaries and due to possibly enhanced disorder or even coherent phonon effects that could be introduced. Using this approach, it is possible to control thermal transport of these films through nano-engineering. On the other hand, the nano-meshed power factors are larger in the structures with large pores (and larger distances between pores) rather than the more disordered structures which include denser pores with smaller diameters. The power factors are found to be between $450\,\mu W\,K^{-2}m^{-1}$ and $65\,\mu W\,K^{-2}m^{-1}$, respectively, which seem to be as large as some of the last reported values for bulk $Si_{0.8}Ge_{0.2}$. This is attributed to the fact that the electrical conductivity in the nanomeshes with large inter-pore distance is much larger compared to the denser nanomeshes, whereas the Seebeck coefficient remains almost the same. Nevertheless, it is remarkable that the thermal conductivity in the small pore structures can be reduced to such low values (well below the amorphous limit in some cases), while still retain reasonable power factors, which opens the door for higher efficiency thermoelectric applications for this alloy once it is further optimized to improve its electrical conductivity.

Materials and Methods

Fabrication of highly ordered anodic aluminium oxide templates. The highly ordered hexagonal pore arrays throughout porous anodic alumina templates have been achieved by using simple two-step anodization[58]. Aluminum foils (99.999% purity, 0.5 mm thickness) supplied by Advent Research Materials (England) were first electropolished in perchloric acid/ethanol solution with a volume ratio of 1:4 for 4 min at 20 V after the cleaning and degreasing process. The first of the two anodization processes was applied to 6 h with constant voltage of 205 V at 4 °C in 1 wt% H_3PO_4 and 0.01 M aluminum oxalate (Alox) as electrolyte. The Alox is used as an additive to suppress breakdown of porous anodic alumina in the electrolyte of phosphoric acid at high potentials and comparatively high temperatures[59]. The second anodization was then performed under the same conditions as that of the first anodization after removing the disordered alumina film using the solution of chromic acid and

phosphoric acid. The length of nanocavities can vary from hundreds nanometers to hundreds of microns and is controlled simply by the time of the second anodization process. In this case the time used was 12 h. Finally, a third step was carried out in order to widening the pores up to 350 nm in pore diameter. It consists in a controlled reduction of pore walls with a phosphoric acid solution, 5 wt% at 35 °C during 3 h. For the smaller diameter pores (25–30 nm) the first and the second anodization were performed in 0.3 M H_2SO_4, 25 V, 24 h, 1–2 °C.

Material growth and Characterization Methods. Silicon Germanium thin films were grown in a lab-designed sputtering system with a base vacuum of 10^{-9} mbar. A boron doped $Si_{0.8}Ge_{0.2}$ target (99.999% purity) was bonded onto a cylindrical (4″) magnetron cathode in a vertical configuration. The growth chamber was evacuated to a base pressure of 5×10^{-9} mbar by turbo pumping, using ultrapure argon (99.9999%) as the sputtering atmosphere. DC plasma was activated with a voltage of 720V and 80mA at a pressure of 7×10^{-3} mbar. For the thermal treatment a lab-made substrate heater holder was designed, which can reach temperatures up to 750 °C. The temperature was controlled by means of a *EUROTHERM* 3216 controller and the temperature was measured by a type K thermocouple attached to the center of the sample holder surface. The crystalline structure of the films was studied by X-ray diffraction (*XRD*) using a *Philips* X-PERT diffractometer with a Cu K_α radiation source with a wavelength of 1.54 ± 0.2718 Å in Bragg-Brentano geometry. Diffraction patterns were identified by standard reference patterns, supplied by the International Centre for Diffraction Data (ICDD). Micro-Raman spectrometer (*Horiba Jobin Yvon*) LabRam HR with a 532 nm Nd:YAG laser (8.5 mW) was used for compositional mapping and local crystallization. Scanning electron microscopy has been performed on a *JEOL* JSM-6460LV and the *AFM* images were obtained with a *Nanotec*® *AFM* microscope. *XPS* spectra were recorded on a custom *Specs* X-ray Photoelectron Spectroscopy system (Hemispherical Energy Analyzer PHOIBOS 100/150). Monochromatic Al K_α (E = 1486.6 eV) emission was used as the X-ray source. The pressure of the analysis chamber was kept at 10^{-10} mbar. Survey *XPS* spectra and narrow (for recording high resolution peaks) scan *XPS* spectra were collected with pass energies of 0.5 eV and 0.02 eV, respectively. The analyzed area was approximately 1.4 mm^2. Peak analysis was performed by using Gaussian-Lorentzian convoluted bands, and a Shirley non-linear sigmoid-type baseline. All spectra were calibrated with the C1s peak located at 284.8 eV to set the binding energy scale. The data were analyzed with CasaXPS® software (*CasaSoftware* Ltd). Resistivity measurements and Seebeck coefficient were measured with a home-made four probe system, which was used to cross-check the data obtained from a commercial *Linseis*® LSR-3 system from room-temperature until 500 °C. Thermal conductivity measurements were carried out with a Scanning Thermal Microscope (SThM) working in 3ω mode[61]. More details of the measuring procedure are given in supporting information.

References

1. Cressler, J. D. *Silicon Heterostructure Handbook: Materials, Fabrication, Devices, Circuits and Applications of SiGe and Si Strained-Layer Epitaxy.* (CRC press, 2005).
2. Rowe, D. M. *Thermoelectrics handbook: macro to nano*. (CRC press, 2005).
3. Compano, R., Molenkamp, L. & Paul, D. *Technology Roadmap for Nanoelectronics*, https://cordis.europa.eu/pub/esprit/docs/melnarm.pdf (2001).
4. Seshan, K. *Handbook of thin film deposition*. (William Andrew, 2012).
5. Cressler, J. D. & Niu, G. *Silicon-germanium heterojunction bipolar transistors*. (Artech house, 2002).
6. Böttner, H. Thermoelectric micro devices: current state, recent developments and future aspects for technological progress and applications Paper presented at *Thermoelectrics, 2002. Proceedings ICT'02. Twenty-First International Conference on.* Place (IEEE, doi:10.1109/ICT.2002.1190368 (2002)).
7. Tiwari, P., Gupta, N. & Gupta, K. Advanced Thermoelectric Materials in Electrical and Electronic Applications Paper presented at *Advanced Materials Research.* Place (Trans Tech Publ, (2013)).
8. Martín-González, M., Caballero-Calero, O. & Díaz-Chao, P. Nanoengineering thermoelectrics for 21st century: Energy harvesting and other trends in the field. *Renewable and Sustainable Energy Reviews* **24,** 288–305 (2013).
9. MacDonald, D. K. C. *Thermoelectricity: an introduction to the principles*. (Courier Corporation, 2006).
10. Goldsmid, H. J. *Introduction to thermoelectricity*. Vol. 121 (Springer Science & Business Media, 2009).
11. Rowe, D. M. *CRC handbook of thermoelectrics*. (CRC press, 1995).
12. Yu, J.-K., Mitrovic, S., Tham, D., Varghese, J. & Heath, J. R. Reduction of thermal conductivity in phononic nanomesh structures. *Nature nanotechnology* **5,** 718–721 (2010).
13. Slack, G. A. & Hussain, M. A. The maximum possible conversion efficiency of silicon-germanium thermoelectric generators. *Journal of Applied Physics* **70,** 2694–2718 (1991).
14. Wacker, B. & Aguirre, M. inventors; Alphabet Energy. Inc. Nanostructured thermolectric elements and methods of making the same. United States patent US 14/059, 362, 14 Jul 2015.
15. Zhu, T. & Ertekin, E. Phonon transport on two-dimensional graphene/boron nitride superlattices. *Physical Review B* **90,** 195209 (2014).
16. Rajabpour, A. & Volz, S. Universal interfacial thermal resistance at high frequencies. *Physical Review B* **90,** 195444 (2014).
17. Xie, Z.-X., Chen, K.-Q. & Tang, L.-M. Ballistic phonon thermal transport in a cylindrical semiconductor nanowire modulated with nanocavity. *Journal of Applied Physics* **110,** 124321 (2011).
18. Aksamija, Z. & Knezevic, I. Thermal conductivity of Si 1− x Ge x/Si 1− y Ge y superlattices: Competition between interfacial and internal scattering. *Physical Review B* **88,** 155318 (2013).
19. Sullivan, S. E., Lin, K.-H., Avdoshenko, S. & Strachan, A. Limit for thermal transport reduction in Si nanowires with nanoengineered corrugations. *Applied Physics Letters* **103,** 243107 (2013).
20. Maurer, L., Aksamija, Z., Ramayya, E., Davoody, A. & Knezevic, I. Universal features of phonon transport in nanowires with correlated surface roughness. *Applied Physics Letters* **106,** 133108 (2015).
21. Moore, A. L., Saha, S. K., Prasher, R. S. & Shi, L. Phonon backscattering and thermal conductivity suppression in sawtooth nanowires. *Applied Physics Letters* **93,** 83112 (2008).
22. Martin, P., Aksamija, Z., Pop, E. & Ravaioli, U. Impact of phonon-surface roughness scattering on thermal conductivity of thin Si nanowires. *Physical review letters* **102,** 125503 (2009).
23. Boukai, A. I. *et al.* Silicon nanowires as efficient thermoelectric materials. *Nature* **451,** 168–171 (2008).
24. Hochbaum, A. I. *et al.* Enhanced thermoelectric performance of rough silicon nanowires. *Nature* **451,** 163–167 (2008).

25. Chen, J., Zhang, G. & Li, B. Impacts of atomistic coating on thermal conductivity of germanium nanowires. *Nano letters* **12,** 2826–2832 (2012).
26. Wingert, M. C. *et al.* Thermal conductivity of Ge and Ge–Si core–shell nanowires in the phonon confinement regime. *Nano letters* **11,** 5507–5513 (2011).
27. Xiong, S., Kosevich, Y. A., Sääskilahti, K., Ni, Y. & Volz, S. Tunable thermal conductivity in silicon twinning superlattice nanowires. *Physical Review B* **90,** 195439 (2014).
28. Cocemasov, A., Nika, D., Fomin, V., Grimm, D. & Schmidt, O. Phonon-engineered thermal transport in Si wires with constant and periodically modulated cross-sections: A crossover between nano-and microscale regimes. *Applied Physics Letters* **107,** 011904 (2015).
29. Termentzidis, K. *et al.* Modulated sic nanowires: Molecular dynamics study of their thermal properties. *Physical Review B* **87,** 125410 (2013).
30. Blandre, E., Chaput, L., Merabia, S., Lacroix, D. & Termentzidis, K. Modeling the reduction of thermal conductivity in core/shell and diameter-modulated silicon nanowires. *Physical Review B* **91,** 115404 (2015).
31. Nika, D. L., Cocemasov, A. I., Crismari, D. V. & Balandin, A. A. Thermal conductivity inhibition in phonon engineered core-shell cross-section modulated Si/Ge nanowires. *Applied Physics Letters* **102,** 213109 (2013).
32. Markussen, T. Surface disordered Ge–Si core–shell nanowires as efficient thermoelectric materials. *Nano letters* **12,** 4698–4704 (2012).
33. Karamitaheri, H. & Neophytou, J. A. P., 2016, to appear.
34. Bhandari, C. M. & Rowe, D. M. Boundary scattering of phonons. *Journal of Physics C: Solid State Physics* **11,** 1787 (1978).
35. Savvides, N. & Rowe, D. Altering the thermal conductivity of phosphorus-doped Si-Ge alloys by the precipitation of dopant. *Journal of Physics D: Applied Physics* **15,** 299 (1982).
36. Basu, R. *et al.* Improved thermoelectric performance of hot pressed nanostructured n-type SiGe bulk alloys. *Journal of Materials Chemistry A* **2,** 6922–6930 (2014).
37. Dechaumphai, E. *et al.* Ultralow thermal conductivity of multilayers with highly dissimilar debye temperatures. *Nano Lett.* **14,** 2448–2455 (2014).
38. Taborda, J. A. P. *et al.* Low thermal conductivity and improved thermoelectric performance of nanocrystalline silicon germanium films by sputtering. *Nanotechnology* **27,** 175401 (2016).
39. Erofeev, R., Iordanishvili, E. & Petrov, A. Thermal conductivity of doped Si-Ge solid solutions (Thermoconductivity of alloyed solid silicon- germanium solutions). *Sov. Phys.Solid State* **7,** 2470–2476 (1966).
40. Dismukes, J., Ekstrom, L., Steigmeier, E., Kudman, I. & Beers, D. Thermal and Electrical Properties of Heavily Doped Ge-Si Alloys up to 1300° K. *J. Appl. Phys.* **35,** 2899–2907 (1964).
41. Abeles, B., Beers, D., Cody, G. & Dismukes, J. Thermal conductivity of Ge-Si alloys at high temperatures. *Phys. Rev.* **125,** 44 (1962).
42. Chen, J., Zhang, G. & Li, B. Tunable thermal conductivity of Si Ge x nanowires. *Appl. Phys. Lett* **95,** 073117 (2009).
43. Cheaito, R. *et al.* Experimental Investigation of Size Effects on the Thermal Conductivity of Silicon-Germanium Alloy Thin Films. *Phys. Rev. Lett.* **109,** 195901 (2012).
44. Joshi, G. *et al.* Enhanced thermoelectric figure-of-merit in nanostructured p-type silicon germanium bulk alloys. *Nano Lett.* **8,** 4670–4674 (2008).
45. Tajima, K. *et al.* Thermoelectric properties of RF-sputtered SiGe thin film for hydrogen gas sensor. *Japanese journal of applied physics* **43,** 5978 (2004).
46. Usenko, A. *et al.* Optimization of ball-milling process for preparation of Si–Ge nanostructured thermoelectric materials with a high figure of merit. *Scripta Materialia* **96,** 9–12 (2015).
47. Zebarjadi, M. *et al.* Power factor enhancement by modulation doping in bulk nanocomposites. *Nano letters* **11,** 2225–2230 (2011).
48. Shi, L., Yao, D., Zhang, G. & Li, B. Large thermoelectric figure of merit in Si Ge x nanowires. *Applied Physics Letters* **96,** 173108 (2010).
49. Bathula, S. *et al.* Enhanced thermoelectric figure-of-merit in spark plasma sintered nanostructured n-type SiGe alloys. *Applied Physics Letters* **101,** 213902 (2012).
50. Nozariasbmarz, A. *et al.* Enhancement of thermoelectric power factor of silicon germanium films grown by electrophoresis deposition. *Scripta Materialia* **69,** 549–552 (2013).
51. Zhu, G. *et al.* Increased phonon scattering by nanograins and point defects in nanostructured silicon with a low concentration of germanium. *Physical review letters* **102,** 196803 (2009).
52. Wei, J. *et al.* Theoretical study of the thermoelectric properties of SiGe nanotubes. *RSC Advances* **4,** 53037–53043 (2014).
53. Wingert, M. C. *et al.* Sub-amorphous Thermal Conductivity in Ultrathin Crystalline Silicon Nanotubes. *Nano Lett.* **15,** 2605–2611 (2015).
54. Hsiao, T.-K. *et al.* Observation of room-temperature ballistic thermal conduction persisting over 8.3 [micro]m in SiGe nanowires. *Nat Nano* **8,** 534–538, doi: 10.1038/nnano.2013.121 (2013).
55. Tang, J. *et al.* Holey silicon as an efficient thermoelectric material. *Nano letters* **10,** 4279–4283 (2010).
56. Wolf, S., Neophytou, N. & Kosina, H. Thermal conductivity of silicon nanomeshes: Effects of porosity and roughness. *Journal of Applied Physics* **115,** 204306 (2014).
57. Neophytou, N. Prospects of low-dimensional and nanostructured silicon-based thermoelectric materials: findings from theory and simulation. *The European Physical Journal B* **88,** 1–12.
58. Masuda, H. & Fukuda, K. Ordered metal nanohole arrays made by a two-step replication of honeycomb structures of anodic alumina. *Science* **268,** 1466–1468 (1995).
59. Sun, C., Luo, J., Wu, L. & Zhang, J. Self-ordered anodic alumina with continuously tunable pore intervals from 410 to 530 nm. *ACS applied materials & interfaces* **2,** 1299–1302 (2010).
60. Shiraki, Y. & Usami, N. In *Silicon-germanium (SiGe) nanostructures: Production, properties and applications in electronics* Vol. 1 Ch. 1, 4–23 (Elsevier, 2011).
61. Wilson, A. A. *et al.* Thermal conductivity measurements of high and low thermal conductivity films using a scanning hot probe method in the 3 ω mode and novel calibration strategies. *Nanoscale* **7,** 15404–15412 (2015).
62. Maiz, J. *et al.* Enhancement of thermoelectric efficiency of doped PCDTBT polymer films. *RSC Advances* **5,** 66687–66694 (2015).
63. Rojo, M. M. *et al.* Fabrication of Bi2Te3 nanowire arrays and thermal conductivity measurement by 3ω-scanning thermal microscopy. *Journal of Applied Physics* **113,** 054308 (2013).
64. Rojo, M. M. *et al.* Decrease in thermal conductivity in polymeric P3HT nanowires by size-reduction induced by crystal orientation: new approaches towards thermal transport engineering of organic materials. *Nanoscale* **6,** 7858–7865 (2014).
65. Rojo, M. M., Calero, O. C., Lopeandia, A., Rodriguez-Viejo, J. & Martín-Gonzalez, M. Review on measurement techniques of transport properties of nanowires. *Nanoscale* **5,** 11526–11544 (2013).
66. Sze, S. M. & Ng, K. K. *Physics of semiconductor devices*. (John Wiley & Sons, 2006).
67. Jeong, C., Datta, S. & Lundstrom, M. Thermal conductivity of bulk and thin-film silicon: A Landauer approach. *Journal of Applied Physics* **111,** 093708 (2012).
68. Wang, Z. & Mingo, N. Diameter dependence of SiGe nanowire thermal conductivity. *Applied Physics Letters* **97,** 101903 (2010).
69. Bera, C. *et al.* Thermoelectric properties of nanostructured Si1− xGex and potential for further improvement. *Journal of Applied Physics* **108,** 124306 (2010).

70. Klemens, P. Thermal resistance due to point defects at high temperatures. *Physical review* **119,** 507 (1960).
71. Garg, J., Bonini, N., Kozinsky, B. & Marzari, N. Role of disorder and anharmonicity in the thermal conductivity of silicon-germanium alloys: A first-principles study. *Physical review letters* **106,** 045901 (2011).
72. Iskandar, A., Abou-Khalil, A., Kazan, M., Kassem, W. & Volz, S. On the interplay between phonon-boundary scattering and phonon-point-defect scattering in SiGe thin films. *Journal of Applied Physics* **117,** 125102 (2015).
73. Rowe, D., Shukla, V. & Savvides, N. Phonon scattering at grain boundaries in heavily doped fine-grained silicon-germanium alloys. *Nature* **290,** 765–766 (1981).
74. Ju, Y. & Goodson, K. Phonon scattering in silicon films with thickness of order 100 nm. *Applied Physics Letters* **74,** 3005–3007 (1999).
75. Zhang, H. *et al.* The investigation of thermal properties on multilayer Sb 2 Te 3/Au thermoelectric material system with ultra-thin Au interlayers. *Superlattices and Microstructures* **89,** 312–318 (2016).
76. Zhang, G., Wang, W. & Li, X. Enhanced thermoelectric properties of core/shell heterostructure nanowire composites. *Advanced Materials* **20,** 3654–3656 (2008).
77. Yu, B. *et al.* Enhancement of thermoelectric properties by modulation-doping in silicon germanium alloy nanocomposites. *Nano letters* **12,** 2077–2082 (2012).
78. Neophytou, N. *et al.* Simultaneous increase in electrical conductivity and Seebeck coefficient in highly boron-doped nanocrystalline Si. *Nanotechnology* **24,** 205402 (2013).
79. Lorenzi, B. *et al.* Paradoxical enhancement of the power factor of polycrystalline silicon as a result of the formation of nanovoids. *Journal of Electronic Materials* **43,** 3812–3816, doi: 10.1002/pssa.201300130 (2014).
80. Lin, C. *et al.* Low thermal conductivity of amorphous Si/Si0. 75Ge0. 25 multilayer films with Au-interlayers. *EPL* (*Europhysics Letters*) **105,** 27003 (2014).
81. Shen, B., Zeng, Z., Lin, C. & Hu, Z. Thermal conductivity measurement of amorphous Si/SiGe multilayer films by 3 omega method. *International Journal of Thermal Sciences* **66,** 19–23 (2013).
82. Ye, F., Zeng, Z., Lin, C. & Hu, Z. The investigation of electron–phonon coupling on thermal transport across metal–semiconductor periodic multilayer films. *JMatS* **50,** 833–839 (2015).

Acknowledgements

This work has been supported by 7th framework European project NANOHITEC 263306, national project PHOMENTA MAT2011-27911, CONSOLIDER NANOTHERM Grant No. CSD2010-00044, and INFANTE. J.A. Pérez acknowledges *Ministerio de Economia y Competitividad* for his FPI grant and Banco Santander for a special grant for a short stay in Brazil (Brazilian Center of Physical Researches-Rio de Janeiro). M. M. R. wants to acknowledge JAE Pre-Doc grant for PhD financial support. NN acknowledges funding from the European Research Council (ERC) under the European Union's Horizon 2020 research and innovation programme (grant agreement No 678763). NN also acknowledges Dr. Hossein Karamitaheri for helpful discussions. MMG wants also to acknowledge the Salvador Madariaga Fellowship.

Author Contributions

J.A.P.-T. performed the fabrication of Si-Ge nanomeshes, structural, compositional, morphological characterization, and electrical conductivity, Seebeck coefficient measurements. M.M.-R. performed the Thermal conductivity measurements and the *AFM* images. J.M. performed the fabrication of highly ordered anodic Aluminum oxide templates. N.N. has performed theoretical calculations consider the influence of the nanopores on the thermal conductivity. All authors analyzed the results. J.A.P.-T. and M.M.-G. wrote the manuscripts. All authors reviewed the manuscripts. M.M.-G. got the idea, supervised and discussed the work and the manuscript, and got the funding to develop the idea.

Additional Information

Supplementary information accompanies this paper at http://www.nature.com/srep

Competing financial interests: The authors declare no competing financial interests.

How to cite this article: Perez-Taborda, J. A. *et al.* Ultra-low thermal conductivities in large-area Si-Ge nanomeshes for thermoelectric applications. *Sci. Rep.* **6**, 32778; doi: 10.1038/srep32778 (2016).

SUPPORTING INFORMATION:

Ultra-low thermal conductivities in large-area SiGe nanomeshes for thermoelectric applications

Jaime Andrés Pérez-Taborda[†], Miguel Muñoz-Rojo[†], Jon Maiz[†‡], Neophytos Neophytou[§], Marisol Martín-González[†*]

[†] Instituto de Microelectrónica de Madrid (IMM-CSIC), Calle de Isaac Newton 8, Tres Cantos, 28760 Madrid, Spain, [§]School of Engineering, University of Warwick, Coventry, CV4 7AL, UK

KEYWORDS: Nano-meshes, Silicon Germanium, Thermoelectric Materials, DC – Sputtering, Thermal Conductivity

S1. Structural characterization techniques

The crystalline structure of the films was studied by X-ray diffraction (*XRD*) using a *Philips* X-PERT diffractometer with a Cu K_α radiation source with a wavelength of 1.5418 Å in Bragg-Brentano geometry. Diffraction patterns were identified by standard reference patterns, supplied by the International Centre for Diffraction Data (ICDD). Micro-Raman spectrometer (*Horiba Jobin Yvon*) LabRam HR with a 532 nm Nd:YAG laser (8.5 mW) was used for compositional mapping and local crystallization. Scanning electron microscopy has been performed on a *JEOL* JSM-6460LV and the *AFM* images were obtained with a *Nanotec AFM* microscope. Resistivity measurements and Seebeck coefficient were measured with a commercial *Linseis* LSR-3 system.

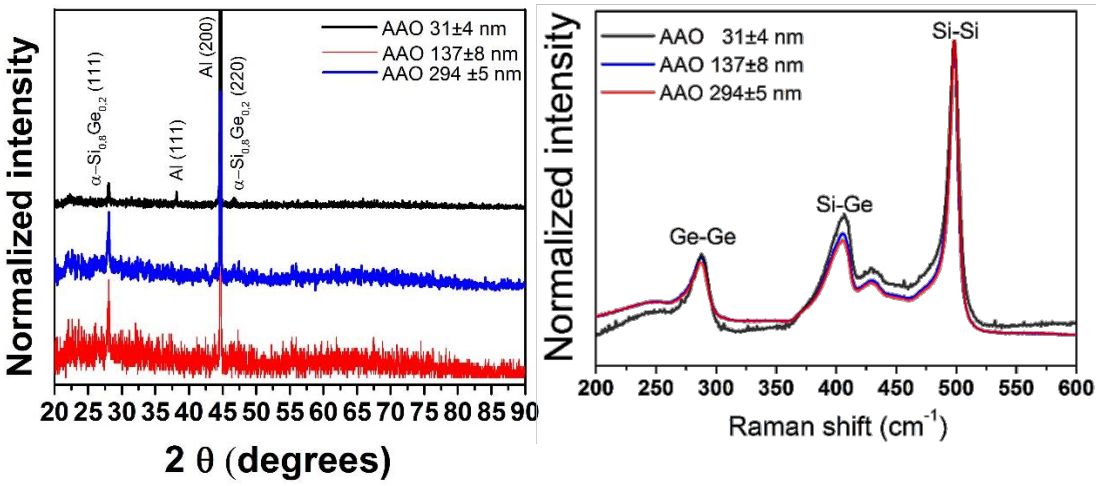

Figure S1. a) X-Ray and b) Raman spectra of a $Si_{0.8}Ge_{0.2}$ grown on nano-meshes with pore diameter of 31 nm (black line) 137 nm (blue line) and 294 nm (red line).

Substrate	[111] $Si_{0.8}Ge_{0.2}$ 2θ (º)	Peak Width (degrees)	Approx. Crystallite size
AAO 25nm	28,0608	0,1692	≈ *50 nm*
AAO 137nm	28,07	0,1342	≈ *65 nm*
AAO 294nm	28,0474	0,2497	≈ *35 nm*
$SrTiO_3$	28,0255	0,1235	≈ *70 nm*

Table SI. Average $Si_{0.8}Ge_{0.2}$ crystallite size. They have been calculated from XRD data using the Scherrer equation with a copper Kα (λ = 1.54056 Å) and a constant of 0.94.

S2. Porous alumina fabrication.

The highly ordered hexagonal pore arrays throughout porous anodic alumina templates were achieved by using a two-step anodization.[2] Aluminum foils (99.999% purity, 0.5 mm thickness) supplied by Advent Research Materials (England) were first electropolished in perchloric acid/ethanol solution with a volume ratio of 1:4 for 4 min at 20 V after the cleaning and degreasing process. The first of the two anodization processes was applied to 6 h with constant voltage of 205 V at 4ºC in 1 wt% H_3PO_4 and 0.01 M aluminum oxalate (Alox) as electrolyte. The Alox is used as an additive to suppress breakdown of porous anodic alumina in the electrolyte of phosphoric acid at high potentials and comparatively high temperatures.[3] The second anodization was then performed under the same conditions as that of the first anodization after removing the disordered alumina film using the solution of chromic acid and phosphoric acid. The length of nanocavities can be varied from hundreds nanometers to hundreds of microns and it is controlled by the time of the second anodization process. In this case the time used was 12 h. Finally, a third step was carried out in order to widening the pores up to 350 nm in pore diameter. It consists in a controlled reduction of pore walls with a phosphoric acid solution, 5 wt% at 35ºC during 3 h.

The sputtering of the $Si_{0.8}Ge_{0.2}$ on top of these templates resulted in films that replicated the porous structure, i.e. nano-meshed $Si_{0.8}Ge_{0.2}$ films. Figure S2 shows an optical image of the porous alumina before and after depositing $Si_{0.8}Ge_{0.2}$ film on top.

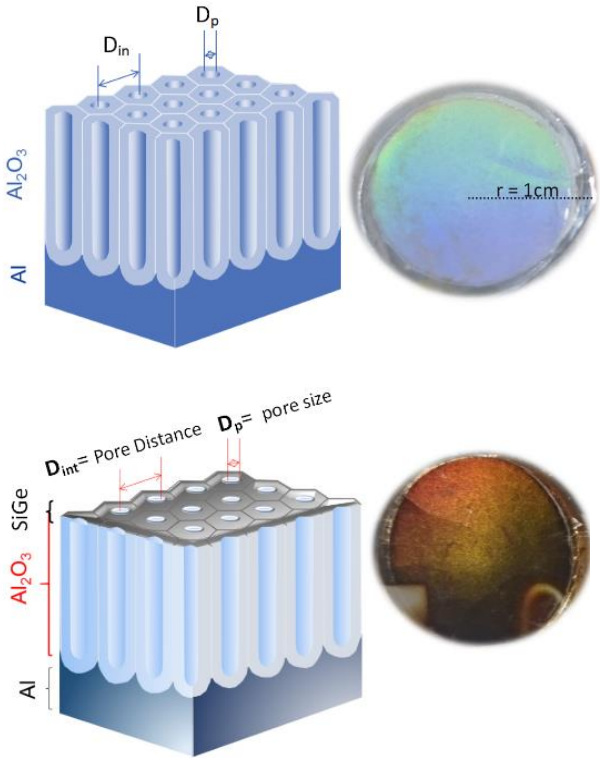

Figure S2. Sketch and optical image of a) a porous alumina template and b) the SiGe film nano-mesh.

S3. Continuous film fabrication.

A $Si_{0.8}Ge_{0.2}$ film without pores was grown through DC plasma sputtering system. The conditions used to fabricate were similar to those used for nano-meshes. A thickness of 400 nm and average roughness of 2,5 nm was observed from a profilemeter and an Atomic Force Microscopy (AFM) **Figure S3**. The structural and transport properties of these films are shown in reference[1].

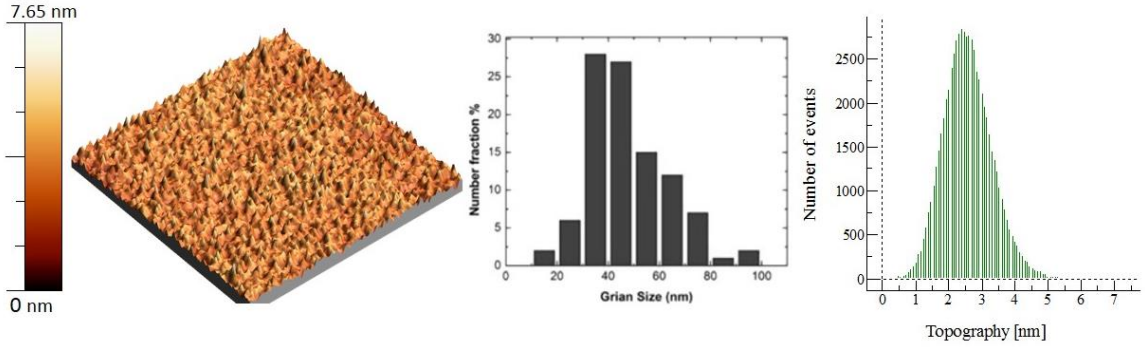

Figure S3. Roughness of the continuous thin film on $SrTiO_3$ substrate. The statistical average of the roughness is 2.5±0.3 nm.

S4. AFM and KPM analysis for the $Si_{0.8}Ge_{0.2}$ nano-meshed films.

Images of the topography of the porous $Si_{0.8}Ge_{0.2}$ nano-meshed films were taken with an atomic force microscope (AFM). The porous mean diameter was studied with this technique. Figures S4, S5 and S6 show the images obtained with the AFM.

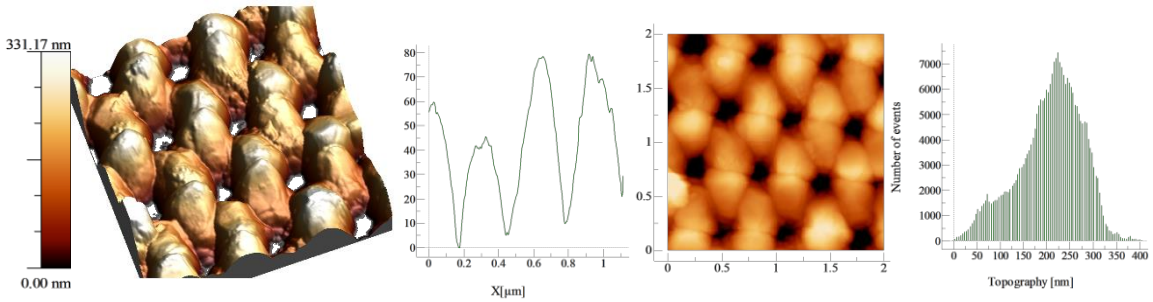

Figure S4. Roughness of the SiGe film deposited on the template alumina with pore size of 294±5 nm. The statistical average of the roughness is 53±7 nm.

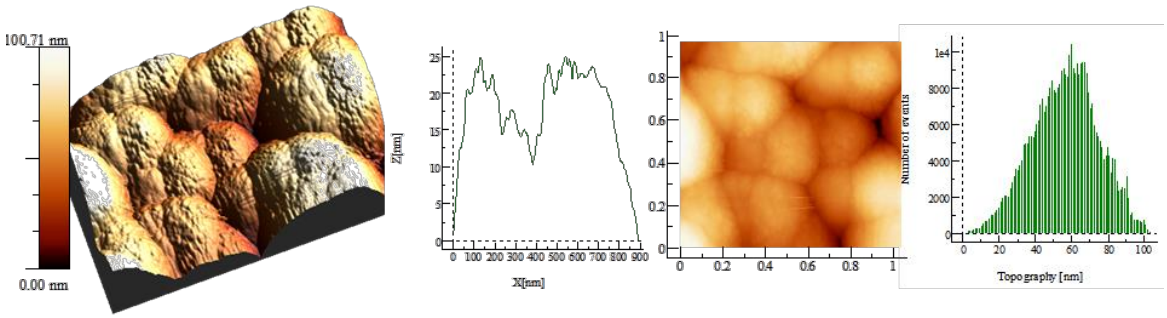

Figure S5. Roughness of the SiGe film deposited on the template alumina with pore size of 137±8 nm. The statistical average of the roughness is 14±8 nm.

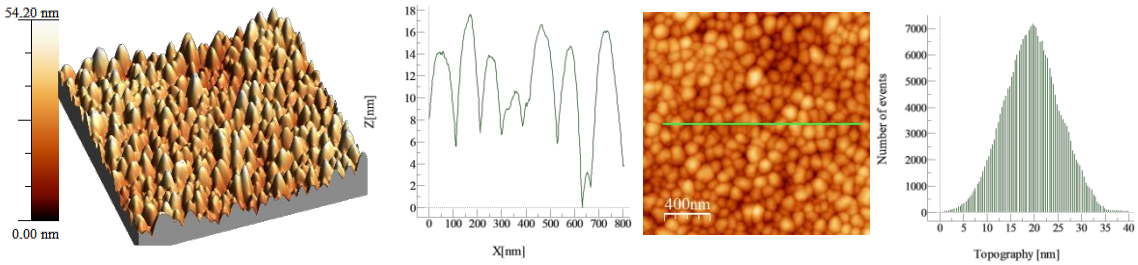

Figure S6. Roughness of the SiGe film deposited on the template alumina with pore size of 31±4 nm. The statistical average of the roughness is 5±2 nm.

Moreover, Kelvin Probe Microscopy (KPM) images were taken for the three nano-meshed films with pore diameter ranging from 294±5 nm to 31±4 nm diameter. Figure S7 show these pictures were homogeneous surface potential is observed for the samples.

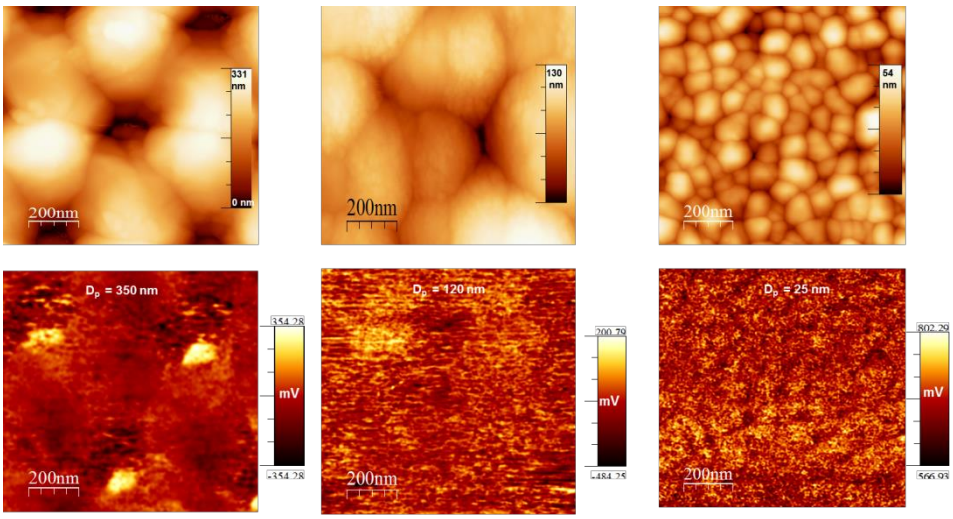

Figure S7. a),b) and c) are topographic images of the surface of nano-meshed films with pore diameters of 294±5 nm, 137±8 nm and 31±4 nm, respectively. d), e) and f) are the surface potential images of these films, which reveal an homogeneity in the material composition.

S8. Scanning Thermal Microscopy (SThM) in 3ω mode.

The thermal conductivity measurements of the SiGe nanomeshes were performed using the SThM working in 3ω mode, which has been successfully used to measure the thermal conductivity of films and nanowires [4,5-8]. For that purpose, an AFM system from Nanotec® Company was used to position a thermoresistive probe on top of the sample. The probes used in this case were Wollaston probes from Bruker® company. The measuring and analysis procedure was similar to those presented in reference [4].

Firstly, the probe needs to be calibrated[4] in order to obtain the thermal exchange radius, *b*, and the contact resistance, *Rc*, between the probe and the sample. Following the same procedure as shown in ref. [4], we measured a set of three samples with well-defined thermal conductivity. These calibration samples were polyaniline (PANI) with 5% and 7% graphene platelets and borosilicate glass with thermal conductivities of k=0.49 W/K·m, k=0.65 W/K·m and k=1.1 W/K·m, respectively. As in reference[4], Figure S8 shows the crossing between curves for the probe and calibration samples used, giving a value of b=(2.27±0.09) µm and Rc= 29365±6925 (K/W). The probe convection coefficient was determined to be, h=3324 W/K·m^2.

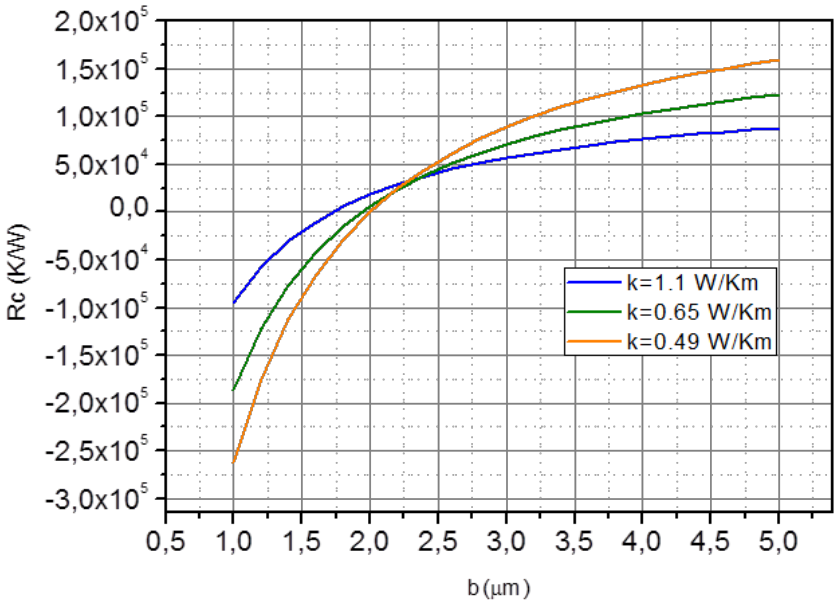

Figure S8. Thermal exchange radius vs contact resistance graph obtained during the calibration process for the Wollaston probe used.

After the calibration was carried out, the thermal resistance of our SiGe nanomeshed samples, with pore diameters of 294±5 nm, 137±8 nm and 31±4 nm were obtained with this technique in a similar way as explained in reference[4]. Due to its small film thickness (around 1μm or less), the heat flows across the SiGe film but also through the alumina substrate underneath the film. The thermal resistances of the 294±5 nm, 137±8 nm and 31±4 nm porous size diameter samples, whose values are influenced by the SiGe film, the air of the porous and the alumina substrate, were determined to be 124829 K/W, 127366 K/W and 165795 K/W, respectively. As a consequence, the semi-infinite theory to extract the thermal conductivity of the intrinsic SiGe film (R=1/4kb) cannot be used. Instead, 2D COMSOL® simulations were performed to determine the intrinsic thermal conductivity of this film [4].

We considered the geometry of the sample, in which the thickness of the SiGe film, the porosity and the size porous were considered. On top of the film, a Gaussian heat disc source with the same radius as the thermal exchange radius of the Wollaston probe was set. Regarding the material properties, the thermal conductivity of the alumina was measured with the photoacoustic technique resulting to be 1.33 W/Km while the one for the SiGe film is unknown. Therefore, the thermal conductivity of the SiGe nanomesh film will be varied until the thermal resistance obtained from the simulation, R_{simult}, matches with the thermal resistance obtained experimentally, R_{experm}. The symmetry of the sample/measurement is taken as an advantage in the simulation to speed it up[4].

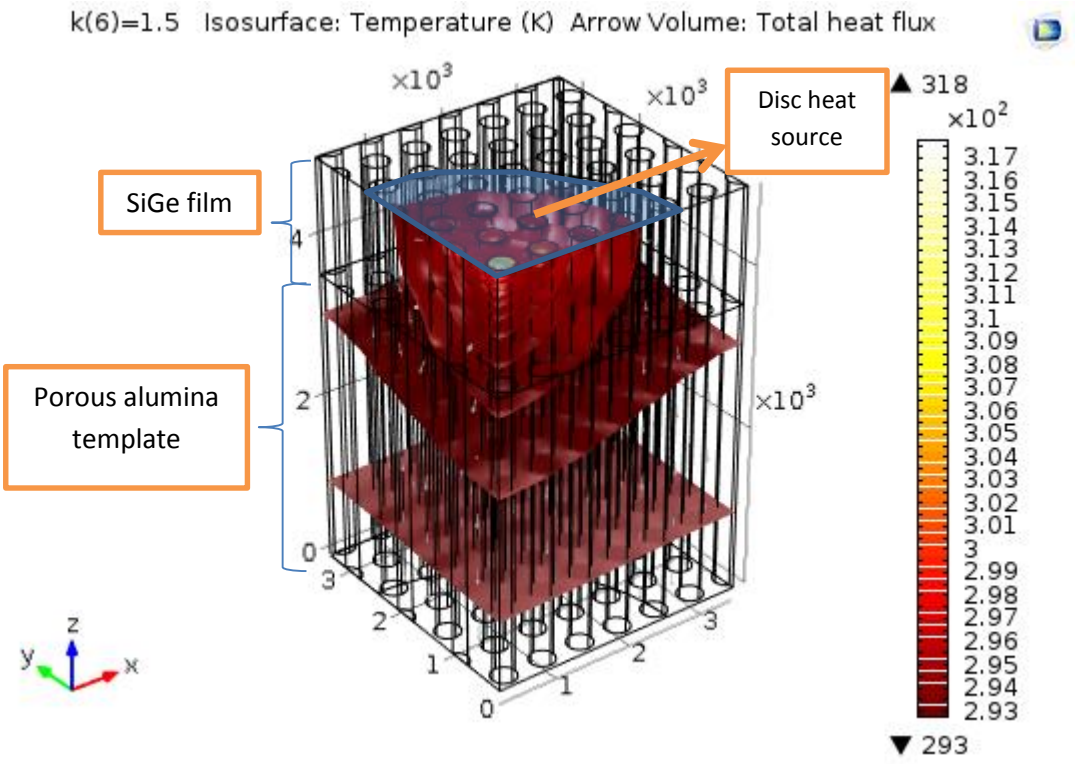

Figure S8a shows the isothermal contour obtained from the simulation of the 294±5 nm SiGe nanomesh. Figure S8b-d shows the comparison between the simulation (R_{simult}) and the experimental result (R_{experm}).

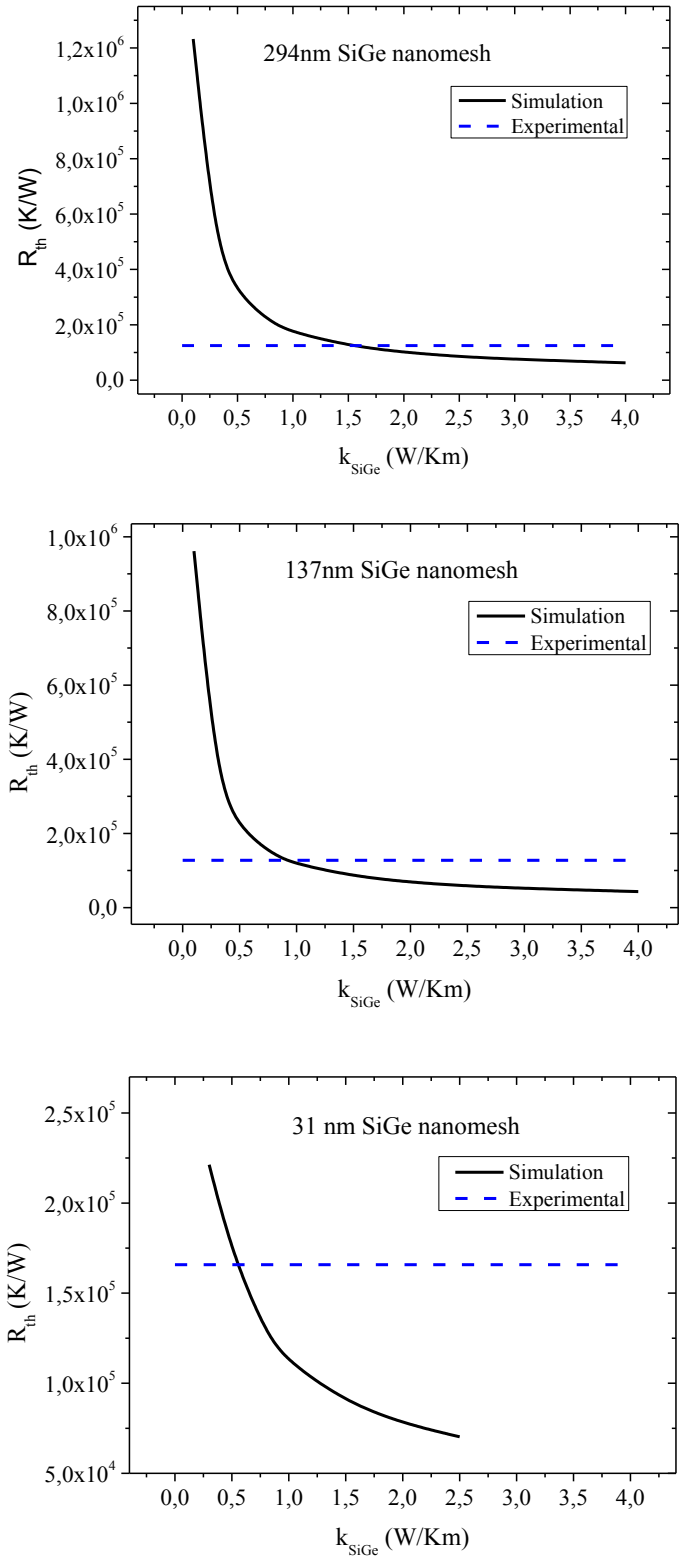

Figure S8. a) Simulation result for the 294 nm SiGe nanomesh. The SiGe film is on top of the poropus alumina substrate. b), c) and d) show the thermal resistances obtained from simulation (black line) and from the experiment (blue line). The matching point indicates the thermal conductivity of the SiGe film.

Table IIS summarizes the thermal conductivity results obtained for the 294 nm, 137 nm and 31 nm SiGe nanomeshes after the simulation was performed.

Table IIS. Thermal conductivities obtained for the SiGe nanomeshes.

SiGe nanomesh-porous size	Thermal Conductivity (W/Km)
294±5 nm	**1.54±0.27**
137±8 nm	**0.93±0.15**
31±4 nm	**0.55±0.10**

REFERENCES

1 Taborda, J. A. P. *et al.* Low thermal conductivity and improved thermoelectric performance of nanocrystalline silicon germanium films by sputtering. *Nanotechnology* **27**, 175401 (2016).

2 Masuda, H. & Fukuda, K. Ordered Metal Nanohole Arrays Made by a Two-Step Replication of Honeycomb Structures of Anodic Alumina. *Science* **268**, 1466-1468 (1995).

3 Sun, C., Luo, J., Wu, L. & Zhang, J. Self-ordered anodic alumina with continuously tunable pore intervals from 410 to 530 nm. *ACS Applied Materials and Interfaces* **2**, 1299-1302 (2010).

4 Wilson, A. *et al.* Thermal conductivity measurements of high and low thermal conductivity films using a scanning hot probe method in the 3[small omega] mode and novel calibration strategies. *Nanoscale* **7**, 15404-15412, doi:10.1039/C5NR03274A (2015).

5 Maiz, J. *et al.* Enhancement of thermoelectric efficiency of doped PCDTBT polymer films. *RSC Advances* **5**, 66687-66694 (2015).

6 Wilson, A. A. *et al.* Thermal conductivity measurements of high and low thermal conductivity films using a scanning hot probe method in the 3 ω mode and novel calibration strategies. *Nanoscale* **7**, 15404-15412 (2015).

7 Rojo, M. M. *et al.* Decrease in thermal conductivity in polymeric P3HT nanowires by size-reduction induced by crystal orientation: new approaches towards thermal transport engineering of organic materials. *Nanoscale* **6**, 7858-7865, doi:10.1039/C4NR00107A (2014).

8 Muñoz Rojo, M., Caballero Calero, O., Lopeandia, A. F., Rodriguez-Viejo, J. & Martin-Gonzalez, M. Review on measurement techniques of transport properties of nanowires. *Nanoscale* **5**, 11526-11544, doi:10.1039/C3NR03242F (2013).

PAPER IV

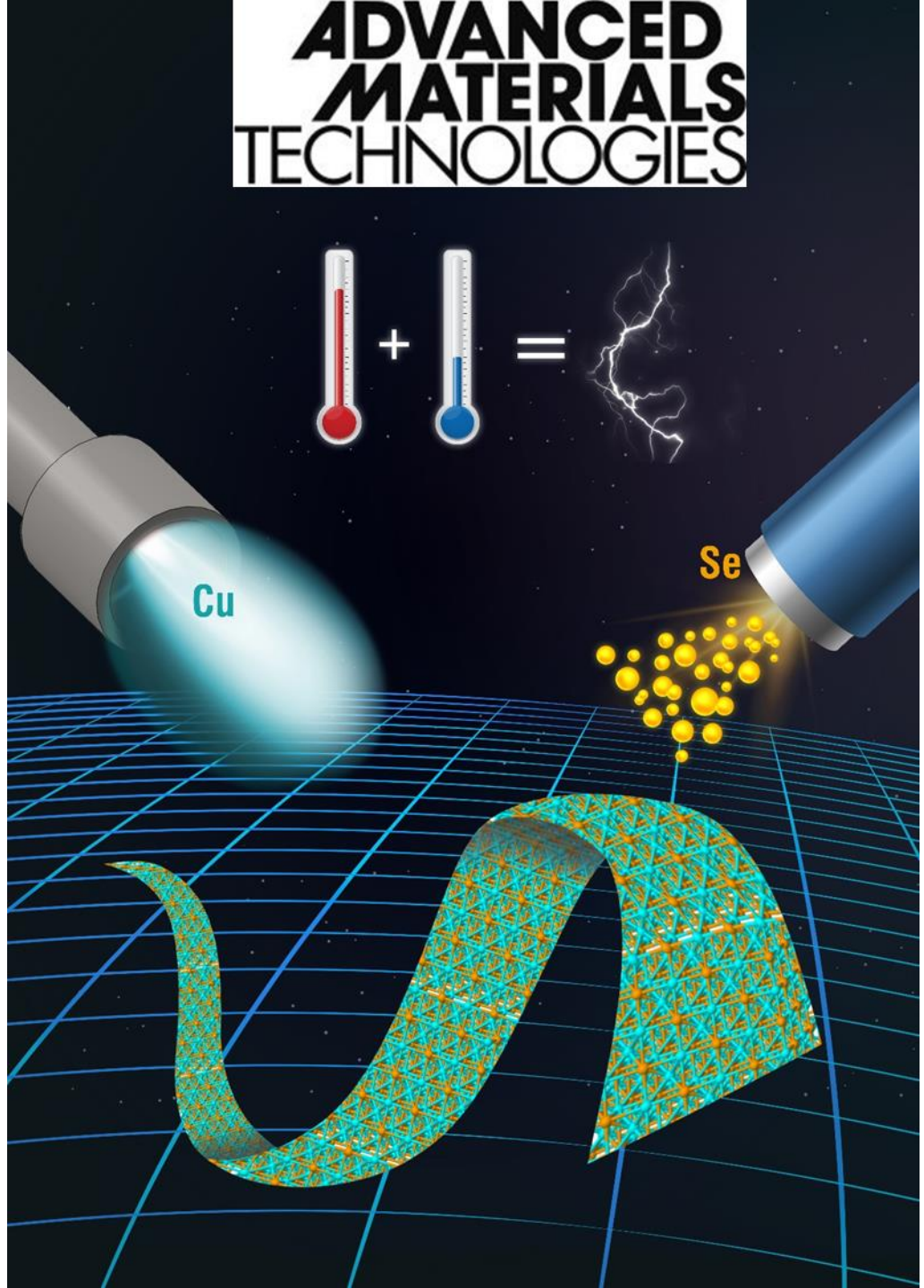
ADVANCED MATERIALS TECHNOLOGIES
Cu
Se

PORTADA:

Se presenta un nuevo enfoque tecnológico para depositar películas delgadas de Ag_{2-x}Se y Cu_{2-x}Se con alta eficiencia termoeléctrica. Una variación de la pulverización catódica reactiva que hemos llamado: "Pulsed hybrid reactive magnetron sputtering (PHRMS)" ha sido puesta en marcha. Esta nueva técnica nos permite en un solo paso e incluso a temperatura ambiente obtener bajos valores de conductividad térmica y altos valores de factor de potencia. Esta imagen ha sido seleccionada como portada de revista en [83]

Pulsed Hybrid Reactive Magnetron Sputtering for High *zT* Cu_2Se Thermoelectric Films

*Jaime A. Perez-Taborda, Liliana Vera, Olga Caballero-Calero, Elvis O. Lopez, Juan J. Romero, Daniel G. Stroppa, Fernando Briones, and Marisol Martin-Gonzalez**

Thermoelectric films on flexible substrates are of interest for the integration of thermoelectric in wearable devices. In this work, copper selenide films are achieved by a novel low-temperature technique, namely pulsed hybrid reactive magnetron sputtering (PHRMS). A brief introduction to the basic chemistry and physics involved during growth is included to explain its fundamentals. PHRMS is a single-step, room temperature (RT), fabrication process carried out in another ways conventional vacuum sputtering system. It does not require high-temperature post-annealing to obtain films with great thermoelectric performance. It is, therefore, compatible with polymeric substrates like Kapton tape. Several sets of films covering a large exploratory compositional range (from Cu/Se = 1 to 9) are deposited and their microstructure and thermoelectric properties are analyzed at RT. Power factors as high as 1.1 mW m^{-1} K^{-2} in the in-plane direction and thermal conductivities as low as $\kappa = 0.8 \pm 0.1$ W m^{-1} K^{-1} in the out-of-plane direction have been obtained for β-Cu_2Se films. Consequently, a figure of merit of 0.4 at RT can be estimated under the assumption that for this polycrystalline cubic phase no additional anisotropy in the thermoelectric properties is introduced by the planar configuration. Moreover, PHRMS is also industrially scalable and compatible with the in-line fabrication of other selenides.

1. Introduction

Nowadays, advanced thermoelectric materials (TE) exhibit conversion efficiencies between 5% and 20%.[1] In principle, those efficiencies can be further improved by new materials and/or appropriate strategies such as nanostructuration.[2] Considering that the efficiency of a thermoelectric material is proportional to its figure of merit, *zT*, defined as $zT = (S^2 \cdot \sigma) \cdot \kappa^{-1} \cdot T$, an ideal thermoelectric material must exhibit high electrical conductivity (σ), high Seebeck coefficient (S), and low thermal conductivity (κ), simultaneously, to maximize its efficiency for the desired temperature range.

In this context, there has been a significant increase of reports in the literature on $Cu_{2-x}Se$ as a p-type material with high power factor (PF)[3] (being the PF = $S^2 \cdot \sigma$).[1,3,4] Therefore, copper selenides have become a hot topic in the TE field, with reported figures of merit as high as $zT \approx 1.6$ @ 727 °C.[5] Moreover, $Cu_{2-x}Se$ has a crystallographic phase transition at $T \approx 130$ °C, and it has been shown that around this transition temperature *zT* can reach values as high as 2.3.[6] Thermoelectric thin films occupy an industrial niche for microfabricated multielement planar devices on flexible substrates as low-current voltage generators for room temperature (RT) applications. In this range of temperatures, the highest *zT* reported value for bulk crystalline material is 0.28 (Liu et al.[5]).

$Cu_{2-x}Se$ films are typically p-type, highly conducting, semitransparent, and with a bandgap varying between 1.1 and 1.4 eV. Numerous methods have been reported for the deposition of $Cu_{2-x}Se$ films at low substrate temperatures, such as a chemical bath deposition,[7–9] galvanic synthesis,[10] solution growth,[11] hydrothermal method,[12] or electrochemical deposition.[10,13] Other methods, such as adsorption/diffusion (selenization),[14–16] SILAR method,[17] and pulsed laser deposition[18,19] require high-temperature post growth treatments to improve and stabilize the thermoelectric properties. In any case, those different manufacturing film methods have not been able to surpass the thermoelectric efficiencies at room temperature of the $Cu_{2-x}Se$ bulk samples prepared by solid-state reaction.[20,21] In the case of bulk samples other methods, such as spark plasma sintering,[4,5,22–28] ball milling followed by hot pressing,[24,29] and quenched bulk[30] have also been reported. In all these cases, high temperatures and long manufacturing times (even weeks) are necessary.

In this work, we have developed a fabrication approach namely pulsed hybrid reactive magnetron sputtering (PHRMS) based on reactive sputtering, a vacuum technique that is widely used in industry as particularly suitable for thin film devices

J. A. Perez-Taborda, L. Vera, Dr. O. Caballero-Calero,
Dr. J. J. Romero, Prof. F. Briones, Dr. M. Martin-Gonzalez
IMM-Instituto de Microelectrónica de Madrid (CNM-CSIC)
Isaac Newton 8, PTM, E-28760 Tres Cantos, Madrid, Spain
E-mail: marisol@imm.cnm.csic.es

Dr. E. O. Lopez
Department of Applied Physics
Brazilian Center for Physics Research
Urca, Rio de, Janeiro 22290-180, Brazil

Dr. D. G. Stroppa
International Iberian Nanotechnology Laboratory (INL)
Av. Mestre Jose Veiga, 4715-330 Braga, Portugal

The ORCID identification number(s) for the author(s) of this article can be found under https://doi.org/10.1002/admt.201700012.

DOI: 10.1002/admt.201700012

integration. However, conventional reactive sputtering presents some serious challenges (when trying to control composition and crystallinity of chalcogenide compounds) due to the poisoning of the targets and the vacuum system by the Se overpressure needed to obtain the adequate chalcogenide stoichiometry in the thin film. Another general problem is the presence of negatively charged ions of chalcogen elements O, S, Se, or Te in the sputtering with energies of the order of 100 eV, which cause heavy damage of the growing film.[16,31] In alternative hybrid sputtering systems, the films are grown by sputtering from the metallic targets and the introduction in the system of chalcogen by thermal vapor source such as an effusion cell (similar to those used for molecular beam epitaxy (MBE)) or a gas source (such as H_3Se). However, problems still caused by negative ions, high substrate temperatures, and chalcogenides overpressure make difficult to accurately control composition uniformity over large substrate areas. These issues are well known in the fabrication of solar cells modules based on CIGS, for example.[32] In the present work, a novel hybrid sputtering process named PHRMS, developed by our team, is successfully employed. It allows overcoming the above-cited drawbacks by adequate periodic pulsing of the selenium source, which drastically modifies the chemical reactivity of the film surface and the incorporation kinetics of anionic/cationic species on the surface of the growing film. PHRMS is a single-step fabrication process done at room temperature. It does not require any further high-temperature post-preparation annealing treatment to optimize the thermoelectric properties. And, it is, therefore, compatible with the use of polymer substrates for producing wearable devices.

2. Results and Discussion

A scheme of the experimental setup is shown in **Figure 1**. The cationic element (copper in this case) is deposited in direct current (DC) sputtering mode, while the anodic element (selenium) is introduced into the deposition chamber as a beam of atomic selenium vapor, via a pulsed cracker valve effusion cell.[33] Therefore, the selenium flux impinging the growing film can be controlled by changing the opening time of the heated cracker valve. Moreover, PHRMS offers an additional advantage, which is the highly reactive kinetics of the alternated deposition, which provides a fine control over the stoichiometry of the film, along with a fast growth rate (>1 nm s^{-1}). This is produced thanks to the combination of DC sputtering of the metallic element without the presence of selenium in the chamber (in the time that the valve is closed), which allows the presence of copper atoms onto the film surface. Metals have a high sticking coefficient.[34] Then, selenium is introduced into the chamber, and although the sticking coefficient of selenium is low, in this case, when it reaches the film it reacts with the copper atoms already there, forming Cu–Se nucleation sites due to the negative enthalpy of formation that the compound has. This produces a more homogeneous incorporation of selenium without the need of having a selenium overpressure or without increasing the temperature of the substrate, as in more conventional sputtering systems. The physico–chemistry of the process at the surface is in some ways mimicking that of

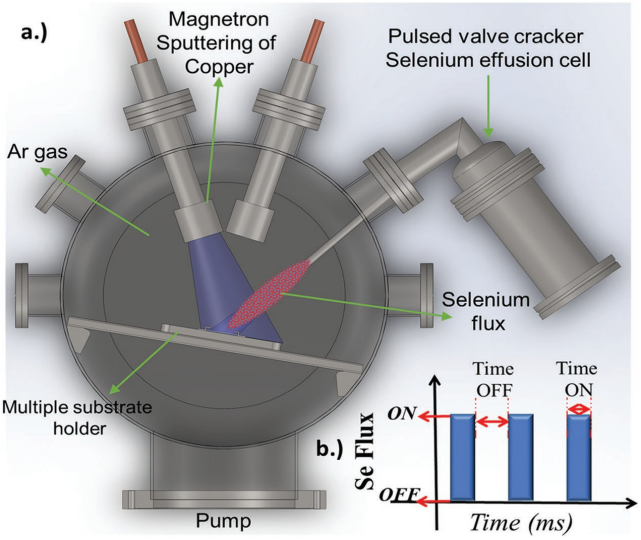

Figure 1. A cross-sectional scheme of the pulse hybrid reactive magnetron sputtering (PHRMS) deposition system is presented: a) shows the different flange feed-troughs used for deposit rate measurements (quartz balance method), substrate holder with heater and capability of having up to 10 samples per batch, and the copper magnetron sputtering target, b) represents the typical pulses used to control the opening of the selenium cell valve. The pulse width (in ms) allows the control of the atomic selenium gas dosage into the chamber.

atomic layer deposition (ALD) or a nucleation enhanced III–V growth by UHV(MBE)[35,36] (where the use of modulated beams produces an enhancement in the nucleation thanks to a change in the kinetics of the reaction by the generation of reactive surfaces), but much faster (up to 1 nm s^{-1} growth rate) since it is not a layer by layer process. Nevertheless, the importance of this mechanism is that when the valve is closed, it provides enough time without selenium in the chamber to generate enough copper atoms at the film surface and that the opening time of the valve provides enough supply of selenium for obtaining the desired final composition of the film. So, depending on the periodicity of the opening of the valve, different Cu–Se ratios can be obtained. As said before, the kinetics of the pulse hybrid reactive magnetron sputtering allows the fabrication of polycrystalline Cu–Se films at room temperature, and no further postannealing treatments are needed. This is of interest to prepare films on flexible substrates (such as polymers) that otherwise will degrade with temperature. In Figure 1S (Supporting Information), a photograph of a 1 µm thick Cu_2Se film grown on a flexible Kapton substrate is shown. The fabrication of films of Cu_2Se on flexible substrates opens the possibility of using these materials in wearable devices, for example. Furthermore, recent works on 2D materials[37–39] show a new field of study of selenide films, making the PHRMS a great technique for their fabrication due to the high control that the system allows. Finally, it is important to highlight that the process is fully reproducible and scalable.

Since the stoichiometry of the material and the segregation of selenium is a controversial topic in $Cu_{2-x}Se$ thermoelectrics, in this work, we took advantage of the high tunability of the fabrication system to study the composition effect on the

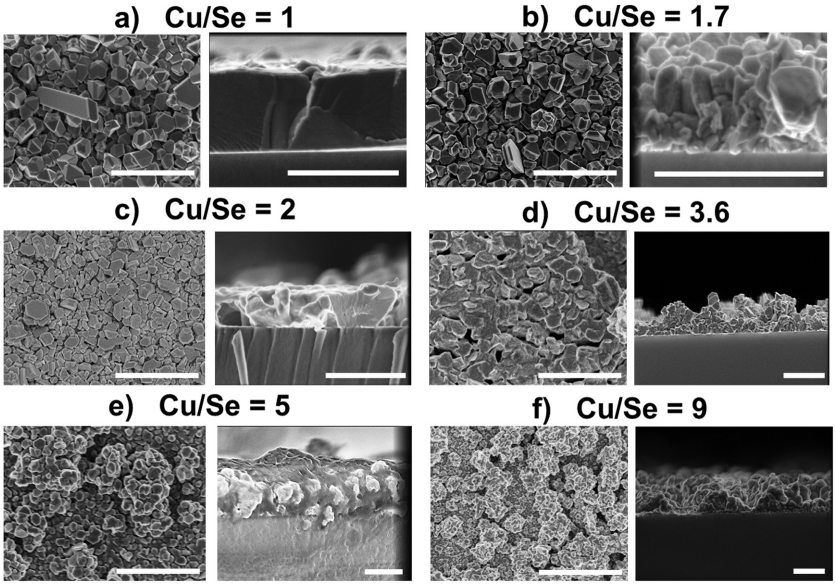

Figure 2. SEM images recorded by secondary electron (SE) detector. Top and cross-sectional view for the films with different copper/selenium ratios showing the morphological evolution depending on the copper content, being a) Cu/Se = 1, b) Cu/Se = 1.7, c) Cu/Se = 2, d) Cu/Se = 3.6, e) Cu/Se = 5, f) Cu/Se = 9. The scale shown in all the images is 1 µm.

morphology and on the properties for different Cu/Se film ratios on glass. To this aim, a wide range of Cu/Se nominal ratios (from 1.0 to 9.0) were deposited on glass substrates at room temperature, by changing the width and frequency of the pulses. Films with thicknesses between 600 and 850 nm were fabricated. In Table 1S (see the Supporting Information) the composition of the films was studied by energy-dispersive X-ray spectroscopy (EDS) and backscattered electrons (BSE) (see Figure 2S in the Supporting Information) analysis by scanning electron microscopy (SEM) (**Figure 2**) and confirmed by EDS in a transmission electron microscopy (TEM)–EDS, (see Figures 5S and 6S in the Supporting Information).

In Figure 2, the morphologies of some of the just prepared films for different Cu/Se ratios (top and side views) are shown. The films with lower copper content (Cu/Se ratio = 1), Figure 2a shows a compact morphology with a total thickness of 653 nm. For films with a Cu/Se = 1.7 (Figure 2b), one can see a more columnar growth, with a thickness of 833 nm. For a ratio of Cu/Se = 2 (Figure 2c), the film presents a columnar growth with a total thickness of 733 nm. Some hexagonal nanoplates can also be observed on the surface. Hexagonal nanoplates observed in samples grown with other techniques have been associated with the Cu_2Se cubic thermodynamically stable phase in (111) orientation.[40] Films with the highest copper content, such as those shown in Figure 2d–f, which correspond to Cu/Se of 3.6, 5, and 9, respectively, are less dense with an increased porosity. Even a loss of continuity can be observed in the cross-sectional view and back-scattered electrons analysis (see Figure 2S in the Supporting Information) showing that they resulted quite inhomogeneous.

A structural analysis of some films with different copper content is presented in **Figure 3**, which shows in the $20° < 2\theta < 65°$ range the synchrotron radiation grazing incidence X-ray diffraction (SR-GIXRD) patterns obtained. From this analysis, the crystallite size of the different films can be calculated (see Table 1S, Supporting Information). Starting with the film with the lowest copper content Cu/Se = 1, the SR-GIXRD pattern shows sharp and narrow peaks in 24.8°, 40.4°, and 47.3°, which correspond to the (102), (110), and (201) planes, respectively, and with average crystallite size ≈113 nm as calculated by Debye Scherrer's formula (Table 1S, Supporting Information). This diffraction pattern can be indexed as a hexagonal γ-CuSe phase with lattice parameters of $a = 3.98$ Å, and $c = 17.28$ Å (JCPDS: 00-027-0185). For the Cu/Se = 2 ratio, the SR-GIXRD pattern shows only the peaks corresponding to the β-Cu_2Se phase with a lattice parameter of $a = 5.816$ Å (JCPDS: 04-015-3687). In this case, the medium crystallite size observed is reduced to 65 nm. For films with higher copper/selenium ratio (Cu/Se > 2), α-Cu_2Se and α-Cu are present in the film. Upon Cu/Se ratio increase, it can be observed a relative decrease of α-Cu_2Se phase versus the cubic α-Cu phase. In the Cu/Se = 9 films, the α-Cu phase is the main contribution with peaks at 38.5°, 44.7°, and 65.2°, corresponding to (111), (200), and (220) planes, respectively. Also, for these films, one can appreciate a smaller crystallite size ranging from 25 to 84 nm.

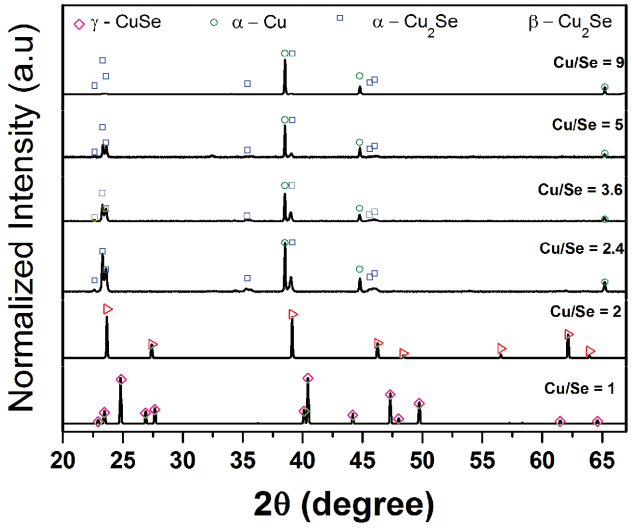

Figure 3. Grazing incidence synchrotron X-ray diffraction patterns taken from thin films with nominal compositions of Cu/Se = 1, Cu/Se = 2, Cu/Se = 2.4, Cu/Se = 3.6, Cu/Se = 5, and Cu/Se = 9, respectively, are shown. Likewise, diffraction peaks fitted for synchrotron wavelength ($\lambda = 1.3775$ Å) are displayed. The penetration depth of the SR-GIXRD has been calculated to be for the Cu/Se = 1, 2, and 9 ratios with attenuation length values of 813, 654, and 503 nm, respectively (more details Figure 3S in the Supporting Information). Hexagonal γ-CuSe (diamond symbol JCPDS: 00-027-0185), Cubic α-Cu (circle symbol JCPDS: 00-004-0836), orthorhombic α-Cu_2Se (square symbol JCPDS: 00-047-1448) and Cubic β-Cu_2Se (triangle symbol, JCPDS: 04-015-3687) phases are marked.

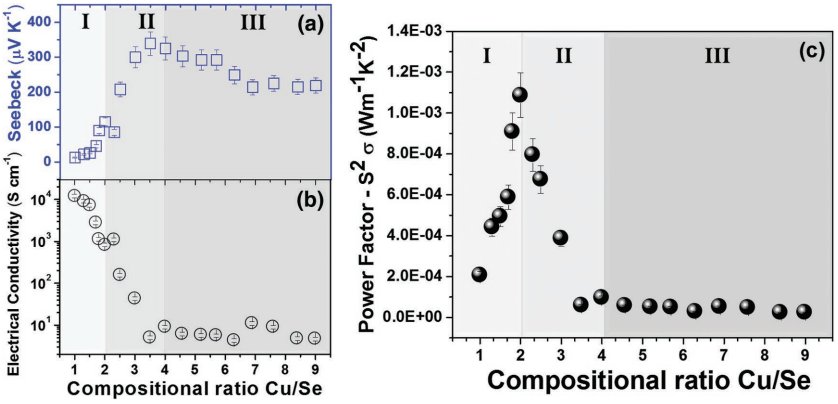

Figure 4. The compositional dependence of a) the Seebeck coefficient and b) the electrical conductivity are shown, for clarity the graph has been divided into three different zones: Cu/Se ratio <2, 2 < Cu/Se < 4, and Cu/Se > 4. c) Shows the variation of the power factor as a function of the Cu/Se ratio. All values were measured at room temperature.

Additional results from high-resolution transmission electron microscopy (HRTEM) are shown in Figure 5S and 6S (Supporting Information), corresponding to the films with nominal Cu/Se = 2 and Cu/Se = 2.5 ratios, being the compositions confirmed also by EDS measurements in the HRTEM. In the case of the Cu/Se = 2, the electron diffraction pattern shows the (111), (220), and (200) diffraction peaks, and in the high-resolution image, an interplanar spacing of 0.34 nm is found, which matches very well with the (111) planes of the β-Cu_2Se, being these planes the most atomically dense, which confirms the previous results of SR-GIXRD.

Once the parameters to deposit films with different nominal Cu/Se ratios were optimized and the films were characterized from a structural and morphological point of view, their thermoelectric performances were analyzed (see **Figure 4**). The evolution of the Seebeck coefficient (Figure 4a) and electrical conductivity (Figure 4b) measured in the in-plane direction at room temperature as a function of the copper content has been divided into three differentiated regions. The first zone (I) corresponds to lower Seebeck coefficient and higher electrical conductivity, marked in light gray. These samples present mainly the orthorhombic α-Cu_2Se and α-Cu phases, according to XRD, with crystalline sizes smaller than 100 nm. Regarding the second area (II), it corresponds to Cu/Se ratios between 2 and 4. In this region, the highest values of PF (Figure 4c) are observed. The maximum PF is of 1.1 mW m^{-1} K^{-2}, for the film with ratio Cu/Se = 2. For that ratio, the cubic β-Cu_2Se phase is the only one present. The measured power factor 1.1 mW m^{-1} K^{-2} at room temperature is on the state of the art compared to bulk samples, and five times larger than those reported previously for films. Finally, in the region of Cu/Se ratios between 4 and 9, the region (III), even though the Seebeck coefficient values are still high, these films show very low values of electrical conductivity, which translates into low power factors, as expected for granular films with high porosity. For these films, the crystalline structure is a mixture of dirty metallic α-Cu and α-Cu_2Se. This second phase, which is present even for the films with highest content in copper (see Figure S4 of the Supporting Information), is the responsible of the high Seebeck coefficient measured. The low electrical conductivity found in these films can be explained by looking at the cross-sectional images of SEM, where it can be observed that the films are not continuous.

In order to fully characterize from a thermoelectric point of view the cross-plane thermal conductivity κ of the film with the highest power factor, that is Cu/Se = 2, was measured by the scanning thermal microscopy technique in the 3ω mode (3ω-SThM) at room temperature. **Figure 5** shows a comparison between the morphology observed by SEM, the topographic, and the thermal images obtained with the atomic force microscope. Through the thermal image, it is possible to determine an average thermal conductivity κ of 0.8 ± 0.1 W m^{-1} K^{-1}. Additional information about the parameters used for the thermal conductivity calculations and the tip calibration can be found in Figure 7S (see Supporting Information).

Therefore, taking into account that the β-Cu_2Se phase is cubic (and therefore isotropic as far as Seebeck, electrical conductivity, and thermal conductivity are concerned) and assuming no additional anisotropy in the properties induced by the shape, one can calculate a total zT value of 0.4 at room temperature. In order to correlate these values with those found in the literature for Cu_2Se, a comparison of the power factors obtained with this growth technique with those found in the literature for copper selenide compounds is shown in **Figure 6**. It is important to highlight that the power factors obtained in this work are not only in good agreement with

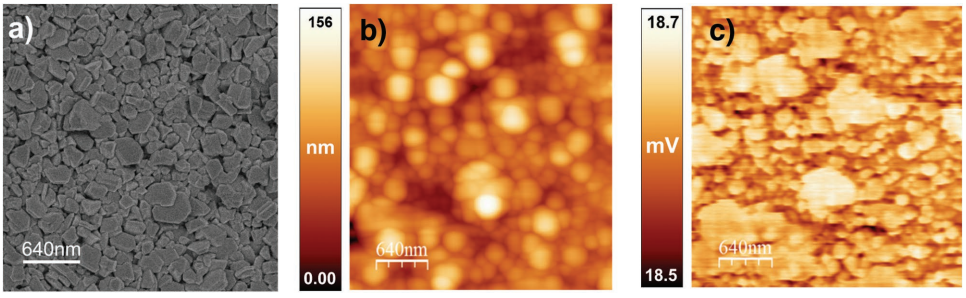

Figure 5. SEM and topographical information of the area of the Cu_2Se film where the measurement of thermal conductivity was carried out are shown: in a) SEM micrograph of the sample, b) AFM topography, which an statistical average of the roughness is 20 ± 5 nm, and c) the thermal image obtained during the 3ω-SThM scans on the same area.

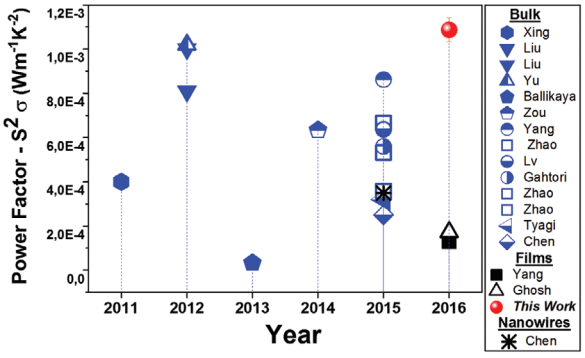

Year	zT	Reference
2012	0.2	Liu
2012	0.3	Yu
2016	0.4	This work

Figure 6. On the right-hand side, a summary of the most recent reported power factor values in the literature for copper selenides is found. These samples were obtained by different routes, such as Spark plasma sintering technique,[4,5,22–28] ball milling and hot pressing,[24,29] quenched bulks,[30] electrodeposition,[43] solvothermal method,[40] pulsed laser deposition,[41] galvanic deposition,[42] and our pulse hybrid reactive magnetron sputtering (PHRMS). On the left hand, there is a table with the highest values of zT at room temperature reported for Cu_2Se.

what is being currently reported, but also slightly higher than the state of the art values for bulk materials[4,5,29] and five times higher than any previously reported value for films prepared by other methods.[40–42] This highlights the quality of the films obtained by PHRMS. Likewise, a table showing the evolution of the figure of merit at room temperature is shown in Figure 6. Having a figure of merit of 0.4 at room temperature means an increase of around 30% compared with the best previously reported value for bulk material[5] at room temperature. These promising values open the door to manufacturing selenide films with high quality for different applications, such as thermoelectric and solar industries with the PHRMS developed in this work.

3. Conclusions

The particular type of surface reaction and incorporation kinetics, characteristic of the PHRMS technique that we describe in this work, allows for a single-step direct sputtering deposition of excellent quality selenide films at reduced growth temperatures compatible with flexible polymeric substrates and at high growth rates. Characterization of various sets of samples, with outstanding thermoelectric properties for Cu/Se = 2 nominal composition ratio, were performed. High zT values at room temperature are achieved comparable, if not superior, to those obtained for bulk samples prepared by other methods. Actually, the best-measured values for room temperature are on the state of the art as far as power factor (1.1 mW m^{-1} K^{-2}) is concerned, and even five times larger than those reported previously for films. A thermal conductivity of 0.8 ± 0.1 W m^{-1} K^{-1} was measured at room temperature and, assuming no anisotropy in the thermoelectric properties, a zT of 0.4 at room temperature is obtained.

It can be also concluded that the PHRMS concept developed in this work is not only valid for the fabrication of thermoelectric Cu_2Se thin films, which has been used as proof of concept material, but it can also be used for a wide range of different selenide films (such as $MbSe_2$, WSe_2, AgSe, SnSe, CIGS, etc.), which present interesting applications, as 2D materials, solar cells, etc. Therefore, the PHRMS growth technique is a feasible strategy for the selection and design of promising high-performance selenide-based materials in the future. This fabrication method can be done at room temperature, which allows the use of organic and/or flexible substrates. Finally, it is important to highlight that it is scalable to the industry.

4. Experimental Section

The deposition of the Cu/Se films was carried out in a modified reactive sputtering system equipped with high throughput corrosion resistant turbopump operating at a pressure of 6×10^{-3} mbar of 99.995 purity Ar and computer controlled. The PHRMS process was implemented with a standard magnetron with a 2.00" diameter × 0.250" thickness metallic target of copper 99.999% purity, (from Kurt Lesker), and a specially built Pulsed Valve Effusion cell charged with Selenium pellets, <5 mm particle size of 99.999% purity (from Sigma–Aldrich) and temperature stabilized at 330.0 °C by an EUROTHERM device with 0.1 °C resolution. The sample holder is able to positioning successively through a mask up to 12 samples per run without breaking the vacuum, and could be heated up to 600 °C, but it was left at room temperature for present deposition experiments. The maximum temperature registered at the sample holder thermocouple after 1 h continuous deposition growth was around 150 °C.

The structural analysis of films with different copper content was performed at the XRD2 beamline of the National Synchrotron Light Source at the Brazilian Synchrotron (LNLS) (λ = 1.3775 Å) in the $20° < 2\theta < 65°$. The detector is a Mythen detector 1 K from Dectris, mounted on grazing-incidence diffraction, and the measurements were performed at room temperature. The morphology was observed by field-emission SEM with an FEI Verios 460 at 3 kV accelerating voltage, and chemical composition was determined with a SEM with electron-dispersive X-ray analysis JEOL JSM6335F microscope at the Interdepartmental Research Service of the Universidad Autónoma de Madrid (SIdI-UAM). The microstructure and chemical composition of the samples were also examined by transmission electron microscopy (FEI Titan ChemiSTEM operating at 200 kV) with high-angle annular dark Field (HAADF) acquisition of simultaneous EDS/EELS. The in-plane electrical resistivity and Seebeck coefficient were measured at room temperature using a commercial LSR-3 Linseis system. This system is periodically calibrated by a constantan standard to ensure its accuracy. Moreover, cross-check of the obtained values has been carried out in an Ecopia Hall Effect Measurement System. The film thickness was measured by a profilometer Dektak 150 (Veeco) (see Table 1S in the Supporting information).

The cross-plane thermal conductivity was determined at room temperature by a 3ω-SThM method. The equipment used in these measurements is a commercial AFM from Nanotec Electronica connected to an ultrahigh-frequency lock-in amplifier from Zurich Instruments to process the 3ω bridge voltage signal generated (see Figure 7S in the Supporting Information for calibration and metrology). The tip is heated up with an AC current and it exchanges heat with the ambient and with the surface of the sample when operating in a contact mode.[44] The changes in the temperature of the tip due to joule heating will be dependent on the thermal conductivity of the sample. This effect will cause a 3ω electrical signal response in the tip that can be measured.[45] The use of a commercial V-shaped Pd/SiN thermoresistive probe from Bruker AFM allows obtaining thermal images with submicron spatial resolution, at the same time that the topographic information of the sample is recorded.

Supporting Information

Supporting Information is available from the Wiley Online Library or from the author.

Acknowledgements

This work was supported by 7th framework European project Nano-structured High-efficiency Thermo-Electric Converters project NANOHITEC 263306, ERC Nano-TEC project, the national project PHOMENTA MAT2011-27911 and Intramural project INFANTE. J.A.P.-T. acknowledges the Spanish Ministerio de Economia y Competitividad for their FPI grant. The authors wish to thank the National Synchrotron Light Source at the Brazilian Synchrotron (LNLS)—XRD2 beamline—in Campinas, Brazil, for the SR-GIXRD measurements. The authors acknowledge the X-SEM Laboratory at IMM (VERIOS 460 from FEI) and funding from MINECO under project CSIC 13-4E-1794 with support from EU (FEDER, FSE).

Conflict of Interest

The authors declare no conflict of interest.

Keywords

copper selenide, cross-plane thermal conductivity, flexible Cu_2Se, new pulse controlled reactive magnetron sputtering, PHRMS, thermoelectric properties, thin films

Received: January 20, 2017
Revised: April 6, 2017
Published online:

[1] C. Gayner, K. K. Kar, *Prog. Mater. Sci.* **2016**, *83*, 330.
[2] M. Martín-González, O. Caballero-Calero, P. Díaz-Chao, *Renewable Sustainable Energy Rev.* **2013**, *24*, 288.
[3] P. Qiu, X. Shi, L. Chen, *Energy Storage Mater.* **2016**, *3*, 85.
[4] B. Gahtori, S. Bathula, K. Tyagi, M. Jayasimhadri, A. Srivastava, S. Singh, R. Budhani, A. Dhar, *Nano Energy* **2015**, *13*, 36.
[5] H. Liu, X. Shi, F. Xu, L. Zhang, W. Zhang, L. Chen, Q. Lin, C. Uher, T. Day, G. J. Snyder, *Nat. Mater.* **2012**, *11*, 422.
[6] H. Liu, X. Yuan, P. Lu, X. Shi, F. Xu, Y. He, Y. Tang, S. Bai, W. Zhang, L. Chen, *Adv. Mater.* **2013**, *25*, 6607.
[7] P. P. Hankare, A. S. Khomane, P. A. Chate, K. C. Rathod, K. M. Garadkar, *J. Alloys Compd.* **2009**, *469*, 478.
[8] V. M. García, P. K. Nair, M. T. S. Nair, *J. Cryst. Growth* **1999**, *203*, 113.
[9] M. Dhanam, P. K. Manoj, R. R. Prabhu, *J. Cryst. Growth* **2005**, *280*, 425.
[10] C.-C. Ting, W.-Y. Lee, *Electrochem. Solid-State Lett.* **2011**, *15*, H1.
[11] S. R. Gosavi, N. G. Deshpande, Y. G. Gudage, R. Sharma, *J. Alloys Compd.* **2008**, *448*, 344.
[12] A. Sobhani, M. Salavati-Niasari, *Ceram. Int.* **2014**, *40*, 8173.
[13] A. Zyoud, R. S. Al-Kerm, R. S. Al-Kerm, M. Waseem, H. S. H. Mohammed, D. Park, G. Campet, N. Sabli, H. S. Hilal, *Electrochim. Acta* **2015**, *174*, 472.
[14] A. Cho, S. Ahn, J. H. Yun, J. Gwak, S. K. Ahn, K. Shin, J. Yoo, H. Song, K. Yoon, *Thin Solid Films* **2013**, *546*, 299.
[15] R. Ivanauskas, J. Baltrusaitis, *Appl. Surf. Sci.* **2013**, *283*, 360.
[16] Z. Tang, K. Aoyagi, Y. Nukui, K. Kosaka, H. Uegaki, J. Chatana, D. Hironiwa, T. Minemoto, *Sol. Energy Mater. Sol. Cells* **2015**, *143*, 311.
[17] B. Güzeldir, M. Sağlam, *Spectrochim. Acta, Part A* **2015**, *150*, 111.
[18] H. Okimura, T. Matsumae, R. Makabe, *Thin Solid Films* **1980**, *71*, 53.
[19] Y. Lv, J. Chen, R.-K. Zheng, X. Shi, J. Song, T. Zhang, X. Li, L. Chen, *Ceram. Int.* **2015**, *41*, 7439.
[20] A. Casu, A. Genovese, L. Manna, P. Longo, J. Buha, G. A. Botton, S. Lazar, M. U. Kahaly, U. Schwingenschloegl, M. Prato, *ACS Nano* **2016**, *10*, 2406.
[21] T. Ohtani, M. Shohno, *J. Solid State Chem.* **2004**, *177*, 3886.
[22] H. Liu, X. Shi, M. Kirkham, H. Wang, Q. Li, C. Uher, W. Zhang, L. Chen, *Mater. Lett.* **2013**, *93*, 121.
[23] L. Zou, B.-P. Zhang, Z.-H. Ge, L.-J. Zhang, *J. Mater. Res.* **2014**, *29*, 1047.
[24] X. Xing-Xing, X. Wen-Jie, T. Xin-Feng, Z. Qing-Jie, *Chin. Phys. B* **2011**, *20*, 087201.
[25] K. Tyagi, B. Gahtori, S. Bathula, M. Jayasimhadri, S. Sharma, N. K. Singh, D. Haranath, A. Srivastava, A. Dhar, *Solid State Commun.* **2015**, *207*, 21.
[26] X. Chen, Z. Li, J. Yang, Q. Sun, S. Dou, *J. Colloid Interface Sci.* **2015**, *442*, 140.
[27] X. Q. Chen, Z. Li, S. X. Dou, *ACS Appl. Mater Interfaces* **2015**, *7*, 13295.
[28] S. Ballikaya, H. Chi, J. R. Salvador, C. Uher, *J. Mater. Chem. A* **2013**, *1*, 12478.
[29] B. Yu, W. Liu, S. Chen, H. Wang, H. Wang, G. Chen, Z. Ren, *Nano Energy* **2012**, *1*, 472.
[30] L.-L. Zhao, X.-L. Wang, J.-Y. Wang, Z.-X. Cheng, S.-X. Dou, J. Wang, L.-Q. Liu, *Sci. Rep.* **2015**, *5*, 7671.
[31] J. O. Jeon, K. D. Lee, L. Seul Oh, S. W. Seo, D. K. Lee, H. Kim, J. h. Jeong, M. J. Ko, B. Kim, H. J. Son, *ChemSusChem* **2014**, *7*, 1073.
[32] G. Hanna, J. Mattheis, V. Laptev, Y. Yamamoto, U. Rau, H. Schock, *Thin Solid Films* **2003**, *431*, 31.
[33] F. Briones, I. Fernández, A. Wennberg, Pulsed valve cracker effusion cell, **2014**, WO 2014170503 A1.
[34] D. L. Smith, *Thin-Film Deposition: Principles and Practice*, Vol. *108*, McGraw-Hill, New York **1995**.
[35] F. Briones, L. González, A. Ruiz, *Appl. Phys. A: Mater. Sci. Process.* **1989**, *49*, 729.
[36] Y. Horikoshi, H. Yamaguchi, F. Briones, M. Kawashima, *J. Cryst. Growth* **1990**, *105*, 326.
[37] L.-C. Zhang, G. Qin, W.-Z. Fang, H.-J. Cui, Q.-R. Zheng, Q.-B. Yan, G. Su, *Sci. Rep.* **2016**, *6*, 19830.
[38] J. Y. Kim, J. C. Grossman, *Nano Lett.* **2015**, *15*, 2830.
[39] Y. Guo, J. Mu, C. Hou, H. Wang, Q. Zhang, Y. Li, *Carbon* **2016**, *107*, 146.
[40] L. Yang, Z.-G. Chen, G. Han, M. Hong, J. Zou, *Acta Mater.* **2016**, *113*, 140.
[41] Y. Lv, J. Chen, R.-K. Zheng, X. Shi, J. Song, T. Zhang, X. Li, L. Chen, *Ceram. Int.* **2015**, *41*, 7439.
[42] A. Ghosh, C. Kulsi, D. Banerjee, A. Mondal, *Appl. Surf. Sci.* **2016**, *369*, 525.
[43] M. Yang, Z. Shen, X. Liu, W. Wang, *J. Electron. Mater.* **2016**, *45*, 1974.
[44] A. Majumdar, *Annu. Rev. Mater. Sci.* **1999**, *29*, 505.
[45] A. A. Wilson, M. M. Rojo, B. Abad, J. A. Perez, J. Maiz, J. Schomacker, M. Martín-Gonzalez, D.-A. Borca-Tasciuc, T. Borca-Tasciuc, *Nanoscale* **2015**, *7*, 15404.

ADVANCED MATERIALS TECHNOLOGIES

Supporting Information

for *Adv. Mater. Technol.*, DOI: 10.1002/admt.201700012

Pulsed Hybrid Reactive Magnetron Sputtering for High *zT* Cu_2Se Thermoelectric Films

*Jaime A. Perez-Taborda, Liliana Vera, Olga Caballero-Calero, Elvis O. Lopez, Juan J. Romero, Daniel G. Stroppa, Fernando Briones, and Marisol Martin-Gonzalez**

Supporting Information

Pulsed Hybrid Reactive Magnetron Sputtering for high *zT* Cu_2Se thermoelectric films

Jaime A. Perez-Taborda,[1] Liliana Vera,[1] Olga Caballero-Calero,[1] Elvis O. Lopez,[2] Juan J. Romero, [1] Daniel G. Stroppa,[3] Fernando Briones, [1] and Marisol Martin-Gonzalez [1]

[1] IMM-Instituto de Microelectrónica de Madrid (CNM-CSIC), Isaac Newton 8, PTM, E-28760 Tres Cantos, Madrid, Spain

[2] Department of Applied Physics, Brazilian Center for Physics Research, Urca, Rio de Janeiro 22290-180, Brazil

[3] International Iberian Nanotechnology Laboratory (INL), Av. Mestre Jose Veiga, 4715-330 Braga, Portugal

This Supporting Information contains:

- **Section I (Figure 1S)**
  A photograph of a Cu_2Se film grown on a flexible substrate.

- **Section II (Figure 2S)**
  Additional SEM images with Secondary electron (SE) analysis and Backscattered electrons (BSE) of the films cross-section for some Cu/Se ratios.

- **Section III (Table 1S and Table 2S, Figure 3S, 4S)**
  Table of crystal size, thickness values for different composition ratios extracted from the SR-GIXRD measured spectra. Table of SR-GIXRD measurements and their penetration depth in the film (Figure 3S). Detailed spectra for the Cu/Se = 9 film (Figure 4S).

- **Section IV. (Figures 5S and 6S)**

  High Angle Annular Dark Field (HAADF) STEM -EDS, compositional and local diffraction pattern for samples with ratios Cu/Se of 1.9, 2 and 2.1.

- **Section V (Figure 7S)**
  Cross-plane thermal conductivity measurement of a Cu_2Se film by the 3ω-SThM technique performed at room temperature, along with details of the experimental setup.

SECTION I

Polymer substrates have drawn attention for the fabrication of flexible thermoelectric devices due to their high thermal and chemical stability [1-3]. One of the advantages of the technique *Pulsed hybrid magnetron sputtering* (PHRMS) described here is the possibility of depositing Cu_2Se films on flexible substrates at room temperature (see **Figure 1S.)**.

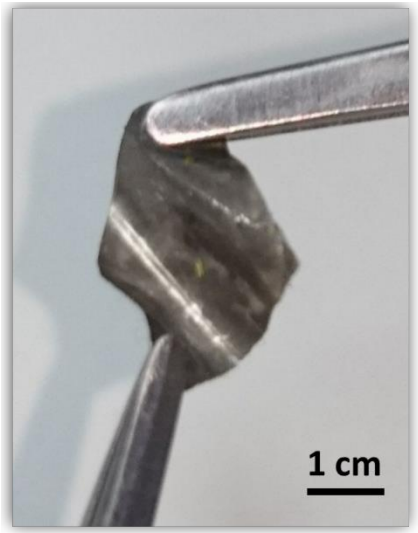

Figure 1S: A photograph of a 1 μm thick Cu_2Se film deposited on Kapton® Polyimide tape grown by Pulsed reactive magnetron sputtering (PC-RMS).

SECTION II

A morphological study through the topographic contrast measured by SEM images with secondary electron (SE) in cross-section for different content Cu/Se ratios has been performed (See **Figure 2S**, marked as SE). Simultaneously, by the use of a backscattered electrons detector (BSE), it is possible to quickly distinguish the different compositional zones present in the films. In the case of images obtained by detecting BSE, the average greyscale differences correspond to the different phases present in the films for each Cu/Se ratio (See **Figure 2S**, marked as BSE). Thus, a brighter BSE intensity correlates with a greater atomic number (Z) (Selenium) in the sample, and dark areas have a lower Z (Copper). This is observed for Cu/Se > 2 ratio compositions, where the films show a darker contrast (excess in copper) along with brighter areas associated with phases with selenium content.

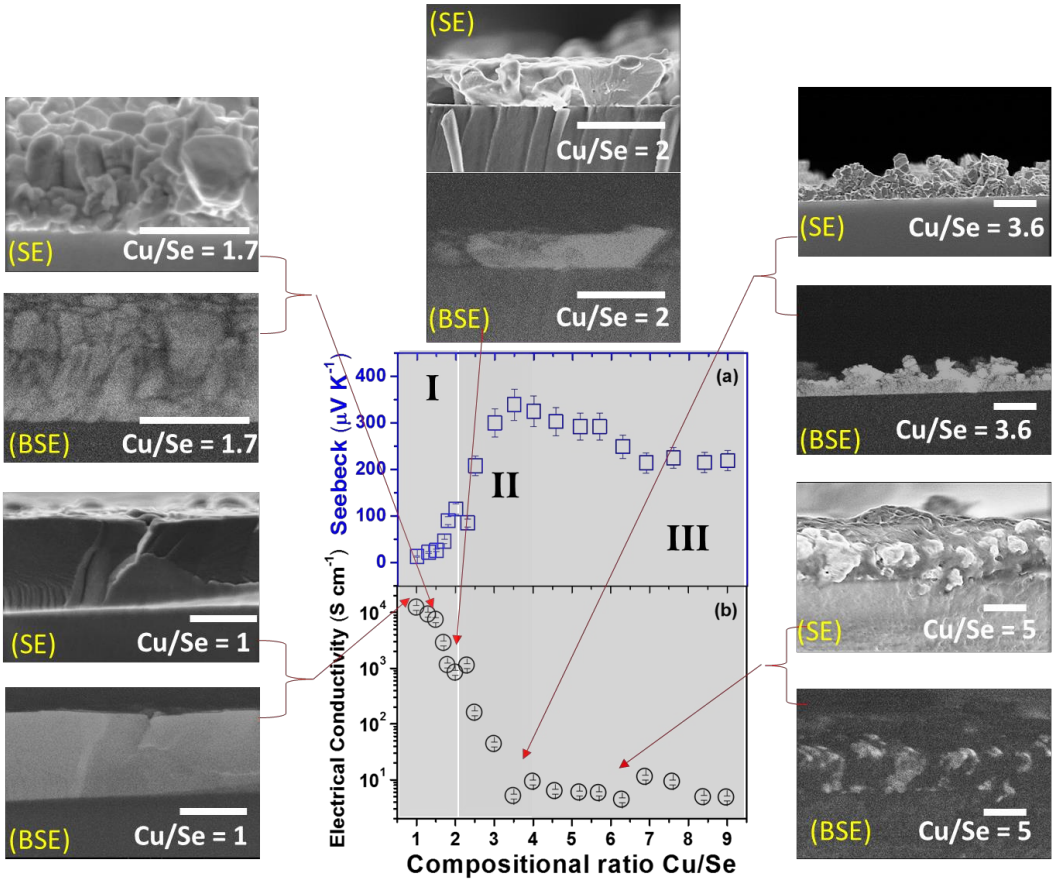

Figure 2S: SEM images with detection of secondary electrons (SE) in cross-section for different Cu/Se ratios and *Backscattered Electron Detector* (BSE) images detected simultaneously in the same zone, showing a loss of continuity of the film due to porosities and phase-segregation for samples with Cu/Se ratio > 2.

SECTION III

The crystallinity and crystal orientation of the $Cu_{2-x}Se$ crystalline films have been investigated by SR-GIXRD diffraction, presented in **Figure 2.** A variation of the full-width at maximum (FWHM) of the XRD peaks is observed as the incorporation of copper in the films increases. Crystallite size (*D*) was calculated using Debye Scherrer´s formula:

$$\boldsymbol{D = 0.94\lambda/\beta cos\theta}$$

where $\boldsymbol{D}$ is the crystallite size, $\boldsymbol{\lambda}$ is the wavelength, $\boldsymbol{\beta}$ is the full width at half maxima (**FWHM**) in radians and $\boldsymbol{\theta}$ is the Bragg's angle. In **table 1S** it is observed that the cristalline size changes as the Cu/Se ratio changes, from 113 nm for the γ- Hexagonal phase (Cu/Se=1), to 65 nm β - Cubic phase (Cu/Se =2), and even to smaller grain sizes, around 26 nm, for Orthorhombic phase (Cu/Se = 9). This trend is also follwed by the grain sizes observed in the SEM images.

Composition Ratio Cu/Se	2 Theta (degree)	(hkl)	FWHM degree	Calculated Crystallite size (nm)	Thicknesses of Films (nm)
α - Orthorhombic phase					
2.4	23.60	221	0.090698	83.60	833.3
3.6	23.57	221	0.14872	50.98	613.4
5	23.63	221	0.145	52.30	602.1
9	23.59	221	0.29243	25.93	846.5
β - Cubic phase					
2	39.13	220	0.11751	65.41	732.6
γ - Hexagonal phase					
1	24.81	102	0.06707	113.3	653.8

Table 1S. Values of FWHM and crystallite size calculated from the measurements of SR-GIXRD (with λ =1.3775 Å) for the different Cu/Se ratios, according to the assigned phases. For the assignment of (*hkl*) of the phases: Hexagonal **γ-CuSe,** orthorhombic **α-Cu_2Se** and Cubic **β-Cu_2Se** have been done with standard identification cards JCPDS: 00-027-0185, 00-047-1448 and 04-015-3687 respectively. Values have been obtained using Scherrer equation.

In order to determine whether SR-GIXRD measurements describe the entire sample, the penetration depth ($\boldsymbol{\tau}$) has been calculated. The penetration depth of the beam is dependent on the wavelength (λ=1.3775 Å in our case) and incidence angle (5º in our case) through the law of Beer-Lambert law [4] $\boldsymbol{I = I_0 e^{-\mu x}}$, where $\boldsymbol{I_0}$ is the intensity of the incoming radiation, $\boldsymbol{\mu}$ is the linear attenuation coefficient, and $\boldsymbol{x}$ is the path length [5]. The parameter $\boldsymbol{\mu}$ depends on the wavelength of the X- rays, as well as on the chemical composition and density, which we will take as that of Cu_2Se 6.803(g/cm^3) for simplicity. The penetration depth calculated with these parameters is shown in **Figure 3S** for the Cu/Se = 1, 2 and 9 ratios. This value has been confirmed by the online database of X-ray Data Booklet of Lawrence Berkeley National Laboratory's (LBNL) Materials Sciences Division [6].

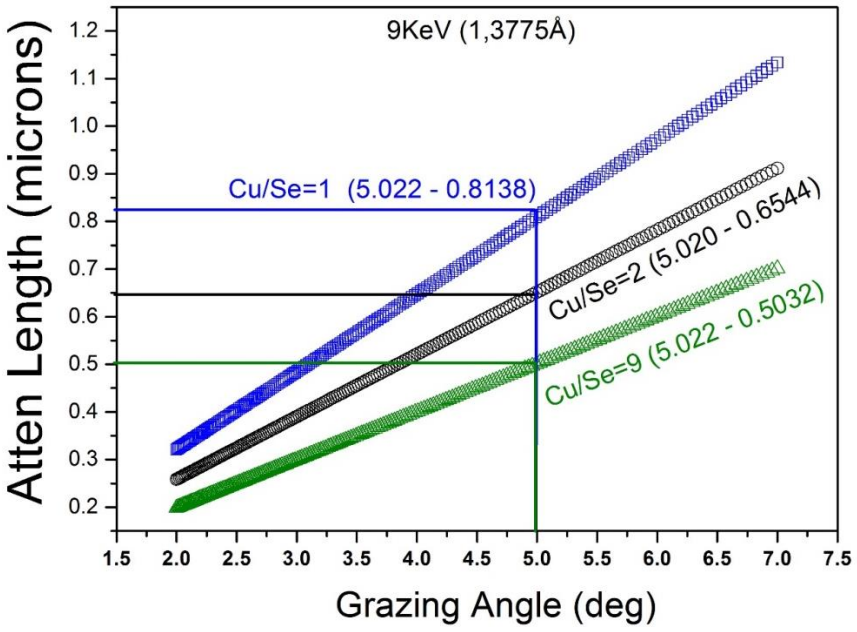

Figure 3S: shows the approximate length attenuation for grazing angle with a wavelength 1.3775 Å and an energy of 9KeV. In black circles, it is shown for the stoichiometry of Cu_2Se with a penetration of the X-ray around 654 nm. For the case of CuSe marked in blue squares the penetration is of 813 nm. Finally, for a ratio Cu / Se = 9 is shown in green triangles for a penetration of up to 503 nm at a 5° angle of incidence.

Finally, to confirm the contribution of the Cu_2Se phase even in the films with the highest content in copper (namely the Cu/Se=9), **Figure 4S** shows the data of SR-GXRD with two magnified regions, where the contribution from the α-Cu_2Se phase can be clearly seen.

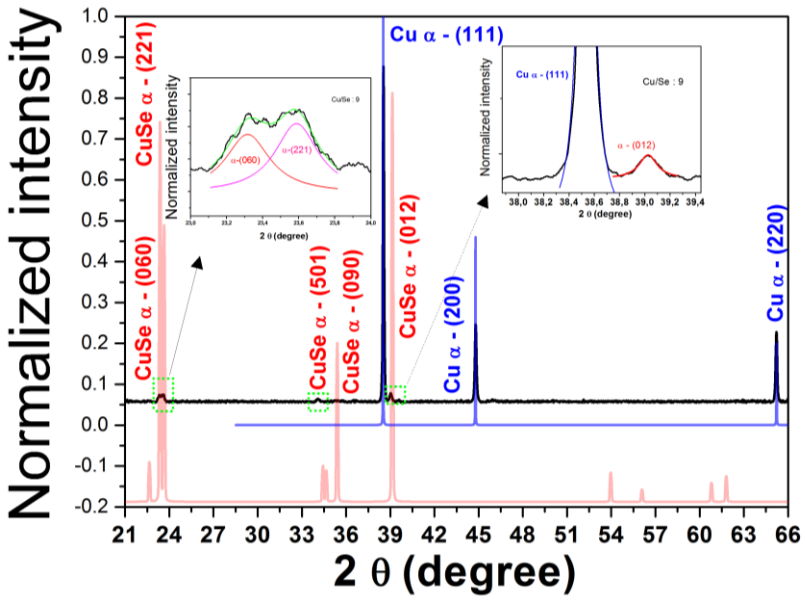

Figure 4S Theoretical XRD Patterns in red for α-Cu_2Se orthorombic phase PDF - 00-047-1448 and blue for Cubic phase α-Cu PDF 00-004-0836 are shown. In black color we show the diffractogram corresponding to the Cu / Se = 9 composition, with two magnified regions, where the contribution from α-Cu_2Se can be seen.

SECTION IV (Local diffraction pattern for samples of ratios Cu/Se of 2 and 2.5)

- **Cu/Se = 2.0**

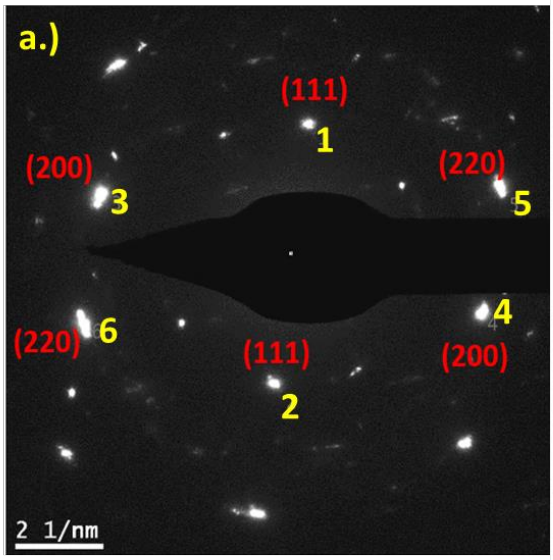

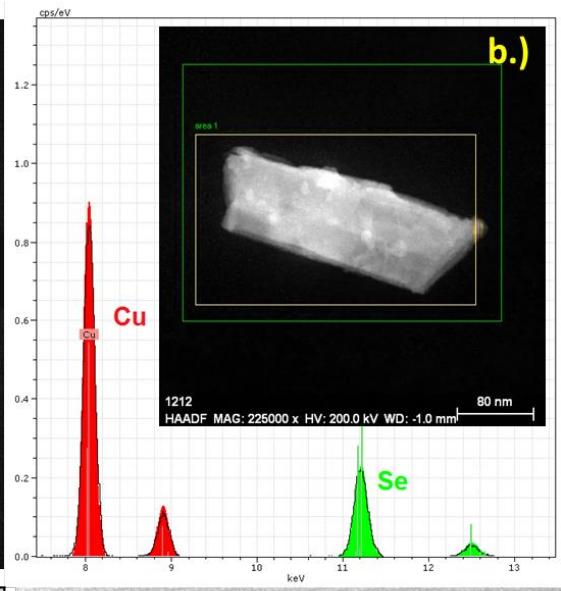

d.)

Spot #	d-Spacing (nm)	Rec. Pos.(1/nm)	Degrees to Spot 1
1	0.3446	2.902	0.00
2	0.3453	2.896	179.95
3	0.2219	4.506	80.79
4	0.2216	4.512	99.26
5	0.2024	4.942	65.34
6	0.2020	4.952	116.05

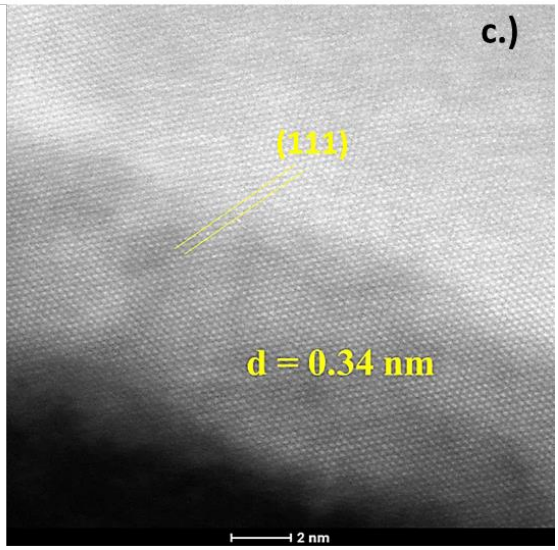

Element	series	[norm. wt.%]	[norm. at.%]	Error in wt.% (1 Sigma)
Copper	K-series	63.096	66.977	1.811785
Selenium	K-series	36.904	33.023	1.073677
	Sum:	100	100	

Figure 5S: In **a.)** the electron diffraction pattern for the β-Cu_2Se is shown**.** The inset in **b.)** shows the STEM image corresponding to a Cu/Se ratio= 2 obtained with 2 measurement regions of approximated area: 0.30 μm^2. In **c.)** an HRTEM image is shown for Cu/Se= 2 ratio with an [111] plane (marked as yellow lines), with an interplanar spacing of ~0.34 nm. Finally, in **d.)** a table with the d-spacing values for the 6 local diffraction spots corresponding to the image **a.)** is shown. The compositional analysis of b.) is shown in the table.

- **Cu/Se = 2.5**

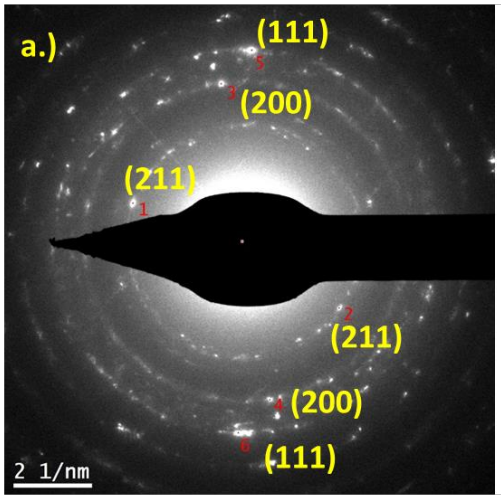

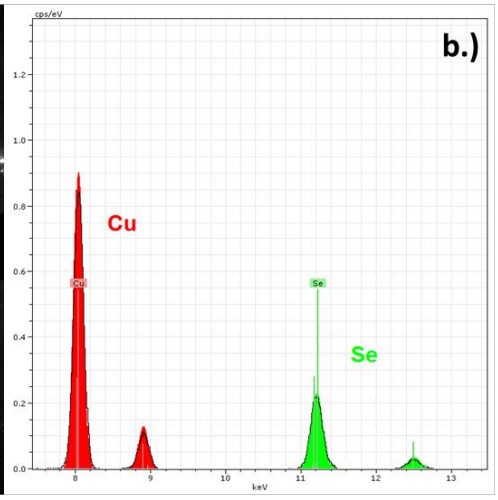

d.) Spot #	d-Spacing (nm)	Rec. Pos.(1/nm)	Degrees to Spot 1
1	0.3422	2.923	0.00
2	0.3350	2.985	164.76
3	0.2219	4.506	63.21
4	0.2216	4.512	119.23
5	0.2063	4.848	73.65
6	0.2060	4.855	108.15

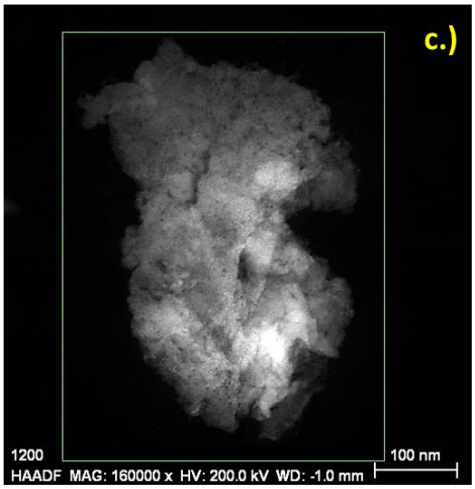

Element	series	[norm. wt.%]	[norm. at.%]	Error in wt.% (1 Sigma)
Copper	K-series	66.856	71.479	1.945499
Selenium	K-series	33.144	28.521	0.989598
	Sum:	100	100	

Figure 6S: In **a.)** the electron diffraction pattern for the Cu/Se = 2.5 sample corresponding to a highly polycrystalline material. In **b.)** there is the STEM image corresponding to Cu/Se ratio: 2.5 as calculated from the at%, obtained in 2 measurement regions of approximated area: 0.30 μm^2 in the zone shown in **c.)** In **d.)** a table with the d-spacing values for the 6 points shown in the local diffraction in the image **a)** is shown. Finally, the compositional analisis obtained from b.) is shown in the table.

SECTION IV

The thermal conductivity measurement of the Cu_2Se film was performed with the 3ω-SThM technique using a similar procedure as in ref [7]. The AFM from Nanotec Electronica® was used to position on top of the sample, a micro-fabricated silicon nitride probe that is coated with a thermoresistive element at the end of the tip. The SThM probe used in this experiment was purchased from Bruker®. The AFM is coupled with a Wheatstone bridge and the small fluctuations on the tip resistance can be detected and amplified by a lock-in system. In order to carry out the measurement in the Cu_2Se film, a previous calibration process has to be performed, as in ref [8]. The aim of this calibration is to determine the thermal exchange radius b and the thermal contact resistance $R_{th,c}$, between the tip and the sample as in [8,9]. The samples used to find the cross point between b and $R_{th,c}$, were polyaniline (PANI) with 7% graphene platelets, tellurium film and borosilicate glass with well-defined thermal conductivities of 0.65 $W \cdot m^{-1} \cdot K^{-1}$, 0.75 $W \cdot m^{-1} \cdot K^{-1}$ and 1.1 $W \cdot m^{-1} \cdot K^{-1}$ respectively. In **Figure 7S** the curves obtained with these calibration samples are shown.

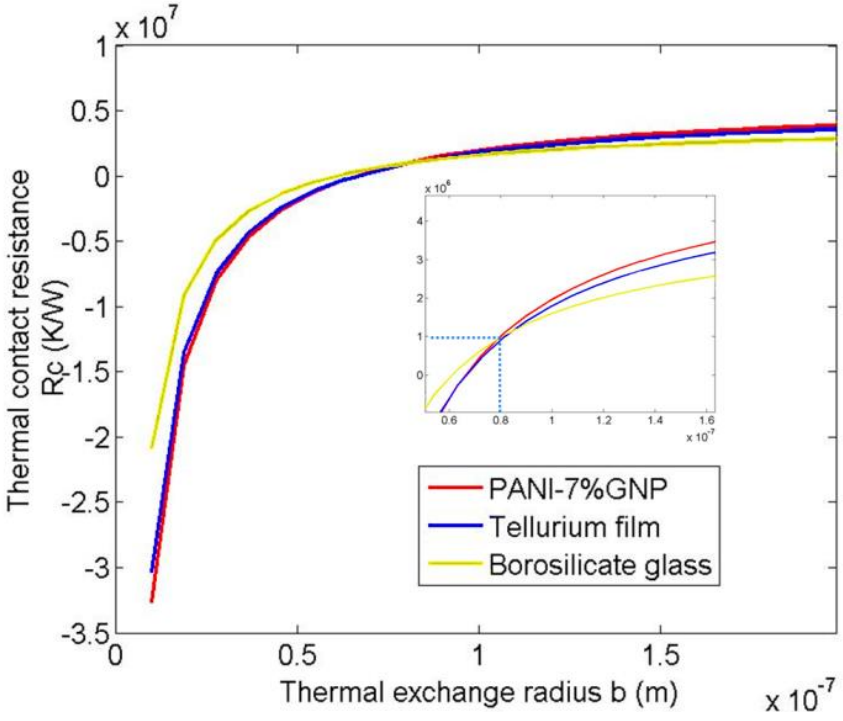

Figure 7S.Thermal contact resistance as a function of thermal exchange radius. In the inset of the figure, the crossing among the three calibration samples can be seen. The dotted blue line shows the cross point used for the calculations, obtaining $b = (8.12 \pm 0.27) \times 10^{-8}$ m and $(1.02 \pm 0.11) \times 10^{6}$ $K \cdot W^{-1}$.

REFERENCES

[1] J.-H. Bahk, H. Fang, K. Yazawa, and A. Shakouri, Journal of Materials Chemistry C **3**, 10362 (2015).

[2] T. Varghese, C. Hollar, J. Richardson, N. Kempf, C. Han, P. Gamarachchi, D. Estrada, R. J. Mehta, and Y. Zhang, Scientific Reports **6** (2016).

[3] Z. Lu, M. Layani, X. Zhao, L. P. Tan, T. Sun, S. Fan, Q. Yan, S. Magdassi, and H. H. Hng, Small **10**, 3551 (2014).

[4] H. C. Van de Hulst and V. Twersky, Physics Today **10**, 28 (1957).

[5] B. L. Henke, E. M. Gullikson, and J. C. Davis, Atomic data and nuclear data tables **54**, 181 (1993).

[6] M. Birkholz, *Thin film analysis by X-ray scattering* (John Wiley & Sons, 2006).

[7] E. Puyoo, S. Grauby, J.-M. Rampnoux, E. Rouvière, and S. Dilhaire, Journal of Applied Physics **109**, 024302 (2011).

[8] A. A. Wilson, M. M. Rojo, B. Abad, J. A. Perez, J. Maiz, J. Schomacker, M. Martín-Gonzalez, D.-A. Borca-Tasciuc, and T. Borca-Tasciuc, Nanoscale **7**, 15404 (2015).

[9] J. A. Perez-Taborda, M. M. Rojo, J. Maiz, N. Neophytou, and M. Martin-Gonzalez, Scientific Reports **6**, 32778 (2016).

PAPER V
Submitted to Advanced Energy Materials

Advanced Energy Materials
DOI: 10.1002/((please add manuscript number))
Article type: Communication or Full Papers:

Title: Ultrahigh Thermoelectric Performance in n-type Silver Selenide films

*Jaime Andres Perez-Taborda, Olga Caballero-Calero, Liliana Vera-Londoño, Fernando Briones, Marisol Martin-Gonzalez**

IMM-Instituto de Microelectrónica de Madrid (CNM-CSIC), Isaac Newton 8, PTM, E-28760 Tres Cantos, Madrid, Spain
*E-mail: marisol@imm.cnm.csic.es

Keywords: Thermoelectricity, Selenides, Reactive Sputtering, Thin film.

According to the most recent global energy demand reports[1] and energy outlook, the global energy consumption[2] will continue to increase around 50% the next 23 years [1,2]. Only a fraction of the energy produced is actually used for its intended purpose; the majority of the energy is wasted as useless heat. On average, two-thirds of all energy produced is lost as heat [4]. It is this wasted heat one of the most abundant untapped resources on the planet and it could be recovered through thermoelectric materials in the form of electricity. Actually, many companies contemplate this possibility [5-7]. A possible scenario with thermoelectric materials with an efficiency of 5% and a current energy loss in the form of heat of about 208,000 terawatt hours (TWh) the potential size of the thermoelectric market is around $ 1 trillion per year [8].

The efficiency of a thermoelectric (TE) material is controlled by its figure of merit, denoted as *zT*. This parameter is defined as $(S^2 \cdot \sigma) \cdot T \cdot \kappa^{-1}$ where S is the Seebeck coefficient, T is the absolute temperature, σ is the electrical conductivity, κ is the total thermal conductivity and wherein $(S^2 \cdot \sigma)$ is known as the Power Factor (PF). The thermal conductivity itself is a sum of the lattice and electronic contributions, $\boldsymbol{\kappa_L}$ and $\boldsymbol{\kappa_e}$, respectively. The search for more efficient thermoelectric materials and how to enhance their properties is a hot topic in the field.

Motivated by the promising TE properties and new advanced approaches in liquid-like superionic thermoelectric materials, such as Cu_2Se[9,10], Cu_2S[11,12], and Ag_2Se[13,14], many authors have focused their attention in these materials due to their particular low lattice thermal conductivity and high thermoelectric figure of merit. The idea of using the superionic conductors phonon-liquid electron-crystal (PLEC)[10] in thermoelectric applications may be considered an extension of the phonon-glass electron-crystal concept (materials that can simultaneously exhibit high electrical conductivity and low thermal conductivity).[10,13] The elements of these types of binary chalcogenides are found in more abundance in the Earth's crust than others widely used for thermoelectric applications, such as Bi_2Te_3 (with a high price of Tellurium) [15], and are even present as earth minerals as Berzelianite (Cu_2Se), Chalcocite (Cu_2S), and Naumanite (Ag_2Se). [16]

These superionic conductor compounds point out a new direction to search for outstanding thermoelectric materials. On the one hand, for p-type semiconductors, bulk Cu_2Se stands out, showing an exceptional *zT* value of 2.1 at 700ºC [17]. This is possible due to the low value of its thermal conductivity, 0.34 $Wm^{-1}K^{-1}$, which comes from a full scale scattering of phonons by atomic dislocations, nanocrystalline grain boundaries and large nanopores [17]. Additionally, it has been reported [9] a critical scattering of electrons and phonons in bulk samples of I-doped Cu_2Se, obtaining a record *zT* as high as 2.3 near the transition temperature (~ 127 °C). Another outstanding p-type bulk material is policrystalline $Cu_{1.97}S$, with *zT* values near 1.9 at 700 ºC [18]. This high value is a result of its exceptional low thermal conductivity ($\boldsymbol{\kappa}$ values between 0.3 and 0.5 $Wm^{-1}K^{-1}$) combined with its high electrical conductivity values, between 120 and 185 $S \cdot cm^{-1}$, both in a wide temperature range, from 427 to 727ºC [12,18].

On the other hand, n-type superionic conductor compounds, such as bulk Ag_2Se, have been reported to have a *zT* value near 1 at room temperature.[13,19,20]. In this case, slight variations in the stoichiometry in bulk Ag_2Se influence greatly its figure of merit, as it was shown by Lee *et al.*[21], where silver to selenium ratio of Ag_xSe prepared by a mechanical alloying was varied between $1.73 < x < 2.33$. It was found that an excess of silver atoms or clusters increases the carrier concentration and decrease the Hall mobility, which has a crucial effect on the *zT*, which showed values from 0.09 to 0.60 at room temperature. Other effects of the stoichiometry were studied by Mi *et al.*[22], who sintered by spark plasma (SPS) Se-rich Ag_2Se pellets at 407ºC. They reported an improvement in PF and *zT* when small amounts of Se were added, which decreases the values of carrier concentrations, reaching *zT* values of 0.84 at

room temperature for $Ag_2Se_{1.06}$ samples, which had carrier concentrations of $5x10^{18}$ cm^{-3}. In general, it becomes clear that the Ag/Se ratio affects the electronic properties of the material, and in particular, the carrier concentration. The highest *zT* value reported at room temperature is 0.99, measured by Aliev *et al.* [19] for samples with Hall mobility values as high as 6100 cm^2 V^{-1} s^{-1} and carrier concentration of $6.5x10^{18}$ cm^{-3}. The highest PF reported was of 3.5 $mW \cdot m^{-1} \cdot K^{-2}$ for a polycrystalline Ag_2Se ingot obtained by direct reaction at 10^{-4} Torr and heated to about 1000 °C for 10 h, reported by Ferhat *et al.*[20]. In this case, a *zT* value of 0.96 at room temperature was found, due to its high electrical conductivity (1928 $S \cdot cm^{-1}$), Hall mobility (11610 $cm^2 \cdot V^{-1} \cdot s^{-1}$) and carrier concentration ($1.07x10^{18}$ cm^{-3}) values. Lower carrier concentrations, such as the $4.1 \cdot 10^{17}$ cm^{-1} reported by Wang *et al.*[23] for β-Ag_2Se powders obtained by a hydrothermal process and densified by SPS, revert in lower *zT* values, 0.6 in this case.

This influence of the Ag/Se ratio in the electronic properties of $Ag_{2+x}Se$, in particular for the carrier concentration, which drastically affects its thermoelectric properties, was the object of a theoretical work carried out by Day *et al.*[13], who used single parabolic band model calculations of the electronic transport properties of n-type $Ag_{2+x}Se$. Their result suggests that a *zT* greater than 1 from room temperature to 327ºC can be achieved if the carrier concentration is reduced to $1.6x10^{18}$ cm^{-3}. Nevertheless, the actual control over the stoichiometry is quite challenging for the way in which bulk $Ag_{2+x}Se$ is normally manufactured, due to Ag ion movement during both ingot consolidation and hot pressing. Moreover, these fabrication methods present further problems as far as homogeneity of the samples is concerned, making it difficult to establish a correlation between carrier concentration and the Ag or Se content.

In this work, we propose a new route to obtain $Ag_{2+x}Se$, which consists of a reactive sputtering method that gives rise to highly crystalline films of controlled stoichiometry in a matter of minutes. We have previously reported the development and fabrication of this new system, namely *Pulsed Hybrid Reactive Magnetron Sputtering* (PHRMS) [24], which is based on a DC reactive sputtering. This method includes a fine control on the amount of selenium present in the alloy, fast growth rate, accurate control over the stoichiometry, and it is easily scalable for industrial production. For more details on the physico-chemistry of the process see ref. 24.

Figure 1 shows the Power Factor ($S^2 \cdot \sigma$) -PF- measurements at room temperature of the different films grown in this work as a function of their compositional ratio Ag/Se, compared to the best values found in the literature for bulk $Ag_{2+x}Se$, discussed above. In our case, the stoichiometry was varied by varying the amount of selenium in the chamber during the deposit of the films.

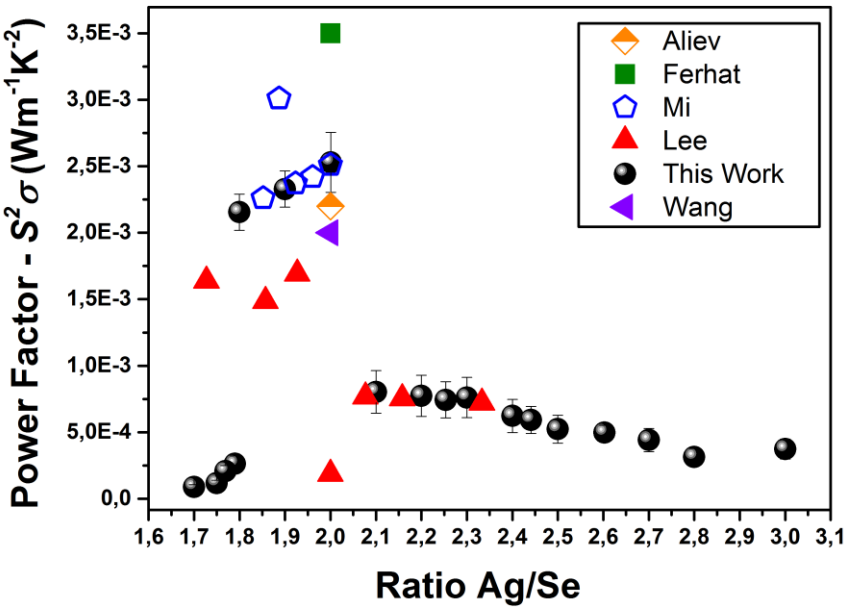

Figure 1. Power Factor as a function of the compositional Ag/Se ratio at room temperature. In black spheres our values obtained for thin films for different Ag/Se rations as grown by PHRMS [24] are shown. In other colors, values reported for the state-of-the-art $Ag_{2-x}Se$ bulk samples: in orange half-full diamond Aliev *et al.*[19] , green squares Ferhat *et al.*[20], blue pentagons Mi *et al.*[22], in red triangles Lee *et al.*[21] and purple triangle Wang *et al.*[23]

From the power factor reported in **Figure 1**, it can be observed that the value of the obtained films measured at room temperature are among the state-of-the-art values when compared with bulk samples[22]. With the PHDMS system used to grow Ag-Se films a PF as high as 2900 $\mu W \cdot m^{-1} \cdot K^{-2}$ at room temperature is obtained for Ag/Se ratio of 2. Although, high PF (above 2000 $\mu W \cdot m^{-1} \cdot K^{-2}$) can be observed in the 1.8>Ag/Se>2 range. This value is noticeable high value for a p-type material, since the best thermoelectric materials for room temperature applications $Bi_{0.5}Sb_{1.5}Te_3$ has a PF around 25 $\mu W \cdot m^{-1} \cdot K^{-2}$.

Nevertheless, it is worth to mention that the control over composition that we achieve is not possible to obtain by other techniques, where the different stoichiometries arise from a not-controlled surplus in the components (excess of selenium, which implies a more isolating nature, or excess of silver, which reduces the Seebeck coefficient). Another advantage of our

technique, the PHRMS, is the possibility of obtaining thin films, which have several advantages over bulk samples, such as being flexible (providing the ability to grow them at room temperature and without further selenization processes on polymers or different flexible substrates), reducing manufacturing costs by using less material inputs, less waste in manufacturing and the possibility of obtaining multiple geometries and coatings of complex parts with a high reproducibility. The different morphologies for the obtained films with different compositions studied with Scanning Electron Microscopy (SEM) can be found in the *supporting information* (**Figure S1**).

Being the highest power factor found for the Ag_2Se (naumannite) stoichiometry, we will focus now on an in-deept study of the properties of these films. It is known that Ag_2Se has two temperature-dependent phases, termed as low-temperature orthorhombic (β)-phase and high-temperature cubic (α)-phase, with the structural phase transition temperature around 133 °C. In the high-temperature phase, the selenium atoms form a body-centred cubic (bcc) packing, while the silver atoms are statistically distributed over several interstitial sites [25]. This is similar to that reported for Cu_2Se [9,10,26,27]. In a similar way, Ag_2Se high-temperature α-phase is characterized by the melting of the silver sublattice along with a liquid-like diffusion of the Ag^+ ions through the defective bcc lattice formed by the Se^- ions, and therefore, it is also known as a superionic phase. Another striking and important characteristic of this phase transition in Ag_2Se is that it is reversible. Nowadays, undertanding these phase transitions in stoichiometric Cu_2Se or Ag_2Se is a hot topic that many authors have approached [10,22,25,28]. One of the major challenges faced in these studies is the rapidity of the transition between semiconductor and superionic conductor. In this sense, Miller *et al.*[29] have observed a reversible switching between the low-temperature β-phase and high-temperature α-phase of Cu_2S in less than 20 ps. In such cases, Ag_2Se was investigated by means of time-resolved temperature dependent synchrotron radiation grazing incidence X-ray diffraction (SR-GIXRD). So the structural changes of the film could be tracked with *in-situ* heating and subsequent controlled cooling, as well as a microstrip detector system that allows fast readout time of about milliseconds to capture the transition. The results of such an experiment with can be found in **figure 2**. The SR-GIXRD diffraction patterns obtained from room temperature to 300 °C and its subsequent controlled cooling to room temperature again in a controlled argon atmosphere are shown. All measurements were carried out in the range of $18° < 2\theta < 62°$. The diffraction pattern shows only two distinct phases. The first phase is the orthorhombic β-phase, associated with low temperature, and appears in the range from room temperature to 125 °C. Its peaks are indexed from the JCPDS card 024-1041 chart, showing

sharp and narrow peaks in 20.3º, 27.5º, 29.8º, 32.8º, 37.8º, 38.4º, 41.4º, 43º and 47.1º, which correspond to the (002), (102), (112), (013), (113), (201), (004), (014) and (114) respectively.

Similarly, from 150ºC and up to 300ºC only the cubic phase (α) is observed, that is, the one corresponding to high temperature. Its diffraction peaks can be indexed by the JCPDS card 04-003-6358 at positions 22.5º, 32.1º, 39.5º and 45.9º, which correspond to the (110), (200), (211) and (311) plans respectively. These values are consistent with literature reports for bulk material and are the first reported for thin films.[30,31]

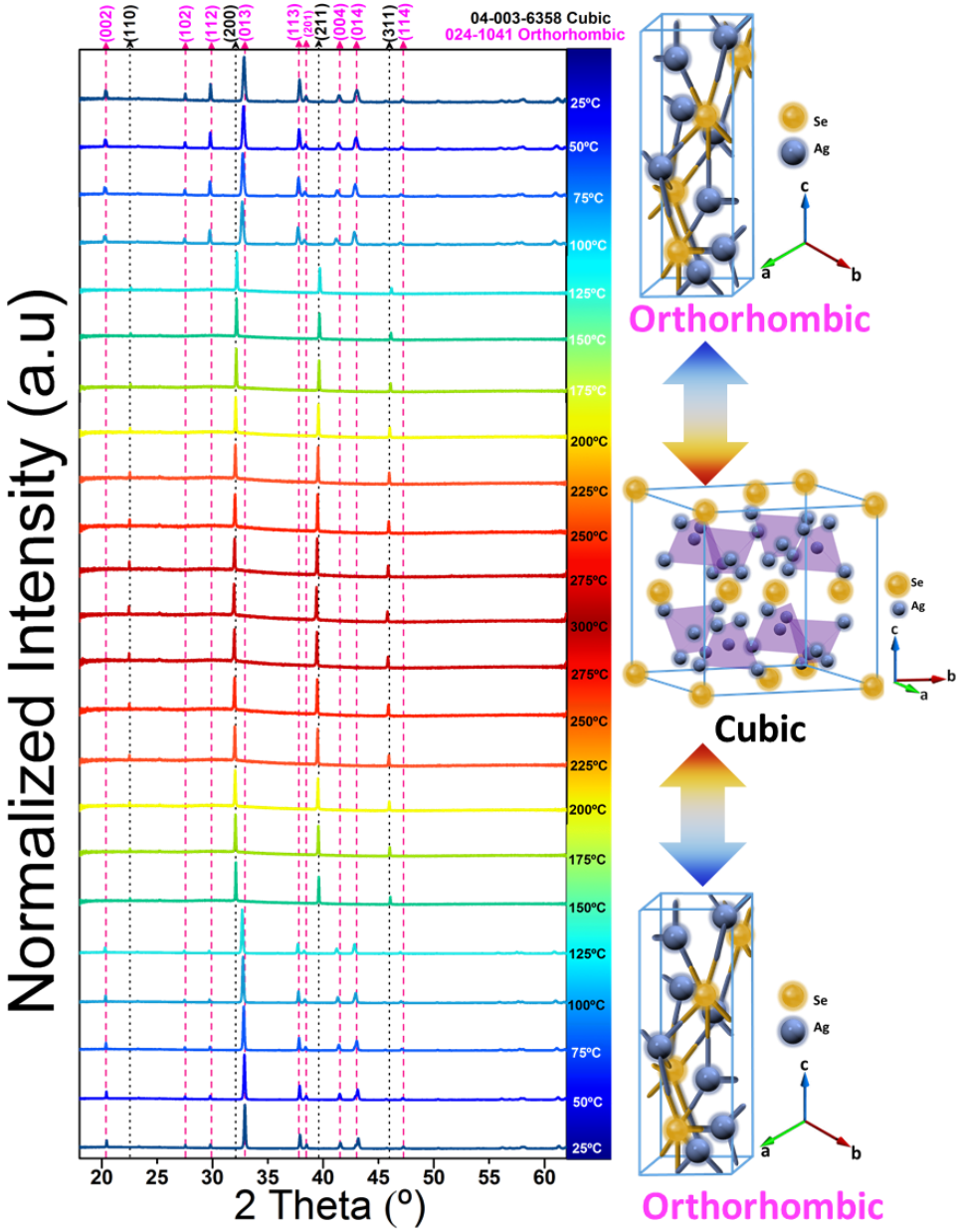

Figure 2: Grazing incidence synchrotron X-ray diffraction (SR-GIXRD) patterns with *in-situ* heating for different temperatures of a heating-cooling cycle. The initial temperature is 25ºC (at the bottom, light blue) and then it was increased up to 300ºC (in red) and then cooled down to 25ºC (up, light blue) while measuring. It can be seen that over 125ºC there is a phase transition from orthorhombic (β) to

cubic (α), which is reversible according to SR-GIXRD when the temperature is decreased again below 125ºC. Orthorhombic β -Ag_2Se and Cubic α -Ag_2Se phases are marked.

In both heating and cooling, silver or selenium segregation is not observed, suggesting that the reversible phase transformation is determined by the intrinsic dynamics of the structure reorganization and not by the probability of a nucleation event.[25,29] It is observed that the critical transition temperature is between 125ºC and 150ºC, being the first time that this complete reversibility phase transition is reported for thin films of Ag_2Se.

This phase transition clearly affects the thermoelectric properties of the Naumannite (Ag_2Se)[13,19,21-23], given that the conduction behavior changes from a semiconductor type to a superionic conductor phase, which results in an increase of the carrier concentration. This effect can be seen for the Ag_2Se film in **Figure 3**, where the carrier concentration (*n*) (**Figure 3a**), the electrical conductivity (σ) (**Figure 3b**) and mobility (μ) (**Figure 3c**) as a function of the temperature are shown. All three measurements have been carried out simultaneously in a nitrogen environment for a temperature range from -190 °C to 500 °C in a commercial equipment for Hall measurements. A zoom of both regions can be found in the *supporting information* **Figure S2** for the low-temperature zone (β-phase) and for the high temperature (α-phase). In the three figures, there are two clearly differentiated areas with a clear transition around 135ºC. The first one, between -190 to 133ºC, marked with a violet background, corresponds to the low temperature orthorhombic β-Ag_2Se region, and the second one (light pink background) corresponds to the high-temperature cubic α-Ag_2Se. In the first region, a typical increase in *carrier concentration* (Figure 3a) and electrical conductivity (Figure 3b) are observed, with values for the carrier concentration which go from $1.67x10^{18}cm^{-3}$ up to $1.33x10^{19}cm^{-3}$, and for the electrical conductivity from 458 $S{\cdot}cm^{-1}$ to 1120 $S{\cdot}cm^{-1}$. The carrier concentration at room temperature is of $6.63x10^{19}$ cm^{-1}. Then, over the transition temperature to the superionic conduction, the carrier concentration increases even more, with a first increase to $3.18x10^{19}$ over 135ºC and reaching values as high as $1.13x10^{20}$ cm^{-3} for 500ºC (Figure 3a). The electrical conductivity also increases drastically at the beginning of this second region, up to a 42% with values as high as 1934 $S{\cdot}cm^{-1}$ at 255ºC, but after this maximum decreases to values around 1400 $S{\cdot}cm^{-1}$ at 500ºC. Finally, **Figure 3c** shows the mobility, which is reduced by 46% in the first region, from 1160 cm^2 $V^{-1}s^{-1}$ at -190 °C to 625 cm^2 $V^{-1}s^{-1}$ at 133 °C in the orthorhombic phase. After a marked decrease at the transition

temperature, from 625 to 427 $cm^2 \cdot V^{-1} \cdot s^{-1}$, the mobility decreases even further, reaching values as low as 269 $cm^2\ V^{-1}s^{-1}$ at 500 ºC.

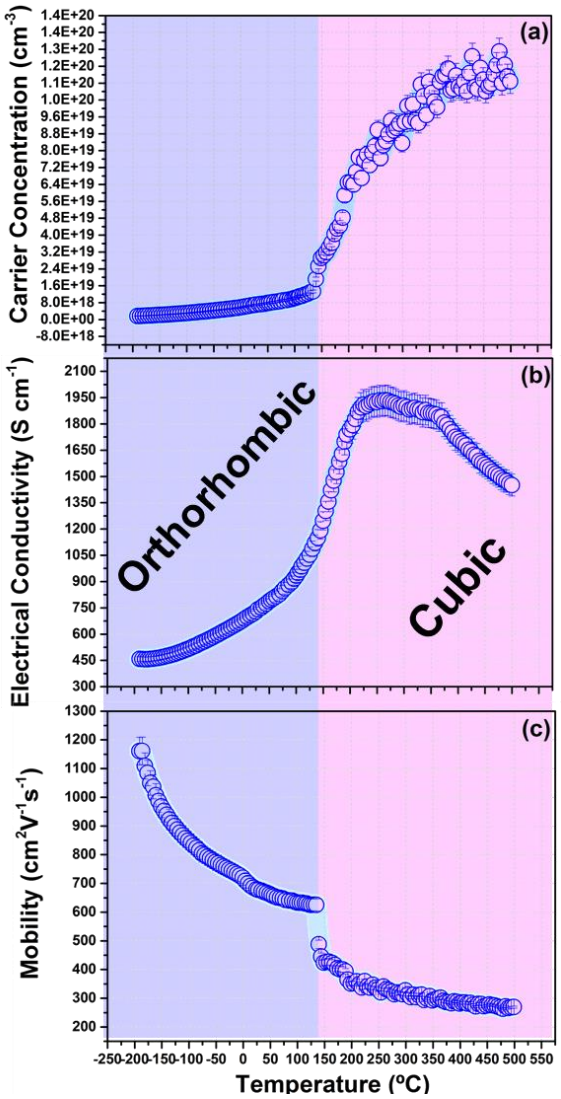

Figure 3: Temperature dependence for **a)** carrier concentration -*n*-, **b)** electrical conductivity -*σ*- and **c)** Hall mobility -*μ*- for the temperature range -190 to 500ºC for the films with Ag_2Se composition.

In order to study if we find an effect on the thermal properties of 300 nm thin Ag_2Se films upon nanostructuration, this parameter was measured at room temperature with the 3ω-Scanning Thermal Microscopy (3ω-SThM) method, shown in **Figure 4**. **Figure 4a** shows the morphological SEM image of the surface of the film, which is similar to the morphology measured by AFM, shown in **Figure 4b**. In both figures, large grains can be distinguished, which present the same composition when measured by EDX. The surface potential image obtained by Kelvin Probe Microscopy is shown in **Figure** 4c, where small changes in the surface potential difference, $\Delta\Phi_{SP,}$ can be found. Some of them are related to changes in the topography height, as it can be seen when the figure is compared with the topographical

images. The other changes found in the surface potential can be associated to silver-rich clusters with sizes from 25 nm to 50 nm of height and with contact potential difference (CPD) around 350 mV. However, the profile of relative CPD in Ag_2Se is quite homogeneous, around 500 mV, indicating a homogeneous work function of the film despite these silver clusters regions (see details of this measurement in the *supporting information*). The Scanning Thermal Microscopy map for the same region is shown in **Figure 4**, where the 3ω voltage measured when the sample is excited with a voltage at a frequency ω is shown. As it can be seen in this thermal image, the thermal conductivity within the big grains is quite homogeneous, and the few variations that can be seen are due to the topography of the sample. Finally, from these data, the thermal conductivity of the film was calculated, obtaining $\kappa = 0.64 \pm 0.1$ $W \cdot m^{-1} \cdot K^{-1}$.

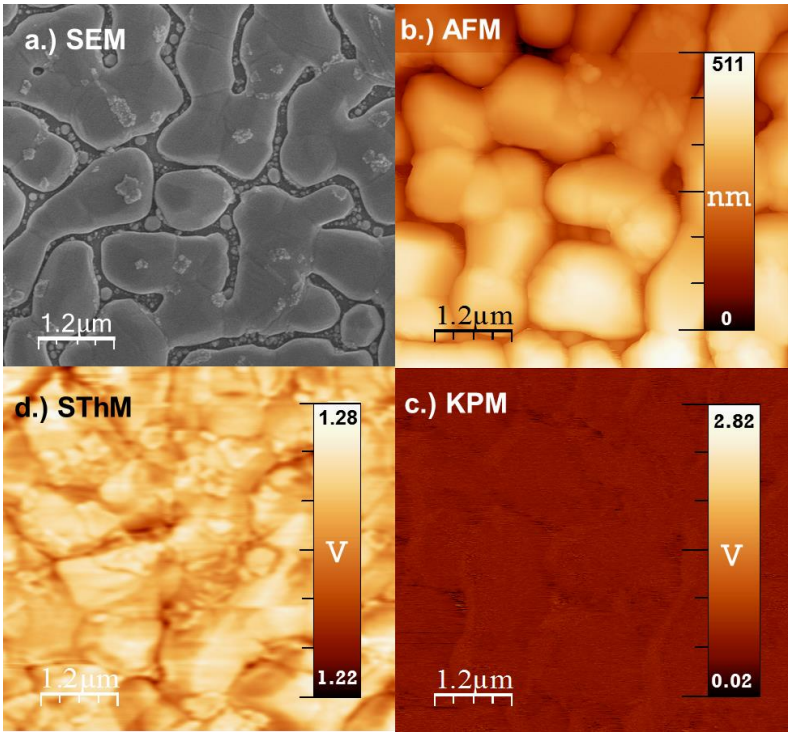

Figure 4: a) SEM micrograph and **b)** Atomic Force Micrograph of the morphology of the surface of the Ag_2Se film. **c)** Kelvin Probe Microscope image and **d)** Scanning Thermal Microscopy images of the same region of the Ag_2Se film.

To fully characterize these Ag_2Se films from a thermoelectrical point of view, the Seebeck coefficient (***S***) as a function of the temperature was measured with ha commercial LSR-3 equipment, in helium environment. Given that the electrical conductivity (σ) is simultaneously measured in this equipment, both S, σ, as well as the power factor (**PF**) are

shown in **Figure 5a**. The Seebeck coefficient shows a value of -244 $\mu V \cdot K^{-1}$ at room temperature, which varies slightly until just before the transition temperature, around 130 °C, suffering a reduction from -248 $\mu V \cdot K^{-1}$ to -94 $\mu V \cdot K^{-1}$ at a temperature of 160 °C. As far as the electrical conductivity, the reproducibility of the measurement when compared with that shown in Figure 3b for a higher temperature range is very good, with the same behavior showed there. From these values, it is clear that the orthorhombic β-phase (marked with violet background) behaves as a semiconductor, with higher Seebeck coefficients than metals, but lower electrical conductivity, and the superionic cubic α-phase (marked with light pink background) presents a drastic reduction of Seebeck coefficient while simultaneously increases the electrical conductivity. This is reflected in the power factor, which has a value at room temperature of 2.5 $mW \cdot m^{-1} \cdot K^{-2}$, which increases to 4m $W \cdot m^{-1} \cdot K^{-2}$ around the transition temperature (130 °C) and then is drastically reduced to 0.2m $W \cdot m^{-1} \cdot K^{-2}$ at 350 °C.

If one takes the value of thermal conductivity at RT, along with the Seebeck coefficient and electrical conductivity for the Ag_2Se film, the resulting *zT* value is as high as 1.2 at room temperature, as it is shown in **Figure 5b**, compared with the state of the art values for different Ag/Se stoichiometries found in the literature. It is worth noting that this value is the highest found for this material, and also a quite competitive one for applications around room temperature, where other materials with *zT* around 1, such as Bi_2Te_3, are commonly used for commercial applications. Finally, **Figure 5c** shows the current zT values at room temperature versus carrier concentration, which is 6.63×10^{19} cm^{-3} in our films, which is very close to the 1.6×10^{18} cm^{-3} value proposed theoretically by Day *et al.*[13] for a maximum *zT* value inAg_2Se.

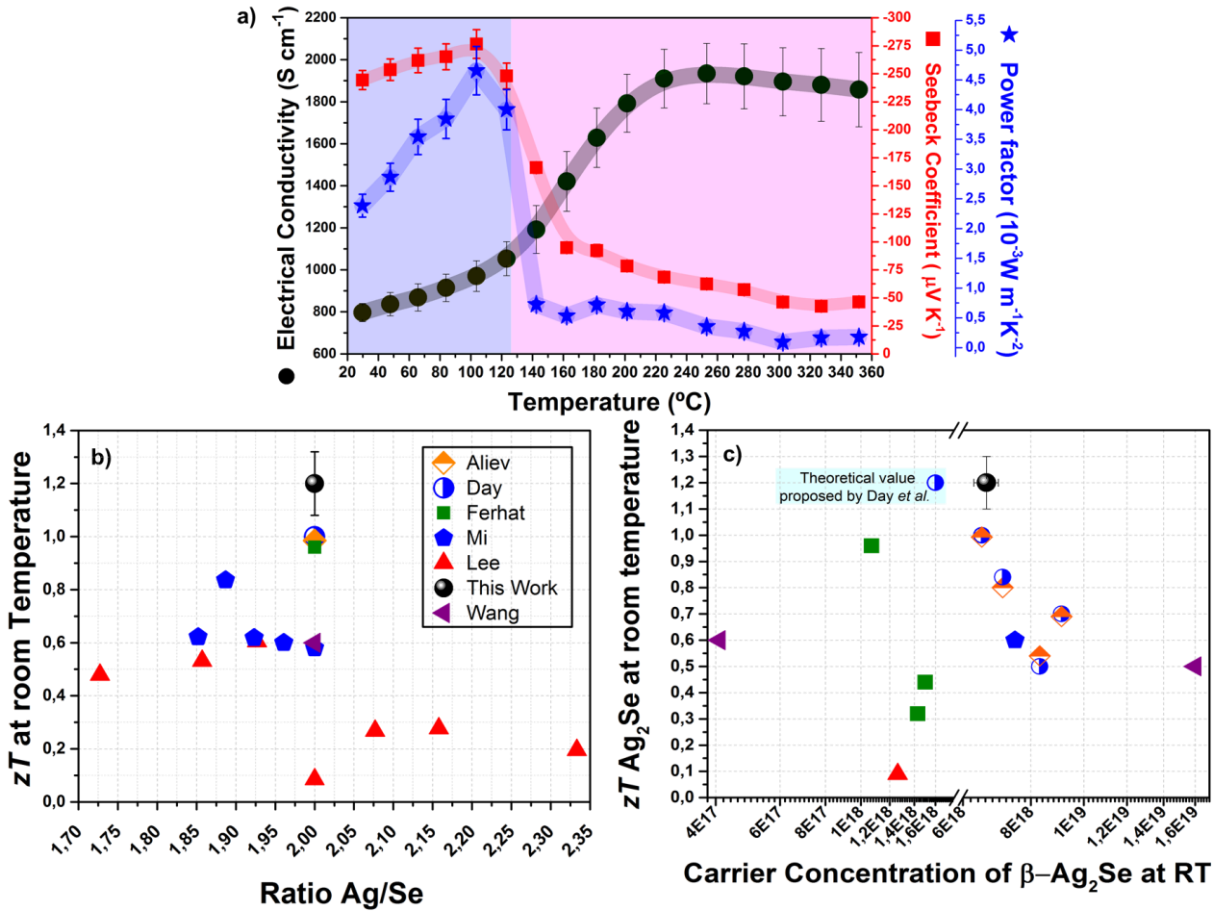

Figure 5: In **a)** Seebeck coefficient values in red boxes, electrical conductivity black dots and blue star power factor depending on the temperature measurement are shown. In **b.)** Figure of merit, *zT* values, at room temperature for different Ag/Se stoichiometries. Our thin films are the highest values due to the drastic reduction in thermal conductivity. In **c.)** the dependence of the different values of *zT* for Ag_2Se at room temperature of the carrier concentration is shown.

In summary, we have presented in this work the growth of thin films of Ag_xSe with a novel method, *Pulsed Hybrid Reactive Magnetron Sputtering* (PHRMS), that allows us to grow thin films of Ag_xSe with controlled stoichiometry in a highly reproducible way. The Power Factors measured for these films are in the state-of-the-art of the material grown in bulk by other techniques, but the fine control over the composition, along with the growth in the way of thin films, opens a door to a higher control of the properties of these films.

The study of how the phase transition affects the different transport properties of the Ag_2Se films has been shown, along with the measurement of the electrical conductivity, Seebeck coefficient, mobility and charge carrier concentration as a function of the temperature for the most stoichiometric film. The surface of the Ag_2Se film, studied with AFM and SEM, shows a very smooth morphology and continuous conduction along the in-plane direction. From these measurements, a maximum Power Factor value around the phase transition temperature was found. Finally, a value of $zT \sim 1.2$ at RT (where the Power Factor is not maximum) has been measured, which is a relatively high thermoelectric figure of merit, even higher than other materials commonly used in thermoelectric devices at RT, such as Bi_2Te_3.

This breakthrough in the manufacture of thin films of A_2Se with high thermoelectric efficiency opens the door to the development of possible thermoelectric devices that can be easily integrated into unusual topologies and maximizing the area of heat absorption, even as flexible devices.

Experimental Section

The samples of this study have been grown on glass substrates via a *Pulsed Hybrid Reactive Magnetron Sputtering* (PHRMS)[24]. The novelty of the process lays in the presence of selenium gas in a controlled way in the chamber, while the target that is being sputtered is made of silver (High purity silver (Ag) target, 4" dia. x 0.25" 5N). Therefore, controlling the silver sputter yield and the amount of selenium in the deposition chamber one can control the stoichiometry of the deposited film, which cannot be achieved by other fabrication methods. The selenium gas is added by a specially designed Selenium effusion cell, which consists of a cell connected to the main deposit chamber by an electromagnetic valve, where selenium powder is evaporated in a controlled way. Then, changing the frequency and opening time of the valve, one can control the selenium pressure in the deposit chamber and thus, the final composition of the film. In this work, the temperature of the substrate was maintained at 300º C, the ultra-pure argon (6N) pressure in the chamber was constant, with values around $6.8 \cdot 10^{-3}$ mbar, and the used DC power is around 60 W. With these conditions, deposition rates up to 38 nm/minute have been achieved. A scheme of the experimental setup is shown in reference[24].

Characterization methods

The structural analysis of films with different copper content was performed at the XRD2 beam-line of the National Synchrotron Light Source at the Brazilian Synchrotron (LNLS) (λ = 1.3775 Å) in the $20° < 2\theta < 65°$. The detector is a Mythen detector 1K from Dectris, mounted on grazing-incidence diffraction, and the measurements were performed at room temperature. The morphology was observed by field emission scanning electron microscopy (SEM) with an FEI Verios 460 at 3 kV accelerating voltage, and chemical composition was determined with a Scanning Electron Microscope (SEM) with Electron-Dispersive X-ray (EDX) analysis JEOL JSM6335F microscope at the Interdepartmental Research Service of the Universidad Autónoma de Madrid (SIdI-UAM). In order to measure the transport properties of the films, a home-made system for measuring the Seebeck coefficient and electrical conductivity at room temperature was used to make the first screening.

The in-plane electrical resistivity and Seebeck coefficient were measured from room temperature to 350ºC using a commercial LSR-3 Linseis® system. This system is periodically calibrated by a constantan standard to ensure its accuracy. Moreover, the Hall coefficient was measured concurrently with the electrical conductivity via the Van der Pauw method at 0.5 Tesla. The Hall carrier concentration and Hall mobility were thereby determined on heating and cooling. The cross–check of the obtained values has been carried out in an Ecopia Hall Effect Measurement System. The film thickness was measured by a profilometer Dektak 150 (Veeco) Then, temperature dependent measurements were carried out with an LSR-3 equipment (from Linseis Messgeräte GmbH) for the Seebeck coefficient and electrical conductivity from room temperature up to 350º C, and a Ecopia HMS-5000 Hall Effect Measurement System was used to measure the electrical conductivity and carriers (from -190 ºC to 500 ºC).

The cross-plane thermal conductivity measurements were carried out at RT in air conditions using scanning thermal microscopy technique and 3ω voltage (3ω-SThM) in active mode, in which the self-heated probe is cooled by transferring heat to the sample. [32] The temperature variations will induce a DC resistance change and AC fluctuations, leading to a voltage rise in the third harmonic or 3ω voltage ($V_{3\omega}$). The electrical signal response due to heat exchange is related to the thermal conductivity of the sample; since this thermoresistive probe is part of a Wheatstone bridge, its resistance changes can be monitored. The voltage difference is amplified by a lock-in amplifier from Zurich Instruments® and the output signal is connected with an AFM from Nanotec Electronica® that acquires simultaneously the

topography and the thermal information of the sample. After a proper calibration process, the thermal conductivity of the sample can be determined (for more details of this technique and calibration procedure, see **Figure 3S** supporting information).

Supporting Information

- SEM images of the cross-section of films with different Ag/Se ratio
- Additional information measures electrical transport function of temperature (for the low-temperature zone (β-phase) and for the high temperature (α-phase)) is shown.
- Additional information of the cross-plane thermal conductivity measurement of the Ag_2Se film by the 3ω -SThM at room temperature is given.

Acknowledgements

This work has been supported by 7th framework European project Nanostructured High-efficiency Thermo-Electric Converters project NANOHITEC 263306, ERC Nano-TEC project, the national project PHOMENTA MAT2011-27911 and Intramural project INFANTE. J. A. Pérez-Taborda acknowledges the Spanish Ministerio de Economía, Industria y Competitividad for their FPI grant. The authors wish to thank the National Synchrotron Light Source at the Brazilian Synchrotron (LNLS)—XRD2 beamline—in Campinas, Brazil, for the SR-GIXRD measurements. The authors acknowledge the X-SEM Laboratory at IMM (VERIOS 460 from FEI) and funding from MINECO under project CSIC 13- 4E-1794 with support from EU (FEDER, FSE).

Keywords

Silver selenide, Sputtering, Thermoelectric materials, Thin films, Thermal conductivity

Received: ((will be filled in by the editorial staff))
Revised: ((will be filled in by the editorial staff))
Published online: ((will be filled in by the editorial staff))

References

[1] S. Teske, C. Lins, M. Hullin, L. Williamson, and A. Fattal, Renewables Global Futures Report: Great Debates Towards 100% Renewable Energy, Report No. 978-3-9818107-4-5, 2017.

[2] J. C. P. H. J. D. A. L. J. T. T. L. Westfall, International Energy Outlook 2016, Report No. DOE/EIA-0484(2016), 2016.
[3] B. Orr, A. Akbarzadeh, M. Mochizuki, and R. Singh, Applied Thermal Engineering **101**, 490 (2016).
[4] J. Twidell and T. Weir, *Renewable energy resources* (Routledge, 2015).
[5] S. Chakraborty, (Patents (Industrial thermoelectric generator), 2016).
[6] A. Lorimer *et al.*, (Patents (Thermoelectric generators for recovering waste heat from engine exhaust, and methods of making and using same), 2015).
[7] D. Champier, Energy Conversion and Management **140**, 167 (2017).
[8] Thermoelectrics: An old, new tech, (Magazine Berkeley Engineer) http://engineering.berkeley.edu/magazine/spring-2016/thermoelectrics-old-new-tech (Accessed 25/04/2017).
[9] H. Liu *et al.*, Advanced Materials **25**, 6607 (2013).
[10] H. Liu *et al.*, Nature Materials **11**, 422 (2012).
[11] Z. H. Ge, X. Liu, D. Feng, J. Lin, and J. He, Advanced Energy Materials **6** (2016).
[12] Y. He, T. Day, T. Zhang, H. Liu, X. Shi, L. Chen, and G. J. Snyder, Advanced Materials **26**, 3974 (2014).
[13] T. Day, F. Drymiotis, T. Zhang, D. Rhodes, X. Shi, L. Chen, and G. J. Snyder, Journal of Materials Chemistry C **1**, 7568 (2013).
[14] M. Ferhat and J. Nagao, Journal of Applied Physics **88**, 813 (2000).
[15] S. LeBlanc, S. K. Yee, M. L. Scullin, C. Dames, and K. E. Goodson, Renewable and Sustainable Energy Reviews **32**, 313 (2014).
[16] G. B. Haxel, J. B. Hedrick, G. J. Orris, P. H. Stauffer, and J. W. Hendley II, Rare earth elements: critical resources for high technology, Report No. 2327-6932, 2002.
[17] B. Gahtori, S. Bathula, K. Tyagi, M. Jayasimhadri, A. Srivastava, S. Singh, R. Budhani, and A. Dhar, Nano Energy **13**, 36 (2015).
[18] L. Zhao, X. Wang, F. Y. Fei, J. Wang, Z. Cheng, S. Dou, J. Wang, and G. J. Snyder, Journal of Materials Chemistry A **3**, 9432 (2015).
[19] F. Aliev, M. Jafarov, and V. Eminova, Semiconductors **43**, 977 (2009).
[20] M. Ferhat and J. Nagao, Journal of Applied Physics **88**, 813 (2000).
[21] C. Lee, Y.-H. Park, and H. Hashimoto, Journal of applied physics **101**, 4920 (2007).
[22] W. Mi, P. Qiu, T. Zhang, Y. Lv, X. Shi, and L. Chen, Applied Physics Letters **104**, 133903 (2014).
[23] H. Wang, W. Chu, D. Wang, W. Mao, W. Pan, Y. Guo, Y. Xiong, and H. Jin, Journal of electronic materials **40**, 624 (2011).
[24] J. A. Perez-Taborda, L. Vera, O. Caballero-Calero, E. Lopez, J. J. Romero, D. G. Stroppa, F. Briones, and M. Martin-Gonzalez, Advanced Materials Technologies (2017).
[25] H. Billetter and U. Ruschewitz, Zeitschrift für anorganische und allgemeine Chemie **634**, 241 (2008).
[26] H. Liu, X. Shi, M. Kirkham, H. Wang, Q. Li, C. Uher, W. Zhang, and L. Chen, Materials Letters **93**, 121 (2013).
[27] X. Xing-Xing, X. Wen-Jie, T. Xin-Feng, and Z. Qing-Jie, Chinese Physics B **20**, 087201 (2011).
[28] C. Xiao, J. Xu, K. Li, J. Feng, J. Yang, and Y. Xie, Journal of the American Chemical Society **134**, 4287 (2012).
[29] T. Miller, J. Wittenberg, H. Wen, S. Connor, Y. Cui, and A. Lindenberg, Nature communications **4**, 1369 (2013).
[30] J. Yu and H. Yun, Acta Crystallographica Section E: Structure Reports Online **67**, i45 (2011).
[31] M. Oliveria, R. McMullan, and B. Wuensch, Solid State Ionics **28**, 1332 (1988).
[32] A. Majumdar, Annual review of materials science **29**, 505 (1999).